



**AFRL-AFOSR-VA-TR-2017-0012**

---

**OPTICALLY CONTROLLED DISTRIBUTED QUANTUM COMPUTING  
USING ATOMIC ENSEMBLES AS QUBITS**

**Selim Shahriar  
NORTHWESTERN UNIVERSITY  
633 CLARK ST EVANSTON  
EVANSTON, IL 60208-0001**

---

**01/05/2017  
Final Report**

**DISTRIBUTION A: Distribution approved for public release.**

Air Force Research Laboratory  
AF Office Of Scientific Research (AFOSR)/RTA1

# REPORT DOCUMENTATION PAGE

Form Approved  
OMB No. 0704-0188

Public reporting burden for this collection of information is estimated to average 1 hour per response, including the time for reviewing instructions, searching data sources, gathering and maintaining the data needed, and completing and reviewing the collection of information. Send comments regarding this burden estimate or any other aspect of this collection of information, including suggestions for reducing this burden to Washington Headquarters Service, Directorate for Information Operations and Reports, 1215 Jefferson Davis Highway, Suite 1204, Arlington, VA 22202-4302, and to the Office of Management and Budget, Paperwork Reduction Project (0704-0188) Washington, DC 20503.

**PLEASE DO NOT RETURN YOUR FORM TO THE ABOVE ADDRESS.**

1. REPORT DATE (DD-MM-YYYY) 23-02-2016	2. REPORT TYPE FINAL	3. DATES COVERED (From - To) 15-08-2009 to 14-08-2015
4. TITLE AND SUBTITLE OPTICALLY CONTROLLED DISTRIBUTED QUANTUM COMPUTING USING ATOMIC ENSEMBLES AS QUBITS		5a. CONTRACT NUMBER
		5b. GRANT NUMBER FA9550-09-01-0652
		5c. PROGRAM ELEMENT NUMBER
6. AUTHOR(S) Selim M. Shahriar		5d. PROJECT NUMBER
		5e. TASK NUMBER
		5f. WORK UNIT NUMBER
7. PERFORMING ORGANIZATION NAME(S) AND ADDRESS(ES) Northwestern University 1801 Maple Ave. 2nd Floor, Suite 2410 Evanston, IL 60201-3149		8. PERFORMING ORGANIZATION REPORT NUMBER AFOSR-QC-FIN
9. SPONSORING/MONITORING AGENCY NAME(S) AND ADDRESS(ES) Air Force Office of Scientific Research 875 North Randolph Street Arlington, Virginia 22203-1768 USA		10. SPONSOR/MONITOR'S ACRONYM(S) AFOSR
		11. SPONSORING/MONITORING AGENCY REPORT NUMBER
12. DISTRIBUTION AVAILABILITY STATEMENT DISTRIBUTION A: Distribution approved for public release.		
13. SUPPLEMENTARY NOTES		
14. ABSTRACT The goal of this project was to demonstrate the feasibility of realizing a large quantum computer by linking a series of elementary quantum computers (EQCs), using ensembles of atoms as qubits. We built all the tools for making an EQC. However, experimental work revealed that use of light shift imbalance only is not enough to achieve the required blockade. We have now shown why this is the case, and have identified how the blockade can be restored by using Rydberg interaction assisted light-shift imbalance. However, due to lack of necessary lasers, we were unable to demonstrate the EQC using this scheme. Instead, we focused on exploring other aspects of collective state entanglement for precision metrology. Specifically, we have shown how to realize spin-squeezed collective state atomic interferometer (COSAIN) and collective state atomic clock (COSAC), capable of improving the performance by a factor of root-N, thus reaching the Heisenberg limit. Significant experimental work has been carried out to demonstrate these devices, and this work will be carried to completion in the near future.		
15. SUBJECT TERMS Quantum Computing, Quantum Communication, Atomic Ensemble, Quantum Bit, Light-Shift, Rydberg-Excitation, Spin-Squeezing, Collective-State-Atomic-Clock, Collective-State-Atomic-Interferometer, Entanglement		
16. SECURITY CLASSIFICATION OF:		17. LIMITATION OF ABSTRACT Same as Report
a. REPORT Unclassified	b. ABSTRACT Unclassified	c. THIS PAGE Unclassified
18. NUMBER OF PAGES 124	19a. NAME OF RESPONSIBLE PERSON Selim M. Shahriar	
		19b. TELEPHONE NUMBER (Include area code) 847-491-5306

**OPTICALLY CONTROLLED  
DISTRIBUTED QUANTUM COMPUTING  
USING ATOMIC ENSEMBLES AS QUBITS**

*AFOSR Grant #: FA9550-09-01-0652*

**Final Progress Report**

*Period Covered: 8-15-09 to 8-14-15*

*Submitted by:*

*Prof. Selim M. Shahriar, PI*

*Department of Electrical Engineering and Computer Science  
Department of Physics and Astronomy  
Northwestern University, Evanston, IL 60208*

## SUMMARY

The goal of this project is to develop the technology for producing high-fidelity quantum bits that can be entangled to one another, thus forming an elementary quantum computer (EQC), and the ability to link multiple EQCs via quantum channels, thus forming a distributed quantum computer (DQC). To achieve this goal, atomic ensembles of trapped Rb atoms are to be used as quantum bits (qubits). Ordinarily, a single atom restricted to a two-level transition is used as a quantum bit. Two such qubits can be coupled to one another by exchanging quantum states through a cavity photon. However, the coupling of a single atom to a cavity photon is rather weak, so that a very high finesse cavity with extremely small mode volume is needed, making the process very difficult to implement in practice. A possible solution to this problem is to use collective excitations in a cluster of atoms, which couple very strongly to a cavity photon, so that a low-finesse, high mode volume cavity would suffice. However, even if each atom in a cluster is restricted to a two-level transition, the collective excitations lead to a cascade of many degenerate transitions, thus making it apparently impossible to use the cluster as a quantum bit. We proposed to use the technique of light shift blockade to truncate this cascade to just two levels, so that the whole cluster can act as a single qubit.

We realized experimentally all the tools necessary for implementing the collective state qubits. These included realization of an ensemble of trapped atoms which were then further cooled using the technique of polarization-gradient cooling, transferring the atoms to an array of dipole force traps using a launch-and-capture system, realization of a quantum motor to move the trapped ensembles around, and placing an optical cavity around the array of ensembles, all inside a large chamber maintained at ultra-high vacuum. Given the limited resources allocated to this project, coupled with the inordinate degree of difficulty of the task, building these tools took a very long time. We then proceeded to demonstrate the light shift blockade effect. For this demonstration, we realized a Hanbury-Brown-Twiss interferometer to measure the so-called  $g_2$  correlation signal. If the blockade occurred as expected, this signal would have a dip in the middle. However, the experiment revealed no such dip in the signal. In order to understand this result, we revisited our theoretical model for the light-shift blockade, and determined that our scheme had to be augmented by adding a Rydberg excitation. The analysis that shows how the Rydberg-aided light-shift blockade would work has been published in a peer-reviewed journal. We did not have the additional lasers necessary to implement the Rydberg excitation. We submitted a DURIP proposal seeking this additional equipment. Unfortunately, this proposal was not funded, thus making it impossible to make further progress in the development of the ensemble-based qubits.

As such, we embarked on exploring, theoretically as well as experimentally, other applications of atomic ensembles, without the need for Rydberg interaction, and made several very important discoveries, most of which have already been published in peer-reviewed journals, and two additional manuscripts are under preparation. Specifically, we have shown that it is possible to realize Collective State Atomic Clocks (COSACs) and Collective State Atomic Interferometers (COSAINs) using atomic ensembles. For an ensemble with  $N$  non-interacting atoms (where  $N$  is typically of the order of  $10^6$ ), the

fringes for both COSAC and COSAIN get narrowed by a factor of  $\sqrt{N}$ . Our analysis shows that the COSAC and the COSAIN are expected to be nearly a factor of ten more sensitive than the conventional atomic clocks and atomic interferometer, respectively. When augmented by the technique of spin-squeezing, the COSAC and COSAIN can lead to an improvement in sensitivity by a factor close to  $\sqrt{N}$ , thus achieving the ultimate sensitivity (the so-called Heisenberg-limited sensitivity) allowed by the laws of quantum physics. We have shown that Rydberg-aided light-shift blockade can be used to implement efficiently the process of so-called two-axes-counter-twist (TACT) spin squeezing for achieving Heisenberg-limited sensitivity with the COSAC and the COSAIN. We have already demonstrated an resonant Raman atomic clock to be used as the platform for realizing the COSAC, and optically off-resonant Raman excitation to be used as the platform for realizing the COSAIN, and expect to demonstrate the operation of the COSAC and the COSAIN within the next three months. This will be followed by realization of TACT spin-squeezing for both the COSAC and the COSAIN.

## A. OVERVIEW OF COLLECTIVE STATE QUANTUM COMPUTING AND COMMUNICATION

In this section, we review briefly the goal of this project, and the approach for achieving these goals.

Figure 1 shows a schematic illustration of the lowest order collective state of  $N$  atoms in a two level system. The ground state of the ensemble is where each atom is in

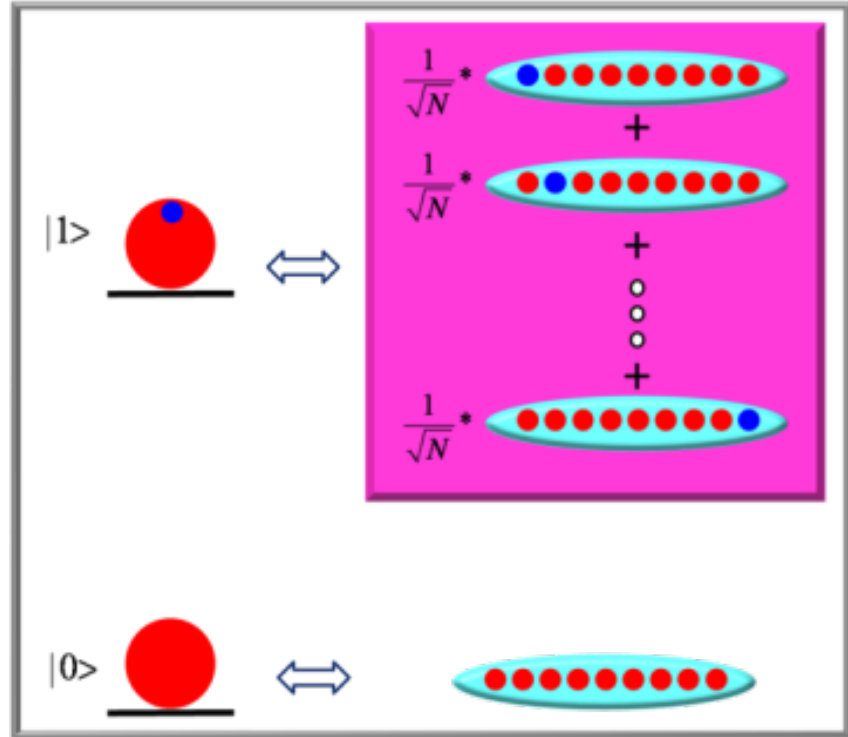


Figure 1: Schematic Illustration of first order collective state of  $N$  atoms in a two level system. the ground state. The first excited state of the ensemble is a superposition of  $N$  states,

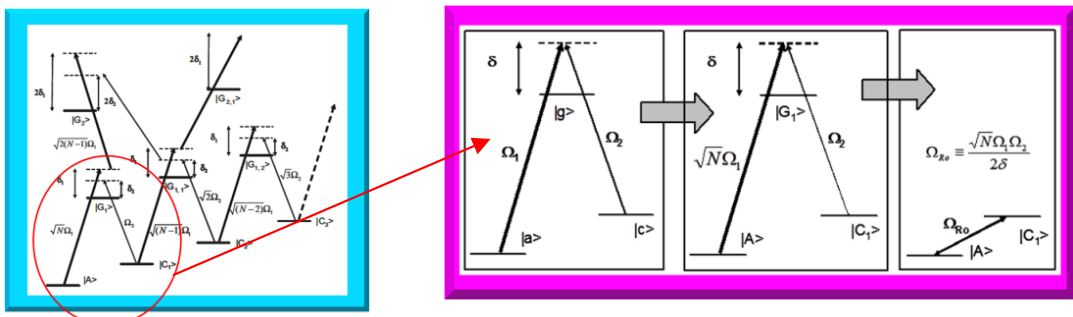


Figure 2: Schematic illustration of how light shift blockade truncates excitations, leading to a qubit.

where in each state only one atom is in the excited state. The next excited collective state (not shown) would be a superposition of states, each of which has two atoms in the excited states, and so on. These collective states are excited only when the interaction Hamiltonian is identical for each atom.

Figure 2 shows how light shift blockade truncates excitations, leading to a qubit. In a three level system, excited by two laser fields, the higher-order excitations lead to a cascade of excited collective states. Under Light Shift Blockade, only the lowest order

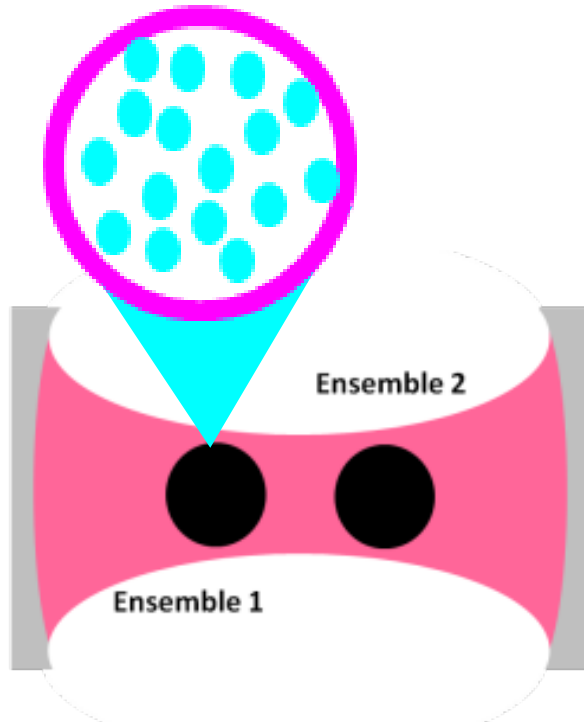


Figure 3: Schematic illustration of two ensembles of atoms held inside an optical cavity..

collective excitation states participate in the interaction. This corresponds to a three level system, shown in the red circle. If the lasers are detuned, this three level system reduces to a two level system. The next result is that the ensemble of atoms now behave as a single two level system --- a qubit.

To couple two ensemble qubits, two ensembles are placed inside a cavity, as shown in figure 5. The quantum state of one qubit is transferred to the quantum state of the cavity

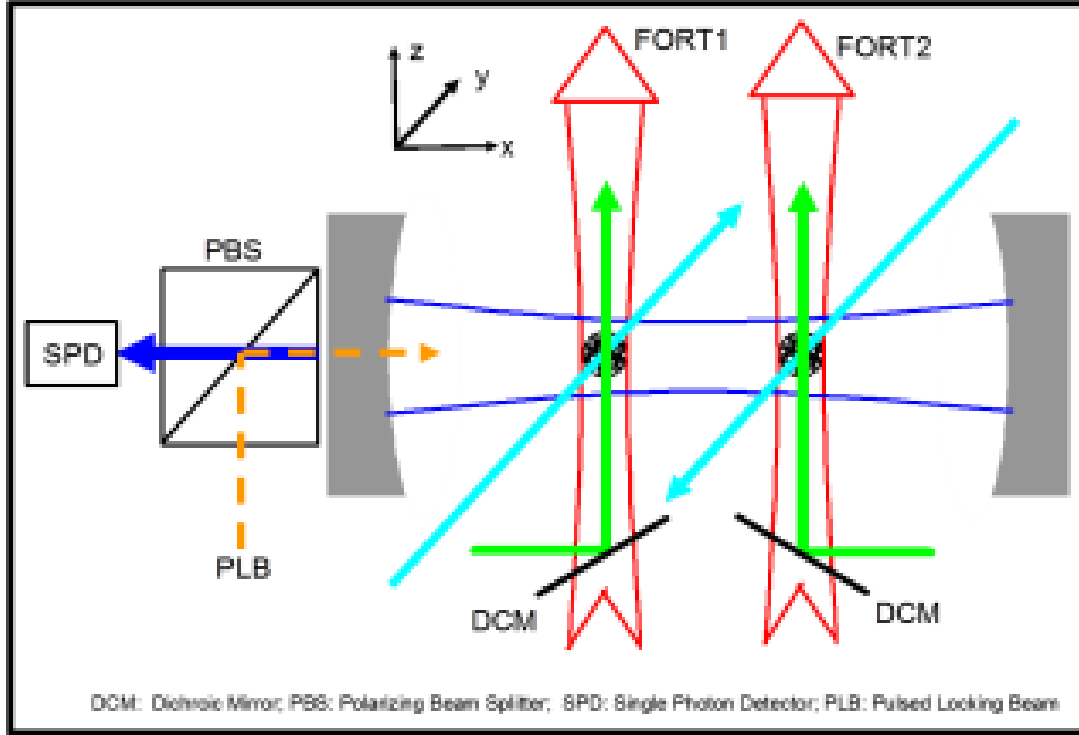


Figure 4: Schematic illustration of the CNOT gate operation using two ensemble qubits held inside a cavity. The CNOT operation is carried out by exchanging quantum information via the cavity photon, with the help of the control laser beams.

photon mode, shown in red in figure 3. The quantum state of the cavity mode is then transferred to the second qubit. Transitions carried out inside the second qubit can be used to realize a Controlled-NOT (CNOT) operation, which is a universal gate for quantum computation. Externally applied control laser are used to carry out these operations, as illustrated schematically in figure 4.

Figure 5 illustrates in some detail the basic architecture of the EQC. Briefly, we start with a magneto-optic trap (MOT), engineered in a compact fashion. Once the atoms are cooled and trapped in a MOT, we turn on a far-off-resonant-trap (FORT) beam, which is imaged through an array of pinholes in order to produce an array of three-dimensional FORT trapping potential wells. Each potential well holds an ensemble of  $^{87}\text{Rb}$  atoms. At a given time, a pair of these ensembles are within the mode volume of a cavity, as shown. Through a series of steps, a CNOT gate operation between these two qubits is carried out, thus entangling this pair. After this is done, the pinhole array is moved using a piezo-driver, and an ensemble qubit enters the cavity mode volume. This qubit can now be entangled with the other qubit. By repeating this procedure, all nearest

neighbors can be entangled to each other, thus realizing the EQC.

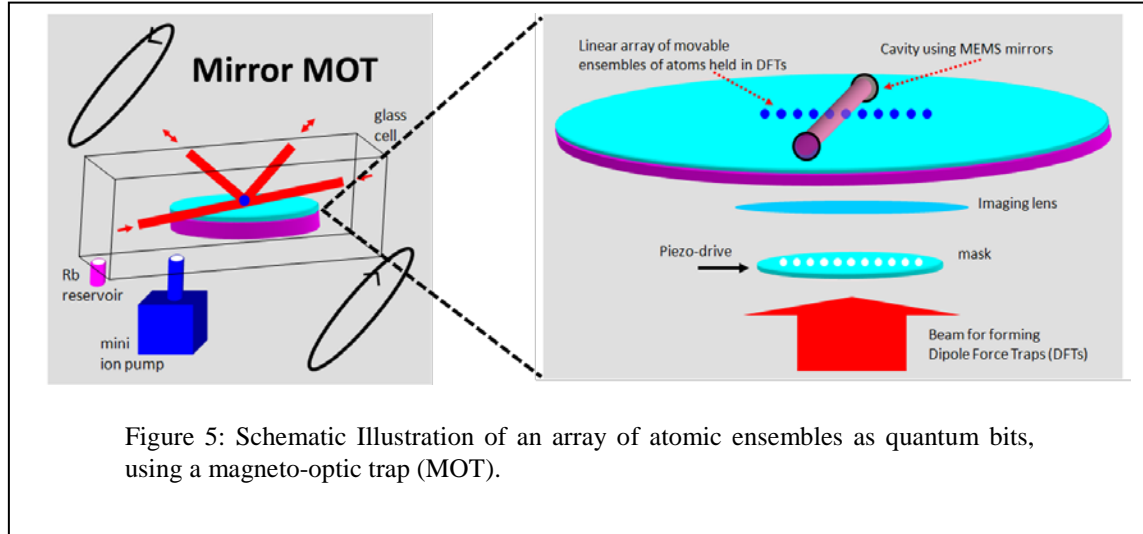


Figure 5: Schematic Illustration of an array of atomic ensembles as quantum bits, using a magneto-optic trap (MOT).

The qubits from one EQC can be connected via a quantum communication link,

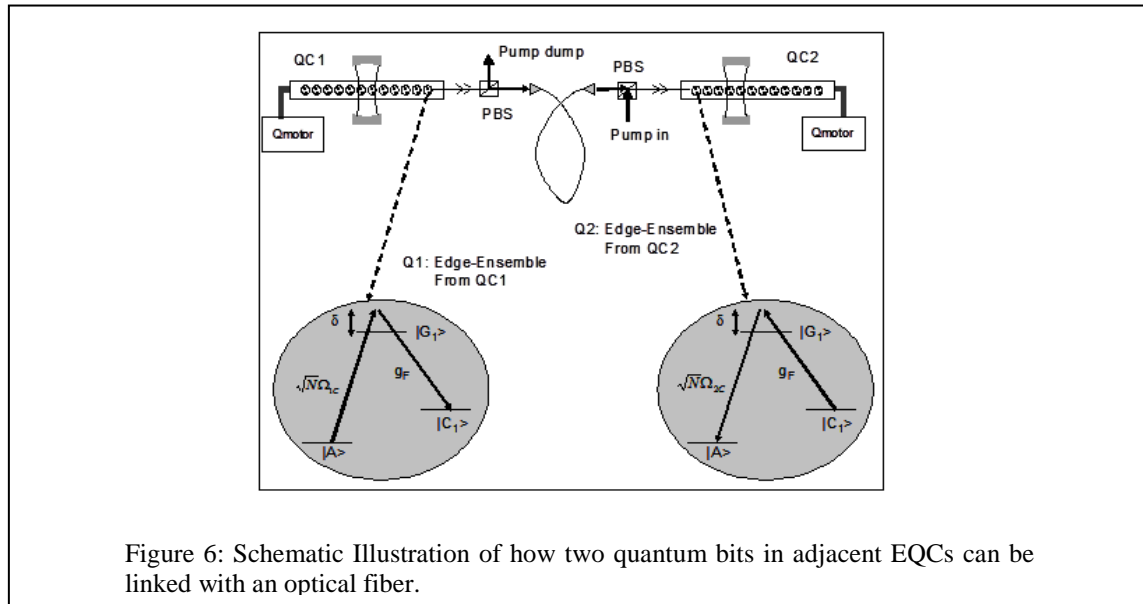
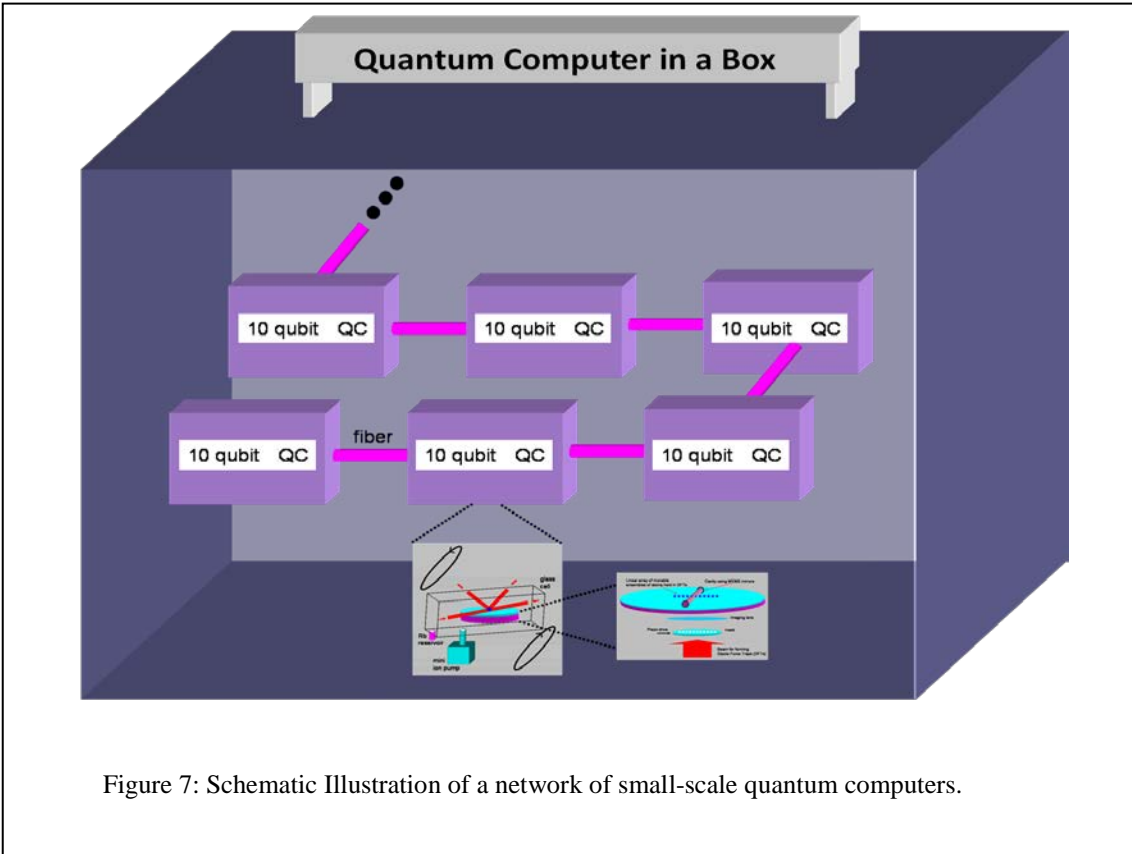


Figure 6: Schematic Illustration of how two quantum bits in adjacent EQCs can be linked with an optical fiber.

implemented with optical fibers, to the qubits from another EQC. This is illustrated schematically in figure 6.

Figure 7 illustrates schematically the overall objective. Briefly, our primary goal was to use ensembles of trapped atoms to create a small scale (e.g., ten coupled qubits) elementary quantum computer (EQC). Another goal was to demonstrate quantum links between a pair of EQCs, using optical fiber. This would then establish the feasibility of a large scale quantum computer by linking many of these EQCs.



## B. DETAILS OF TECHNICAL WORK DONE

As the first task for this project, we built a Magneto-Optic Trap (MOT) in a configuration that is compatible with the mirror-MOT geometry. For this MOT, we used a relatively small vacuum chamber. It was connected to a sorption pump as well as an

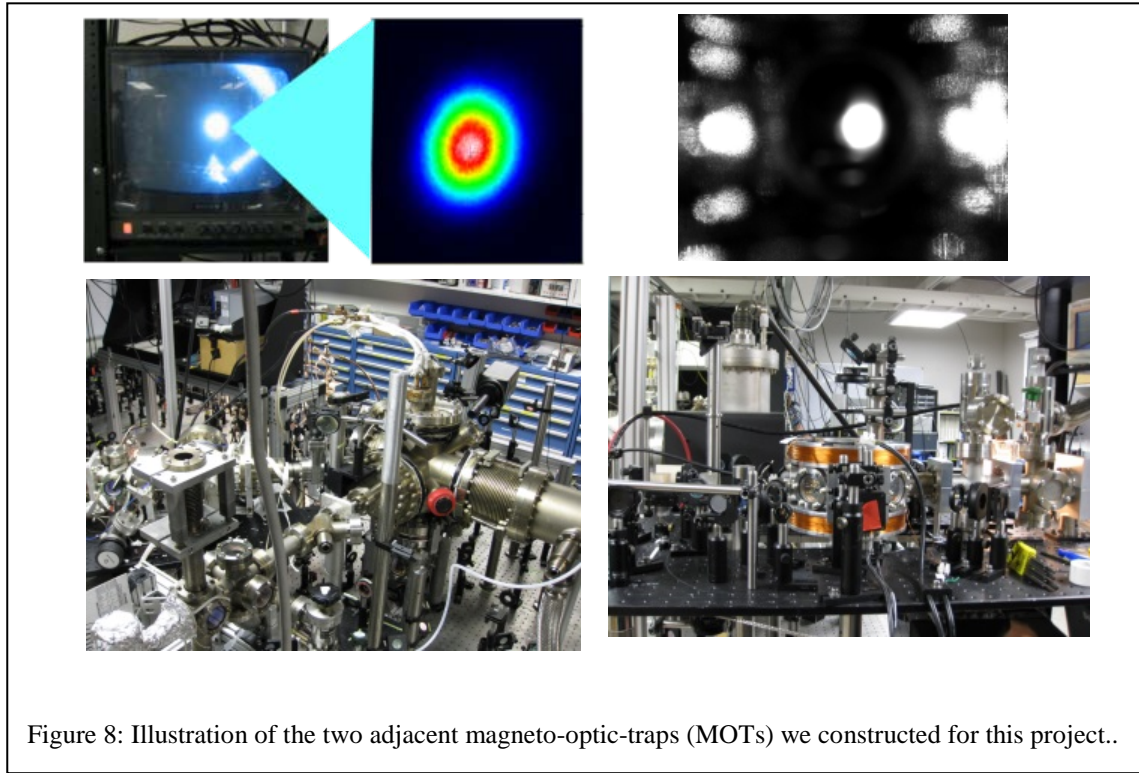


Figure 8: Illustration of the two adjacent magneto-optic-traps (MOTs) we constructed for this project..

ion pump. The sorption pump was used for pumping the system down to a vacuum low enough for starting the ion pump. Once the ion pump was started, the sorption pump port was valved-off. The ion pump allowed us to reach a vacuum as small as  $1 \times 10^{-10}$  Torr in the absence of any Rubidium in the chamber. The two anti-Helmholtz coils for producing the three-dimensional magnetic field gradients at the center were placed outside the trap chamber. In this configuration, it was not necessary to cool the coils with a water flow. A picture of the trap assembly is shown in the bottom right part of figure 8. A typical cloud of cold atoms caught in this MOT is shown in the top right part of figure 8.

In addition, we built another MOT, using a larger chamber. This was pumped down in the same way, using a sorption pump followed by a large ion pump. We were able to reach a vacuum as small as  $7 \times 10^{-11}$  Torr in this chamber. For this MOT, the magnet coils were placed inside the chamber, which were cooled with flowing water during operation of the MOT. This MOT is shown in the bottom right part of figure 8. A typical cloud of cold atoms caught in this MOT is shown in the top left part of figure 8.

In order to realize collective quantum bits, it is necessary to cool atoms further after they are trapped in MOTs. To this end, we implemented the so-called polarization-gradient

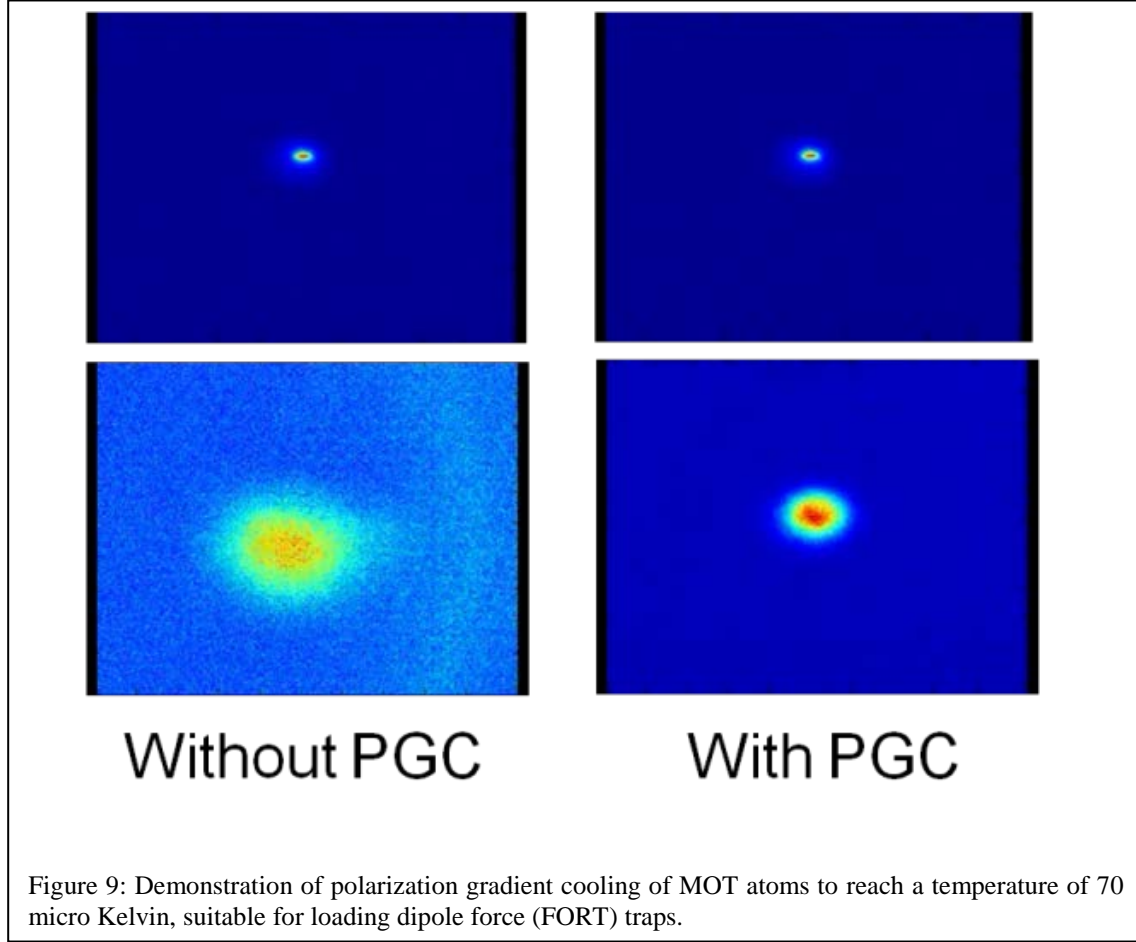
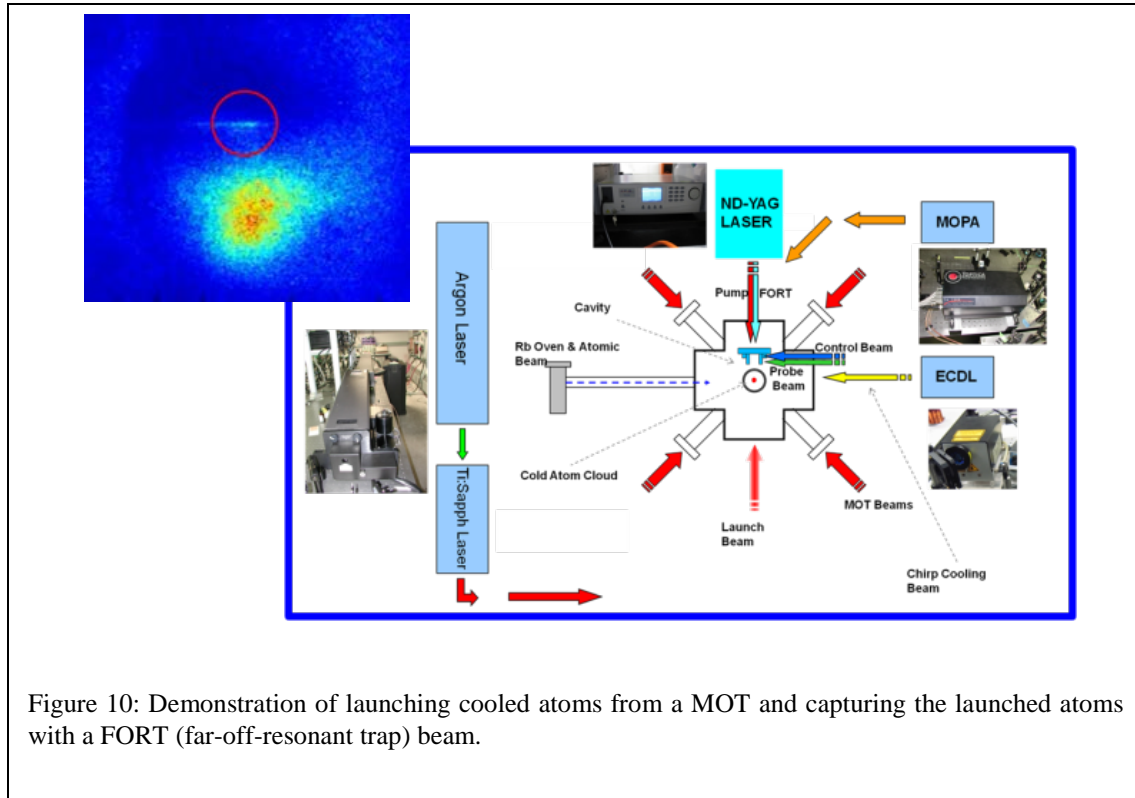


Figure 9: Demonstration of polarization gradient cooling of MOT atoms to reach a temperature of 70 micro Kelvin, suitable for loading dipole force (FORT) traps.

cooling (PGC) to cool atoms down to 70 micro-kelvin. The temperature was measured by monitoring the expansion of the trapped cloud. The left column in figure 9 shows the initial cloud on top, and the expanded cloud on bottom, without PGC. The right column in figure 9 shows the corresponding clouds in the presence of PGC. As can be seen, the cloud expands much less since the atoms are colder.

Another important step in realizing collective quantum bits is capturing the atoms in the arrays of FORT after they are pushed (launched) in the vertical direction out of the MOT. In figure 10, we show our implementation of this step for the case when the FORT consists of a single focused beam. The figure shows the various components and tools used for this experiment. Specifically, the trapping beams for the MOT were generated from a Ti:Sapphire laser pumped by an Argon ion laser. The repump beams were produced by a master-oscillator power amplifier (MOPA) laser. The frequency chirped beam for slowing the atomic beam that loads the MOT was produced by an external cavity diode laser (ECDL). The beams for launching the atoms vertically were derived from variants of the MOT beams, using additional acousto-optic modulators. The FORT (far-off-resonant trap) beam was generated by focusing a beam from an Nd:YAG laser.

The FORT beam was centered between two partially reflected mirrors forming a cavity.



The probe and control beams for manipulating the quantum state of the trapped atoms were produced from yet another ECDL. The inset (left corner) shows the captured atoms in the red circle, with the un-captured part of the cloud dropping down.

Once the FORT was demonstrated using a single beam, we proceeded to realize an array of trapped atoms, as a key step for making a series of coupled quantum bits (i.e., an elementary quantum computer: EQC). In this process, we started with an optical mask containing ten pin-holes arranged in an array. An Nd:YAG beam passed through this mask was imaged inside the trap chamber, thus forming an array of ten adjacent FORT potentials. These potentials were positioned between the mirrors of a cavity, as shown in the middle inset of figure 11. Atoms caught in a MOT and cooled further with polarization gradient cooling were launched vertically, and the array of FORTs were turned on once the atoms reached the center of the cavity. The density profile of the captured array of atoms, measured with a camera, is shown in the stand-alone inset of figure 11. These arrays can be moved around by moving the pin-hole array which is imaged to produce the FORT potentials, thus realizing a so-called quantum motor. This quantum motor can be used to move a pair of adjacent trapped ensemble of atoms into the volume of the cavity mode for CNOT gate operation between them.

Before attempting to carry out the CNOT gate operation between two adjacent

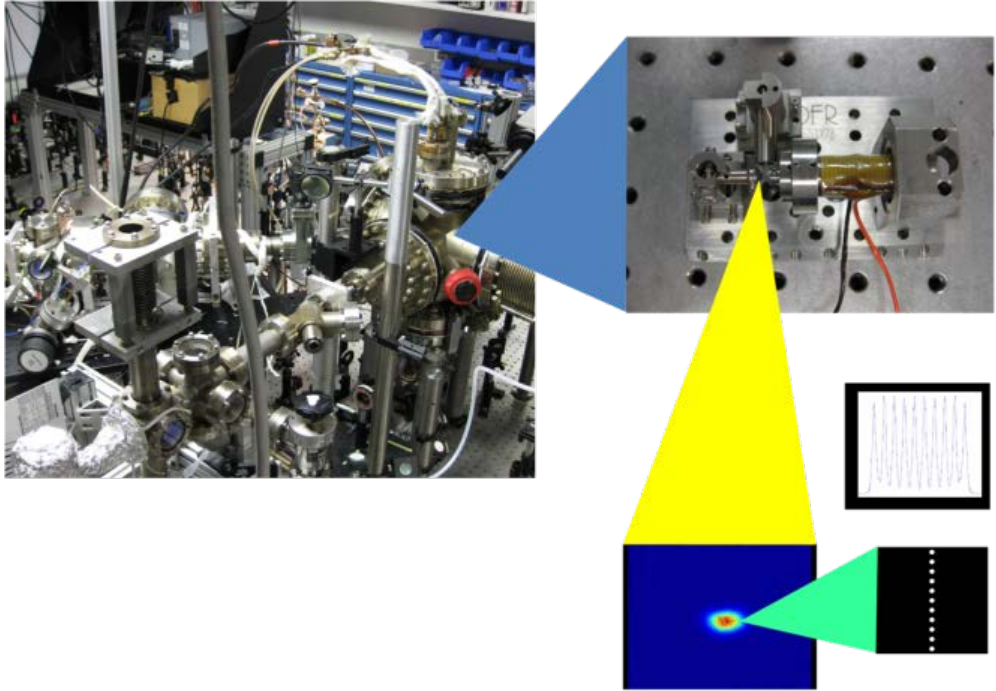


Figure 11: Realization of a quantum motor, an array of ten atomic clusters, located between the mirrors of a cavity inside the trap chamber.

ensembles, it was necessary to establish first the presence of light shift induced blockade

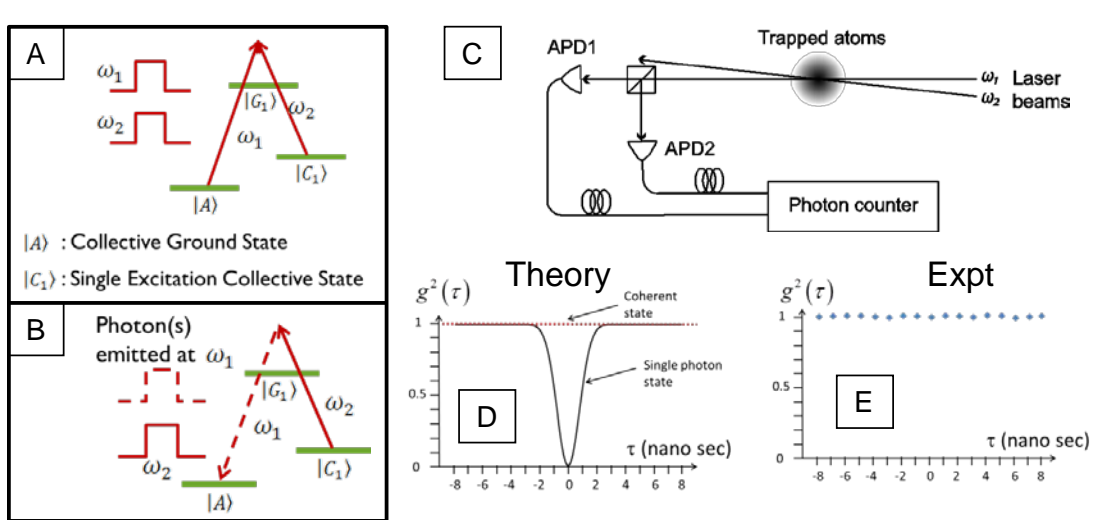


Figure 12: Illustration of the test we carried out to observe evidence of light shift induced blockade. See text for details..

of collective excitation. We carried out an experiment to observe this blockade effect in an ensemble. The steps of this experiment are illustrated schematically in figure 12.. The

panel on the left shows [A] the excitation process, which is an optically detuned but two-photon resonant Raman transition, followed by [B] the testing process where we apply only one of the two Raman beams as a read pulse. The signal at the frequency corresponding to the other transition is observed with a Hanbury-Brown-Twiss

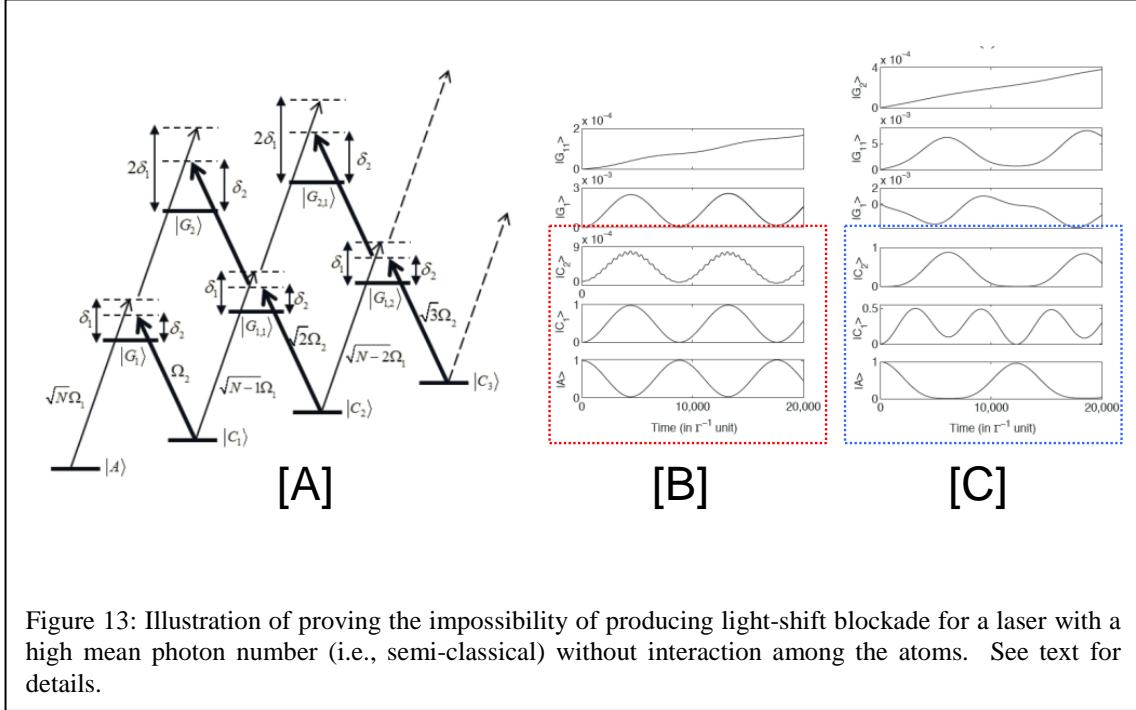


Figure 13: Illustration of proving the impossibility of producing light-shift blockade for a laser with a high mean photon number (i.e., semi-classical) without interaction among the atoms. See text for details.

interferometer (as shown on the right) which shows the so-called  $g^2$  correlation function. If the blockade effect is present, then the resulting signal would have a single photon, which will correspond to a dip in the center of the  $g^2$  function. Experimentally, we were unable to see such a dip under any condition. This led us to review our theory for the light shift blockade, which in turn led to the conclusion that a Rydberg excitation must be added to the system to produce such a blockade, which would then enable us to proceed with realizing single quantum bits and coupled quantum bits using ensembles.

The null result observed in the detection of single photons by the ensemble, as described in the bottom-right corner of figure 13, led us to review our theory for the light shift blockade, which in turn led to the conclusion that without additional non-linear interaction (such as Rydberg excitation), it is impossible to produce the desired blockade. Figure 13[A] shows the first few collective states in an N-atom, non-interacting system. When we ignore the cascaded two-photon excitations (such as to states  $|G_2\rangle$  and  $|G_{21}\rangle$ ), the system oscillates primarily between  $|A\rangle$  and  $|C_1\rangle$ , as shown in figure 13[B]. When these cascaded two photon excitations are taken into account, we see that excitation to  $|C_2\rangle$  is no longer suppressed, as shown in figure 13[C]. This has also been verified by exact numerical calculation for two atoms [Refs: Paper Number C3 and Paper Number C4 in Section D].

As mentioned above, Rydberg excitation can restore the blockade effect. Figure 14[A] shows the addition of Rydberg excitation (which requires a two photon transition) on one

of the legs creates an asymmetry. When two atoms are present simultaneously in the  $|c\rangle$  state (corresponding to the  $|C_2\rangle$  collective state), each of them wants to get excited to the Rydberg state. However, the size of the atoms (extent of the wave-function) for high-n Rydberg state become comparable to the interatomic distance, so that there is dipole-dipole interaction between the atoms, which lowers significantly the energy of the  $|rr\rangle$  state. As a result, the light shift experienced by the  $|C_2\rangle$  collective state is smaller than that experienced by the  $|C_1\rangle$  collective state. The Raman detuning for the a-c transition is now tuned to make the  $|A\rangle$  to  $|C_1\rangle$  transition resonant, while the  $|C_1\rangle$  to  $|C_2\rangle$  transition is off-resonant. This prevents excitation to  $|C_2\rangle$ , thus realizing the blockade effect needed for realizing single and coupled quantum bits, and thereby quantum computing. Figure 14[B] shows that excitation to  $|C_2\rangle$  (which is called  $|CC\rangle$  here) is not blockaded

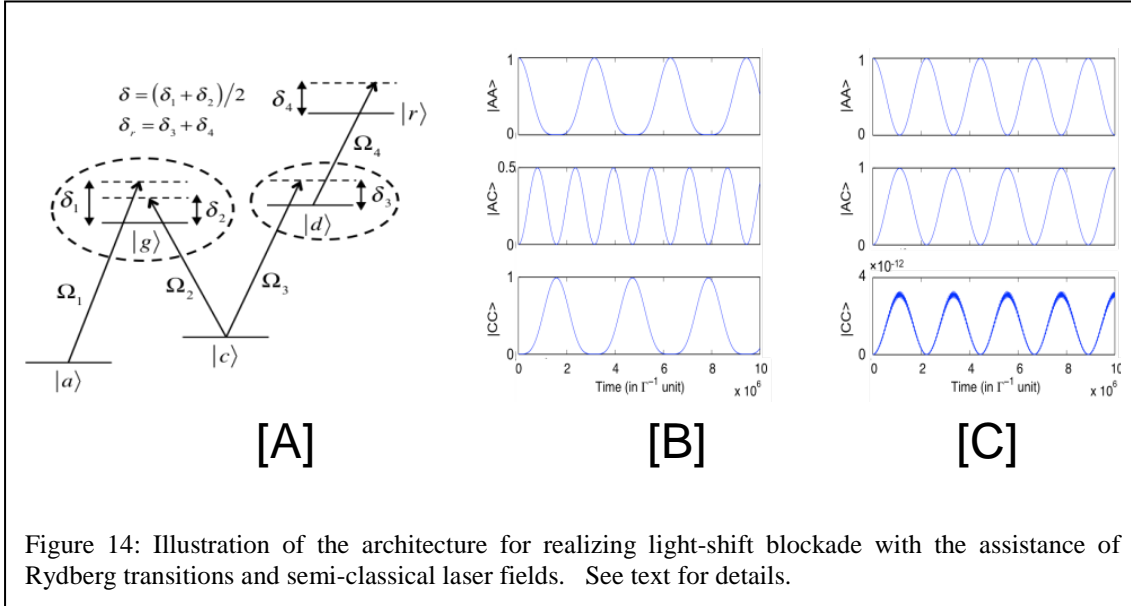


Figure 14: Illustration of the architecture for realizing light-shift blockade with the assistance of Rydberg transitions and semi-classical laser fields. See text for details.

without the Rydberg excitation, while Figure [C] shows that the excitation to  $|C_2\rangle$  (called  $|CC\rangle$  here) is very strongly suppressed [Ref: Paper Number C3 and Paper Number C4 in Section D].

The scheme for quantum computing that involves the use of Rydberg interaction requires the use of two second-harmonic-generation (SHG) frequency-doubled laser, tunable from 474 to 480 nm. These systems are expensive, together costing about \$250K. In October 2013, we submitted a DURIP (DURIP 2014) proposal asking for \$250 K to acquire this equipment. While awaiting decision on this equipment, we proceeded with further analysis of the collective states, especially under Rydberg excitation. The DURIP proposal was not funded. As such, we continued on related studies about producing entanglement in a Rydberg coupled ensemble, and identified two new, potentially game changing metrological devices that are enhanced by quantum entanglement (in the form of spin squeezing). These are the entanglement enhanced (spin-squeezed) collective state atomic interferometer (COSAIN) and entanglement enhanced (spin-squeezed) collective state atomic clock (COSAC). Each of these devices produces fringes that are factor of  $\sqrt{N}$  narrower than the normal fringes, and reduces the effect of quantum noise by the same factor. As such, the sensitivity of each of these devices is improved by the same factor,

reaching the ultimate limit allowed by the laws of quantum mechanics (the Heisenberg limit). Having finished the theoretical models of these devices in great detail, we then embarked on demonstrating the first steps for implementing the COSAIN and the COSAC, using cold atoms released from a MOT. The ultimate demonstration of the Collective State Quantum Computer (CSQC), the COSAIN and the COSAC would all require the lasers mentioned above. We are seeking support from various sources to enable us to buy these lasers.

The left panel of figure 15 shows the schematic illustration of the COSAIN. A novel detection scheme, involving counts of events corresponding to emission of zero photons upon excitation by the read Raman pulse, allows the quantum non-demolition measurement of the amplitude of one of the collective states. This signal thus reveals the interference among all the collective states, which form a series of simultaneous interferometers. The end result is the generation of fringes that are sharper by a factor of  $\sqrt{N}$ , as shown in the right panel of figure 15. These sharp fringes can be understood by

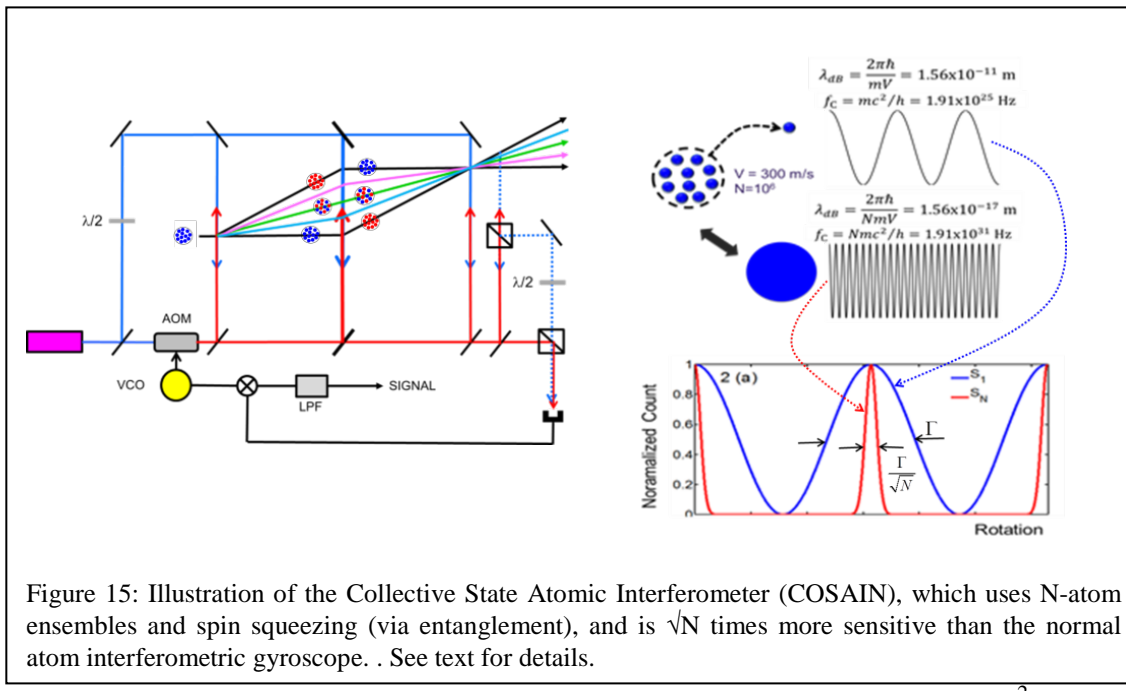


Figure 15: Illustration of the Collective State Atomic Interferometer (COSAIN), which uses  $N$ -atom ensembles and spin squeezing (via entanglement), and is  $\sqrt{N}$  times more sensitive than the normal atom interferometric gyroscope. . See text for details.

noting that the relevant frequency (which is the Compton frequency:  $mc^2/h$ ) for an ensemble of  $N$  atoms is very high: about  $10^{31}$  Hz. Alternatively, the de Broglie wavelength of such an ensemble is about  $10^{-17}$  m. Thus, this device will reveal atomic interference at these scales [Ref: Paper Number C7 in Section D].

The left panel of figure 16 shows the schematic illustration of the COSAC. Again, a novel detection scheme, involving counts of events corresponding to emission of zero photons upon excitation by the read Raman pulse, allows the quantum non-demolition measurement of the amplitude of one of the collective states. This signal thus reveals the interference among all the collective states, which form a series of simultaneous clocks. The end result is the generation of fringes that are sharper by a factor of  $\sqrt{N}$ , as shown in the right panel of figure 16. These sharp fringes can be understood by noting that the effective transition frequency for each of these simultaneous clocks ranges from  $F$  to  $N*F$

(where  $F$  is the single atom clock transition frequency). Averaging over all these clocks produce a next effective clock frequency of  $F/\sqrt{N}$ , which in turn means a reduction in the fringe with by a factor of  $\sqrt{N}$  [Ref: Paper Number C5 in Section D].

As mentioned above, in order achieve the  $\sqrt{N}$  enhancement in sensitivity for the COSAIN and the COSAC, the novel detection schemes have to be augmented by generation of pair-wise entanglement among the atoms, via use of the Rydberg blockade effect. Generation of such entanglement leads to squeezing of the uncertainty in the spin projection preferentially in one direction, at the expense of increasing uncertainty in the orthogonal direction. Figure 17[A] shows how any two level excitation (including Raman excitation) is formally equivalent to a transition that flips the spin of particles from the  $-z$  direction to the  $z$  direction. For  $N$  atoms in the ensemble, the net spin vector

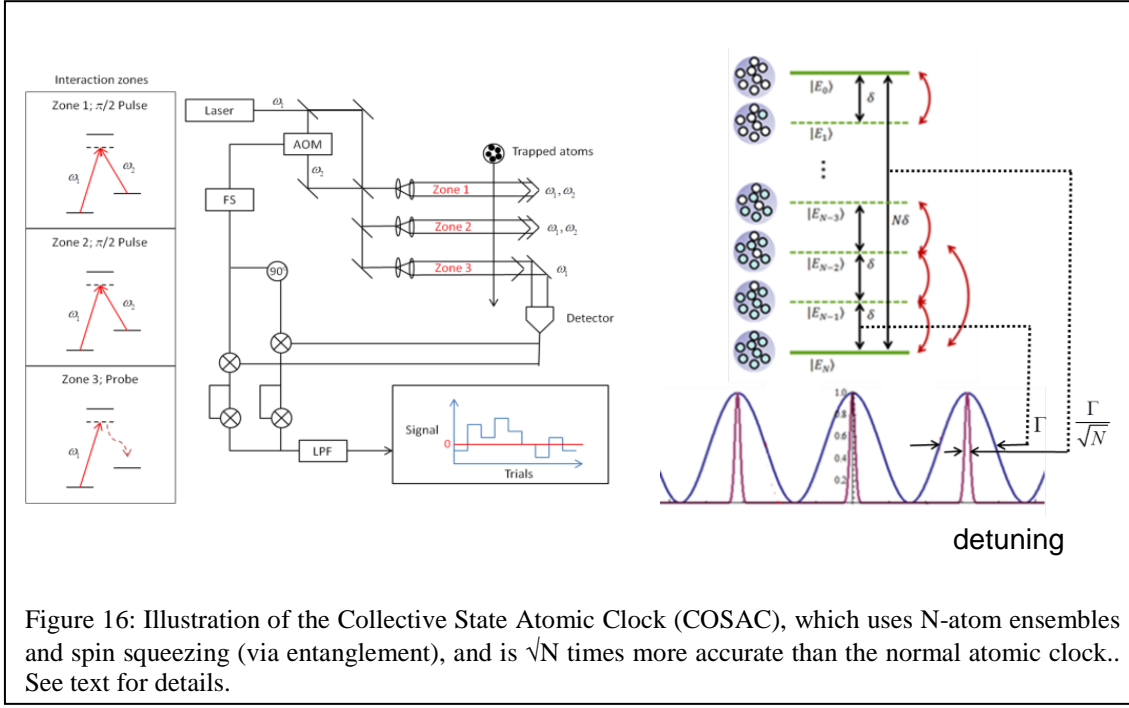


Figure 16: Illustration of the Collective State Atomic Clock (COSAC), which uses  $N$ -atom ensembles and spin squeezing (via entanglement), and is  $\sqrt{N}$  times more accurate than the normal atomic clock.. See text for details.

is the sum of all the spins of individual atoms. A  $\pi/2$  pulse orients the spins in the  $x$ -direction, for example, as shown in figure 17[B]. Figure 17[C] shows the so-called Husimi quasi-probability distribution of this system, which maps clearly the uncertainty in the spin alignment, which is circular. Next, the Rydberg excitation is activated, by applying a two-photon transition coupling the spin-up state to the Rydberg state, as shown in figure 17[E]. When a pair of atoms is excited simultaneously to the  $|rr\rangle$  state, the energy of the  $|rr\rangle$  state is shifted due to the Rydberg excitation, as shown in figure 17[E]. With the proper choice of excitation fields and parameters, it allows the creation of an interaction Hamiltonian that is either proportional to square of the net spin operator in the  $z$ -direction, or to the difference between the squares of the net spin operators in the  $x$  and  $y$  direction. The first scheme produces the so-called one-axis twist (OAT) spin squeezing, while the second scheme produces the so-called two-axes counter-twist (TACT) spin squeezing. Using the TACT spin squeezing reduces the spin projection quantum noise by a factor of  $\sqrt{N}$ , reaching the Heisenberg (ultimate) limit of enhancement in sensitivity [Ref: Paper Number C10 in Section D].

We have proceeded with an experimental realization of the COSAC using cold atoms released from a magneto-optic trap (MOT). Once this is achieved, we will then add the spin squeezing (i.e, entanglement) effect, which must await the acquisition of two second-harmonic generation frequency doubled lasers tunable from 474 to 480 nm. The left panel in figure 18 show the various beams that we are using to generate the MOT. The middle panel shows the various lasers and modulators being used to produce a pulsed excitation of a Raman clock. On the right, we show a typical set of Raman resonances

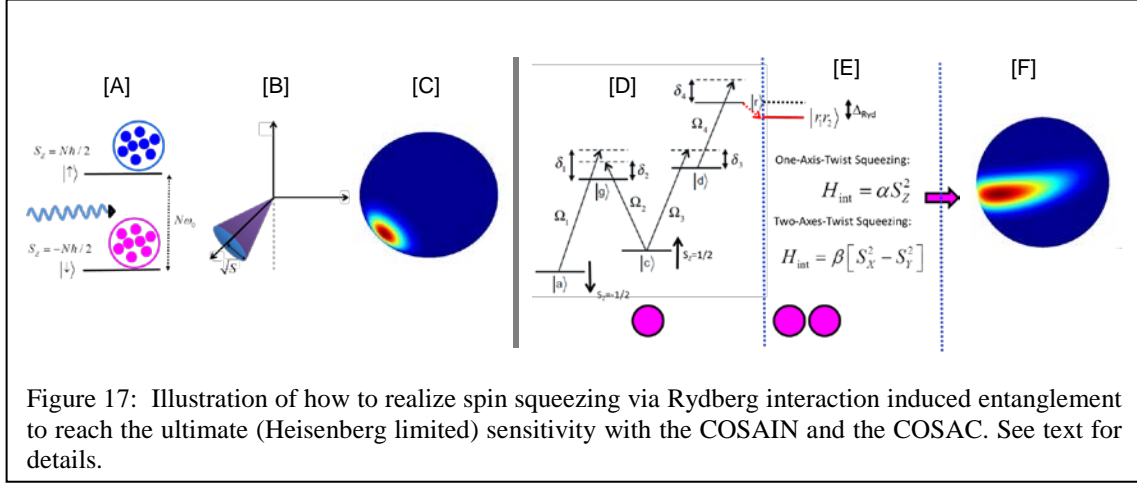


Figure 17: Illustration of how to realize spin squeezing via Rydberg interaction induced entanglement to reach the ultimate (Heisenberg limited) sensitivity with the COSAIN and the COSAC. See text for details.

we see in the presence of a large bias magnetic field, which lifts the degeneracies of the Zeeman sublevels. We then focus on the  $m_F=0$  to  $m_F=0$  clock transition (the center peak). Use of a pair of Raman pulses separated in time by  $T$  then produces transit time limited Raman-Ramsey fringes with a width of  $1/T$ , as shown in the zoomed-in view. The next step is to implement the Quantum Non-Demolition detection scheme, which will reduce

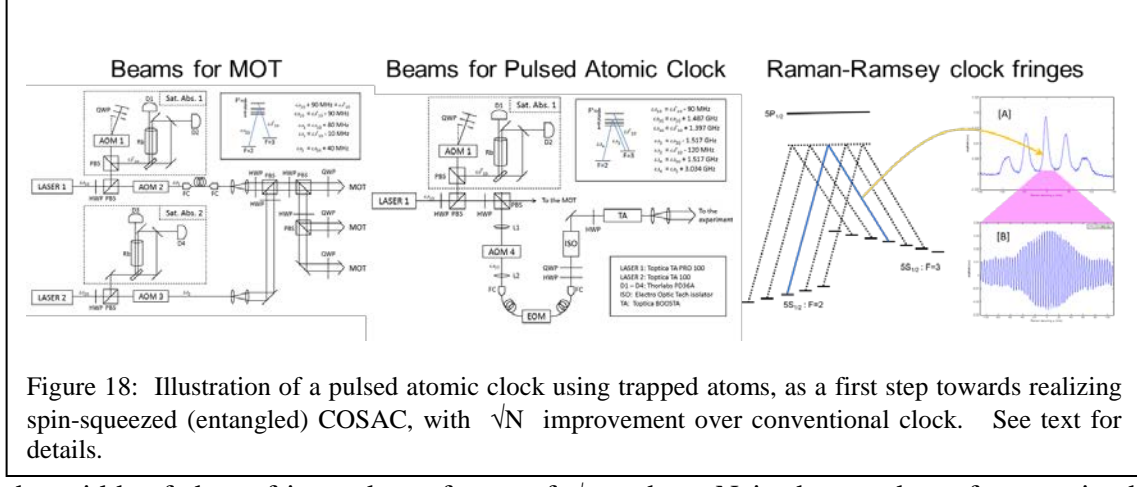


Figure 18: Illustration of a pulsed atomic clock using trapped atoms, as a first step towards realizing spin-squeezed (entangled) COSAC, with  $\sqrt{N}$  improvement over conventional clock. See text for details.

the width of these fringes by a factor of  $\sqrt{N}$ , where  $N$  is the number of atoms in the released MOT, which is about  $10^6$ .

We have also proceeded with an experimental realization of the COSAIN using cold atoms released from a magneto-optic trap (MOT). Once this is achieved, we will then add the spin squeezing (i.e, entanglement) effect. The left panel in figure 19 shows the experimental configuration for generating the Optically Off-Resonant (OOR) Raman-

Ramsey fringes using off-resonant Raman excitation, using cold atoms released from a trap. The first two zones produce the OOR Raman-Ramsey fringes. In the initial phase,

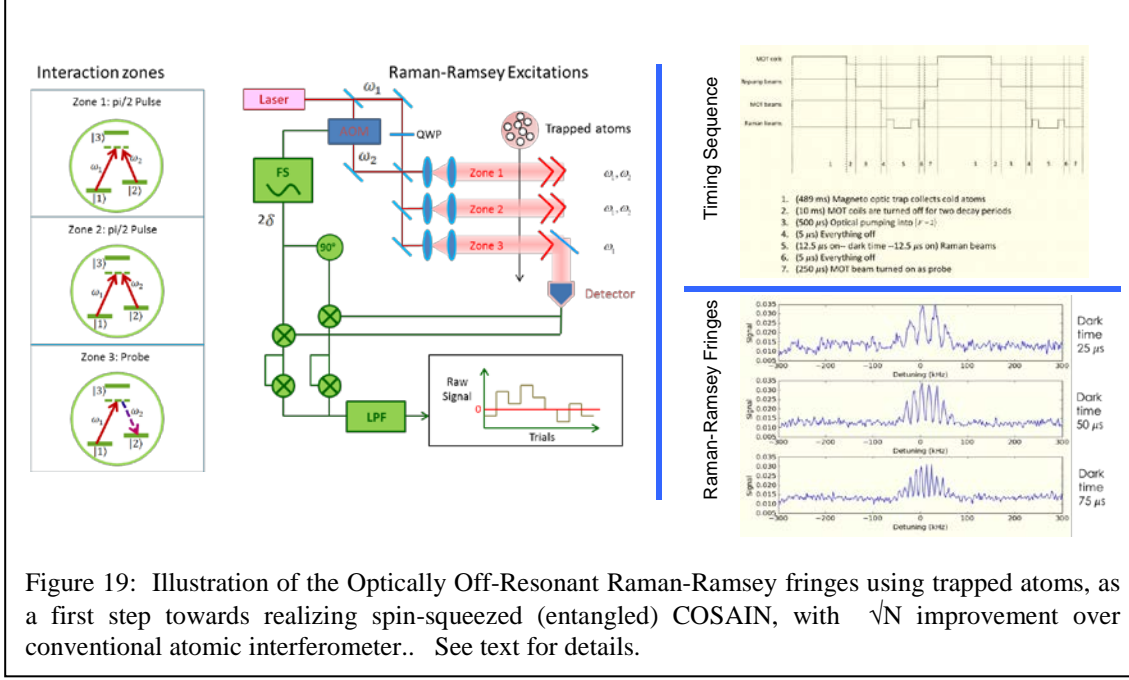


Figure 19: Illustration of the Optically Off-Resonant Raman-Ramsey fringes using trapped atoms, as a first step towards realizing spin-squeezed (entangled) COSAIN, with  $\sqrt{N}$  improvement over conventional atomic interferometer.. See text for details.

we have used co-propagating Raman beams. For the COSAIN experiment, the Raman beams in each of these two zones will be made to counter-propagate. The third zone is for the special Quantum Non-Demolition detection scheme used for observing the COSAIN signal. The top right panel in figure 19 shows the timing sequence we employ for observing the OOR Raman-Ramsey fringes. The bottom right panel shows the OOR Raman-Ramsey fringes for three different time separation between the first two zones, with increasingly narrower fringes. The next step is to implement the Quantum Non-Demolition detection scheme, which will reduce the width of these fringes by a factor of  $\sqrt{N}$ , where  $N$  is the number of atoms in the released MOT, which is about  $10^6$ . This will be followed by the addition of the spin-squeezing effect.

## C. CONCLUSION

The goal of this project was to demonstrate the feasibility of realizing a large scale quantum computer by linking a series of elementary quantum computer (EQC), within which ensembles of atoms were used as quantum bits (qubits). Since the coupling strength of an ensemble to a cavity photon scales as the square-root of the number of atoms, this approach would require a relatively low finesse cavity with a large volume, which in turn could accommodate many qubits. We built all the tools for making an EQC. However, experimental work revealed that use of light shift only, as envisioned in the proposal, is not enough to achieve the required blockade effect. We have now shown why this is the case, and have identified how the blockade can be restored by using Rydberg interaction assisted light-shift imbalance. However, due to lack of necessary lasers, we were unable to demonstrate the operation of the EQC using this scheme.

Instead, we focused on exploring other aspects of collective state excitation , and entanglement within them, for precision metrology. Specifically, we have shown how to realize spin-squeezed collective state atomic interferometer (COSAIN) and collective state atomic clock (COSAC) that are capable of improving the performance by a factor of root-N compared to conventional counterparts thereof, thus reaching the Heisenberg limit. Significant experimental work has been carried out to demonstrate both of these devices, and this work will be carried to completion in the near future.

## **D. LIST OF JOURNAL PUBLICATIONS, CONFERENCE PAPERS, AND PREPRINTS**

### **Journal Papers Published or Accepted for Publication:**

C1. "Connecting processing-capable quantum memories over telecommunication links via quantum frequency conversion," M.S. Shahriar, P. Kumar, and P.R. Hemmer, *J. Phys. B: At. Mol. Opt. Phys.* 45, 124018 (June, 2012)

C2 "Evolution of an N-level system via automated vectorization of the Liouville equations and application to optically controlled polarization rotation," M.S. Shahriar, Ye Wang, S.Krishnamurthy, Y. Tu , G.S. Pati, and S. Tseng, Volume 61, Issue 4, pp. 351-367 (February 2014)

C3. "A long-distance quantum repeater gets one step closer," Selim M. Shahriar, *Physics* 4, 58 (2011)

C4 "Rydberg assisted light shift imbalance induced blockade in an atomic ensemble," Y. Tu, M. E. Kim, S. M. Shahriar, *Optics Communications* 339, pp 157-166 (March 2015)

C5. "An N-atom Collective State Atomic Clock with Root-N Fold Increase in Effective Frequency and Root-N Fold Reduction in Fringe Width," M. E. Kim, R. Sarkar, R. Fang, and M.S. Shahriar, *Phys. Rev. A* 91, 063629 (2015).

C6 "Effects of Non-idealities and Quantization of the Center of Mass Motion on Symmetric and Asymmetric Collective States in a Collective State Atomic Interferometer", R. Sarkar, M. E. Kim, R. Fang, Y. Tu, and M.S..Shahriar, *Journal of Modern Optics*, Vol. 62, No. 15, 1253–1263 (2015).

C7. "An N-atom Collective State Atomic Interferometer with Ultra-High Compton Frequency and Ultra-Short de Broglie Wavelength, with root-N reduction in Fringe Width," R. Sarkar, M. E. Kim, R. Fang, and M. S. Shahriar, *Phys. Rev. A* 92, 063612 (2015)

C8. "Quantum Noise Limits in White-Light-Cavity-Enhanced Gravitational Wave Detectors," M. Zhou, Z. Zhou, and M.S. Shahriar, *Phys. Rev. D* 92, 082002 (2015)

C9. "Master Equation Approach for Quantum Noise in Phase-Insensitive Linear Amplifier based on Atomic Systems," M. Zhou, Z. Zhou, and M.S. Shahriar, to appear in *Phys. Rev. A* (2016)

Journal Papers Under Review or Preprints:

C10. "Two-Axes Twist Spin Squeezing with Heisenberg limited sensitivity for Collective State Atomic Clock and Collective State Atomic Interferometer ,” R. Sarkar, M. Kim, R. Fang, Y. Tu, and M. S. Shahriar, preprint, to be submitted to Phys. Rev. A.

C11. “A Collective State Atomic Clock Using Coherent Population Trapping,” M. Kim, R. Fang, R. Sarkar, and M.S. Shahriar, to be submitted to Phys. Rev. A.

Conference Proceedings

D1. “Quantum Information Processing with Light Shift Blockaded Atomic Ensembles Coupled to a Cavity,” M.S. Shahriar, M. Kim and Y. Tu, presented at the SPIE Quantum Communications and Quantum Imaging IX Conference (OP514), San Diego, California, August 2011 (**Invited**)

D2. “Light-Shift Blockaded Collective States for Atomic Interferometry and Quantum Information Processing,” M. Kim, Y. Tu, R.P. Fang and M.S. Shahriar, presented at the Midwest Cold Atom Workshop, Evanston, November 2011 (**invited**)

D3. “Interferometry with Atom Lasers and Schrodinger Cats: Nanolithography, Atomic Holograms, and High Compton Frequency Gyroscopes,” M.S. Shahriar, M. Fouda, R.P. Fang, R. Sarkar, M. Kim, and Y. Tu, presented at the Laser Physics Conference 12, Calgary, Alberta, CA, 2012 (**invited**)

D4. “A Schrödinger Cat Matter Wave Gyroscope Using Collective Excitation of Atomic Ensembles,” DAMOP, 2012, Anaheim, CA

D5. “Ultra-High Compton Frequency Atomic Interferometric Gyroscope Using Collective States,” R. Sarkar, M. Kim, Y. Tu and M.S. Shahriar, presented at the Conference on Lasers and Electro-Optics, Anaheim, CA, May 2012

D6. “Enhancement of Sensitivity of an Atom Interferometer by a Factor of N Using High Compton Frequency of N-atom Collective-States,” R. Sarkar, M. Kim, Y. Tu and M.S. Shahriar, presented at the Physics of Quantum Electronics conference, Snowbird, Utah, January 2012 (**invited**)

D7. “Effect of Interatomic Separation and Spatial Spread of Individual Atoms in a Collective State Interferometer,” Resham Sarkar, May E. Kim, Yanfei Tu, and Selim M. Shahriar, Conference on Lasers and Electro-Optics, San Jose, CA, June 2013

D8. “Experimental verification of light shift imbalance induced blockade in an atomic ensemble via collective state Rabi oscillation and coincidence detection,” M. Kim, Y. Tu,

S. Krishnamurthy and M.S. Shahriar, APS DAMOP conference in Quebec City, Canada, June 2013

D9. "Effect of Interatomic Separation and Wavepacket Spreading on the Behavior of a High Compton Frequency Collective State Interferometer," R. Sarkar, M. Kim, Y. Tu, and M.S. Shahriar, APS DAMOP conference in Quebec City, Canada, June 2013

D10. "Verification of light shift imbalance induced blockade in an atomic ensemble via collective state Rabi oscillations," M. Kim, Y. Tu, S. Tseng, R. Sarkar, M. Fouda, and M.S. Shahriar, the conference on Quantum Information And Computation Xi (Ds222), SPIE International Symposium on Defense, Security and Sensing, April 2013, Baltimore, MD, USA

D11. "New Directions in Atom Optics: Collective State Atomic Interferometry and Atomic Holography with BEC," Selim M. Shahriar, Quantum Optics and Nanomaterials VI, Beijing, China, May 2013. (**Invited**)

D12. "Verification of light shift blockade via collective state Raman-Rabi oscillations for ensemble based quantum computing," Selim M. Shahriar, May Kim, Yanfei Tu, Resham Sarkar, SPIE Optics and Photonics conference, San Diego, CA, August, 2013. (**Invited**)

D13. "Sensitivity Enhancement via Detection of Interference With All Orders in a Collective State Atom Interferometer," Resham Sarkar, May E. Kim, Yanfei Tu, and Selim Shahriar, OSA Annual Meeting, Orlando, FL, October 2013.

D14. "Rydberg Interaction Assisted Light Shift Blockade Of Collective Excitations For Quantum Information Processing," Y. Tu, M. Kim, R. Sarkar, and M.S. Shahriar, OSA Annual Meeting, Orlando, FL, October 2013.

D15. "Constraints in Collective State Atomic Interferometry Due to Inhomogeneities in Laser Intensity and Atomic Velocity," R. Sarkar, M. E. Kim, R. Fang, and M.S. Shahriar, in Proceedings of the Frontiers in Optics and Laser Science Conference, Tucson, AZ, October, 2014.

D16. "Rydberg excitation assisted light shift blockade in Rb atoms for realizing a collective state quantum bit and quantum memory," M.S. Shahriar, M.E. Kim, and Y. Tu, in Proceedings of the SPIE OPTO Conference, San Diego, CA, August, 2014 (**Invited**)

D17. "Effect of Interatomic Separation in Ensembles in Determining the Fidelity of Collective Excitation," R. Sarkar, M.E. Kim, Y. Tu, R. Fang, and M.S. Shahriar, in Proceedings of the Division of Atomic, Molecular and Optical Physics Conference, Madison, WI, June, 2014.

D18. "Collective State Raman Atomic Clock Using Trapped Atoms," M.E. Kim, R. Sarkar, R. Fang, Y. Tu, and M.S. Shahriar, in Proceedings of the Division of Atomic, Molecular and Optical Physics Conference, Madison, WI, June, 2014.

D19. "The Rydberg-assisted Light-shift Blockade for Ensemble Quantum Computing," M. E. Kim, Y. Tu, and M.S. Shahriar, in Proceedings of the Conference on Lasers and Electro-Optics, San Jose, CA, June, 2014.

D20. "Collective state atomic interferometer with ultra-high Compton frequency," R. Sarkar, M. Kim and S. M. Shahriar, SPIE Photonics West Conference, San Francisco, CA, February, 2015.

D21. "Collective state Raman-Ramsey atomic clock with trapped atoms," M. Ki, R. Sarkar, and S. M. Shahriar, SPIE Photonics West Conference, San Francisco, CA, February, 2015.

D22. "Coherent Population Trapping Based Collective State Atomic Clock Using Trapped Atoms," M. Kim, R. Fang, R. Sarkar and S.M. Shahriar, in Proceedings of the Division of Atomic, Molecular and Optical Physics Annual Meeting, Columbus, OH, June, 2015

D23. "Effect of One Axis Twist and Two Axes Twist Spin Squeezing on Collective State Atomic Interferometer and Clock," R. Sarkar, R. Fang, M. Kim, and S.M. Shahriar, in Proceedings of the Division of Atomic, Molecular and Optical Physics Annual Meeting, Columbus, OH, June, 2015.

D24. "Collective State Atomic Clock: Experimental Investigation and Application to Spin-Squeezing," R. Fang, M. Kim, R. Sarkar and S. M. Shahriar, in Proceedings of the Frontiers in Optics and Laser Science Conference, San Jose, CA, October, 2015

D25. "Master Equation Approach for Quantum Noise in Atomic Systems for Gravitational-Wave Detection," M. Zhou and S. M. Shahriar, in Proceedings of the Frontiers in Optics and Laser Science Conference, San Jose, CA, October, 2015.

D26. "Spin Squeezed Scalar and Vector Magnetometry with Coherent Population Trapping," R. Fang, R. Sarkar, M. Kim, Z. Zhou and S.M. Shahriar, to be presented at the SPIE Photonics West Conference, San Francisco, CA, February, 2016.

D27. "Spin Squeezed Collective State Atomic Interferometer and Clock," R. Sarkar, M. Kim, R. Fang, and S.M. Shahriar, to be presented at the SPIE Photonics West Conference, San Francisco, CA, February, 2016.

## **E. REPRODUCTION OF PUBLISHED JOURNAL PAPERS**

# Connecting processing-capable quantum memories over telecommunication links via quantum frequency conversion

M S Shahriar<sup>1,2</sup>, P Kumar<sup>1,2</sup> and P R Hemmer<sup>3</sup>

<sup>1</sup> Department of EECS, Northwestern University, 2145 Sheridan Road, Evanston, IL 60208, USA

<sup>2</sup> Department of Physics and Astronomy, Northwestern University, 2145 Sheridan Road, Evanston, IL 60208, USA

<sup>3</sup> Department of EECS, Texas A&M University, 3128 TAMU, College Station, TX 77843, USA

E-mail: [prhemmer@ece.tamu.edu](mailto:prhemmer@ece.tamu.edu)

Received 5 January 2012, in final form 24 February 2012

Published 8 June 2012

Online at [stacks.iop.org/JPhysB/45/124018](http://stacks.iop.org/JPhysB/45/124018)

## Abstract

For quantum information processing (QIP), it is important to have a long-lived quantum memory (QM), coupled to other QMs and quantum processors (QP). However, QM and QP systems demonstrated so far suffer from many limitations, and in the near future a single platform will not have the optimal version of all the components needed for QIP. Thus, it is also important to be able to couple quantum bits in different systems, for example, Rb atoms and NV diamond, preferably using telecom fibres. In this paper, we describe a quantum frequency converter (QFC) that will perform this telecom band qubit conversion. The QFC is based on periodically poled lithium niobate waveguides. For concreteness, we consider specific examples: the conversion of a 780 nm or 795 nm Rb qubit to the telecom band and the conversion of a 637 nm photonic NV diamond qubit to the telecom band, as well as the inverse processes. We show that interface fidelity exceeding 95% should be feasible. Given the storage times  $\sim 1$  s already demonstrated in the solid-state systems, and the recent demonstrations of spin-photon entanglement with the NV and entanglement of the NV spin with a superconducting flux qubit operating in the microwave region near 2.88 GHz, such a link would provide the key interface needed to build a quantum internet.

(Some figures may appear in colour only in the online journal)

## 1. Introduction

In any quantum information system, such as those used for secure communication and computation, one needs the ability to send quantum information between the nodes of the system and to store this information in a manner that retains the necessary quantum correlations. Quantum memories also play an important role in entanglement purification protocols. For example, a modified form of the Duan–Lukin–Cirac–Zoller protocol [1] uses atomic memories by collecting one photon of an entangled pair after its twin has been detected [2]. This system thus allows for the long-haul quantum key distribution. The optimum strategy for transmitting and storing quantum information can be quite different for different subsystems even within a given system. For example, entanglement

involving orbital angular momentum states [3, 4], such as Laguerre–Gauss states, is a preferred way of transmitting quantum information over a free-space link, whereas time-energy entanglement [5] is preferred for transmitting quantum information over a fibre-optic link or within a guided-wave geometry. Also, even within the context of quantum memories, different strategies may be optimal for the construction of a short-term quantum memory (such as a buffer) versus a long-term memory. Thus, there is a need to develop complementary strategies for the transmission and storage of quantum information. There is also a need to develop means for converting quantum resources, such as entanglement, from one physical degree of freedom to another within a quantum network.

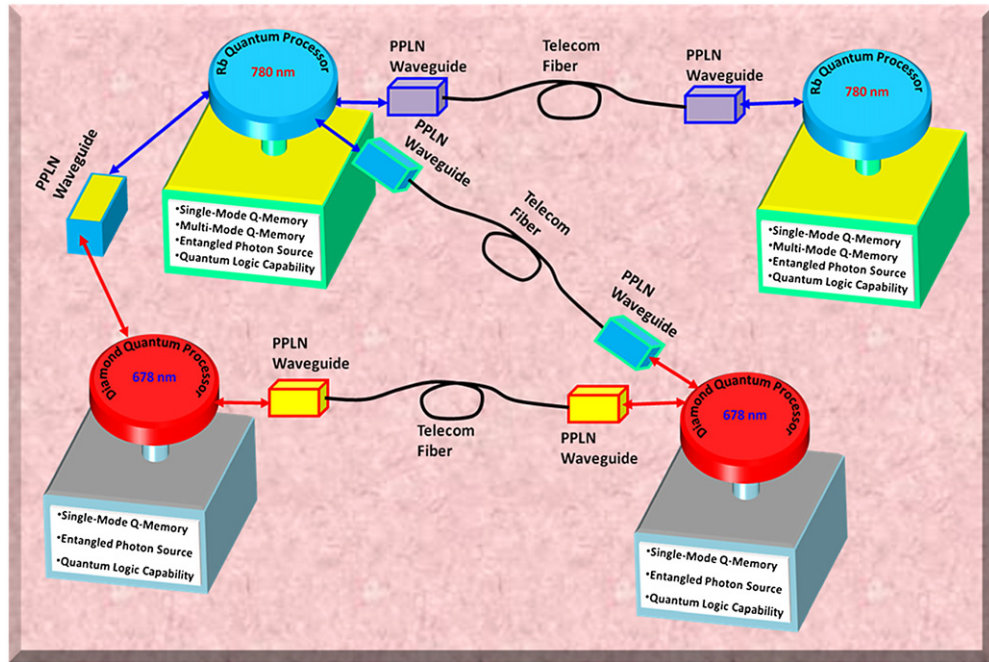


**Figure 1.** Schematic illustration of telecommunication band links between quantum memories of different types.

In this paper, we describe possible techniques for connecting different types of quantum memories over telecommunication band (TB) links, using quantum frequency converters (QFCs) [6] based on periodically poled lithium niobate (PPLN) waveguides. The quantum memory linking system is illustrated schematically in figure 1. Briefly, we consider two types of quantum memories: one using  $^{87}\text{Rb}$  atoms and the other using nano-structures of diamond containing single nitrogen-vacancy colour centres (NVCC). The Rb quantum memory, augmented for processing capabilities, is assumed to have the following capabilities: single-mode quantum memory, multi-mode quantum memory, conversion of atomic qubits to photonic qubits (PQs) at 780 nm, deterministic quantum logic operations among memory elements, production of entangled photons and measurement of Bell states. The diamond quantum memory, also augmented for processing capabilities, is assumed to have the following capabilities: single-mode quantum memory, production of entangled photons and measurement of Bell states. A processing-capable quantum memory, which can also be called an active quantum memory, is defined as a QM that can couple to another QM via quantum logic. Note that for NVCC the recently demonstrated entanglement of photons with spin [7] as well as entanglement of spin with superconducting flux qubits [8] may allow extending this network to include superconducting qubits operating near the 2.88 GHz NV spin transition frequency. A more detailed discussion of the different types of qubits available appears in [9, 10].

Using the technique of difference frequency generation in a PPLN waveguide, we consider here the prospect of developing three different types of QFCs: (a) converting 637 nm (diamond) photonic qubit to TB, (b) converting 780 or 795 nm (Rb) photonic qubit to TB and then to 637 nm,

and (c) converting 637 nm PQ to a 780 nm PQ. Consider, for example, the parameters involved in realizing the QFC in item (a) above. A PPLN waveguide pumped with a YAG laser at 1064 nm can be quasi phase matched for the process of generating the difference frequency between 637 and 1064 nm, corresponding to 1593.5 nm. For a 2 cm long and 5  $\mu\text{m}$  mode-diameter waveguide, and with a quasi CW pump for a photon of 100 ns duration, the average power will be only 10 mW. For cases (b) and (c), the parameters needed are similarly accessible.

The rest of the paper is organized as follows. In section 2, we describe the architectures of using PPLN-based waveguides for linking different types of quantum memories. In section 3, we describe a quantum memory based on ensembles of Rb atoms, augmented for processing capabilities. In section 4, we describe an NV-diamond-based quantum memory, also augmented for processing capabilities. In section 5, we present the summary and the outlook.

## 2. Quantum frequency converters

Quantum frequency conversion (QFC) is a process in which an input light beam is converted into an output beam of different optical frequency while preserving its quantum state [11]. It plays an important, twofold role in the proposed quantum-memory network. In the first place, it serves as the interface between memory devices in different material form where photonic qubits of different wavelengths are involved. Secondly, it enables quantum telecommunication between distant memory devices using the existing fibre-based, low-loss telecommunication infrastructure. Here, we describe a complete set of QFC devices that are suitable for the interface between the Rb-ensemble and NV-diamond-based memory devices, as well as the fibre-based quantum telecommunication among them.

The proposed QFC devices are based on the second-order nonlinear process in  $\chi^{(2)}$  media. To see how this comes about, let us consider the coupling of three  $z$ -propagating optical waves of angular frequencies  $\omega_j$  satisfying  $\omega_3 = \omega_1 + \omega_2$ . The coupling is described by the following general coupled equations [12]:

$$\begin{aligned}\frac{dE_3}{dz} &= i\frac{\omega_3 K}{n_3 c} E_1 E_2 e^{i\Delta kz}, & \frac{dE_1}{dz} &= i\frac{\omega_1 K}{n_1 c} E_3 E_2^* e^{-i\Delta kz}, \\ \frac{dE_2}{dz} &= i\frac{\omega_2 K}{n_2 c} E_3 E_1^* e^{-i\Delta kz}, & \Delta k &= k_1 + k_2 - k_3,\end{aligned}\quad (1)$$

where  $k_j = n_j \omega_j / c$  is the wave-vector magnitude for each wave  $E_j$  and  $K$  is the effective nonlinear coupling coefficient in the waveguide— $d_{33}$ , for example, in the  $z$ -cut PPLN waveguide. The above coupled equations can be solved exactly for the arbitrary phase-mismatch  $\Delta k$  in terms of hypergeometric functions. For the QFC purpose, however, we consider only the phase-matching case with  $\Delta k = 0$ .

There are three cases of interest to us. The first case is of second-harmonic generation (SHG), in which the fundamental field ( $E_1 = E_2 = E_\omega$ ) is monotonically converted into a frequency-doubled field  $E_3 = E_{2\omega}$ . The second case of interest is of sum-frequency generation (SFG) wherein one of the lower-frequency fields is allowed to deplete, say the  $E_1$  field at  $\omega_1$ , whereas the other lower-frequency field  $E_2$  remains strong and undepleted. (Usually, the depleted and undepleted fields are referred to as the signal and the pump, respectively.) In this case, the power of the signal field is periodically exchanged between the  $\omega_1$  field  $E_1$  and the sum-frequency field  $E_3$ . The period of power exchange is dependent on the intensity of the pump field at  $E_2$  and hence is optically controllable. Full exchange of power between  $E_1$  and  $E_3$  can occur under the condition of phase-matching, i.e.  $\Delta k = 0$ , for which one obtains

$$E_3(z) = E_3(0) \cos \kappa z + i e^{i\phi_2} (n_1 \omega_3 / n_3 \omega_1)^{1/2} E_1(0) \sin \kappa z, \quad (2)$$

where  $\phi_2$  is the phase of the pump field  $E_2$  and  $\kappa = (\omega_1 \omega_3 K^2 / n_1 n_3 c^2)^{1/2} E_2$  is the SFG coefficient proportional to the square root of pump power. A similar equation for  $E_1(z)$  is obtained by interchanging 1 and 3. The third case of interest is the difference frequency generation (DFG) process, which is similar to SFG but with a higher frequency field depleted to create a lower frequency field. For both DFG and SFG, by choosing  $\kappa z = (j+1/2)\pi$  where  $j$  is an integer, the power exchange is (ideally) 100%, whereby the input signal converts completely into an output light of different frequency.

The above analysis is classical. In the quantum domain, the equation of motion for optical fields can be obtained by the routine second-quantization method. Consider, for example, the case of SFG. For a strong coherent pump and a weak propagation loss of light travelling through the waveguide, the annihilation operators of input ( $\hat{a}_1, \hat{a}_3$ ) and output ( $\hat{b}_1, \hat{b}_3$ ) signal fields obey [13]

$$\hat{b}_1 = \hat{a}_1 \cos \kappa z - \hat{a}_3 \sin \kappa z, \quad \hat{b}_3 = \hat{a}_3 \cos \kappa z + \hat{a}_1 \sin \kappa z. \quad (3)$$

Choosing the pump intensity such that  $\kappa z = \pi/2$ , the above equations become

$$\hat{b}_1 = -\hat{a}_3, \quad \hat{b}_3 = \hat{a}_1. \quad (4)$$

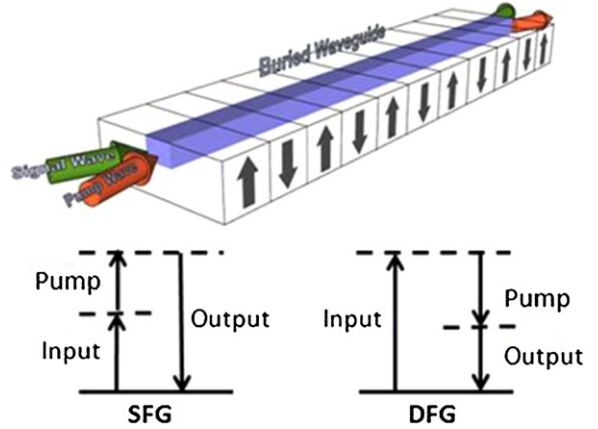


**Figure 2.** The QFC schematic. Upper: the buried PPLN waveguide; lower left and right: the relevant SFG and DFG processes, respectively.

This result shows that with appropriate pump intensity and waveguide length, the input signal can be completely converted into an output of a different frequency while its quantum state is preserved. It is this state-preserving feature of SFG and DFG that enables the QFC operation.

To build QFC devices compatible with the quantum-memory devices described in sections 3 and 4, we consider the use of planar PPLN waveguides as the second-order nonlinearity media. The use of such waveguides has several advantages. First of all, they are commercially available with well-developed fabrication technology. Second, the lithium niobate material has a large nonlinear coefficient ( $>20 \text{ pm V}^{-1}$ ) for efficient QFC and a wide transparent window ( $\sim 350\text{--}5200 \text{ nm}$ ) that allows applications over a broad wavelength band. Third, the quasi-phase matching (QPM) technique, in which periodic domain inversion is used to compensate for the material phase mismatching ( $\Delta k \neq 0$ ), has been well established for both SFG and DFG over a wide range of wavelengths. Lastly, the background scattering in the lithium niobate material is weak, resulting in a rather low quantum noise and thus high purity of the frequency-converted photons. We consider using double-layer ('buried') PPLN waveguides, whose schematic is shown in figure 2. For fabrication, such waveguides are produced by first applying proton exchange (PE) to a bulk PPLN substrate to create a layer strip of  $\text{HNB}_3$ . (Alternatively, one can apply PE during the growth stage of PPLN.) Then, a reverse PE process is applied to create a second layer of  $\text{LiNbO}_3$  on top of the  $\text{HNB}_3$  layer. For this structure, only extraordinary light can be guided. Compared to in-diffusion or PE PPLN waveguides, the buried PPLN waveguides have the advantage of stronger second-order nonlinearity and a weaker waveguide loss. Also in figure 2, we show the SFG and DFG level schemes that can be employed to perform QFC.

Using the buried PPLN waveguides as basic elements, we now describe the process for constructing the quantum-state-preserving QFC circuits. First of all, to preserve the time-energy states of photons, one needs to use a pump beam that is flat over the entire time interval containing the temporal Hilbert space of the signal photons. Then, to preserve the polarization

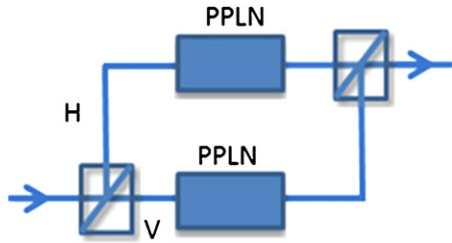


**Figure 3.** Polarization-preserving QFC element. See the text for details.

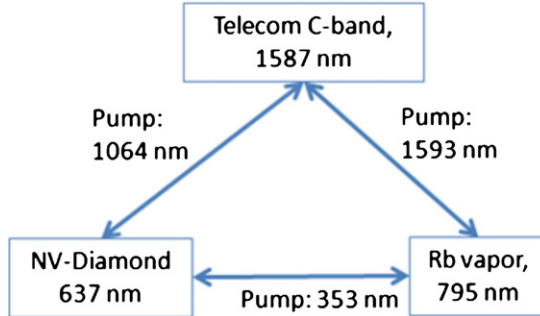


**Figure 4.** The QFC scheme for use with Rb D1-line transition.

states, one would use a two-PPLN setup, as shown in figure 3. It consists of a polarized beamsplitter (PBS) to separate the H and V polarization components of input photons. The H and V components then each undergo two separate QFC processes in two independent PPLN waveguides. The two waveguides are identical but with the optical axis of the waveguide rotated by 90° relative to each other. The two polarization components are then recombined at the second PBS to produce a frequency-converted output whose polarization state is preserved.

Using the above QFC circuit, it is possible to develop systematical QFC schemes for use with the atomic-ensemble and NV-centre-based QM devices. As both the Rb D<sub>1</sub>-line (795 nm) and D<sub>2</sub>-line (780 nm) transitions can be used for ensemble-based QMs, we describe two QFC schemes that are compatible with the two transitions. The first QFC scheme is shown in figure 4, wherein three wavelengths of interest are involved. They are 637 nm associated with NV-diamonds, 795 nm with the Rb D<sub>1</sub> line and 1587 nm in the telecom L-band for use in quantum telecommunication via low-loss optical fibres. For the QFC between 637 and 1587 nm, one would use a Nd:YAG laser at 1064 nm as the pump. The PPLN waveguide is designed to be QPM for the 1587 nm + 1064 nm | 637 nm process. For the QFC between 795 and 1587 nm, one would use a 1593 nm pump with the waveguide QPM for the 1587 nm + 1593 nm | 795 nm process. Finally, for the direct QFC between 795 and 637 nm, a pump at 353 nm is used, and the waveguide is periodically poled to be QPM for the 795 nm + 637 nm | 353 nm process. Here, in order to obtain the 353 nm pump, a 1059 nm fibre laser could be used as the source. The 1059 nm laser is first frequency doubled to create a 529.5 nm light using a PPLN that is QPM for the SHG for this wavelength. The 529.5 nm light is then combined with the 1059 nm laser to create the desired 353 nm pump via SFG. In practice, the two processes of SHG and

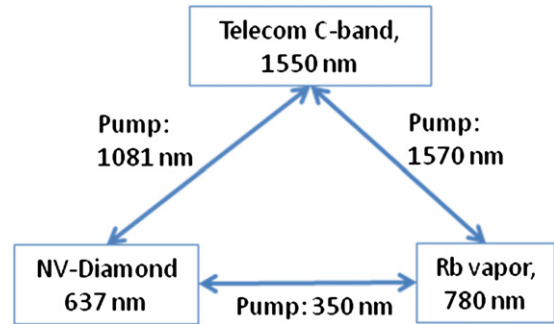


**Figure 5.** The QFC scheme for use with Rb D<sub>2</sub>-line transition.

SFG can be implemented in a single PPLN waveguide with two poling periods.

Similarly, the second QFC scheme deals with 637 nm photons associated with NV-diamonds, 780 nm photons with the Rb D<sub>2</sub>-line transition and 1550 nm photons in the telecom C-band, as shown in figure 5. To drive the QFC between 637 and 1550 nm, one would use a 1081 nm pump and a waveguide that is QPM for the 1550 nm + 1081 nm | 637 nm process. For QFC between 780 and 1550 nm, one would use a 1570 nm pump with a waveguide QPM for the 1550 nm + 1570 nm | 780 nm process. Finally, to implement QFC for the 637 and 780 nm light, one would use a pump at 350 nm and a waveguide QPM for the 637 nm + 780 nm | 350 nm process. Again, the 350 nm laser can be produced adopting successive SHG and SFG processes using a 1050 nm laser from a ytterbium fibre amplifier.

### 3. Rubidium quantum memory

A neutral alkali atom held in a far-off-resonant trap (FORT) represents a potentially ideal quantum system which can serve as a processing-capable QM, when coupled strongly to a cavity photon. However, such a system requires the use of a high finesse cavity with a microscopic volume. This geometry severely constrains the usage of such a system. An alternative approach makes use of an ensemble of atoms as the quantum system. Such an ensemble can serve as a QM, and can be used to produce entangled states of photons. It can also be used to entangle two QMs separated spatially. However, this process is probabilistic, which vastly limits the utility of such a protocol. While ‘the single atom in a cavity’ and ‘an ensemble in free space’ appear to be two distinctly different systems, we have recently shown [14, 15] that these two processes merely represent two extremes of a generalized technique:  $M$  atoms in a cavity with finesse  $N$ . The first case represents one extreme, where  $M = 1$  and  $N$  is a large number. The second case represents the other extreme, where  $M$  is a large number and  $N = 1$ . Specifically, we have shown how the general system with  $M > 1$  and  $N > 1$  can be used to realize a deterministic quantum bit, via the process of light shift blockade (LSB) that occurs naturally [14, 15]. In particular, if one uses a modest number of atoms (e.g.,  $M \sim 10^5$ ) with a relatively low finesse cavity ( $N \sim 10^2$ ), the resulting system allows one to get around the limitations of both extremes.

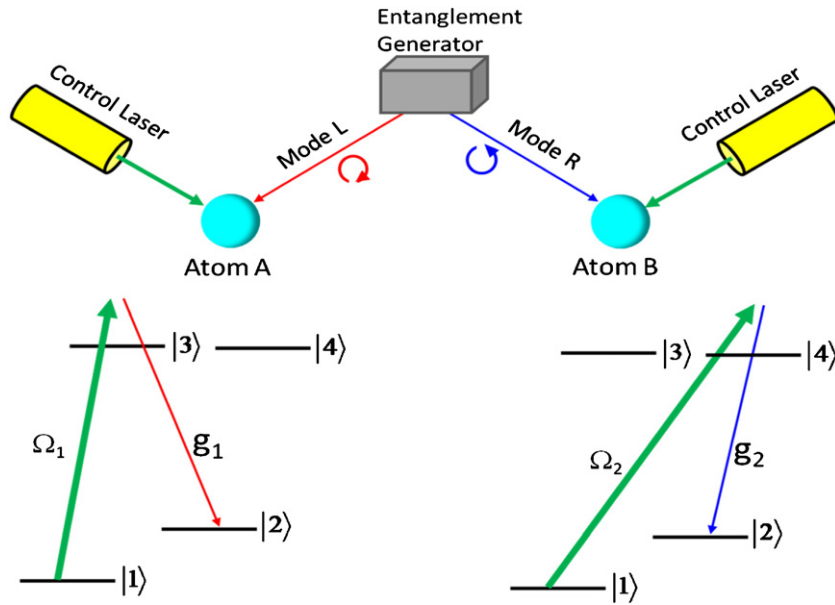


Figure 6. Schematic illustration of storage in an atomic quantum memory.

Experimentally, an array of such ensembles could be realized by using an array of FORT potentials, loaded from a magneto-optic trap (MOT), enclosed inside a relatively large MEMS-based cavity. Using two such apparatuses, it would be possible to demonstrate [14]: (1) loading of an arbitrary PQ into an atomic ensemble QM, with a storage time of more than 1 s, and a fidelity  $>90\%$ ; (2) generation of entanglement between two QMs within the same apparatus; (3) generation of entanglement between two remote QMs, in a deterministic manner, using the Pellizari–Gardiner–Cirac–Zoller protocol [16]; and (4) measurement of all four Bell states, using the Lloyd–Shahriar–Hemmer–Shapiro protocol [17]. These capabilities, in turn, imply that the system could be used for realizing essentially any protocol in QIP, including entanglement swapping quantum teleportation and entanglement purification [18].

The basic concept for an atomic quantum memory is illustrated in figure 6. Consider an unspecified source that produces a pair of entangled photons, in two spatial modes: L and R. In general, such a state can be written as  $\alpha|0\rangle_L|0\rangle_R + \beta|0\rangle_L|1\rangle_R + \gamma|1\rangle_L|0\rangle_R + \xi|1\rangle_L|1\rangle_R$ . For example,  $\alpha = 0$ ,  $\xi = 0$  and  $\beta = -\gamma = 1/\sqrt{2}$  would represent a maximally entangled state. Each mode is now made to interact with a distinct atom. Prior to the interaction, the quantum state of the two atoms is unentangled and expressed simply as  $|1\rangle_A|1\rangle_B$ . For the particular example of parameters, the joint state of the photons and atoms is thus given by  $(1/\sqrt{2})(|0\rangle_L|1\rangle_R - |1\rangle_L|0\rangle_R)|1\rangle_A|1\rangle_B$ . We assume that the L mode is coupled to the 1–3 transition and the R mode is coupled to the 1–4 transition. By applying a properly timed pair of pulses (with the Rabi frequencies  $\Omega_1$  and  $\Omega_2$ ) from the two control laser beams, an optically off-resonant but two-photon resonant Raman transition is carried out in each atom. Here, the Rabi frequencies due to the L and R photons are  $g_1$  and  $g_2$ , respectively. The strength of a given  $g$  is determined by three factors: the dipole

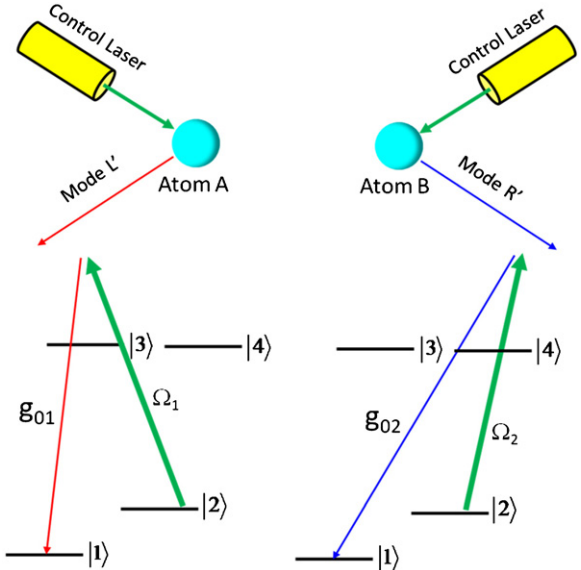


Figure 7. Schematic illustration of readout from an atomic quantum memory.

moment of the transition, the energy of a single photon and the mode volume of the photon. For a free space photon, the effective mode volume is determined by the transverse spatial profile and the finite temporal duration. After the Raman interactions, the quantum state of the combined system becomes  $(1/\sqrt{2})|0\rangle_L|0\rangle_R(|1\rangle_A|2\rangle_B - |2\rangle_A|1\rangle_B)$ , producing a maximally entangled state between the atoms.

The process for transferring the quantum information from the pair of atoms to a pair of photons is illustrated schematically in figure 7. For atom A, the readout laser pulse is now applied on the 2–3 transition. If the atom were in state 2, this will produce an anti-Stokes photon, corresponding to the 1–3 transition, and detuned to match the two-photon resonance condition, designated again as the L'-mode. Here,

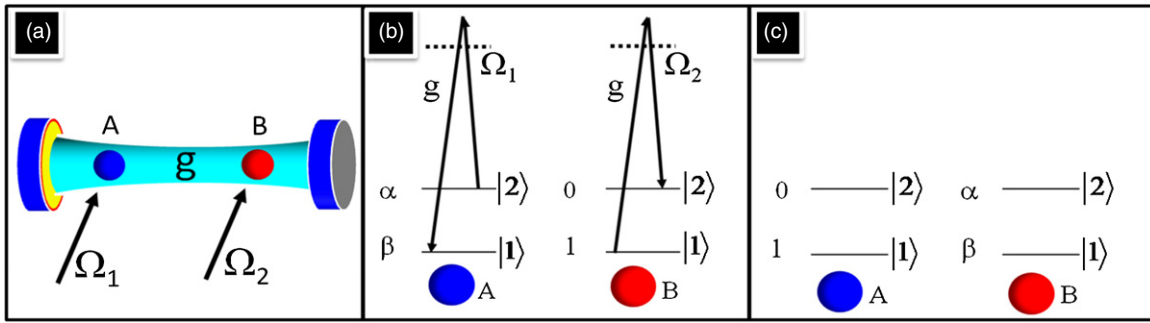


Figure 8. Illustration of quantum state transfer between atoms in a cavity.

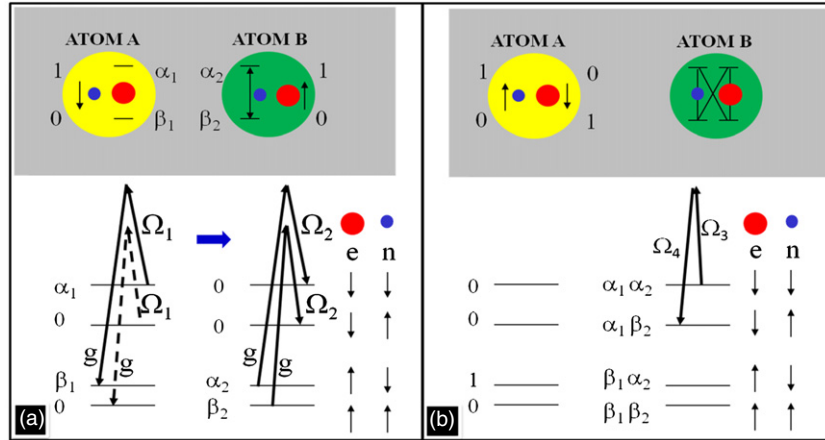


Figure 9. Illustration of loading two qubits into a single atom, for a CNOT gate operation between the atoms.

the Rabi frequency for the single photon will correspond to the mode that is most efficiently matched to the readout pulse. If the atom were in state 1, no photon would be produced. A similar process is carried out in atom B, and the net result after the readout process is a quantum state given by  $(1/\sqrt{2})(|0\rangle_L|1\rangle_R - |1\rangle_L|0\rangle_R)|1\rangle_A|1\rangle_B$ .

Such a passive quantum memory (PQM) is adequate for situations where the primary objective is to convert a flying qubit to a stationary qubit, serving as a buffer, in order to extend the useful lifetime of the quantum information. However, a more useful quantum memory would be a system that can perform arbitrary quantum gate operations: an active quantum memory (AQM). In principle, the single-atom PQM system described above can be modified to act as an AQM by making use of a cavity to couple the atoms. The basic process behind such a coupling is illustrated in figure 8. Consider two atoms inside a cavity, with atom B in the ground state and atom A in a quantum superposition (figure 8(a)). A laser pulse applied to atom A transfers the quantum state to the cavity, in a superposition of zero photon and one photon (figure 8(b)). Another laser pulse applied to atom B then transfers this quantum state to atom B (figures 8(b) and (c)). Here, the Rabi frequency corresponding to a single photon is determined by the cavity mode volume.

A generalization of this basic concept can be used to realize a controlled-NOT (CNOT) between the two atoms, as illustrated in figure 9. Here, each atom is assumed to have four metastable ground states, which can be modelled effectively as the space spanned by the spin-up and spin-down states of an

electron and the nucleus, for example. At the onset, the qubit in atom A is encoded in the nucleus (blue circle), while the qubit in atom B is encoded in the electron (red circle). A laser field applied to atom A converts the electronic quantum state to the cavity. Another laser field applied to atom B transfers this quantum state to the electron in atom B (figure 9(a)). The net result is that both bits of quantum information, unentangled, are now inside atom B (figure 9(b)). An internal transition between two of the four states, realized by another Raman transition using two laser beams, entangles the electron and the nucleus inside atom B. For example, a transition between the top two states (figure 9(b)) would correspond to a CNOT operation where the electron nuclear spin is flipped if and only if the electron spin is down. The reverse of the process shown in figure 9(a) transfers the electronic quantum state from atom B to atom A. The end result is that atoms A and B are now entangled, having undergone a CNOT operation. It is well known that a CNOT is a universal quantum gate, so that the ability to carry out this operation is tantamount to the ability to perform any quantum logic operation.

The process for storing and retrieving an entangled photon pair, as illustrated in figures 6 and 7, is impractical because the vacuum Rabi frequencies achievable in free space are too weak. However, this scheme can easily be modified to a pair of atoms held in a cavity, with the richer set of energy levels, as shown in figures 8 and 9. In this case, the photon modes would be coupled into the cavity prior to storage. Similarly, the retrieved information will be encoded in the cavity mode first, and can then be released into a free space mode, or into

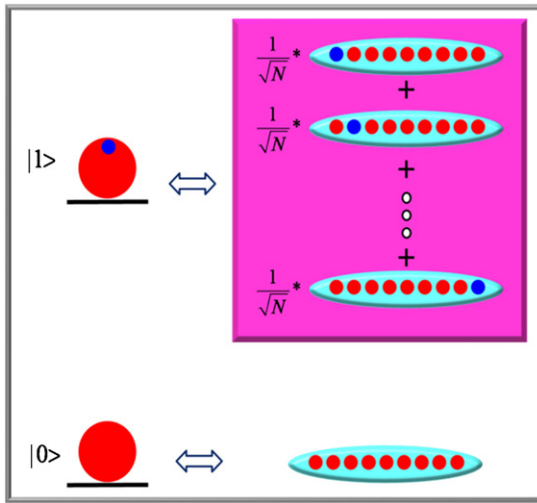


**Figure 10.** Illustration of collective excitation in an ensemble.

an optical fibre, for long distance propagation. Furthermore, as shown in [17], it is possible to perform measurements of all four Bell states in such a system as well. Thus, two atoms held inside a cavity form the type of AQM that would satisfy virtually all requirements of quantum information processing (QIP).

There are several technological challenges in realizing such a system. The most significant of these challenges is the fact that the vacuum Rabi frequency for a single atom, even inside a cavity, is rather weak. To make this strong enough, it is necessary to employ a very small cavity, with a very high finesse. The geometry of such a cavity makes it difficult to trap a set of single atoms and to perform the necessary control operations.

This problem can be circumvented by using an ensemble of atoms as an individual quantum system. The basic concept behind this approach is illustrated in figure 10, where each

atom is assumed to be a two-level system. The ground state of the ensemble corresponds to each of the  $N$  atoms being in the ground state. The first excited state is a coherent superposition of  $N$  states, each of which has only one of the atoms in the excited state. For a single photon interacting identically with each atom, the ensemble also behaves as a two-level system, with the property that the coupling rate is now enhanced by  $\sqrt{N}$ .

In order to realize a simple quantum memory, it is necessary to consider a situation where each atom has three energy levels: two metastable levels and one high-energy state coupled optically, forming a  $\Lambda$  system. A typical excitation with such an ensemble would use an optical field on each leg. Under such an excitation, the ensemble no longer behaves as a three-level ( $\Lambda$ ) system. Instead, we get a cascade of states, corresponding to absorptions of the  $n$  photons from each mode, where  $n$  can range from 1 to a very large integer. This is illustrated in figure 11, with the collective states defined in figure 12. The cascade corresponding to the optical transitions alone can be ignored under most circumstances, because of detuning. However, the cascades corresponding to the Raman transitions must be taken into account.

In the case where mode 2 corresponds to a quantum state with zero or one photon, the Raman process is terminated within a single- $\Lambda$  system, as indicated by the shaded region. This is the case corresponding to the storage and recall of single-photon quantum states, akin to what is shown in figures 6 and 7. Thus, it is possible to use an ensemble to realize a robust PQM; several groups have demonstrated such a memory already.

Consider next the prospect of using such an ensemble to perform quantum gate operations, of the type illustrated in figure 9. For the CNOT gate operation, it is necessary to use a Raman transition where both legs are excited by coherent states with a large mean number of photons. Similar operations are also necessary for quantum rotations within a single qubit, as

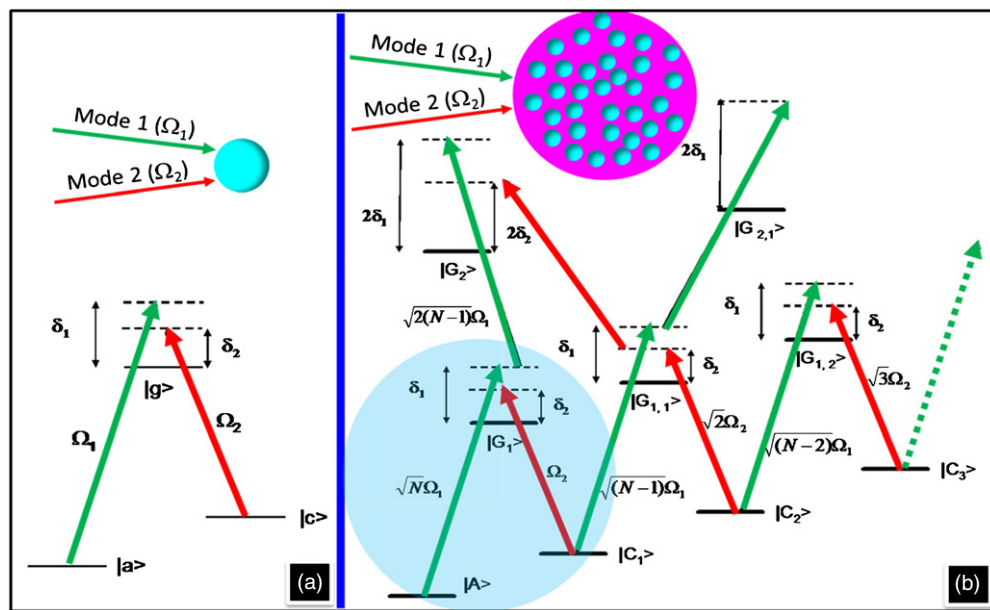


**Figure 11.** Illustration of cascades of transitions in an ensemble.

$$\begin{aligned}
|A\rangle &\equiv |a_1, a_2, \dots, a_N\rangle; \quad |G_1\rangle \equiv \frac{1}{\sqrt{N}} \sum_{j=1}^N |a_1, a_2, \dots, g_j, \dots, a_N\rangle \\
|C_1\rangle &\equiv \frac{1}{\sqrt{N}} \sum_{j=1}^N |a_1, a_2, \dots, c_j, \dots, a_N\rangle \\
|G_2\rangle &\equiv \frac{1}{\sqrt{N} C_2} \sum_{j,k (j \neq k)}^{N C_2} |a_1, a_2, \dots, g_j, \dots, g_k, \dots, a_N\rangle \\
|C_2\rangle &\equiv \frac{1}{\sqrt{N} C_2} \sum_{j,k (j \neq k)}^{N C_2} |a_1, a_2, \dots, c_j, \dots, c_k, \dots, a_N\rangle \\
|G_{1,1}\rangle &\equiv \frac{1}{\sqrt{2^N C_2}} \sum_{j,k (j \neq k)}^{2^N C_2} |a_1, a_2, \dots, g_j, \dots, c_k, \dots, a_N\rangle \\
|G_{2,1}\rangle &\equiv \frac{1}{\sqrt{Z}} \sum_{(j \neq k, l)}^Z |a_1, a_2, \dots, g_j, \dots, g_k, \dots, c_l, \dots, a_N\rangle \quad [Z = 3^N C_3] \\
|G_{1,2}\rangle &\equiv \frac{1}{\sqrt{Z}} \sum_{(j \neq k, l)}^Z |a_1, a_2, \dots, g_j, \dots, c_k, \dots, c_l, \dots, a_N\rangle \quad [Z = 3^N C_3]
\end{aligned}$$

**Figure 12.** Collective states of figure 11 defined. For example,  $|A\rangle$  represents a state where all  $N$  atoms are in the single-atom state  $|a\rangle$ ,  $|G_1\rangle$  represents a symmetrized and normalized superposition of all states where only one of the  $N$  atoms is in the single-atom state  $|g\rangle$  and the rest are in the single-atom state  $|a\rangle$  and so on.

well as for measurements of Bell states [17], which in turn lie at the heart of many QIP protocols. However, as can be seen in figure 11, under such an excitation, the single- $\Lambda$  transition turns into a cascade of  $\Lambda$  transitions, involving collective states defined [14] in figure 12. As an aside, note that the number of states in the cascade depends on  $N$ , the number of atoms in the ensembles. For  $N = 1$ , the cascade disappears and is reduced to a simple  $\Lambda$  system.

In order to use ensembles as AQMs capable of performing useful functions in QIP, it is thus necessary to truncate this cascade. In [14, 15], we have shown how to do this, by making use of the so-called light shift blockade (LSB). Briefly, a light shift is the change in the energy of a state in the presence of a highly detuned laser field coupling it to another state. For off-resonant Raman transitions excited by unequal Rabi

frequencies, the difference in the shifts of the two metastable states is routinely taken into account in order to reach the two-photon resonance condition. For the Raman transitions shown in the cascades in figure 11, an imbalance in the Rabi frequencies can thus be used to prevent all but the primary (shown in shades) Raman transition from being two-photon resonant. The net effect, as summarized in figure 13, is that under the LSB, the ensemble acts as a single atom, so that the type of quantum storage, recall and processing illustrated in figure 6 through figure 9 can now be done with ensembles, loaded inside a cavity.

The advantage of using ensembles is that the coupling to a single photon is now enhanced by a factor of  $\sqrt{N}$ . However, since the Rabi frequencies in the cascade depend on  $N$ , the imbalance needed for truncating the cascade also depends on  $N$ . In particular, the blockade necessary for carrying out at least 100 operations is optimized for a value of about  $N = 1.5 \times 10^5$ , with an enhancement of about 400 in the vacuum Rabi frequency. It is well known that the vacuum Rabi frequency scales linearly with the length of a confocal cavity. Thus, a cavity about 2 cm long will have the same coupling strength as that of a 50  $\mu\text{m}$  long cavity typically used in a single-atom cavity QED experiment. For a given mirror reflectivity, the cavity storage time also increases with length. Therefore, the mirrors used in this cavity do not have to be as highly reflective as those used for the 50  $\mu\text{m}$  long cavity. We have previously identified the proper set of hyperfine levels and Zeeman sublevels necessary for quantum storage and processing using ensembles of  $^{87}\text{Rb}$  atoms [14].

A simple configuration used for linking two such memory elements is illustrated in figure 14. Briefly, the quantum state encoded in the end ensemble of the quantum memory array on the left is read out, using the approach shown in figure 7. The resulting photonic qubit is then stored in the edge ensemble of the quantum memory array on the right. Of course, variations of this geometry can be used to store quantum information from a photonic qubit arriving from other

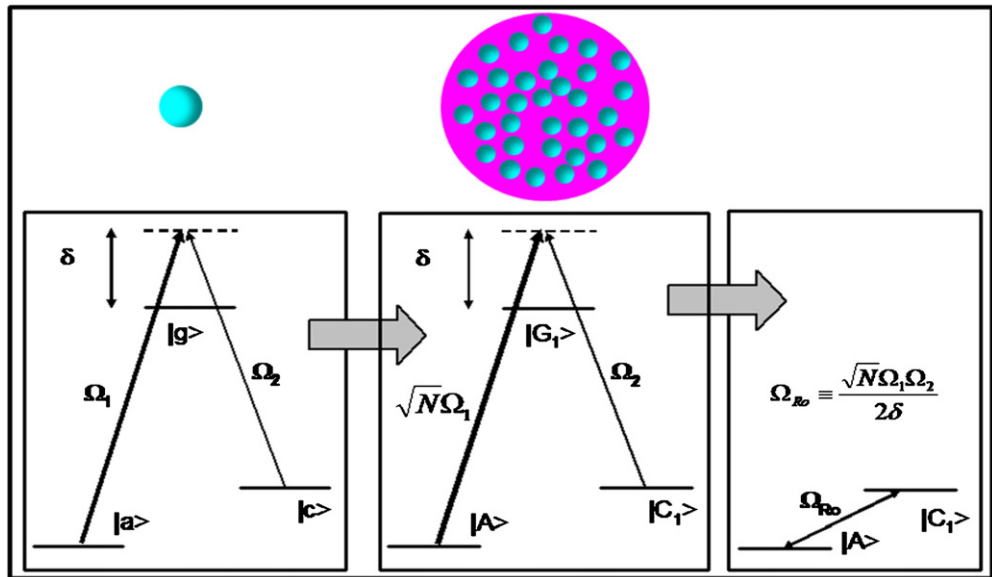


**Figure 13.** Summary of the LSB process, rendering an ensemble equivalent to a single atom.

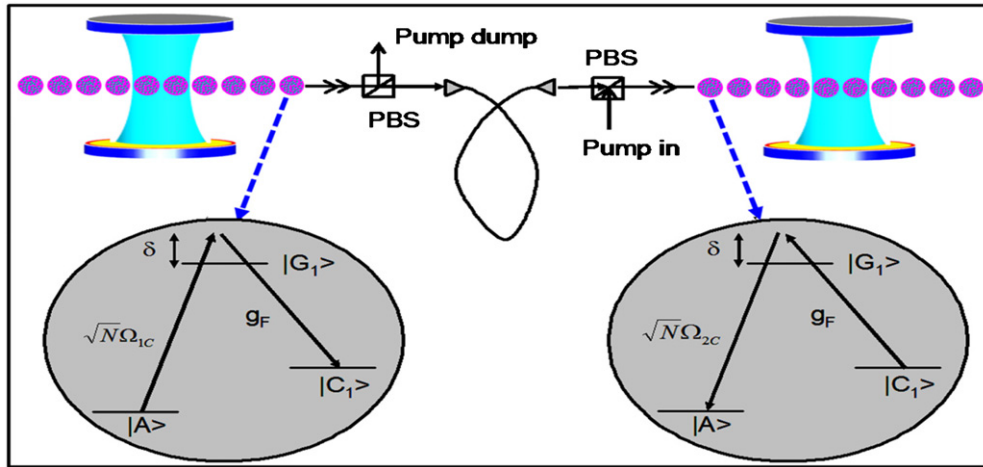


Figure 14. Illustration of quantum information retrieval and transfer.

sources. Furthermore, the photonic qubit restored from one ensemble can be converted to another frequency, and loaded into another quantum memory, as described in section 2.

#### 4. NV-diamond quantum memory

Bulk diamond and nanostructures of diamond containing an individually addressable nitrogen-vacancy colour centres (NVCC) have emerged as a very promising candidate medium for many of the tools needed for QIP, as evidenced by a large body of work [7, 19–25]. A single NVCC in a nanostructure is nearly an ideal quantum system. Under cryogenic conditions (at 10 K, for example), it should be possible to reach a quantum memory lifetime far exceeding 1 s using the electron spin, due to the fact that the electron spin population lifetime exceeds 100 s at cryogenic temperature [26], or a much longer lifetime by transferring the qubit into the nuclear spin [27]. Using a cryogenically cooled and spatially distinct colour centre, addressed by a confocal lens system, it is possible to realize a quantum memory and a source of entangled photons. Using a pair of such systems, it would then be feasible to realize important QIP functionalities, including storage and retrieval of quantum information and Bell state measurement, as key steps for quantum teleportation and quantum repeating.

To understand how NV diamond can become entangled with photons, it is first necessary to determine the energy level structure and selection rules for optical transitions. Solid-state systems are considerably more complex than free atoms. In particular, the spin-orbit coupling in free atoms which allows optical transitions to induce electron spin flips is usually quenched for colour centres in solids. Thus, the Raman schemes that were so central to the photon entanglement and storage schemes outlined earlier were predicted to be strictly forbidden. As a result of these predictions, progress towards spin-photon entanglement in NVCC and other solid-state systems was delayed by many years. However, recent developments showed that these negative predictions were too simplistic, and in fact spin-photon quantum entanglement was recently demonstrated for NV diamond [7].

NV diamond consists of a carbon vacancy in the diamond lattice with one of the neighbouring carbon atoms substituted

by a nitrogen atom, as illustrated in figure 15(a). This vacancy can be thought of as a carbon atom with zero nuclear charge. The outer s and p orbitals of the carbon atoms in diamond satisfy the octet rule, and so the vacancy will also be assumed to prefer a full shell of eight electrons distributed among one s and three p orbitals. However, unlike a free atom, the p orbitals are not all degenerate. In particular, the NV centre has a symmetry of C<sub>3v</sub>, which means that there is a z-axis distortion. As a result, the s and p<sub>z</sub> levels are split out from the p<sub>x</sub> and p<sub>y</sub> orbitals. This is illustrated in figure 15(b), where the p<sub>x</sub> and p<sub>y</sub> orbitals are replaced by p<sub>+</sub> and p<sub>-</sub> which have orbital angular momentum projections of +1 and -1 along the z-axis, respectively. Of course in the presence of non-axial strain or electric fields, the C<sub>3v</sub> symmetry is lowered and the p<sub>x</sub> and p<sub>y</sub> orbitals are no longer degenerate, as illustrated in figure 15(b).

The negatively charged NV-complex is the one of interest and has six electrons: four from the dangling bonds of the neighbouring atoms, one extra electron on the nitrogen, plus the electron needed to give the negative charge. Assuming that Hund's rule for adding electrons to free atoms applies, the ground state will be a spin-1 triplet, as illustrated by the small arrows in the energy level diagram of figure 15(c). Since the shell is mostly full, it is more convenient to work with holes than electrons and these are shown by the large arrows in the level diagrams of figures 15(b) and (c).

Thus, the NV diamond ground state has equal contributions from p<sub>-</sub> and p<sub>+</sub> orbitals which gives it a net orbital angular momentum projection of zero,  $m_L = 0$ . The electron spin triplet on the other hand has three possible projections,  $m_S = 0, -1, +1$ . Due to a weak spin-orbit interaction with the excited state, these levels split into a state with A-symmetry, |0> and a degenerate pair of E-states |−1> and |+1> as illustrated in figure 15(d). This splitting is approximately 2.88 GHz. Of course, if an axial magnetic field is applied, the  $m_S = \pm 1$  states can also split (not shown).

In contrast, the excited state has a contribution from either p<sub>+</sub> or p<sub>-</sub> but not both, and thus there are two orbital excited states, where the p<sub>+</sub> triplet state for holes is shown in figure 15(c). Note that a singlet state is also possible but details

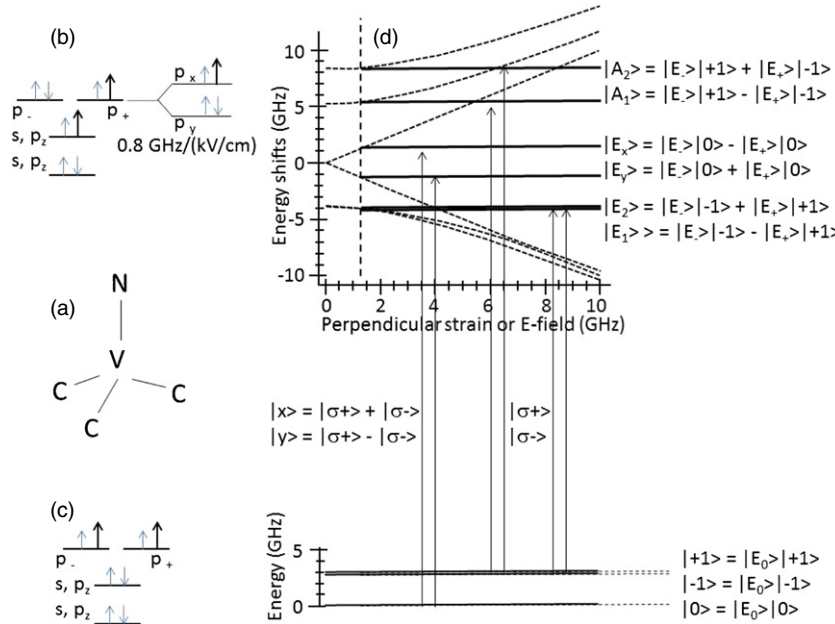


**Figure 15.** (a) The nitrogen-vacancy (NV) centre. (b) The excited-state energy levels showing the effects of strain. (c) The ground-state triplet. (d) The excited- and ground-state assignments are as labelled. The shifts of the energy levels with strain or electric field are shown as the dotted lines. At the strain shown by the vertical dashed line, the energy levels are extended in the horizontal direction to show the allowed optical transitions.

of this are not yet fully known and there are no allowed optical transitions to the singlet from the triplet ground state, since optically induced electron spin flips are forbidden. When the electron spin is included, there are a total of six excited states. The first two correspond to opposing orbital and spin quantum numbers  $m_L = +1, m_S = -1$  and  $m_L = -1, m_S = +1$ . Mutual spin flips between these levels are fully allowed and hence there is a strong interaction which leads to well-split superposition states with symmetries A1 and A2 as shown in figure 15(d). The next two states are the  $m_S = 0$  states. Mutual spin flips between these would correspond to  $\Delta m = 2$  and hence are forbidden. Nonetheless, even the slightest perturbation lifts the degeneracy of these states converting them into  $E_x$  and  $E_y$  as shown in figure 15(d). Finally, there are the states with total angular momentum quantum numbers of 2,  $m_L = +1, m_S = +1$  and  $m_L = -1, m_S = -1$ . Again spin flips are forbidden as these would require  $\Delta m = 4$ . Due to the relative insensitivity of electron spin to strain, these levels are not strongly split by strain. Although for large strains, the interaction with the  $E_y$  state can cause mixing as shown in figure 15(d). Note that the ground state levels are also insensitive to strain.

From the requirement that electron spin is preserved on optical excitation, the allowed optical transitions can be easily determined and are shown in figure 15(d) and in more detail in figure 16. Note that these transitions include fully allowed electron spin-flip Raman transitions, for example,  $|-1\rangle \rightarrow |A_2\rangle \rightarrow |+\rangle$  even though all the optical spin-flip transitions are forbidden.

Using the transition manifold of figure 16, it is easy to show how to generate photons that are entangled with electron spin. For example, starting from the  $|A_2\rangle$  excited state, it is seen that an NV decaying to the  $|-1\rangle$  electron spin ground state

will emit a  $\sigma +$  photon, whereas decay to the  $|+1\rangle$  electron spin state will result in a  $\sigma -$  photon [7]. If this emitted photon is converted into the telecom band and then into a wavelength resonant with rubidium, it can be captured by the rubidium atom and in so doing produce entanglement between the NV spin and a distant Rb spin.

The inverse process of capturing an entangled photon emitted by a Rb atom and converting it into an entanglement between the NV and Rb is more complicated. Actually the first part is very simple, as shown in figure 16, since an NV starting from the spin  $|0\rangle$  ground state can absorb either an  $|x\rangle$  or a  $|y\rangle$  polarized photon to selectively populate states  $|E_y\rangle$  or  $|E_x\rangle$  as shown, in analogy to the Rb memory. However, to verify that absorption has occurred, the excited-state populations must be shelved to other long-lived states so that a cycling transition with either  $x$  or  $y$  polarization can verify whether or not a photon was absorbed, in analogy to the Rb case. How this can be accomplished is not immediately obvious from figure 16 since there are no optical transitions from  $|E_x\rangle$  or  $|E_y\rangle$  to a ground state other than  $|0\rangle$ , and hence there is no optical Raman transition that can be used to adiabatically transfer the population to any other states.

To overcome this problem, we introduce a microwave transition in the excited state. The relevant allowed transitions are as labelled in figure 17(a). This excitation scheme is known as the double dark technique [28]. It is not difficult to drive the ground- and excited-state microwave transitions in NV diamond at Rabi frequencies of the order of 1 GHz or larger which is much faster than the tens of MHz inhomogeneous width of the excited states. Thus, well-resolved Rabi splitting can be produced in the excited-state spin sublevels as illustrated in figure 17(b) for realistic parameters. As seen in figure 17(b), high-contrast Raman dark resonances are easily

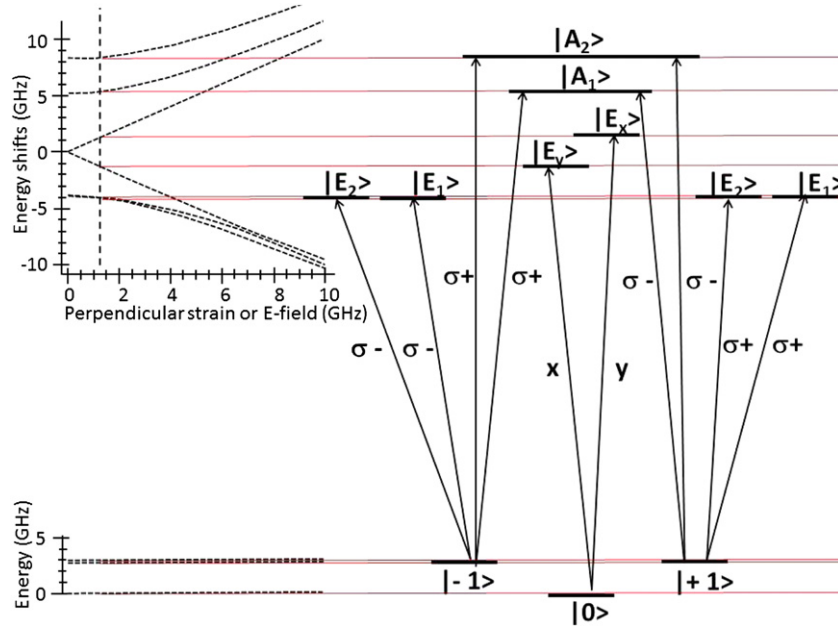


**Figure 16.** Details of the optical selection rules for the NV diamond transitions from the ground to excited triplet manifolds. As can be seen, electron-spin-flip Raman transitions are allowed even though the optical transition cannot flip electron spin.

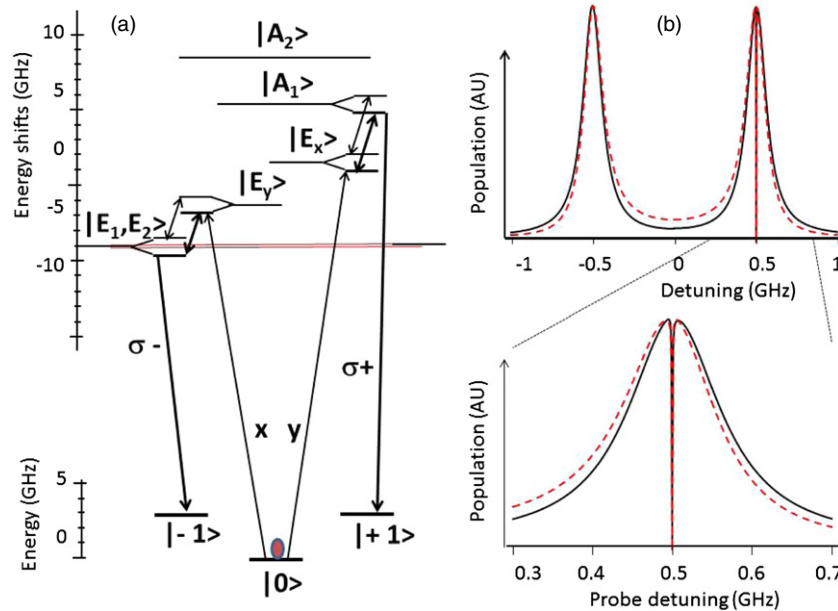


**Figure 17.** (a) Excitation scheme to transfer  $x,y$  polarization entanglement of an input (probe) photon into NV electron spin entanglement. As shown, the  $x$ -polarization is mapped onto the  $| -1 \rangle$  spin state and the  $y$ -polarization is mapped onto the  $| +1 \rangle$  spin state. (b) A representative plot of excited-state population versus detuning of input (probe) frequency showing efficient excitation of a Raman dark state. For these plots, the excitation scheme involving  $|E_x\rangle$  (solid curve) and  $|A_1\rangle$  (dashed curve) excited states is used. The microwave field is resonant with the  $|E_x\rangle$  to  $|A_1\rangle$  transition and has a Rabi frequency of 1 GHz. The probe and  $\sigma+$  Rabi frequencies are 10 MHz, where the  $\sigma+$  de-excitation field is detuned by half the microwave Rabi frequency, or 0.5 GHz, from the excited  $|A_1\rangle$  state. The excited-state linewidth is 100 MHz, and the ground-state linewidth is 1 kHz.

excited. Here it is worth emphasizing that the optical fields are not resonant with transition from the ground to excited state since then there would be no dark state. Instead the optical fields are detuned by one-half of the microwave Rabi frequency as shown in figure 17(a). Using this excitation scheme, the polarization and/or frequency entanglement present on an incoming photon can be stored in the NV spin states, just as was the case in the Rb memory. To verify that a photon

was captured, the optical transitions, labelled  $y$  in figure 17(a), starting from the  $m_S = 0$  ground can be driven. Since this is a cycling transition, many photons will be generated if the  $m_S = 0$  state is still populated. No detected photons means that the electron is in either of the  $m_S = +/ - 1$  states. In this way, the successful storage of the input photon can be verified without disturbing its quantum state, in analogy with the technique used in Rb. Here it is worth noting that this double-dark excitation

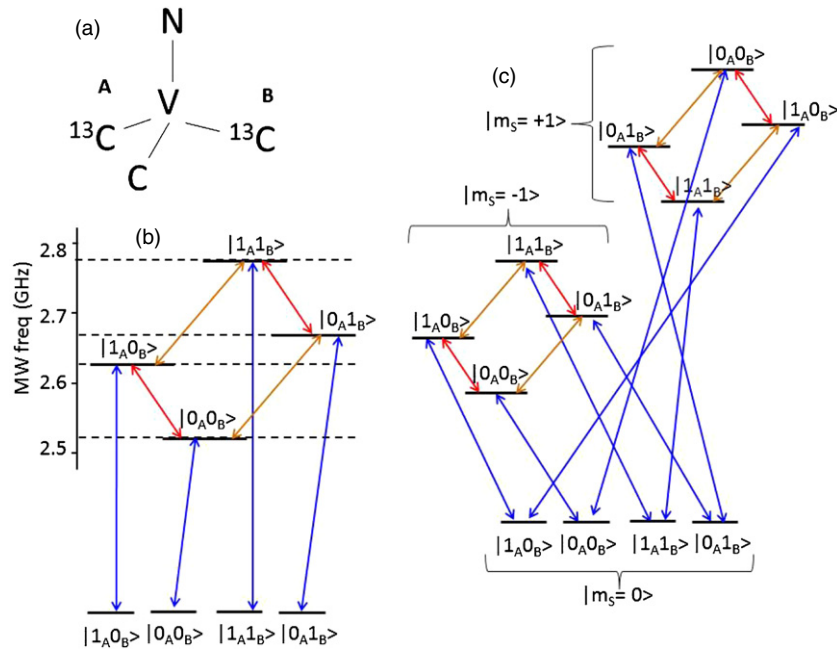


**Figure 18.** (a) NV with two adjacent <sup>13</sup>C nuclei labelled A and B. (b) Partial energy level scheme and allowed transitions from the  $m_s = 0$  electron spin state to the  $m_s = -1$  state in a weak axial magnetic field. The nuclear spin state  $|0\rangle$  corresponds to spin up and  $|1\rangle$  to spin down. (c) The complete system including  $m_s = -1, 0, +1$ .

scheme is very general and can be used to produce efficient spin-flip Raman dark resonances in almost any system, even though no optical spin-flip transitions exist.

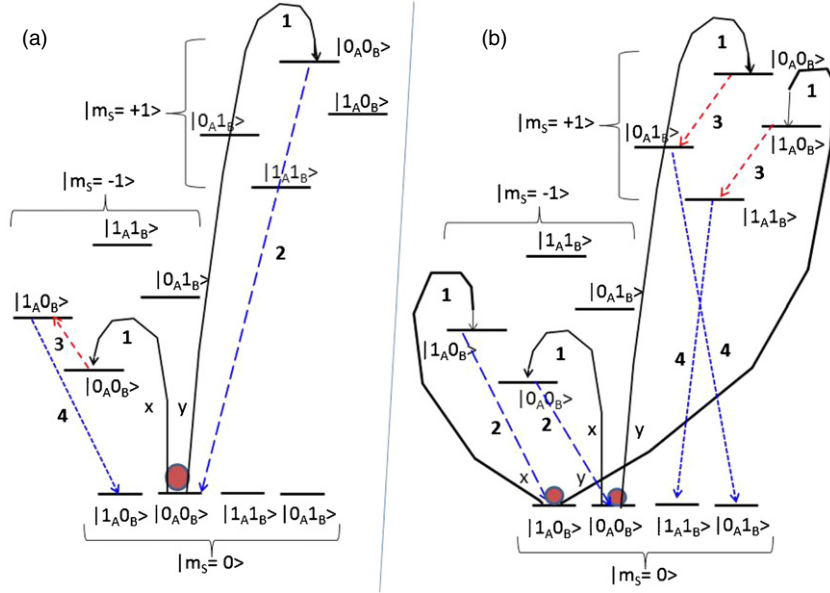
Once the quantum information has been deposited into a superposition of electron spin  $|+1\rangle$  and  $| -1\rangle$  states, it can be transferred into nuclear spin states where it can be stored for seconds to minutes or longer at low temperature. To perform quantum operations on the stored photons, like Bell state measurements, there are a variety of options. First, a pair of NVs with entangled electron spin can be used. Scalable quantum logic has already been demonstrated with such a pair coupled by magnetic dipole–dipole interactions at room temperature. Second, the optical dipole–dipole interaction between nearby NVs can be used to create an entangled pair for quantum logic. Third, cavity-mediated optical coupling can be used, or possibly microwave coupling using superconducting cavities. Fourth, for simple Bell state measurements involving two qubits as in quantum teleportation, a single NV with a pair of near-neighbour <sup>13</sup>C nuclei can be used. In fact, efficient Bell state excitation was already demonstrated with this system at room temperature [24].

Figure 18 shows one possible scheme for capturing the quantum information from two photons and storing them on adjacent <sup>13</sup>C spins of a single NV. Figure 18(a) shows two <sup>13</sup>C nuclear spins labelled A and B in a single NV. Figure 18(b) shows how the  $m_s = 0$  to  $m_s = -1$  electron spin transition is split by the hyperfine interaction with the two adjacent <sup>13</sup>C nuclei. As seen, each of the four nuclear spin combinations can be independently and conditionally driven between electron spin 0 and  $-1$  states with resonant microwave (MW) fields. In addition, radio frequency (RF) fields can drive spin flips of one nuclear spin at a time. Note that the two-spin states  $|1_A 0_B\rangle$  and  $|0_A 1_B\rangle$  are degenerate and can undergo mutual

spin flip-flops. This leads to a strong interaction that gives superposition eigen-states with a relatively large splitting as shown. However, for the purpose of quantum storage, it does not matter whether these states are pure two-spin states or not as long as the transitions shown are allowed. Therefore, for simplicity the pure-state notation is used.

To store the photon quantum state in the nuclear spins, both  $m_s = -1$  and  $m_s = +1$  transition manifolds are needed and these are shown in figure 18(c). Storage of the quantum state of the first photon begins by initializing the nuclear spins into a single-composite state as shown in figure 19(a). This can be done by simultaneously driving the  $m_s = +/ - 1$  optical transitions, plus the  $m_s = 0 \rightarrow +/ - 1$  ground-state microwave transitions for all nuclear spin states except the  $|0_A 0_B\rangle$  state (not shown). Electron and nuclear flip-flops in the optical excited state eventually put all the nuclear spins into the  $|0_A 0_B\rangle$   $|m_s = 0\rangle$  ground state because this state is not excited by either optical or microwave fields.

Once initialized, the quantum state encoded in the polarization of the first photon is mapped onto the NV electron spin using the technique of figure 17, and illustrated schematically by step ‘1’ in figure 19(a). This mapping of quantum information from the photon to the electron spin preserves nuclear spin states. Next the quantum information stored on the electron spin must be transferred to one of the nuclear spins. This is done using the remaining steps in figure 19(a). In particular, step ‘2’ shelves the  $|0_A 0_B\rangle$  state, originally in the  $m_s = +1$  manifold, into the  $m_s = 0$  manifold with a microwave  $\pi$  pulse, as shown by the transitions labelled ‘2’. Next the first nuclear spin is flipped conditioned on the electron being in the  $m_s = -1$  manifold by using a RF  $\pi$  pulse as shown by the transition labelled ‘3’. Thus, the first nuclear spin is flipped only if the input photon was x-polarized.



**Figure 19.** (a) NV with two adjacent  $^{13}\text{C}$  nuclei labelled A and B. (b) Partial energy level scheme and allowed transitions from the  $m_s = 0$  electron spin state to the  $m_s = -1$  state in a weak axial magnetic field. The nuclear spin state  $|0\rangle$  corresponds to spin up and  $|1\rangle$  to spin down. (c) The complete system including  $m_s = -1, 0, +1$ .

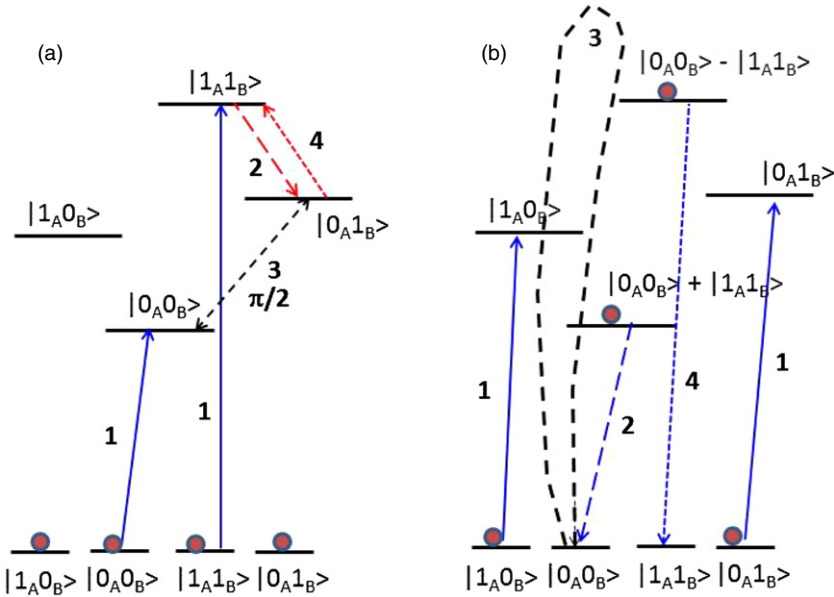


**Figure 20.** (a) Bell state readout starts by moving the desired composite states into the  $m_s = -1$  manifold. To rotate these into the Bell basis, a  $\pi/2$  pulse, labelled 3, is needed. Due to selection rules, this is preceded and followed by  $\pi$  pulses labelled 2 and 4. (b) Once rotated into the Bell basis, the states can be read out one at a time using the optical cycling transition on the  $m_s = 0$  manifold. This is illustrated for  $\Phi+$ .

Finally, this flipped nuclear spin is also shelved into the  $m_s = 0$  manifold, as shown by the transitions labelled '4', to complete the electron to nuclear quantum state mapping, and to preparation for the second photon.

The second photon is then captured and its quantum information stored in its polarization state is mapped onto the electron spin  $m_s = +/ - 1$  states, as for the first photon, as shown by step 1 in figure 19(b). Again this is done without changing nuclear spins, on which the quantum state of the first photon is stored. Step 2 protects the information in the  $m_s = -1$  manifold by transferring it to the  $m_s = 0$  manifold

with dual  $\pi$  pulses as shown. Then step 3 flips the second nuclear spin B conditioned on the electron being in the  $m_s = +1$  manifold without disturbing the coherence on nuclear spin A. Finally, these flipped nuclear spins are transferred to the  $m_s = 0$  manifold in step 4 in preparation for Bell state measurements.

The Bell state measurement sequence is illustrated in figure 20. In figure 20(a), step 1 selectively transfers the  $|00\rangle$  and  $|11\rangle$  states onto the  $m_s = -1$  manifold with dual  $\pi$  pulses. To convert these into Bell states, a  $\pi/2$  pulse is needed on the transition between them. However, this transition is forbidden

by selection rules and so the  $\pi$  pulses in steps 2 and 4 are needed before and after the  $\pi/2$  pulse (step 3). To read out the Bell state probabilities, the remaining nuclear spin states are first transferred out of the  $m_s = 0$  manifold (step 1 in figure 20(b)) as this has the cycling transition needed for readout. In step 2, the desired Bell state is selectively transferred to the  $m_s = 0$  manifold by a MW  $\pi$  pulse as shown. Step 3 is the optical readout which determines if  $\Phi+$  was occupied. Step 4 shows the transfer of  $\Phi-$  for readout in the event  $\Phi+$  was found to be unoccupied. The remaining steps are not shown but follow a similar procedure.

In this section, the basic scheme for transferring the quantum information of two incoming photons, for example, from a Rb atomic memory, onto the NV electron spin has been outlined. The inverse process of generating photons whose polarization state is entangled with the NV electron spin was previously demonstrated experimentally [7]. Furthermore, the technique for transferring the electron-spin quantum states onto  $^{13}\text{C}$  nuclear spins for long-term storage has also been outlined. Finally, the use of two  $^{13}\text{C}$  nuclei on a single NV for making Bell state measurements was outlined. Thus, NV diamond has all the key elements needed for interfacing to trapped Rb atoms in a telecom-based quantum internet.

## 5. Summary and outlook

We have described techniques for creating quantum links at the telecom band between different types of quantum memories, using PPLN waveguides. The specific QMs we consider are based on ensembles of Rb atoms and nitrogen vacancy colour centres, each configured for processing capabilities. Memories based on spectral hole burning media could also be connected in this manner [29]. Links of this type could serve as the key interface needed for building a quantum internet.

## Acknowledgments

This work was supported in part by AFOSR grant FA9550-09-01-0652 and DARPA QuEST.

## References

- [1] Duan L M, Lukin M D, Cirac J I and Zoller P 2001 *Nature* **414** 413
- [2] Sangouard N *et al* 2007 *Phys. Rev. A* **76** 050301
- [3] Molina-Terriza G, Torres J P and Torner L 2002 *Phys. Rev. Lett.* **88** 013601
- [4] Mair A, Vaziri A, Weihs G and Zeilinger A 2001 *Nature* **412** 313
- [5] Broadbent C J, Camacho R M, Xin R and Howell J C 2008 Preservation of energy-time entanglement in a slow light medium *Phys. Rev. Lett.* **100** 133602
- [6] Huang J and Kumar P 1992 Observation of quantum frequency conversion *Phys. Rev. Lett.* **68** 2153–6
- [7] Togan E *et al* 2010 Quantum entanglement between an optical photon and a solid-state spin qubit *Nature* **466** 730
- [8] Zhu X *et al* 2011 Coherent coupling of a superconducting flux qubit to an electron spin ensemble in diamond *Nature* **478** 221
- [9] Ladd T D, Jelezko F, Laflamme R, Nakamura Y, Monroe C and O'Brien J L 2010 Quantum computers *Nature* **464** 45
- [10] Buluta I, Ashhab S and Nori F 2011 Natural and artificial atoms for quantum computation *Rep. Prog. Phys.* **74** 104401
- [11] Kumar P 1990 Quantum frequency conversion *Opt. Lett.* **15** 1476–8
- [12] Boyd R W 2008 *Nonlinear Optics* 3rd edn (London: Academic)
- [13] Huang J and Kumar P 1992 Observation of quantum frequency conversion *Phys. Rev. Lett.* **68** 2153–6
- [14] Shahriar M S, Pati G S and Salit K 2007 Quantum communication and computing with atomic ensembles using light-shift imbalance induced blockade *Phys. Rev. A* **75** 022323
- [15] Shahriar M S, Pradhan P, Pati G S and Salit K 2007 Light-shift imbalance induced blockade of collective excitations beyond the lowest order *Opt. Commun.* **278** 94–8
- [16] Pellizzari T, Gardiner S A, Cirac J I and Zoller P 1995 Decoherence, continuous observation, and quantum computing: a cavity QED model *Phys. Rev. Lett.* **75** 3785
- [17] Lloyd S, Shahriar M S, Shapiro J H and Hemmer P R 2001 Long distance, unconditional teleportation of atomic states via complete Bell state measurements *Phys. Rev. Lett.* **87** 167903
- [18] Deutsch D, Ekert A, Jozsa R, Macchiavello C, Poescu S and Sanpera A 1996 Quantum privacy amplification and the security of quantum cryptography over noisy channels *Phys. Rev. Lett.* **77** 2818–21
- [19] Shahriar M S, Hemmer P R, Lloyd S, Bhatia P S and Craig A E 2002 Solid-state quantum computing using spectral holes *Phys. Rev. A* **66** 032301
- [20] Hemmer P R, Turukhin A V, Shahriar M S and Musser J A 2001 Raman excited spin coherence in NV-diamond *Opt. Lett.* **26** 6
- [21] González G and Leuenberger M N 2009 Optical  $\Lambda$  transitions and quantum computing in the  $^{15}\text{N}-\text{V}^-$  center in diamond *Phys. Rev. B* **80** 201201
- [22] Gaebel T *et al* 2006 Room-temperature coherent coupling of single spins in diamond *Nature Phys.* **2** 408–13
- [23] Childress L, Gurudev Dutt M V, Taylor J M, Zibrov A S, Jelezko F, Wrachtrup J, Hemmer P R and Lukin M D 2006 Coherent dynamics of coupled electron and nuclear spin qubits in diamond *Science* **314** 281–5
- [24] Neumann P, Mizuuchi N, Rempp F, Hemmer P, Watanabe H, Yamasaki S, Jacques V, Gaebel T, Jelezko F and Wrachtrup J 2008 Multipartite entanglement among single spins in diamond *Science* **320** 1326–9
- [25] Jiang L *et al* 2009 Repetitive readout of a single electronic spin via quantum logic with nuclear spin ancillae *Science* **326** 267–72
- [26] Harrison J, Sellars M J and Manson N B 2006 Measurement of the optically induced spin polarisation of N-V centres in diamond *Diamond Relat. Mater.* **15** 586–8
- [27] Balasubramanian G *et al* 2009 Ultralong spin coherence time in isotopically engineered diamond *Nature Mater.* **8** 383–7
- [28] Yelin S F, Sautenkov V A, Kash M M, Welch G R and Lukin M D 2003 Nonlinear optics via double dark resonances *Phys. Rev. A* **68** 063801
- [29] Clausen C, Usmani I, Bussières F, Sangouard N, Afzelius M, Riedmatten H and Gisin N 2011 Quantum storage of photonic entanglement in a crystal *Nature* **469** 508–11



# Rydberg assisted light shift imbalance induced blockade in an atomic ensemble

Yanfei Tu <sup>a,\*</sup>, May E. Kim <sup>b</sup>, Selim M. Shahriar <sup>a,b</sup>

<sup>a</sup> Department of Electrical Engineering & Computer Science, Northwestern University, Evanston, IL 60208, USA

<sup>b</sup> Department of Physics & Astronomy, Northwestern University, Evanston, IL 60208, USA



## ARTICLE INFO

### Article history:

Received 11 September 2014

Received in revised form

30 October 2014

Accepted 6 November 2014

Available online 15 November 2014

### Keywords:

Light shift blockade

Atomic ensemble

Rydberg interaction

Quantum computing

## ABSTRACT

Previously, we had proposed the technique of light shift imbalance induced blockade which leads to a condition where a collection of non-interacting atoms under laser excitation remains combined to a superposition of the ground and the first excited states, thus realizing a collective state quantum bit which in turn can be used to realize a quantum computer. In this paper, we show first that the light shift imbalance by itself is actually not enough to produce such a blockade, and explain the reason why the limitation of our previous analysis had reached this constraint. We then show that by introducing Rydberg interaction, it is possible to achieve such a blockade for a wide range of parameters. Analytic arguments used to establish these results are confirmed by numerical simulations. The fidelity of coupled quantum gates based on such collective state qubits is highly insensitive to the exact number of atoms in the ensemble. As such, this approach may prove to be viable for scalable quantum computing based on neutral atoms.

© 2014 Elsevier B.V. All rights reserved.

## 1. Introduction

In most protocols for quantum computing or quantum information processing, the fundamental building block is the quantum bit (qubit). A single, neutral atom behaving as a two-level system can be used as a qubit. Compared to ions, neutral atoms have the advantage that they are highly decoupled from electromagnetic perturbations. However, coupling two qubits using neutral atoms is difficult to achieve. One approach for such coupling makes use of the Rydberg blockade [1–7]. In another approach, a cavity mode is used to couple atoms held inside the cavity [8–11]. A key parameter in this approach is the single photon Rabi frequency, which must be much larger than atomic and cavity decay rates. This constraint can only be met by making the cavity very small, which in turn makes it difficult to hold many qubits inside.

One approach for circumventing this constraint is to make use of atomic ensembles. The single photon Rabi frequency for an ensemble scales as  $\sqrt{N}$ , where  $N$  is the number of atoms, thus making it possible to make use of a much larger cavity. However, in order to use an ensemble for quantum computing, it is necessary to ensure that it behaves as an effective two-level system.

When exposed to only a single photon (or in a Raman transition, where one leg is exposed to a single photon), an ensemble of two-level atoms does indeed behave like a single two-level system. This property has been used to realize quantum memory elements using such an ensemble [12,13]. However, any protocol that aims to create a two qubit logic gate (such as a CNOT gate) between two ensembles, necessary for realizing a quantum computer, must make use of additional, classical laser fields. Under such excitations, an ensemble no longer behaves like a two-level system. Instead, it exhibits a cascade of energy levels that are equally spaced. When exposed to a classical field, all levels in the cascade get excited [14], making it impossible to realize a quantum logic gate. In order to overcome this constraint, it is necessary to create conditions under which the cascade is truncated to a two-level system.

Previously, our group had proposed a scheme for producing such a blockade, using imbalances in light shifts experienced by the collective states [15,16]. In that model, the light shifts were calculated by using a perturbation method, keeping terms up to second-order in laser intensity. However, it turns out that when the collective excitation is viewed as a product of individual atomic states, an accurate representation for classical laser fields, and in the absence of any interaction between the atoms, the blockade effect disappears. We have verified this conclusion by numerically simulating the evolution of collective states for small values of  $N$ . It is still possible to produce such a blockade for a laser field described as a superposition of photon number states.

\* Corresponding author.

E-mail address: [yanfeitu@gmail.com](mailto:yanfeitu@gmail.com) (Y. Tu).

However, when the mean photon number in such a field is very large, such as in a classical laser field, the blockade tends to vanish. Thus, in order to produce a blockade under excitation with a classical laser field, we must make use of some interaction between the atoms. In this paper, we propose to make use of interaction induced via excitation to Rydberg states to achieve this goal.

The rest of the paper is organized as follows. In [Section 2](#), we review briefly the formulation of collective excitation of lambda-type atoms. In [Section 3](#), we summarize the model we had developed previously for light shift blockade (LSB) of collective excitation using second-order perturbation approximation. In [Section 4](#) we discuss how an alternative formulation of collective excitation allows us to determine the effect of light shift exactly, and identify conditions under which LSB is not possible. In particular, we show that when all excitation fields are classical, there is no blockade. In [Section 5](#), we show how the interaction between two Rydberg states can be used to realize LSB even under classical excitation. In [Section 6](#), we generalize this process for  $N$  atoms and show how LSB works for  $N$ -atom ensembles. Finally, in [Section 7](#), we summarize our results, and present an outlook for using this approach for realizing a multi-qubit quantum computer.

## 2. Collective state model

In order to avoid the deleterious effect of spontaneous emission, it is useful to realize a qubit based on two states that are long-lived. A convenient example for such a system consists of a Zeeman sublevel in one of the ground hyperfine state (e.g.  $m_F=0$ ,  $F=1$ ,  $5^2S_{1/2}$  in  $^{87}\text{Rb}$ ) and another Zeeman sublevel in another ground hyperfine state (e.g.  $m_F=0$ ,  $F=2$ ,  $5^2S_{1/2}$  in  $^{87}\text{Rb}$ ). These levels can be coupled by two laser fields to an intermediate state (e.g.  $m_F=1$ ,  $F=2$ ,  $5^2P_{1/2}$  in  $^{87}\text{Rb}$ ). When the interaction is highly detuned with respect to the intermediate state, the laser fields cause a Raman transition between the two low lying states, thus producing an effective two-level system.

This is generally known as the  $\Lambda$ -system, illustrated schematically in [Fig. 1](#). Here, the two ground states are  $|a\rangle$  and  $|c\rangle$ , and the intermediate state is  $|g\rangle$ . The states  $|a\rangle$  and  $|g\rangle$  are coupled by a field with a Rabi frequency of  $\Omega_1$  and a detuning of  $\delta_1$ . Likewise, states  $|c\rangle$  and  $|g\rangle$  are coupled by a field with a Rabi frequency of  $\Omega_2$  and a detuning of  $\delta_2$ . In the basis of states  $|a\rangle$ ,  $|c\rangle$  and  $|g\rangle$ , the Hamiltonian under electric dipole and rotating wave approximation, and

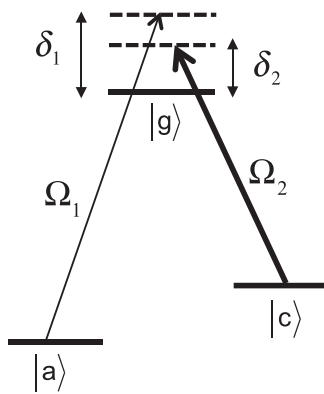


**Fig. 1.** Three-level scheme of single atom in an ensemble.

rotating wave transportation, is given by

$$\tilde{H} = \hbar \begin{bmatrix} \Delta/2 & 0 & \Omega_1/2 \\ 0 & -\Delta/2 & \Omega_2/2 \\ \Omega_1/2 & \Omega_2/2 & -\delta \end{bmatrix}, \quad (1)$$

where  $\delta \equiv (\delta_1 + \delta_2)/2$  is the average detuning and  $\Delta \equiv (\delta_1 - \delta_2)$  is the two-photon detuning. In what follows, we will assume that  $\delta$  is very large compared to  $\Omega_1$  and  $\Omega_2$ , as well as the decay rate,  $\Gamma$ , of the state  $|g\rangle$ . We will further assume that the two lasers are co-propagating.

For  $N$  such non-interacting atoms, the ensemble can be modeled using symmetric collective states, also known as symmetric Dicke states [\[14\]](#). The first few states are defined as follows:

$$|A\rangle \equiv |a_1, a_2, \dots, a_N\rangle,$$

$$|G_1\rangle \equiv \frac{1}{\sqrt{N}} \sum_{j=1}^N |a_1, a_2, \dots, g_j, \dots, a_N\rangle,$$

$$|C_1\rangle \equiv \frac{1}{\sqrt{N}} \sum_{j=1}^N |a_1, a_2, \dots, c_j, \dots, a_N\rangle,$$

$$|G_2\rangle \equiv \frac{1}{\sqrt{N}C_2} \sum_{j,k(j \neq k)}^{N_{C_2}} |a_1, a_2, \dots, g_j, \dots, g_k, \dots, a_N\rangle,$$

$$|C_2\rangle \equiv \frac{1}{\sqrt{N}C_2} \sum_{j,k(j \neq k)}^{N_{C_2}} |a_1, a_2, \dots, c_j, \dots, c_k, \dots, a_N\rangle,$$

$$|G_{1,1}\rangle \equiv \frac{1}{\sqrt{2^N C_2}} \sum_{j,k(j \neq k)}^{2^N C_2} |a_1, a_2, \dots, g_j, \dots, c_k, \dots, a_N\rangle,$$

$$|G_{2,1}\rangle \equiv \frac{1}{\sqrt{3^N C_3}} \sum_{j,k,l(j \neq k \neq l)}^{3^N C_3} |a_1, a_2, \dots, g_j, \dots, g_k, \dots, c_l, \dots, a_N\rangle,$$

$$|G_{1,2}\rangle \equiv \frac{1}{\sqrt{3^N C_3}} \sum_{j,k,l(j \neq k \neq l)}^{3^N C_3} |a_1, a_2, \dots, g_j, \dots, c_k, \dots, c_l, \dots, a_N\rangle. \quad (2)$$

where

$$N_C M \equiv \binom{N}{M} \equiv N! / [M!(N-M)!].$$

In Reference [\[17\]](#), we have shown that the system remains confined to a generalized form of these symmetric collective states, independent of the relative separation between the atoms (and hence the size of the ensemble), as long as it is assumed that each atom sees the same amplitude of the Rabi frequency, and the same laser frequency (i.e., any residual Doppler shift of the Raman transition frequency due to the motion of the atoms is negligible). The generalized form of the symmetric states is formally the same as those in Eq. [\(2\)](#), except that the excited states incorporate the relevant spatial phases of the fields at the location of a given atom. This can be understood by noting that any phase factors accompanying the Rabi frequencies in the Hamiltonian of Eq. [\(1\)](#) can be transformed out to produce a version of the Hamiltonian where the Rabi frequencies are real. The transformation necessary for this transfers the phases to the basis states. We refer the reader to Reference [\[17\]](#) for details.

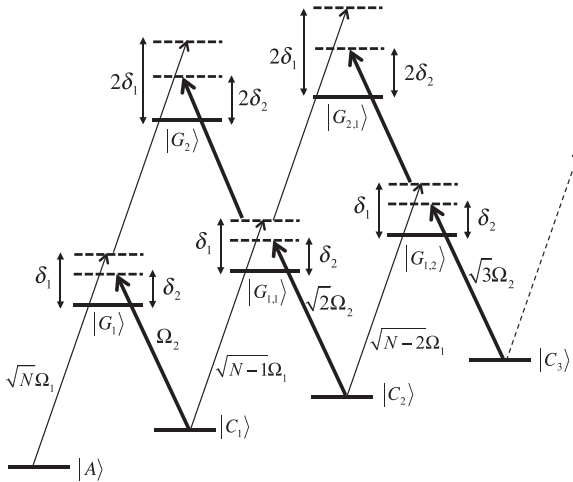


Fig. 2. Schematic illustration of the relevant collective states and the corresponding coupling rates.

The collective states of Eq. (2) are illustrated schematically in Fig. 2. Here, for example,  $|G_1\rangle$  represents a state where only one atom on average is excited to state  $|g\rangle$ , with the rest remaining in state  $|a\rangle$ . Similarly,  $|C_1\rangle$  represents a state where only one atom on average is excited to state  $|c\rangle$ , with the rest remaining in state  $|a\rangle$ , and so on. In our blockade scheme, we try to confine the system to the two lowest energy states  $|A\rangle$  and  $|C_1\rangle$ . If we could achieve this and minimize the excitations to the first few higher energy states, then excitations to even higher states will be almost nonexistent. It can be shown that the total number of symmetric states is  $N_S = (N + 2)!/2N!$ . For large  $N$ ,  $N_S = N^2/2$  so that the size of the Hamiltonian scales as  $N^4$ . Thus, an analysis of the evolution of the complete system exactly in this picture is computationally intractable. However, a plausible way to explore the possibility of finding the condition for the blockade is to truncate the system to a small size, and show that the excitation to the excluded states are negligible.

Here, we choose to truncate the system to six levels:  $|A\rangle$ ,  $|G_1\rangle$ ,  $|C_1\rangle$ ,  $|G_{1,1}\rangle$ ,  $|C_2\rangle$  and  $|G_{1,2}\rangle$ . If the condition we find for the blockade shows negligible excitation to states that have non-zero coupling to the excluded states, the truncation would then be justified. The Hamiltonian for these states can be expressed as [15]

$$H = \hbar \begin{bmatrix} \Delta/2 & \sqrt{N}\Omega_1/2 & 0 & 0 & 0 & 0 \\ \sqrt{N}\Omega_1/2 & -\delta & \Omega_2/2 & 0 & 0 & 0 \\ 0 & \Omega_2/2 & -\Delta/2 & \sqrt{N-1}\Omega_1/22 & 0 & 0 \\ 0 & 0 & \sqrt{N-1}\Omega_1/2 & -(\delta + \Delta) & \sqrt{2}\Omega_2/2 & 0 \\ 0 & 0 & 0 & \sqrt{2}\Omega_2/2 & -3\Delta/2 & \sqrt{N-2}\Omega_1/2 \\ 0 & 0 & 0 & 0 & \sqrt{N-2}\Omega_1/2 & -(\delta + 2\Delta) \end{bmatrix}. \quad (3)$$

### 3. Original model for light shift blockade

The Hamiltonian in Eq. (3) can be further simplified by adiabatically eliminating the states  $|G_1\rangle$ ,  $|G_{1,1}\rangle$ , and  $|G_{1,2}\rangle$  when  $\delta \gg \sqrt{N}\Omega_1$ ,  $\Omega_2$ ,  $\Delta$ , and  $N \gg 1$ . The reduced Hamiltonian in the basis of states  $|A\rangle$ ,  $|C_1\rangle$  and  $|C_2\rangle$  is

$$\tilde{H} = \hbar \begin{bmatrix} \epsilon_A + \Delta/22 & \Omega/2 & 0 \\ \Omega/2 & \epsilon_{C1} - \Delta/2 & \sqrt{\frac{2(N-1)}{N}}\Omega/2 \\ 0 & \sqrt{\frac{2(N-1)}{N}}\Omega/2 & \epsilon_{C2} - 3\Delta/2 \end{bmatrix}, \quad (4)$$

where  $\epsilon_A = N\Omega_1^2/4\delta$ ,  $\epsilon_{C1} = [\Omega_2^2 + (N-1)\Omega_1^2]/4\delta$ , and  $\epsilon_{C2} = [2\Omega_2^2 + (N-2)\Omega_1^2]/4\delta$  are the lowest order light-shifts of the states  $|A\rangle$ ,  $|C_1\rangle$  and  $|C_2\rangle$  respectively, and  $\Omega \equiv \sqrt{N}\Omega_1\Omega_2/2\delta$  is the Raman Rabi frequency. We can work out the LSB conditions with this Hamiltonian. By making the light shifts in the states  $|A\rangle$  and  $|C_1\rangle$  equal and the shift in  $|C_2\rangle$  highly detuned from them, we can eliminate the excitation to  $|C_2\rangle$ .

The states  $|A\rangle$  and  $|C_1\rangle$  are resonant when  $\Delta = \epsilon_{C1} - \epsilon_A \approx (\Omega_2^2 - \Omega_1^2)/4\delta$ . Upon subtraction of a suitably chosen term  $(\epsilon_A + \Delta/2)$  from the diagonal term in the Hamiltonian and the approximation that  $N \gg 1$ , we get

$$\tilde{H} = \hbar \begin{bmatrix} 0 & \Omega/2 & 0 \\ \Omega/2 & 0 & \Omega/\sqrt{2} \\ 0 & \Omega/\sqrt{2} & \Delta_B \end{bmatrix}, \quad (5)$$

where the blockade shift is defined as  $\Delta_B \equiv (\epsilon_{C2} - \epsilon_{C1}) - (\epsilon_{C1} - \epsilon_A)$ . This quantity vanishes for the first-order values of the light shifts  $\epsilon_A$ ,  $\epsilon_{C1}$ , and  $\epsilon_{C2}$  shown above, so that there is no blockade effect. However, for second-order approximation, the blockade shift is  $\Delta_B = -(\Omega_1^4 + \Omega_2^4)/(8\delta^3)$ . If we operate under condition where  $\Delta_B \gg \Omega/\sqrt{2}$ , the transition to  $|C_2\rangle$  becomes inconsequentially small and the ensemble of atoms oscillates between the collective states  $|A\rangle$  and  $|C_1\rangle$ .

We have also determined numerically, for  $N=2500$ , the evolution of the population for the six collective states in the truncated system, using the Hamiltonian of Eq. (3), without resorting to adiabatic elimination. The results are illustrated in Fig. 3, for a set of parameters that satisfy the LSB condition identified above. As can be seen from this figure, nearly all the population stays between levels  $|A\rangle$  and  $|C_1\rangle$ , undergoing Rabi oscillations between them. The residual excitations of the other four states are very small, and can be made smaller by using weaker Rabi frequencies. Note that we have ignored the decay of the  $|g\rangle$  states (at the rate of  $\Gamma$ ), which is a valid approximation for  $\delta \gg \Gamma$ .

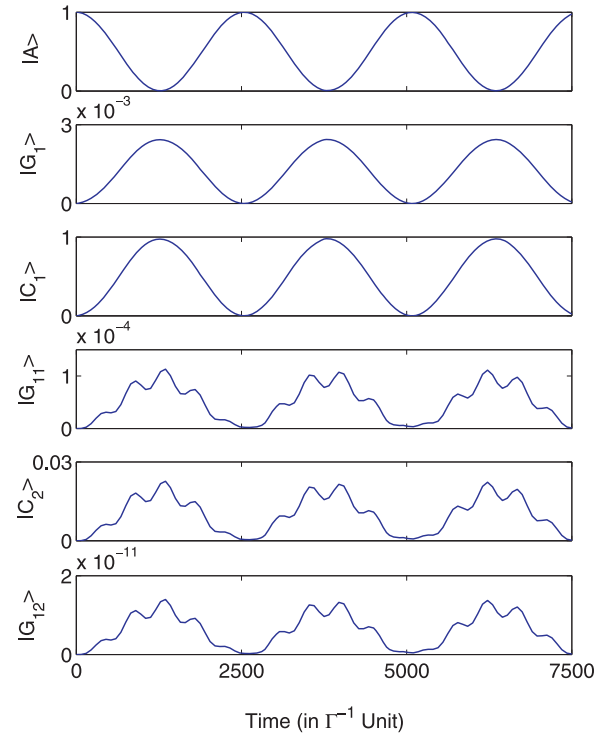
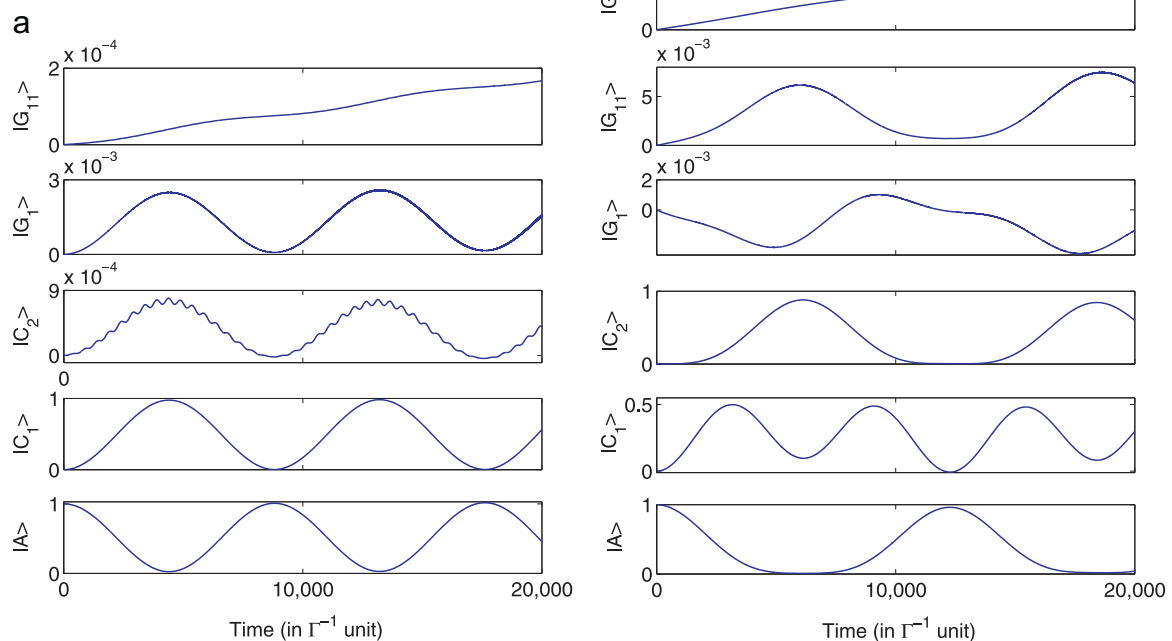


Fig. 3. Exact numerical solution of the evolution of the states using the LSB parameters (in units of  $\Gamma$ ):  $\Omega_1 = 0.001$ ,  $\Omega_2 = 100$ ,  $N=2500$ ,  $\delta = 1000$  and  $\Delta = 2.497$ . The plot is for  $5\pi$  oscillations. The vertical axis is the population of the indicated collective state.

#### 4. Limitations of the original model for light shift blockade

In the preceding section, we showed that the numerical simulation of the truncated system appears to validate the LSB process. For a large value of  $N$ , this result is still an approximation. However, the system can be modeled exactly for very small values of  $N$ . In particular, if we choose  $N=2$ , there are only 6 collective states altogether. Thus, it is possible to check without truncation whether the LSB process holds in this case. Referring back to Fig. 2, the complete set of collective states for  $N=2$  consists of  $|A\rangle$ ,  $|G_1\rangle$ ,  $|G_1\rangle$ ,  $|G_{1,1}\rangle$ ,  $|C_2\rangle$  and  $|G_2\rangle$ . We determined the evolution of this system numerically, starting with the system being in the  $|A\rangle$  state. The results are illustrated in Fig. 4. In Fig. 4a, we show the population of the collective states under the approximation that the state  $|G_2\rangle$  can be neglected completely, since  $\delta \gg \sqrt{N}\Omega_1$  and  $\delta \gg \Omega_2$ , corresponding to very small populations in states  $|G_1\rangle$  and  $|G_{1,1}\rangle$ . As can be seen, the result is consistent with LSB, since the maximum population of  $|C_2\rangle$  is very small. In Fig. 4b, we relax this approximation, and keep the state  $|G_2\rangle$  in the system. This produces an apparently surprising result. The population in  $|C_2\rangle$  can now reach almost unity for some interaction time. Thus, the LSB process is strongly violated. It should be noted that the maximum population of  $|G_2\rangle$  is negligible (Fig. 4a), so that ignoring the excitation to  $|G_2\rangle$  seems to be a reasonable one. Yet, the relaxation of this approximation modifies the population dynamics in a very significant way.

In order to understand this behavior, it is instructive first to consider the process of collective excitation more explicitly. Specifically, it can be shown that for excitation by semi-classical fields, and in the absence of interaction between the atoms, the general quantum state of an ensemble is always given by the outer (tensor) product of the quantum states of the individual atoms [18].



**Fig. 4.** Numerical solution of the evolution of the collective states of two atoms. Here,  $\Omega_1 = 0.001$ ,  $\Omega_2 = 100$ ,  $\delta = 1000$  and  $\Delta = 2.497$ . (in units of  $\Gamma$ ). (a) Collective states of two atoms when  $|G_2\rangle$  is eliminated. (b) Collective states of two atoms with the full Hamiltonian.

The collective states representation of the evolution of such a system is merely an alternative way of describing the process. To illustrate this explicitly, let us consider a case involving two-level atoms, with  $|a\rangle$  and  $|c\rangle$  being the lower and higher energy levels respectively.

Let us denote by  $|\psi_i\rangle$  the quantum state of the  $i$ -th atom. Then, the total quantum state of the system,  $|\Psi\rangle$ , is given by  $|\Psi\rangle = \prod_{i=1}^N |\psi_i\rangle$ . Thus, if we write  $|\psi_i\rangle = \alpha_i|a_i\rangle + \beta_i|c_i\rangle$ , then  $|\Psi\rangle = \prod_{i=1}^N (\alpha_i|a_i\rangle + \beta_i|c_i\rangle)$ . For simplicity, let us assume that  $N=2$ . We then get  $|\Psi\rangle = (\alpha_1|a_1\rangle + \beta_1|c_1\rangle)(\alpha_2|a_2\rangle + \beta_2|c_2\rangle)$ . Consider the product state basis which is spanned by  $|a_1a_2\rangle$ ,  $|a_1c_2\rangle$ ,  $|c_1a_2\rangle$  and  $|c_1c_2\rangle$ . The total state can thus be written as

$$|\Psi\rangle = \alpha_1\alpha_2|a_1a_2\rangle + \alpha_1\beta_2|a_1c_2\rangle + \beta_1\alpha_2|c_1a_2\rangle$$

$$+ \beta_1\beta_2|c_1c_2\rangle = \begin{bmatrix} \alpha_1\alpha_2 \\ \alpha_1\beta_2 \\ \beta_1\alpha_2 \\ \beta_1\beta_2 \end{bmatrix}. \quad (6)$$

Consider next the complete collective state basis spanned by  $|a_1a_2\rangle$ ,  $|+\rangle = (|a_1c_2\rangle + |c_1a_2\rangle)/\sqrt{2}$ ,  $|-\rangle = (|a_1c_2\rangle - |c_1a_2\rangle)/\sqrt{2}$ , and  $|c_1c_2\rangle$ . This basis is simply related to the product state basis by a  $45^\circ$  rotation in the plane of  $|a_1c_2\rangle$  and  $|c_1a_2\rangle$ , so that the rotation matrix can be written as

$$R = \begin{bmatrix} 1 & 0 & 0 & 0 \\ 0 & \frac{1}{\sqrt{2}} & \frac{1}{\sqrt{2}} & 0 \\ 0 & \frac{1}{\sqrt{2}} & -\frac{1}{\sqrt{2}} & 0 \\ 0 & 0 & 0 & 1 \end{bmatrix}. \quad (7)$$

Thus, the total state in the collective state basis can be written as

$$|\Psi\rangle_c = R|\Psi\rangle = \begin{bmatrix} \alpha_1\alpha_2 \\ (\alpha_1\beta_2 + \beta_1\alpha_2)/\sqrt{2} \\ (\alpha_1\beta_2 - \beta_1\alpha_2)/\sqrt{2} \\ \beta_1\beta_2 \end{bmatrix}. \quad (8)$$

Similarly, we can represent the Hamiltonian in these different bases. In the rotating wave picture, the Hamiltonian for a single atom can be expressed as

$$H_1 = \hbar \begin{bmatrix} 0 & \Omega/2 \\ \Omega/2 & -\delta \end{bmatrix}, \quad (9)$$

where  $\Omega$  is the Rabi frequency and  $\delta = \omega - (\omega_c - \omega_a)$  is the detuning of the laser frequency from the resonance frequency of the two states. When there are two atoms, the Hamiltonian in the basis of states  $|a_1a_2\rangle$ ,  $|a_1c_2\rangle$ ,  $|c_1a_2\rangle$  and  $|c_1c_2\rangle$  is  $H = H_1 \otimes I_2 + I_1 \otimes H_2$  where  $I_i$  is the identity matrix and  $H_i$  is the Hamiltonian for the  $i$ -th atom. For example,

$$\begin{aligned} \langle a_1a_2 | H | c_1a_2 \rangle &= \langle a_1a_2 | (H_1 \otimes I_2) | c_1a_2 \rangle + \langle a_1a_2 | (I_1 \otimes H_2) | c_1a_2 \rangle \\ &= \langle a_1 | H_1 | c_1 \rangle \langle a_2 | I_2 | a_2 \rangle + \langle a_1 | I_1 | c_1 \rangle \langle a_2 | H_2 | a_2 \rangle \\ &= \langle a_1 | H_1 | c_1 \rangle = \Omega_1/2 \end{aligned}$$

Thus, the Hamiltonian can be written as

$$H = \hbar \begin{bmatrix} 0 & \Omega_2/2 & \Omega_1/2 & 0 \\ \Omega_2/2 & -\delta & 0 & \Omega_1/2 \\ \Omega_1/2 & 0 & -\delta & \Omega_2/2 \\ 0 & \Omega_1/2 & \Omega_2/2 & -2\delta \end{bmatrix}, \quad (10)$$

where the Rabi frequencies are assumed to be real. Under a 45° rotation in the plane of  $|a_1c_2\rangle$  and  $|c_1a_2\rangle$ , the new Hamiltonian in the basis  $|a_1a_2\rangle$ ,  $|+\rangle$ ,  $|-\rangle$ ,  $|c_1c_2\rangle$  is

$$H' = R^{-1}HR = \hbar \begin{bmatrix} 0 & \frac{\Omega_1 + \Omega_2}{2\sqrt{2}} & -\frac{\Omega_1 - \Omega_2}{2\sqrt{2}} & 0 \\ \frac{\Omega_1 + \Omega_2}{2\sqrt{2}} & -\delta & 0 & \frac{\Omega_1 + \Omega_2}{2\sqrt{2}} \\ -\frac{\Omega_1 - \Omega_2}{2\sqrt{2}} & 0 & -\delta & \frac{\Omega_1 - \Omega_2}{2\sqrt{2}} \\ 0 & \frac{\Omega_1 + \Omega_2}{2\sqrt{2}} & -\frac{\Omega_1 - \Omega_2}{2\sqrt{2}} & -2\delta \end{bmatrix}. \quad (11)$$

For  $\Omega = \Omega_1 = \Omega_2$ , the asymmetric state,  $|-\rangle$ , is decoupled from the other states, and the Hamiltonian becomes

$$H' = \hbar \begin{bmatrix} 0 & \sqrt{2}\Omega/2 & 0 & 0 \\ \sqrt{2}\Omega/2 & -\delta & 0 & \sqrt{2}\Omega/2 \\ 0 & 0 & -\delta & 0 \\ 0 & \sqrt{2}\Omega/2 & 0 & -2\delta \end{bmatrix}. \quad (12)$$

The Hamiltonian in Eq. (12) describes the situation where only symmetric collective states are excited.

This is also evident by noting that the general collective state can now be expressed as  $|\Psi\rangle_c = \alpha^2|aa\rangle + \sqrt{2}\alpha\beta|+\rangle + \beta^2|cc\rangle$ , where  $\alpha = \alpha_1 = \alpha_2$  and  $\beta = \beta_1 = \beta_2$  (since  $\Omega_1 = \Omega_2$ ). The form of this state shows clearly that it is impossible to suppress excitation to the  $|cc\rangle$  state while still exciting the  $|+\rangle$  state. Thus, the degree of excitation of a given collective state is related to the degree of excitation of all other collective states. While the three-level system we are considering is more complicated in the details, this fundamental rule still holds. As such, under this set of conditions (i.e. semiclassical laser field, and no interaction between the atoms) it

is not possible to block the excitation to state  $|C_2\rangle$  while allowing for excitation of state  $|C_1\rangle$ . The result shown in Fig. 4b is merely a manifestation of this constraint. The subtle error that led us to the previous conclusion about the realizability of LSB was the approximation that the role of  $|G_2\rangle$  is negligible. This approximation was entirely logical in a general sense, but turns out, rather surprisingly, not to be valid.

Of course, if the laser field is treated quantum mechanically, by considering it as a superposition of Fock states, the quantum state of the atoms and the photons are inherently entangled. As such, the state of the ensemble cannot be expressed as a product of the states of each atom. Under such a situation, it should in principle be possible to achieve the blockade effect. However, such a blockade works in a clean manner only when the numbers of photons are limited to a few. As discussed earlier, our objective is to achieve a blockade when the laser field has a mean photon number much larger than unity, i.e. the semi-classical limit. In this limit, the only way to achieve a blockade is to allow for interaction between the atoms. Here we describe a scheme where interactions between Rydberg excited levels are used to achieve the LSB effect.

## 5. Rydberg assisted LSB of two atoms

We modify the lambda scheme of a single atom by adding a Rydberg level  $|r\rangle$  and an intermediate level  $|d\rangle$ , which is coupled to  $|r\rangle$  and  $|c\rangle$ , but not to  $|a\rangle$ , as illustrated in Fig. 5a. We denote as  $\hbar\omega_j$  the energy of the state  $|j\rangle$ , for  $j=a, g, c, d$  and  $r$ . The Rabi frequencies are denoted as  $\Omega_1, \Omega_2, \Omega_3$  and  $\Omega_4$  for the  $a \rightarrow g, g \rightarrow c, c \rightarrow d$  and  $d \rightarrow r$  transitions, respectively. For convenience, we also define the relevant detunings as  $\delta_1 = \omega_1 - (\omega_b - \omega_a)$ ,  $\delta_2 = \omega_2 - (\omega_b - \omega_c)$ ,  $\delta_3 = \omega_3 - (\omega_d - \omega_c)$  and  $\delta_4 = \omega_4 - (\omega_r - \omega_d)$ . As before, the average detuning for the  $\Lambda$ -transition is defined as  $\delta = (\delta_1 + \delta_2)/2$ , and the corresponding two photon detuning is defined as  $\Delta = \delta_2 - \delta_1$ . We also define as  $\delta_r = \delta_3 + \delta_4$  to be the two photon detuning for the ladder transition  $c \rightarrow d \rightarrow r$ . After making the usual dipole and rotating wave approximations and upon making the rotating wave transformation, the Hamiltonian in the basis of states  $|a\rangle, |g\rangle, |c\rangle, |d\rangle$  and  $|r\rangle$  can be expressed as

$$H_{IR} = \hbar \begin{bmatrix} \Delta & \Omega_1/2 & 0 & 0 & 0 \\ \Omega_1/2 & -\delta + \Delta/2 & \Omega_2/2 & 0 & 0 \\ 0 & \Omega_2/2 & 0 & \Omega_3/2 & 0 \\ 0 & 0 & \Omega_3/2 & -\delta_3 & \Omega_4/2 \\ 0 & 0 & 0 & \Omega_4/2 & -\delta_r \end{bmatrix}. \quad (13)$$

To illustrate the basic concept, we consider first the collective states of only two atoms, with a distance  $r_{12}$  which is assumed to be comparable to the characteristic distance scale of interatomic Rydberg interaction.

For simplicity, we consider first the symmetric collective states of two atoms, as illustrated in Fig. 5b, where we have adopted the compact notation that, for example,  $|AA\rangle = |aa\rangle$ ,  $|CC\rangle = |cc\rangle$ ,  $|AC\rangle = (|ac\rangle + |ca\rangle)/\sqrt{2}$  and so on. Since the Hamiltonian for the two atoms now contains the interaction between the two atoms, the general quantum state of the total system can no longer be written as a product between the quantum states of individual atoms. As such, it should now be possible to produce the LSB effect. Specifically, note that the dipole-dipole interaction between the atoms when they are both excited to the Rydberg state will shift the energy of the  $|RR\rangle$  state compared to its value when the atoms are far apart. Since there is an asymmetry in the degree to which the  $|r\rangle$  state is coupled to  $|a\rangle$  and  $|c\rangle$ , the shift in the energy of  $|RR\rangle$  will affect differently the light shifts experienced by  $|AA\rangle$ ,  $|AC\rangle$  and  $|CC\rangle$ . This is precisely what is needed for realizing LSB. In

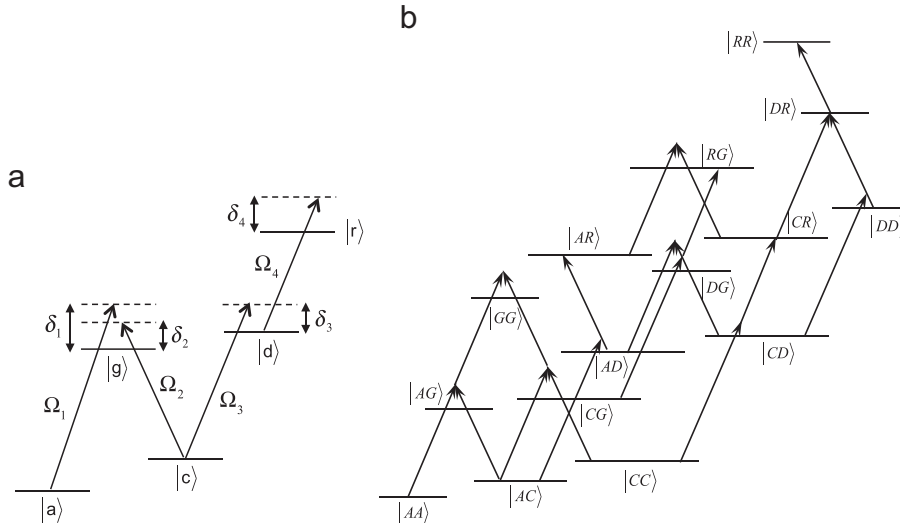


Fig. 5. (a) Modified  $\Lambda$ -system of a single atom. (b) Collective states of two atoms.

what follows, we derive analytically, under adiabatic elimination approximation, the parameters needed for realizing the optimal LSB condition. We then verify the results via exact numerical calculation. This is followed by a derivation of the condition needed for optimal LSB for an arbitrary value of  $N$ , the number of atoms in the ensemble.

As can be seen from Fig. 5b, there are fifteen symmetric collective states for two atoms. In order to establish an approximate analytical result (which would then serve as a guide for choosing parameters for exact numerical calculation), we first simplify the picture by reducing the 5-level system for each atom (see Fig. 6a) to an effective 3-level system (see Fig. 6b) via eliminating adiabatically two of the intermediate states,  $|g\rangle$  and  $|d\rangle$ , that are highly detuned. Once this is done, the effective Hamiltonian for each atom, in the basis of  $|a\rangle$ ,  $|c\rangle$  and  $|r\rangle$ , can be expressed as

$$H_{1R} = \hbar \begin{bmatrix} \Delta + \varepsilon_a & \Omega_{ac}/2 & 0 \\ \Omega_{ac}/2 & \varepsilon_c & \Omega_{cr}/2 \\ 0 & \Omega_{cr}/2 & -\delta_r + \varepsilon_r \end{bmatrix}, \quad (14)$$

where  $\Omega_{ac} = \Omega_1 \Omega_2 / 2\delta$  is the Raman–Rabi frequency of transition  $|a\rangle \rightarrow |c\rangle$ , and  $\Omega_{cr} = \Omega_3 \Omega_4 / 2\delta_3$  is the two-photon Rabi frequency of transition  $|c\rangle \rightarrow |r\rangle$ , while  $\varepsilon_a = \Omega_1^2 / 4\delta$ ,  $\varepsilon_c = \Omega_2^2 / 4\delta + \Omega_3^2 / 4\delta_3$  and  $\varepsilon_r = \Omega_4^2 / 4\delta_3$  are the light shifts of states  $|a\rangle$ ,  $|c\rangle$  and  $|r\rangle$  respectively. If we define two new parameters  $\Delta_{ac} = \Delta + \varepsilon_a - \varepsilon_c$  and  $\Delta_{cr} = \delta_r + \varepsilon_c - \varepsilon_r$ , these become the effective, relevant detunings between the levels. Then we can rewrite the single atom Hamiltonian in the basis of  $|a\rangle$ ,  $|c\rangle$  and  $|r\rangle$  as

$$H_{1R} = \hbar \begin{bmatrix} \Delta_{ac} & \Omega_{ac}/2 & 0 \\ \Omega_{ac}/2 & 0 & \Omega_{cr}/2 \\ 0 & \Omega_{cr}/2 & -\Delta_{cr} \end{bmatrix}. \quad (15)$$

If the distance between the two atoms,  $r_{12}$ , is much larger than the scale of Rydberg interaction, the combined Hamiltonian in the basis of the nine product states ( $|a_1 a_2\rangle$ ,  $|a_1 c_2\rangle$ ,  $|a_1 r_2\rangle$ ,  $|c_1 a_2\rangle$ ,  $|c_1 c_2\rangle$ ,  $|c_1 r_2\rangle$ ,  $|r_1 a_2\rangle$ ,  $|r_1 c_2\rangle$ ,  $|r_1 r_2\rangle$ ) can be written as  $H_T = H_{1R} \otimes I_2 + I_1 \otimes H_{2R}$ , and the 81 elements of  $H_T$  can be easily calculated in the same manner as used in deriving Eq. (10). When transformed to the collective state picture, the asymmetric states become decoupled, just as before, and we are left with a six state system spanned by  $|AA\rangle$ ,  $|AC\rangle$ ,  $|CC\rangle$ ,  $|AR\rangle$ ,  $|CR\rangle$  and  $|RR\rangle$  (using the compact notation introduced in Fig. 5b), which are shown in Fig. 7, and the

Hamiltonian can be expressed as

$$H_T = \hbar \begin{bmatrix} 2\Delta_{ac} & \frac{\sqrt{2}}{2}\Omega_{ac} & 0 & 0 & 0 & 0 \\ \frac{\sqrt{2}}{2}\Omega_{ac} & \Delta_{ac} & \frac{\sqrt{2}}{2}\Omega_{ac} & \frac{1}{2}\Omega_{cr} & 0 & 0 \\ 0 & \frac{\sqrt{2}}{2}\Omega_{ac} & 0 & 0 & \frac{\sqrt{2}}{2}\Omega_{cr} & 0 \\ 0 & \frac{1}{2}\Omega_{cr} & 0 & \Delta_{ac} - \Delta_{cr} & \frac{1}{2}\Omega_{ac} & 0 \\ 0 & 0 & \frac{\sqrt{2}}{2}\Omega_{cr} & \frac{1}{2}\Omega_{ac} & -\Delta_{cr} & \frac{\sqrt{2}}{2}\Omega_{cr} \\ 0 & 0 & 0 & 0 & \frac{\sqrt{2}}{2}\Omega_{cr} & -2\Delta_{cr} \end{bmatrix}. \quad (16)$$

When the distance  $r_{12}$  becomes comparable to the characteristic distance scale for interatomic Rydberg interaction, the Hamiltonian for the collective states,  $H_{TR}$ , is the same as  $H_T$  except for the last diagonal element. Specifically,  $\langle RRI|H_{TR}|RR\rangle = \langle RRI|H_T|RR\rangle - V_r = -2\Delta_{cr} - V_r$ , where  $V_r$  represents the dipole–dipole interaction between two atoms. Thus, we can write

$$H_{TR} = H_T - V_r |RR\rangle \langle RR|. \quad (17)$$

The various terms of  $H_{TR}$  are illustrated schematically in Fig. 7.

When we allow  $\Delta_{cr} \gg \Delta_{ac}$ ,  $\Omega_{ac}$ ,  $\Omega_{cr}$ , the upper levels  $|AR\rangle$ ,  $|CR\rangle$  and  $|RR\rangle$  can be adiabatically eliminated. The reduced Hamiltonian

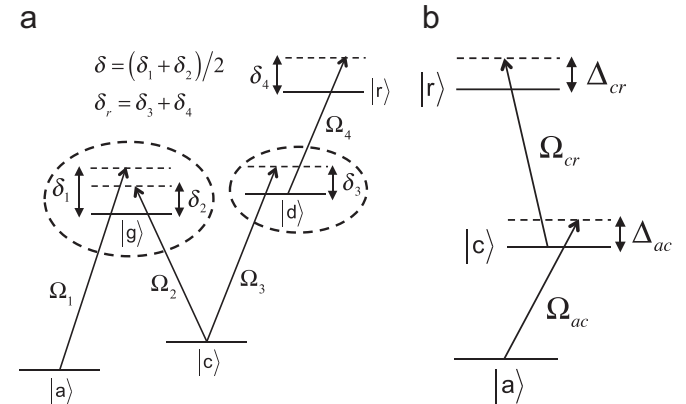


Fig. 6. (a) Single atom five-level scheme. (b) Simplified three-level scheme after adiabatically eliminating  $|g\rangle$  and  $|d\rangle$ .

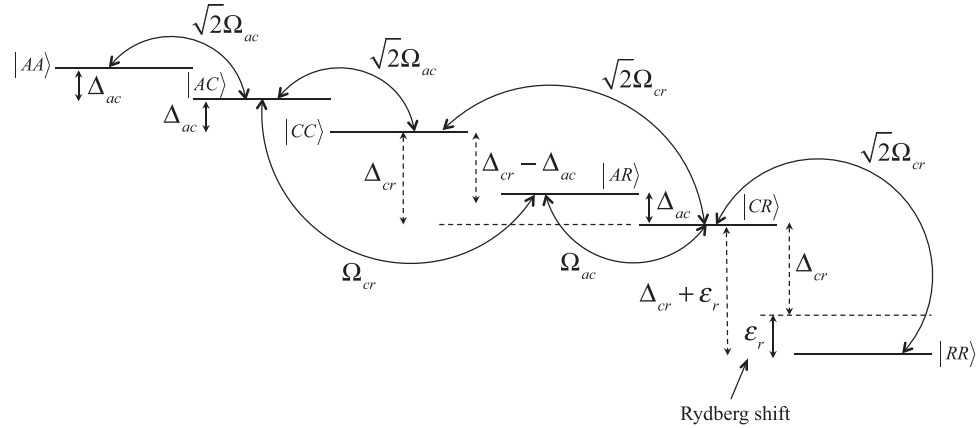


Fig. 7. The coupling rates and detunings of collective states of a simplified two-atom system.

in the basis of  $|AA\rangle$ ,  $|AC\rangle$  and  $|CC\rangle$  is

$$\widetilde{H_{TR}'} \cong \hbar \begin{bmatrix} 2\Delta_{ac} & \frac{\sqrt{2}}{2}\Omega_{ac} & 0 \\ \frac{\sqrt{2}}{2}\Omega_{ac} & \Delta_{ac} + \frac{\Omega_{cr}}{2}\cdot v & \frac{\sqrt{2}}{2}\Omega_{ac} + \frac{\sqrt{2}}{2}\Omega_{cr} \cdot \frac{uv}{1-2vw} \\ 0 & \frac{\sqrt{2}}{2}\Omega_{ac} + \frac{\sqrt{2}}{2}\Omega_{cr} \cdot \frac{uv}{1-2vw} & \Omega_{cr} \cdot \frac{v}{1-2vw} \end{bmatrix}, \quad (18)$$

where, for simplicity, we have defined  $u = \Omega_{ac}/2\Delta_{cr}$ ,  $v = \Omega_{cr}/2\Delta_{cr}$ ,  $w = \Omega_{cr}/2(2\Delta_{cr} + V_r)$ , and we have assumed that  $\Omega_{cr} \gg \Omega_{ac}$ . In order to make the levels  $|AA\rangle$  and  $|AC\rangle$  resonant, we enforce the condition that  $\Delta_{ac} = \Omega_{cr} \cdot v/2$ , which leads to  $\Omega_{cr}^2 = 4\Delta_{ac}\Delta_{cr}$ . When the energy levels are all reduced by  $2\Delta_{ac}$ , Eq. (18) becomes

$$\widetilde{H_{TR}'} = \hbar \begin{bmatrix} 0 & \frac{\sqrt{2}}{2}\Omega_{ac} & 0 \\ \frac{\sqrt{2}}{2}\Omega_{ac} & 0 & \frac{\sqrt{2}}{2}\Omega_{ac} + \frac{\sqrt{2}}{2}\Omega_{cr} \cdot \frac{uv}{1-2vw} \\ 0 & \frac{\sqrt{2}}{2}\Omega_{ac} + \frac{\sqrt{2}}{2}\Omega_{cr} \cdot \frac{uv}{1-2vw} & \Delta_B \end{bmatrix}, \quad (19)$$

where  $\Delta_B \equiv \Omega_{cr} \cdot 2vw/(1-2vw)$  is the blockade shift. When  $\Delta_B$  is much larger than the coupling between the states  $|AC\rangle$  and  $|CC\rangle$ , we are able to block the excitation to state  $|CC\rangle$  and achieve LSB. This can be achieved under the condition where  $V_r + 2\Delta_{cr} \gg \Omega_{cr}/2\Omega_{ac}\Delta_{cr}$ . When these conditions are met, we achieve resonance between states  $|AA\rangle$  and  $|AC\rangle$ , blocking excitation to state  $|CC\rangle$ .

In order to verify the validity of this conclusion, we have simulated the evolution of the three-level system of two atoms (i.e. the system shown in Fig. 6b), using the  $6 \times 6$  collective state Hamiltonian,  $H_{TR}$  (Eq. (17)), which included the effect of Rydberg interaction, but without making use of the adiabatic elimination of states  $|AR\rangle$ ,  $|CR\rangle$  and  $|RR\rangle$ . The parameters we have used are  $\Omega_{ac} = 0.00002$ ,  $\Omega_{cr} = 1$ ,  $\Delta_{ac} = -0.031129$  and  $\Delta_{cr} = -8$  (in units of  $\Gamma$ ), consistent with the requirement of achieving LSB. The result of this simulation is shown in Fig. 8. Fig. 8a represents the case when the Rydberg-interaction parameter,  $V_r$ , is set to zero. In this case, the maximum amplitude of  $|CC\rangle$  reaches unity. When  $V_r = 16$ , the maximum amplitude of  $|CC\rangle$  is nearly zero, and the system oscillates between  $|AA\rangle$  and  $|AC\rangle$ , as shown in Fig. 8b. It should also be noted that under this blockade condition, the oscillation frequency between levels  $|AA\rangle$  and  $|AC\rangle$  is increased by  $\sqrt{2}$ . The upper levels  $|AR\rangle$ ,  $|CR\rangle$  and  $|RR\rangle$  are minimally excited regardless of whether interaction is present or not. This justifies the adiabatic elimination of these states employed in deriving the  $3 \times 3$  reduced Hamiltonian for the collective states, shown in Eq. (18).

The parameters used in the evolution of the simplified two-atom Hamiltonian can be used to extract the values of parameters necessary for the exact two-atom 15-level system shown in Fig. 5b. We choose the parameters as follows:  $\Omega_1 = 0.0004$ ,  $\Omega_2 = 0.8$ ,  $\delta = -8$ ,  $\Delta = -0.0199$ ,  $\Omega_3 = 20$ ,  $\Omega_4 = 320$ ,  $\delta_3 = -3200$ ,  $\delta_4 = 3200$ .

Notice that here we make the choice that  $\Delta \simeq (\Omega_2^2 - \Omega_1^2)/4\delta$  in order to produce full Rabi oscillations between  $|AA\rangle$  and  $|AC\rangle$ . The results of the plots with and without the Rydberg interaction are shown in Fig. 9. Despite the fact that 15 levels are present, only the levels  $|AA\rangle$ ,  $|AC\rangle$  and  $|CC\rangle$  are populated while the excitations to the other states remain under 1%. As was the case with the simplified Hamiltonian, the presence of the Rydberg interaction ( $V_r = 16$ ) suppresses the excitation to level  $|CC\rangle$  so that an effective two-level system is generated, as illustrated in Fig. 10.

## 6. Rydberg assisted LSB in $N$ -atom ensembles

This process can be generalized for  $N$  atoms. Referring back to Fig. 6, we recall first that adiabatic elimination of states  $|g\rangle$  and  $|d\rangle$  reduces the system to three levels (Fig. 6b). The first six collective states involving these single atom states, for  $N$ -atoms, are as follows:

$$|A\rangle \equiv |a_1, a_2, \dots, a_N\rangle,$$

$$|C_1\rangle \equiv \frac{1}{\sqrt{N}} \sum_{j=1}^N |a_1, a_2, \dots, c_j, \dots, a_N\rangle,$$

$$|C_2\rangle \equiv \frac{1}{\sqrt{N}C_2} \sum_{j,k(j \neq k)}^{N_{C2}} |a_1, a_2, \dots, c_j, \dots, c_k, \dots, a_N\rangle,$$

$$|R_1\rangle \equiv \frac{1}{\sqrt{N}} \sum_{j=1}^N |a_1, a_2, \dots, r_j, \dots, a_N\rangle,$$

$$|R_{1,1}\rangle \equiv \frac{1}{\sqrt{2}N_{C2}} \sum_{j,k(j \neq k)}^{2N_{C2}} |a_1, a_2, \dots, r_j, \dots, c_k, \dots, a_N\rangle,$$

$$|R_2\rangle \equiv \frac{1}{\sqrt{N}C_2} \sum_{j,k(j \neq k)}^{N_{C2}} |a_1, a_2, \dots, r_j, \dots, r_k, \dots, a_N\rangle. \quad (20)$$

Of course, there are many more collective states. However, our goal is to find the condition where the system oscillates between  $|A\rangle$  and  $|C_1\rangle$ , with negligible excitation to the remaining collective states. If we can show that the excitation to states  $|C_2\rangle$ ,  $|R_1\rangle$ ,  $|R_{1,1}\rangle$  and  $|R_2\rangle$  are negligible, then it follows that the excitation to all other higher energy collective states is also negligible. Thus, it is justified to limit our consideration to only these six states.

With the single atom Hamiltonian in the basis of  $|a\rangle$ ,  $|c\rangle$  and  $|r\rangle$  shown in Eq. (15), the Hamiltonian formed with states  $|A\rangle$ ,  $|C_1\rangle$ ,  $|C_2\rangle$ ,

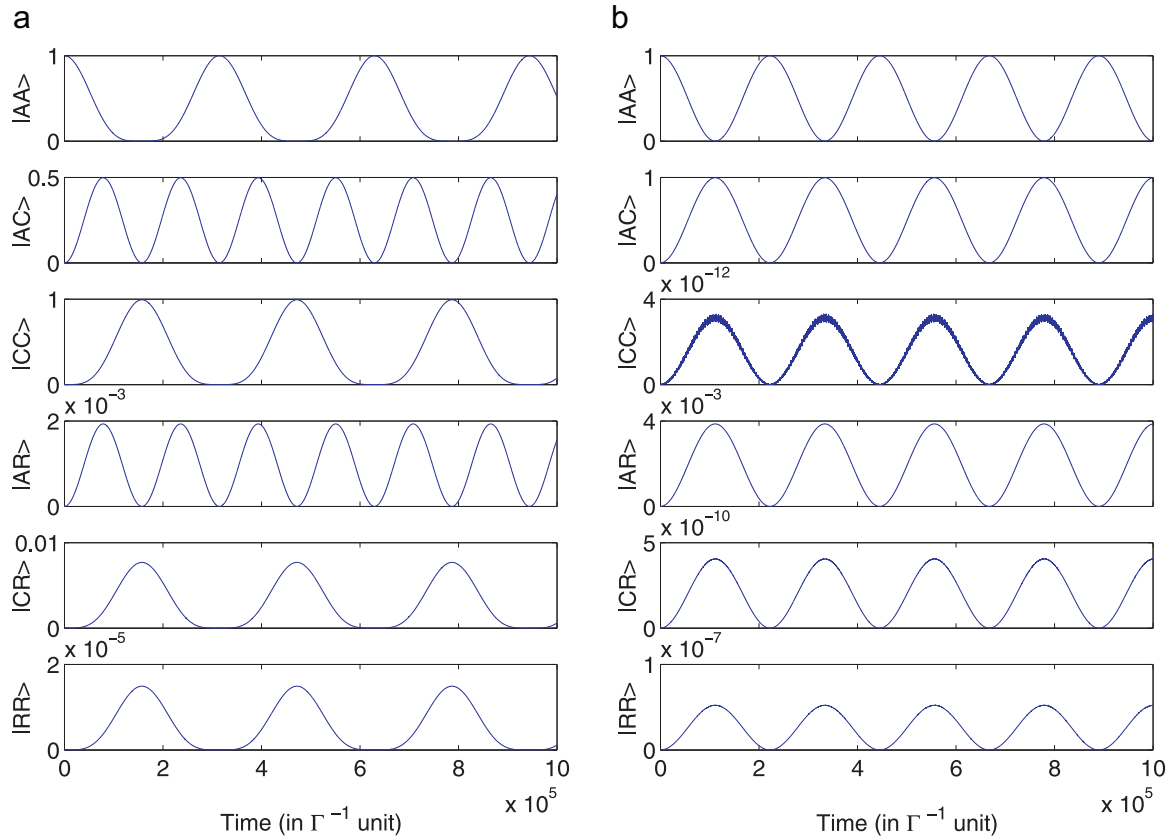


**Fig. 8.** Evolution of population using the simplified two-atom picture in Fig. 6. Figure (a) represents the case when the dipole–dipole interaction is not present ( $V_r = 0$ ). Figure (b) represents the case when the dipole–dipole interaction is present ( $V_r = 16$ ).

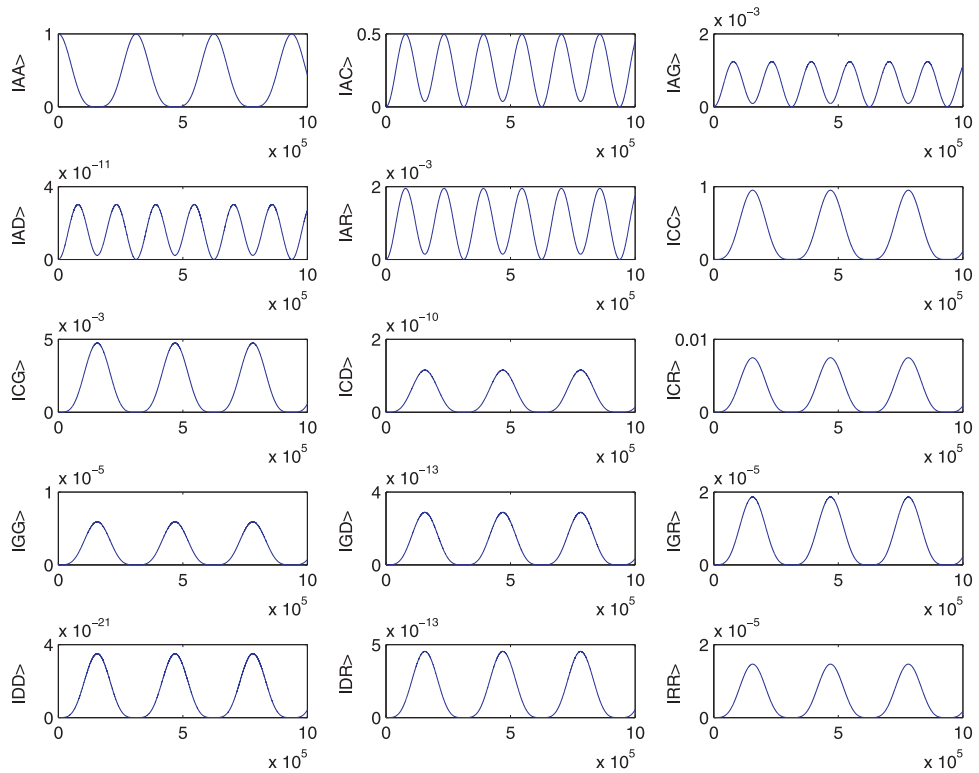


**Fig. 9.** Evolution of population using the full two-atom picture in Fig. 6(b) when the dipole–dipole interaction is not present ( $V_r = 0$ ).

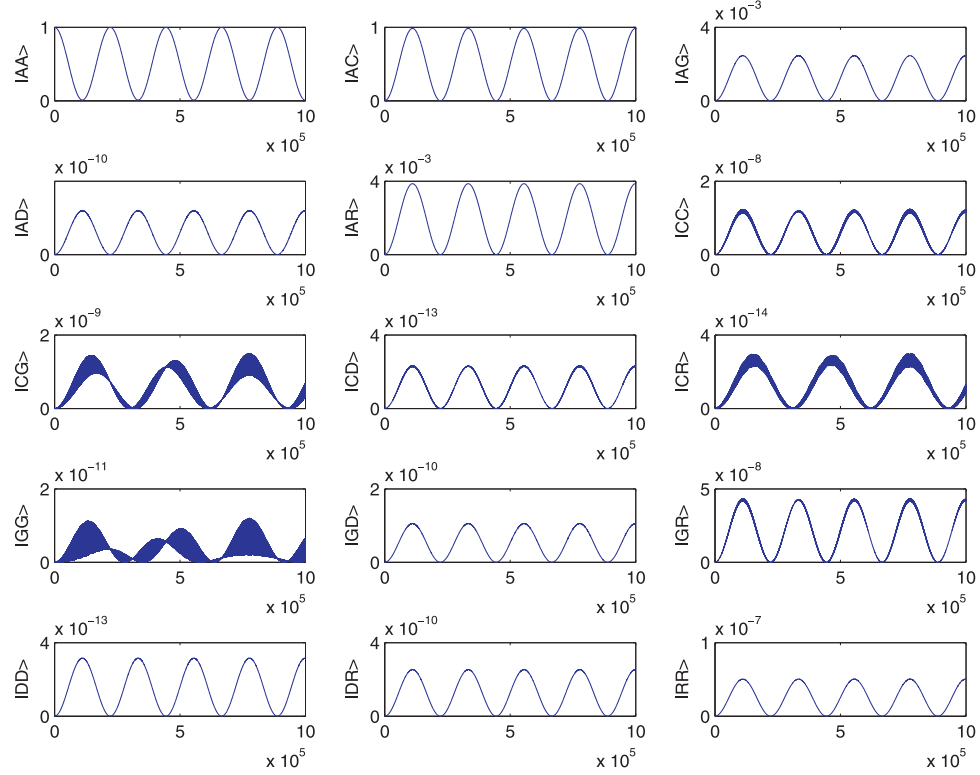


Fig. 10. Evolution of population using the full two-atom picture in Fig. 6(b) when the dipole–dipole interaction is present ( $V_r = 16$ ).

$|R_1\rangle$ ,  $|R_{1,1}\rangle$  and  $|R_2\rangle$  can be written as

$$H_{NR'} = \hbar \begin{bmatrix} 2\Delta_{ac} & \frac{\sqrt{N}}{2}\Omega_{ac} & 0 & 0 & 0 & 0 \\ \frac{\sqrt{N}}{2}\Omega_{ac} & \Delta_{ac} & \frac{\sqrt{2(N-1)}}{2}\Omega_{ac} & \frac{\Omega_{cr}}{2} & 0 & 0 \\ 0 & \frac{\sqrt{2(N-1)}}{2}\Omega_{ac} & 0 & 0 & \frac{\sqrt{2}}{2}\Omega_{cr} & 0 \\ 0 & \frac{\Omega_{cr}}{2} & 0 & \Delta_{ac} - \Delta_{cr} & \frac{\sqrt{N-1}}{2}\Omega_{ac} & 0 \\ 0 & 0 & \frac{\sqrt{2}}{2}\Omega_{cr} & \frac{\sqrt{N-1}}{2}\Omega_{ac} & -\Delta_{cr} & \frac{\sqrt{2}}{2}\Omega_{cr} \\ 0 & 0 & 0 & 0 & \frac{\sqrt{2}}{2}\Omega_{cr} & -2\Delta_{cr} - V_r \end{bmatrix}. \quad (21)$$

Under the condition that  $\Delta_{cr} \ll \Delta_{ac}$ ,  $\sqrt{N}\Omega_{ac}$ ,  $\Omega_{cr}$ , for large  $N$ , this reduces to

$$\tilde{H}_{NR'} = \hbar \begin{bmatrix} 0 & \frac{\sqrt{2}}{2}\Omega_{ac} & 0 \\ \frac{\sqrt{2}}{2}\Omega_{ac} & 0 & \frac{\sqrt{2}}{2}\Omega_{ac} + \frac{\Omega_{cr}}{2} \\ 0 & \frac{\sqrt{2}}{2}\Omega_{ac} + \frac{\Omega_{cr}}{2} & \frac{uv\sqrt{2(N-1)}}{1 - (N-1)u^2 - 2vw} \end{bmatrix} \quad (22)$$

in the basis of  $|A\rangle$  and  $|C_1\rangle$  and  $|C_2\rangle$ , where the first two levels were made resonant by choosing  $\Delta_{ac} = (\Omega_{cr}/2)\cdot v(1 - 2vw)/(1 - (N-1)u^2 - 2vw)$ . The blockade shift is now  $\Delta_B \equiv \Omega_{cr}\cdot 2vw/(1 - (N-1)u^2 - 2vw)$ . Note that when  $N=2$ , the Hamiltonian, the detuning, and the blockade shift are equivalent to the calculations made earlier for the two-atom case. The conditions necessary to block the excitation to state  $|C_2\rangle$  are  $\Omega_{cr} \gg \sqrt{N}\Omega_{ac}$  and  $w \gg \sqrt{N}u$ , which again occur when  $V_r \rightarrow -2\Delta_{cr}$ , just as in the case of  $N=2$ .

Fig. 11 shows the populations of the six collective states of Eq. (20) under the LSB conditions found for 1000 atoms. The parameters are  $\Omega_{ac} = 0.00002/\sqrt{1000}$ ,  $\Omega_{cr} = 1$ ,  $\Delta_{ac} = -0.031129$ ,  $\Delta_{cr} = -8$  and  $V_r = 16$  (in units of  $\Gamma$ ). As can be seen, states  $|A\rangle$  and

$|C_1\rangle$  are resonant, and population in state  $|C_2\rangle$  is very small. With so little excitation into  $|C_2\rangle$ , the Rydberg assisted LSB guarantees the suppression of the higher excitations, thereby validating the use of a truncated Hamiltonian in Eq. (20).

So far, we have shown that the Rydberg assisted LSB works for  $V_r = 16\Gamma$ , where  $\Gamma$  is the decay rate of the state  $|g\rangle$ . Consider, for example, the specific case of  $^{87}\text{Rb}$  atoms. In this case,  $\Gamma \simeq 6$  MHz, so that  $V_r \simeq 96$  MHz, which corresponds to an interatomic distance of  $\sim 10$   $\mu\text{m}$ . We envision a scenario where the collective ensemble would be confined to a sphere with a diameter  $\sim 10$   $\mu\text{m}$ , realizable, for example, by loading atoms from a MOT into a FORT (far-off resonance trap), containing about  $10^3$  atoms. For some pair of atoms, the interatomic distance would be smaller than  $10$   $\mu\text{m}$ . It is

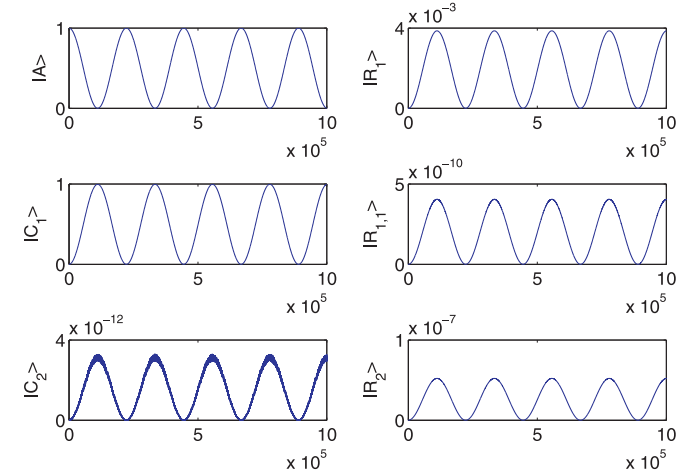
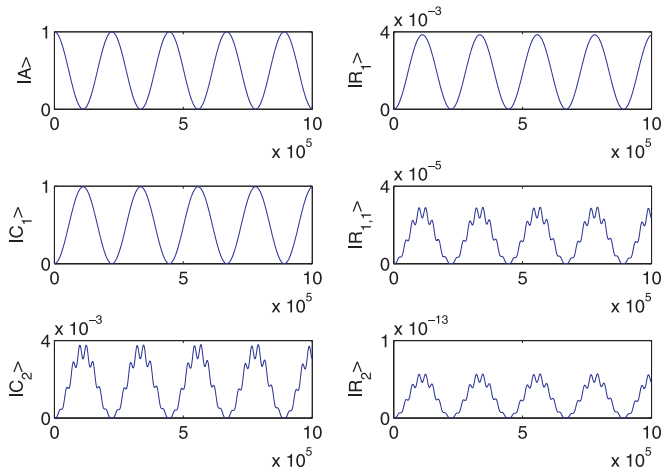


Fig. 11. Evolution of population in the six lowest energy states of Hamiltonian in Eq. (20) for  $N=1000$ , with the same conditions as Fig. 8 except  $\Omega_{ac}$  here is  $\sqrt{N}$  smaller, and the dipole–dipole interaction  $V_r = 16\Gamma$ .



**Fig. 12.** Evolution of population in the six lowest energy states of Hamiltonian in Eq. (20), with the same conditions as Fig. 11 except the dipole-dipole interaction  $V_r = 16000r$ .

well known that  $V_r$  scales approximately as  $r^{-3}$ , where  $r$  is the interatomic distance between a pair of atoms for  $r < 10 \mu\text{m}$  [19]. Thus, for  $r = 1 \mu\text{m}$ ,  $V_r \simeq 16000r \simeq 96 \times 10^3 \text{ MHz}$ . We show in Fig. 12 that the Rydberg assisted LSB works for this value of  $V_r$  for  $N=1000$  atoms.

## 7. Conclusion

The light shift imbalance induced blockade in an atomic ensemble had been studied previously, in which the difference in the light shifts produced in collective state energy levels leads to a condition where the system remains confined to a superposition of the ground and the first excited states. The significance of this result for quantum computing was discussed in Reference [20]. Upon further investigation into the nature of collective states, we found that the light shift imbalance alone is not enough to produce a blockade. By introducing Rydberg interaction, and using the technique of adiabatic elimination, we are able to establish the conditions under which the blockade can be achieved. Numerical simulations confirm the validity of this result.

The ensemble-based qubits realized in this manner can be used to implement a controlled-NOT (CNOT) gate, which is a universal gate for quantum computing, using a variation of the Pellizzari scheme [8]. The details of the process for realizing a CNOT gate in this way, using  $^{87}\text{Rb}$  atoms are essentially the same as what was presented in Reference [16]. Many such gates can be linked to one another, via nearest neighbor quantum coupling, to realize an elementary quantum computer (EQC). The size of an EQC, contained inside a single vacuum chamber, is likely to be limited to a number of the order of ten. However, as shown in Reference [16], many such EQCs can be linked via optical fiber, using photons to transport quantum information, thus making this approach scalable. Of course, it is also possible to realize a CNOT gate between single atoms, caught in FORTs, by making use of Rydberg interactions [21]. However, it is very difficult to load a single atom consistently in a FORT. In contrast, the approach proposed here is relatively insensitive to the actual number of atoms held in the FORT. Thus, this approach may prove to be a more viable alternative for scalable quantum computing using neutral atoms.

## Acknowledgements

This work has been supported by the NSF IGERT program under Grant number 'DGE-0801685' and AFOSR Grant number 'FA9550-09-1-0652'.

## References

- [1] D. Jaksch, J.I. Cirac, P. Zoller, S.L. Rolston, R. Côté, M.D. Lukin, Fast quantum gates for neutral atoms, *Phys. Rev. Lett.* 85 (2000) 2208–2211. <http://dx.doi.org/10.1103/PhysRevLett.85.2208>.
- [2] M.D. Lukin, M. Fleischhauer, R. Cote, L.M. Duan, D. Jaksch, J.I. Cirac, P. Zoller, Dipole blockade and quantum information processing in mesoscopic atomic ensembles, *Phys. Rev. Lett.* 87 (2001) 037901. <http://dx.doi.org/10.1103/PhysRevLett.87.037901>.
- [3] J.D. Pritchard, D. Maxwell, A. Gauguet, K.J. Weatherill, M.P.A. Jones, C.S. Adams, Cooperative atom-light interaction in a blockaded Rydberg ensemble, *Phys. Rev. Lett.* 105 (2010) 193603. <http://dx.doi.org/10.1103/PhysRevLett.105.193603>.
- [4] R. Heidemann, U. Raitzsch, V. Bendkowsky, B. Butscher, R. Löw, L. Santos, T. Pfau, Evidence for coherent collective Rydberg excitation in the strong blockade regime, *Phys. Rev. Lett.* 99 (2007) 163601. <http://dx.doi.org/10.1103/PhysRevLett.99.163601>.
- [5] Y.O. Dudin, A. Kuzmich, Strongly interacting Rydberg excitations of a cold atomic gas, *Science* 336 (6083) (2012) 887–889. <http://dx.doi.org/10.1126/science.1217901>.
- [6] D. Møller, L.B. Madsen, K. Mølmer, Quantum gates and multiparticle entanglement by Rydberg excitation blockade and adiabatic passage, *Phys. Rev. Lett.* 100 (2008) 170504. <http://dx.doi.org/10.1103/PhysRevLett.100.170504>.
- [7] T. Vogt, M. Viteau, J. Zhao, A. Chotia, D. Comparat, P. Pillet, Dipole blockade at Förster resonances in high resolution laser excitation of Rydberg states of cesium atoms, *Phys. Rev. Lett.* 97 (2006) 083003. <http://dx.doi.org/10.1103/PhysRevLett.97.083003>.
- [8] T. Pellizzari, S.A. Gardiner, J.I. Cirac, P. Zoller, Decoherence, continuous observation, and quantum computing: a cavity qed model, *Phys. Rev. Lett.* 75 (1995) 3788–3791. <http://dx.doi.org/10.1103/PhysRevLett.75.3788>.
- [9] L.-M. Duan, H.J. Kimble, Scalable photonic quantum computation through cavity-assisted interactions, *Phys. Rev. Lett.* 92 (2004) 127902. <http://dx.doi.org/10.1103/PhysRevLett.92.127902>.
- [10] L.-M. Duan, B. Wang, H.J. Kimble, Robust quantum gates on neutral atoms with cavity-assisted photon scattering, *Phys. Rev. A* 72 (2005) 032333. <http://dx.doi.org/10.1103/PhysRevA.72.032333>.
- [11] A.S. Sørensen, K. Mølmer, Measurement induced entanglement and quantum computation with atoms in optical cavities, *Phys. Rev. Lett.* 91 (2003) 097905. <http://dx.doi.org/10.1103/PhysRevLett.91.097905>.
- [12] E. Brion, K. Mølmer, M. Saffman, Quantum computing with collective ensembles of multilevel systems, *Phys. Rev. Lett.* 99 (2007) 260501. <http://dx.doi.org/10.1103/PhysRevLett.99.260501>.
- [13] M. Fleischhauer, S. Yelin, M. Lukin, How to trap photons? Storing single-photon quantum states in collective atomic excitations, *Opt. Commun.* 179 (1–6) (2000) 395–410, doi: [http://dx.doi.org/10.1016/S0030-4018\(99\)00679-3](http://dx.doi.org/10.1016/S0030-4018(99)00679-3).
- [14] R.H. Dicke, Coherence in spontaneous radiation processes, *Phys. Rev.* 93 (1954) 99–110. <http://dx.doi.org/10.1103/PhysRev.93.99>.
- [15] M. Shahriar, P. Pradhan, G. Pati, V. Gopal, K. Salit, Light-shift imbalance induced blockade of collective excitations beyond the lowest order, *Opt. Commun.* 278 (1) (2007) 94–98, doi: <http://dx.doi.org/10.1016/j.optcom.2007.05.057>.
- [16] M.S. Shahriar, G.S. Pati, K. Salit, Quantum communication and computing with atomic ensembles using a light-shift-imbalance-induced blockade, *Phys. Rev. A* 75 (2007) 022323. <http://dx.doi.org/10.1103/PhysRevA.75.022323>.
- [17] R. Sarkar, M. E. Kim, R. Fang, Y. Tu, M.S. Shahriar, Generalized collective states and their role in a collective-state atomic interferometer and atomic clock, <http://arxiv.org/abs/1408.2296>.
- [18] F.T. Arezchi, E. Courten, R. Gilmore, H. Thomas, Atomic coherent states in quantum optics, *Phys. Rev. A* 6 (1972) 2211–2237. <http://dx.doi.org/10.1103/PhysRevA.6.2211>.
- [19] M. Saffman, T.G. Walker, K. Mølmer, Quantum information with Rydberg atoms, *Rev. Mod. Phys.* 82 (2010) 2313–2363. <http://dx.doi.org/10.1103/RevModPhys.82.2313>.
- [20] A.M. Steane, M. Chowdhury, C.J. Foot, Radiation force in the magneto-optical trap, *J. Opt. Soc. Am. B* 9 (12) (1992) 2142–2158. <http://dx.doi.org/10.1364/JOSAB.9.002142>.
- [21] E. Urban, T.A. Johnson, T. Henage, L. Isenhower, D.D. Yavuz, T.G. Walker, M. Saffman, Observation of Rydberg blockade between two atoms, *Nat. Phys.* 5 (2009) 110–114. <http://dx.doi.org/10.1038/nphys1178>.

## Effects of non-idealities and quantization of the center of mass motion on symmetric and asymmetric collective states in a collective state atomic interferometer

Resham Sarkar<sup>a\*</sup> , May E. Kim<sup>a</sup>, Renpeng Fang<sup>a</sup>, Yanfei Tu<sup>b</sup> and Selim M. Shahriar<sup>a,b</sup>

<sup>a</sup>Department of Physics and Astronomy, Northwestern University, Evanston, IL, USA; <sup>b</sup>Department of EECS, Northwestern University, Evanston, IL, USA

(Received 27 January 2015; accepted 12 March 2015)

We investigate the behavior of an ensemble of  $N$  non-interacting, identical atoms excited by a laser. In general, the  $i$ -th atom sees a Rabi frequency  $\Omega_i$ , an initial position dependent laser phase  $\phi_i$ , and a motion induced Doppler shift of  $\delta_i$ . When  $\Omega_i$  or  $\delta_i$  is distinct for each atom, the system evolves into a superposition of  $2^N$  intercoupled states, of which there are  $N + 1$  symmetric and  $(2^N - (N + 1))$  asymmetric collective states. For a collective state atomic interferometer (COSAIN), we recently proposed, it is important to understand the behavior of all the collective states under various conditions. In this paper, we show how to formulate the properties of these states under various non-idealities, and use this formulation to understand the dynamics thereof. We also consider the effect of treating the center of mass degree of freedom of the atoms quantum mechanically on the description of the collective states, illustrating that it is indeed possible to construct a generalized collective state, as needed for the COSAIN, when each atom is assumed to be in a localized wave packet. The analysis presented in this paper is important for understanding the dynamics of the COSAIN, and will help advance the analysis and optimization of spin squeezing in the presence of practically unavoidable non-idealities as well as in the domain where the center of mass motion of the atoms is quantized.

**Keywords:** atomic ensembles; symmetric collective states; asymmetric collective states; atomic interferometer

### 1. Introduction

Atom interferometry is emerging as a very important avenue of precision metrology. It has been used as a gyroscope [1–3] as well as an accelerometer [4,5]. It has also been used for accurate measurements of gravity [6,7], gradients in gravity [8], as well as gravitational red-shift [9]. Other applications include measurement of fine structure constants with high precision [10,11], as well as the realization of a matter-wave clock [12]. The rotation sensitivity of an atom interferometric gyroscope (AIG) is due to the phase difference between two paths arising from the Sagnac effect [13–15]. This phase difference is proportional to the area enclosed by the interferometer as well as the mass of each atom.

Motivated by this mass dependence of the rotation sensitivity of an AIG, we have recently proposed an interferometer that exploits the collective excitation of an ensemble of atoms [16]. To explain the principle behind this briefly, we consider an assembly of  $N$  non-interacting identical two-level atoms, as illustrated in Figure 1(a). For a practical atomic interferometer, these levels are actually metastable hyperfine ground levels, coupled to an intermediate state via off-resonant counter-propagating optical fields. However,

the basic concept can be illustrated by considering these two states to be coupled by a single, traveling laser field [17]. The atoms are initially prepared in quantum state  $|g, 0\rangle$ , denoting that in this state, the atoms are stationary along the **z**-axis. A laser beam propagating along the **z**-axis will impart a momentum  $\hbar k$  to an atom upon absorption of a single photon, driving it to a superposition of the states  $|g, 0\rangle$  and  $|e, \hbar k\rangle$ , with the amplitude of each state depending on the intensity of the laser beam,  $\Omega$ , and the time of interaction,  $t$ .

In a single atom interferometer, a two-level atom is first split into an equal superposition of  $|g, 0\rangle$  and  $|e, \hbar k\rangle$  by a  $\pi/2$ -pulse (so that  $\Omega t = \pi/2$ ). After letting this split atom drift freely for time  $T$ , the two states are inverted and redirected by a  $\pi$ -pulse. At the end of another free drift time,  $T$ , the two paths are recombined by another  $\pi/2$ -pulse. This is shown schematically in Figure 1(b). A possible phase difference,  $\Delta\phi$ , between the two paths manifests itself in the amplitude of the states at the end of the  $\pi/2 - \pi - \pi/2$  sequence. For example, the amplitude of  $|g\rangle$  at the end of the interferometric sequence varies as  $\cos^2(\Delta\phi/2)$  [1,14]. It is also possible to make a similar interferometer using only a single zone excitation [18,19].

\*Corresponding author. Email: rsarkar@u.northwestern.edu

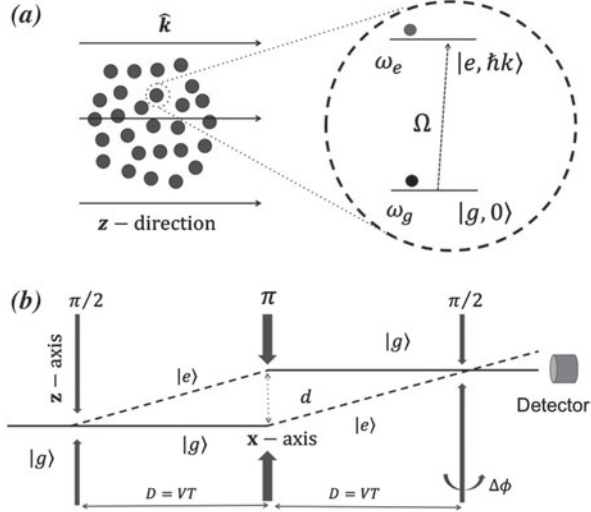


Figure 1. (a) Ensemble of  $N$  two-level atoms in a classical laser field propagating the  $z$ -direction, (b) a single atom interferometer produced via  $\pi/2 - \pi - \pi/2$  sequence of excitation.

We have shown in Ref. [16] how an ensemble of  $N$  atoms can be used to make a Collective State Atomic Interferometer (COSAIN) which also makes use of the  $\pi/2 - \pi - \pi/2$  pulse sequence employing counter-propagating Raman excitations in a  $\Lambda$  system, but has properties that differ very significantly from the Conventional Raman Atomic Interferometer (CRAIN) employing the same pulse sequence. For example, the width of the fringes generated as a function of the differential phase between the two paths (or, equivalently, a rotation applied perpendicular to its plane) is reduced by a factor of  $\sqrt{N}$ , when compared to the same for the CRAIN. The minimum measurable phase shift, under quantum noise limited (QNL) operation, is given by  $\Delta\phi_c^{QNL} = \pi/\sqrt{Nn\tau\eta_c}$ , where  $n$  is the number of interrogations per unit time,  $\tau$  is the total observation time, and  $\eta_c$  is the quantum efficiency of detecting one of the collective states. This is to be compared with the same for a CRAIN, which is given by  $\Delta\phi_s^{QNL} = \pi/\sqrt{m\tau\eta_s}$ , where  $m$  is the flux of atoms per unit time, and  $\eta_s$  is the quantum efficiency of detecting each atom. For comparison, we consider a situation where  $m = Nn$ . Thus,  $\Delta\phi_c^{QNL}$  can be substantially smaller than  $\Delta\phi_s^{QNL}$ , since  $\eta_c$  can be very close to unity, while  $\eta_s$  is generally very small because of geometric constraints encountered in collecting fluorescence from the atoms [16]. In order to understand the basic principles of operation of such an interferometer, it is instructive to recall first the Dicke states [20–22].

In Ref. [20], Dicke showed that for a dilute ensemble of  $N$  atoms where the atoms do not interact, the ensemble evolves to a superposition of  $N+1$  symmetric states (shown in Figure 2). Some of the possible Dicke states are defined as follows

$$|G\rangle = |g_1, g_2, \dots, g_N\rangle,$$

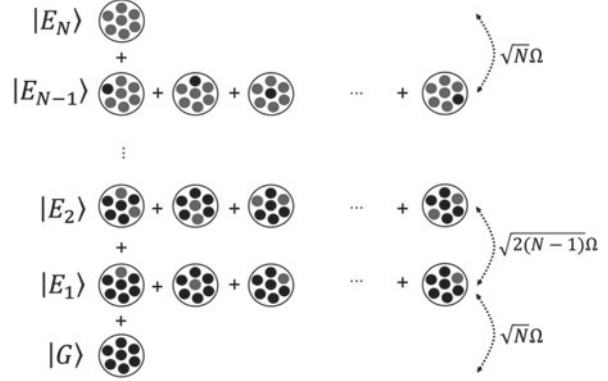


Figure 2. Schematic illustration of some of the possible symmetric collective states and coupling strength to their adjacent states.

$$\begin{aligned} |E_1\rangle &= \sum_{i=1}^N |g_1, g_2, \dots, e_i, \dots, g_N\rangle / \sqrt{N}, \\ |E_2\rangle &= \sum_{j,k (j \neq k)}^N |g_1, \dots, e_j, \dots, e_k, \dots, g_N\rangle / \sqrt{\binom{N}{2}}, \\ |E_{N-1}\rangle &= \sum_{i=1}^N |e_1, e_2, \dots, g_i, \dots, e_N\rangle / \sqrt{N}, \\ |E_N\rangle &= |e_1, e_2, \dots, e_N\rangle, \end{aligned} \quad (1)$$

etc. where  $\binom{N}{n} = N!/n!(N-n)!$ .

A COSAIN is configured essentially the same way as the CRAIN with two exceptions. First, it must make use of trapped atoms, released sequentially to the interferometer. Second, the detection process is designed to measure the probability of finding all the atoms in one of the collective states, such as  $|G\rangle$ . The reduction in the width of the fringe occurs due to a combination of the interferences among all the collective states, which follow different paths. Details of this process can be found in Ref. [16]. We have also shown how a Collective State Atomic Clock (COSAC) can be realized in this way, also with a  $\sqrt{N}$  reduction in the width of the fringes [23]. Just as the COSAIN is a variant of the CRAIN, the COSAC is a variant of the Conventional Raman Atomic Clock (CORAC) [24–27]. In Ref. [23], we show how a conventional microwave clock [28,29] can also be converted into a COSAC.

As noted above, the COSAIN makes use of counter-propagating Raman transitions. As such, the characteristic wave number is  $k$ , where  $k = (k_1 + k_2)$ , and  $k_1$  and  $k_2$  are the wave numbers of the two laser beams. The non-zero temperature of a MOT provides a spread in the velocity of the constituent atoms. Therefore, each atom in the ensemble experiences a Doppler shift leading to a spread in detuning, with a zero mean value. Due to the finite size of the ensemble, each atom may experience a slightly different Rabi frequency depending on the spatial variation

in the intensity profile of the laser beam. These factors contribute to a complex picture of an ensemble in a practical experiment. Furthermore, a semiclassical treatment of a quantum mechanical problem is not adequate. The wave packet nature of the atoms must also be taken into account by considering the center of mass (COM) momentum of the atomic states.

In this paper, we present a description of collective states under generalized and non-ideal conditions, including a situation where the motion of the COM of each atom is treated quantum mechanically. Such a comprehensive model of the collective states currently does not exist in the literature, and is important for understanding the behavior of the COSAIN. This comprehensive model of collective states, including the case where the COM motion is quantized, is also likely to help advance the analysis and optimization of spin squeezing [30–33], under non-idealities that are unavoidable in any practical scheme. The rest of the paper is organized as follows. In Section 2, we describe the semiclassical model of generalized collective excitation to lay down the mathematical framework on which our analysis is based. For the sake of simplicity and transparency, we introduce the concepts first with the example of a 2-atom ensemble identical to the Dicke formalism of collective excitation. Next, we analyze how variable Rabi frequencies and atomic velocities affect this simple ensemble. In Section 3, this investigation is extended to a general  $N$ -atom ensemble. In particular, we show that under certain conditions, the generalized asymmetric states of an ensemble are not decoupled from the symmetric set. We develop the general method of finding the generalized collective symmetric and asymmetric states in an ensemble of arbitrary size. In Section 4, we consider the COM motion degree of freedom of the atoms and investigate the implications of the wave packet nature of the atoms, and therefore, of the ensemble.

## 2. Semiclassical model of generalized collective excitation

Without loss of generality, we consider a collection of  $N$  two-level atoms, released from a cold trap, excited by a laser field traveling in the  $\mathbf{z}$  direction, assuming the field amplitude to be of Gaussian profile in  $\mathbf{x}$  and  $\mathbf{y}$  directions, and constant in the  $\mathbf{z}$  direction. Each atom is modeled as having two energy levels,  $|g_i\rangle$  and  $|e_i\rangle$ . As mentioned earlier, a A-type atomic system excited by a pair of optically off-resonant laser fields propagating in opposite directions can be modeled as an effective two-level system of this type [18], so that the decay rate of the  $|e_i\rangle$  state can be set to zero. This effective two-level system is shown in Figure 1(a), where  $\omega_0 = (\omega_e - \omega_g)$  is the frequency of the laser field, assumed to be resonant for stationary atoms. Each atom, however, experiences a different Doppler shift due to the thermal motion of the atoms, and consequently, a different effective laser frequency,  $\omega_{0i}$ . The net consequence of this is that the  $i$ -th atom picks up a detuning of  $\delta_i$  depending

on its velocity. The Rabi frequency,  $\Omega_i$ , experienced by the  $i$ -th atom depends on its position.

The laser field is assumed, arbitrarily, to be polarized in the  $\mathbf{x}$  direction. In the laboratory frame, the electric field at any point  $\mathbf{r} = x\hat{\mathbf{x}} + y\hat{\mathbf{y}} + z\hat{\mathbf{z}}$ , defined arbitrarily with respect to an origin, can be expressed as  $\mathbf{E}_i(\mathbf{r}, t) = \hat{\mathbf{x}}E_0 \exp[-(x^2 + y^2)/2\sigma_L^2] \cos(\omega_0 t - kz)$ , where  $\sigma_L$  represents the width of the laser beam in the transverse directions. Assume now that, at  $t = 0$ , the  $i$ -th atom is positioned at  $\mathbf{r}_{0i} = x_{0i}\hat{\mathbf{x}} + y_{0i}\hat{\mathbf{y}} + z_{0i}\hat{\mathbf{z}}$ , and is moving at a velocity  $\mathbf{v}_i = v_{xi}\hat{\mathbf{x}} + v_{yi}\hat{\mathbf{y}} + v_{zi}\hat{\mathbf{z}}$ . We ignore for now any change to this velocity due to the interaction with the laser field. This issue will be addressed later when we consider the motion of the COM of the atom quantum mechanically. In the reference frame of this atom, which is defined by the vector  $\mathbf{r}_i = \mathbf{r}_{0i} + \mathbf{v}_i t$ , the electric field can be expressed as  $\mathbf{E}_i(\mathbf{r}_i, t) = \hat{\mathbf{x}}E_0 \exp[-((x_{0i} + v_{xi}t)^2 + (y_{0i} + v_{yi}t)^2)/2\sigma_L^2] \cos(\omega_0 t - k(z_{0i} + v_{zi}t))$ . The transverse motion of the atom will lead to a time-dependent variation of the amplitude of the Rabi frequency. We assume that, for typical systems of interest,  $|v_{xi}t| \ll \sigma_L$  and  $|v_{yi}t| \ll \sigma_L$ , so that this variation can be ignored. We can then write the field seen by the atom in its reference frame as  $\mathbf{E}_i(\mathbf{r}_i, t) = \hat{\mathbf{x}}E_0 \exp[-(x_{0i}^2 + y_{0i}^2)/2\sigma_L^2] \cos(\omega_{0i} t - \xi_i)$ , where  $\omega_{0i} = \omega_0 - kv_{zi}$  is the Doppler shifted frequency seen by the atom, and  $\xi_i = kz_{0i}$  is a reference phase relation, determined by the initial position of the atom, between the atom and the field for all values of  $t$ .

In the electric dipole approximation, the Hamiltonian for the  $i$ -th atom can be written as  $H_i = \mathbf{P}_i^2/2m + H_{0i} + q\rho_i \cdot \mathbf{E}_i$ , where  $\mathbf{P}_i$  is the COM momentum in the  $z$ -direction,  $H_{0i}$  is the internal energy of the atom,  $\rho_i$  is the position of the electron with respect to the nucleus,  $q$  is the electronic charge, and  $m$  is the mass of the atom. As mentioned above, we are treating the motion of the COM of the atom semiclassically, deferring the quantum mechanical model thereof to a later part of this paper. As such, the COM term in the Hamiltonian can be ignored. Upon making the rotating-wave approximation,  $H_i$  can then be expressed in the bases of  $|g_i\rangle$  and  $|e_i\rangle$  as:

$$H_i/\hbar = \omega_g |g_i\rangle \langle g_i| + \omega_e |e_i\rangle \langle e_i| + \Omega_i (\exp(i(\omega_{0i}t - \xi_i)) |g_i\rangle \langle e_i| + h.c.)/2, \quad (2)$$

where  $\Omega_i \equiv \langle g_i | (\mathbf{x} \cdot \rho_i) | e_i \rangle E_i/\hbar = \langle e_i | (\mathbf{x} \cdot \rho_i) | g_i \rangle E_i/\hbar$ .

The state of this atom,  $|\psi_i\rangle$ , evolves according to the Schrödinger equation,  $i\hbar\partial|\psi_i\rangle/\partial t = H_i|\psi_i\rangle$ . We define a transformed state vector  $|\psi'_i\rangle = Q_i|\psi_i\rangle$ , where  $Q_i$  is the unitary transformation, defined as

$$Q_i = \sum_{j=1}^2 \exp(i(a_{ij}t + b_{ij})) |j\rangle \langle j|, \quad (3)$$

where  $a_{ij}$  and  $b_{ij}$  are the arbitrary parameters. The Hamiltonian for this state vector is then  $H'_i = Q_i H_i Q_i^{-1} - \hbar\dot{Q}_i Q_i^{-1}$ , so that  $i\hbar\partial|\psi'_i\rangle/\partial t = H'_i|\psi'_i\rangle$ . To render  $H'_i$

time independent, we set  $a_{i1} = \omega_g$  and  $a_{i2} = \omega_{0i} + \omega_g$ . Now, setting  $b_{i1} = 0$ ,  $b_{i2} = -\xi_i$  makes  $H'_i$  independent of any phase factor as well. In this frame, the  $Q$ -transformed Hamiltonian thus becomes

$$H'_i/\hbar = -\delta_i |e'_i\rangle\langle e'_i| + \Omega_i(|g'_i\rangle\langle e'_i| + h.c.)/2. \quad (4)$$

The new basis vectors,  $|g'_i\rangle$  and  $|e'_i\rangle$ , are related to the original basis vectors as  $\exp(-i\omega_g t)|g_i\rangle$  and  $\exp(-i((\omega_e + \delta_i)t - \xi_i))|e_i\rangle$ , respectively. Assuming that the  $i$ -th atom is initially in the state  $c_{gi}(0)|g'_i\rangle + c_{ei}(0)|e'_i\rangle$ , its quantum state can be written as

$$\begin{aligned} |\psi'_i\rangle = & e^{i\delta_i t/2} \left( \left( c_{gi}(0) \cos\left(\frac{\Omega'_i t}{2}\right) \right. \right. \\ & - i \frac{c_{gi}(0)\delta_i + c_{ei}(0)\Omega_i}{\Omega'_i} \sin\left(\frac{\Omega'_i t}{2}\right) \left. \right) |g'_i\rangle \\ & + \left( -i \frac{c_{gi}(0)\Omega_i - c_{ei}(0)\delta_i}{\Omega'_i} \sin\left(\frac{\Omega'_i t}{2}\right) \right. \\ & \left. \left. + c_{ei}(0) \cos\left(\frac{\Omega'_i t}{2}\right) \right) |e'_i\rangle \right), \end{aligned} \quad (5)$$

where  $\Omega'_i = \sqrt{\Omega_i^2 + \delta_i^2}$  is the effective coupling frequency of this atom.

Since we assume no interaction among the atoms, the ensemble Hamiltonian is the sum of all the individual Hamiltonians corresponding to each atom in the ensemble,  $H'_C = \sum_i H'_i$ . The state of the ensemble, therefore, evolves according to the Schrödinger equation,  $i\hbar\partial|\Psi'_C\rangle/\partial t = H'_C|\Psi'_C\rangle$ . For illustrative purposes, as well as transparency, let us consider first the case of  $N = 2$ .  $H'_C$  can be expressed as  $H'_1 \otimes I'_2 + I'_1 \otimes H'_2$ , where  $I'_i$  is the identity operator in the basis of  $|g'_i\rangle$  and  $|e'_i\rangle$  for the  $i$ -th atom. For instance,  $\langle g'_1 g'_2 | H'_C | g'_1 e'_2 \rangle = \langle g'_1 | H'_1 | g'_1 \rangle \langle g'_2 | I'_2 | e'_2 \rangle + \langle g'_1 | I'_1 | g'_1 \rangle \langle g'_2 | H'_2 | e'_2 \rangle = \langle g'_1 | H'_2 | e'_2 \rangle = \hbar\Omega_2/2$ . Using this process, we can now express  $H'_C$  in the basis of product states of the two atoms,  $|g'_1 g'_2\rangle$ ,  $|e'_1 g'_2\rangle$ ,  $|g'_1 e'_2\rangle$ , and  $|e'_1 e'_2\rangle$  as

$$\begin{aligned} H'_C/\hbar = & -\delta_1 |e'_1 g'_2\rangle\langle e'_1 g'_2| - \delta_2 |g'_1 e'_2\rangle\langle g'_1 e'_2| \\ & - (\delta_1 + \delta_2) |e'_1 e'_2\rangle\langle e'_1 e'_2| \\ & + \Omega_1(|g'_1 g'_2\rangle\langle e'_1 g'_2| + |e'_1 e'_2\rangle\langle g'_1 e'_2| + h.c.)/2 \\ & + \Omega_2(|g'_1 g'_2\rangle\langle g'_1 e'_2| + |e'_1 e'_2\rangle\langle e'_1 g'_2| + h.c.)/2. \end{aligned} \quad (6)$$

Consider first the case where all the Rabi frequencies are the same, and there are no detunings. The  $Q$ -transformed Hamiltonian for each atom is then formally identical, since the phase factors due to different positions are encoded in the transformed basis states  $|g'_i\rangle$  and  $|e'_i\rangle$ . Thus, the coupled collective states would now be formally identical to the symmetric Dicke states. For example,

$$\begin{aligned} |G'\rangle &= |g'_1\rangle|g'_2\rangle, \\ |E'_1\rangle &= (|g'_1 e'_2\rangle + |e'_1 g'_2\rangle)/\sqrt{2}, \\ |E'_2\rangle &= |e'_1\rangle|e'_2\rangle. \end{aligned} \quad (7)$$

It should be noted that each of the constituent individual atomic states in these expressions include the temporal and spatial phase factors. Thus, these states behave the same way as the conventional Dicke symmetric collective states, independent of the distance between the two atoms. It should also be noted that there exists another collective state,  $|E'_{1,1}\rangle \equiv (|g'_1 e'_2\rangle - |e'_1 g'_2\rangle)/\sqrt{2}$  which remains fully uncoupled from the symmetric set. The states  $|E'_1\rangle$  and  $|E'_{1,1}\rangle$  result from a  $\pi/4$  rotation in the Hilbert subspace spanned by  $|e'_1 g'_2\rangle$  and  $|g'_1 e'_2\rangle$ , as illustrated in Figure 3(a).

Consider next the case where there is still no detuning, but the Rabi frequencies are unequal. It is not obvious what the form of the symmetric collective states should be in this case. Consider first the task of finding the first excited symmetric collective state (SCS). Since the  $|G'\rangle$  state will, by definition, be coupled only to this state, we can define this state, in general, as

$$|E'_1\rangle = \frac{H'_C |G'\rangle}{\sqrt{\langle G' | H'_C H'_C | G' \rangle}}, \quad (8)$$

where the denominator ensures that this state is normalized. When applied to the particular case at hand, we thus get  $|E'_1\rangle = (\Omega_1 |e'_1 g'_2\rangle + \Omega_2 |g'_1 e'_2\rangle)/\sqrt{\Omega_1^2 + \Omega_2^2}$ .

A rotation operator,  $R$ , rotates the Hilbert subspace,  $\Phi_{2,1}$ , formed by  $|e'_1 g'_2\rangle$  and  $|g'_1 e'_2\rangle$  by an angle  $\theta = \tan^{-1}(\Omega_1/\Omega_2)$ , such that one of the resulting states is  $|E'_1\rangle$ . This also produces a state  $|E'_{1,1}\rangle = (\Omega_2 |e'_1 g'_2\rangle - \Omega_1 |g'_1 e'_2\rangle)/\sqrt{\Omega_1^2 + \Omega_2^2}$ , which is orthogonal to  $|E'_1\rangle$ . In this rotated frame, the ensemble Hamiltonian,  $\tilde{H}'_C = R H'_C R^{-1}$  becomes

$$\begin{aligned} \tilde{H}'_C/\hbar &= \sqrt{\Omega_1^2 + \Omega_2^2} |G'\rangle\langle E'_1|/2 + \Omega_1\Omega_2 |E'_1\rangle\langle E'_2|/\sqrt{\Omega_1^2 + \Omega_2^2} \\ &+ (\Omega_2^2 - \Omega_1^2) |E'_{1,1}\rangle\langle E'_2|/2\sqrt{\Omega_1^2 + \Omega_2^2} + h.c. \end{aligned} \quad (9)$$

Thus, the asymmetric collective state (ACS),  $|E'_{1,1}\rangle$ , does not remain isolated but is coupled to  $|E'_2\rangle$ , which in turn is coupled to  $|E'_1\rangle$ . Consider next the case where we also allow for potentially different detunings for the two atoms,  $\delta_1$  and  $\delta_2$ . It is easy to see, based on the general definition in Equation (8) of the first excited SCS, that  $|E'_1\rangle$  has the same form as in Equation (8). Similarly, the expression for  $|E'_{1,1}\rangle$  is also the same as above, and these states are generated by the same rotation operator,  $R$ , as given above. However, the coupling between the states in this rotated basis is now modified. Explicitly the ensemble  $Q$ -transformed Hamiltonian in the rotated frame becomes

$$\begin{aligned} \tilde{H}'_C/\hbar = & - \left( \delta_1 \Omega_1^2 + \delta_2 \Omega_2^2 \right) (|E'_1\rangle\langle E'_1| \\ & + |E'_{1,1}\rangle\langle E'_{1,1}|) / (\Omega_1^2 + \Omega_2^2) \end{aligned}$$

$$\begin{aligned}
& -(\delta_1 + \delta_2) |E'_2\rangle\langle E'_2| + \sqrt{\Omega_1^2 + \Omega_2^2} |G'\rangle\langle E'_1|/2 \\
& + \Omega_1\Omega_2 |E'_1\rangle\langle E'_2|/\sqrt{\Omega_1^2 + \Omega_2^2} \\
& + (\Omega_2^2 - \Omega_1^2) |E'_{1,1}\rangle\langle E'_2|/2\sqrt{\Omega_1^2 + \Omega_2^2} \\
& - (\delta_1 - \delta_2)\Omega_1\Omega_2 |E'_1\rangle\langle E'_{1,1}|/(\Omega_1^2 + \Omega_2^2) + h.c.
\end{aligned} \tag{10}$$

Thus, the ACS  $|E'_{1,1}\rangle$  is now coupled directly to the SCS  $|E'_1\rangle$ , in addition to being coupled to the state  $|E'_2\rangle$ . Furthermore, the energies of the states are also shifted with respect to  $|G'\rangle$ . These couplings and shifts are illustrated in Figure 3(b).

In an ensemble with a large number of atoms, the number of asymmetric states is far larger than that of the symmetric states. In the next section, we discuss a more generalized view of collective states, considering the variations in different parameters and manifestations thereof in the behavior of the collective states.

In the preceding discussions, we have taken into account the facts that each atom is at a unique position (which means

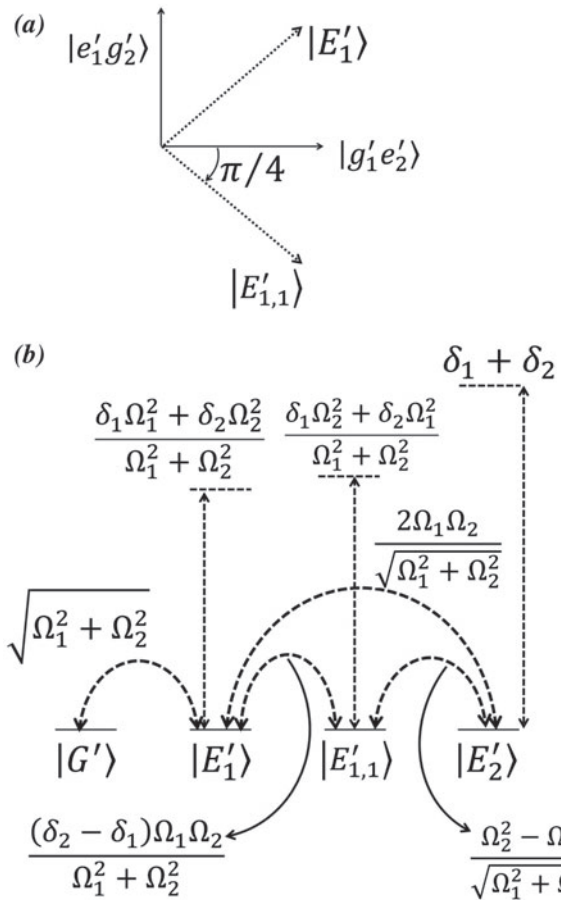


Figure 3. (a) Rotation of basis states to form collective states in a two-atom ensemble, (b) the complete set of all collective states and relevant couplings and detunings in a two-atom ensemble.

that it sees a unique phase of the laser), sees a potentially unique Rabi frequency, and is moving with a particular velocity which in turn produces a Doppler shift. A natural question that may arise is whether we are taking into account the fact that the position of each atom is changing with time, so that it would see a time varying Rabi frequency and laser phase. The temporal variation in Rabi frequency can be ignored because the velocity of each atom is assumed to be very small. In Appendix 1, we show that the temporal change in the laser phase seen by the atom is akin to taking into account the Doppler shift.

### 3. N-Atom ensemble

The Hamiltonian of an ensemble of  $N$  non-interacting and non-overlapping atoms is simply given by the sum of the Hamiltonians of the constituent atoms as noted above. It is convenient to express these as a sum of three parts: raising, lowering, and detuning:  $H'_C = H'_r + H'_l + H'_d$ , where  $H'_r = \sum_i^N \hbar\Omega_i |e'_i\rangle\langle g'_i|/2$ ,  $H'_l = \sum_i^N \hbar\Omega_i |g'_i\rangle\langle e'_i|/2$ , and  $H'_d = -\sum_i^N \hbar\delta_i |e'_i\rangle\langle e'_i|$ . The raising part of the Hamiltonian,  $H'_r$  couples  $|E'_n\rangle$  to its adjacent higher SCS,  $|E'_{n+1}\rangle$ . Similarly, the lowering part of the Hamiltonian,  $H'_l$  couples  $|E'_n\rangle$  to its adjacent lower SCS,  $|E'_{n-1}\rangle$ . The function of the third term,  $H'_d$  is twofold. First, it leads to a shift in the energy of the collective states (symmetric and asymmetric). Second, under certain conditions, it leads to a coupling between the SCS and all the ACS's, as well as among all the ACS's, within the same manifold (i.e. the set of collective states corresponding to the absorption of a given number of photons). Analogous to Equation (8),  $|E'_{n+1}\rangle$  can be generated from  $|E'_n\rangle$ , for any value of  $n$ , using the following prescription

$$|E'_{n+1}\rangle = \frac{H'_r |E'_n\rangle}{\sqrt{\langle E'_n | H'_r^\dagger H'_r | E'_n \rangle}}. \tag{11}$$

To illustrate the use of Equation (11), we first consider the ideal case where each atom sees the same Rabi frequency, and experiences no Doppler shift, but still allowing for the fact that different atoms see different spatial phases. Since  $H'_d = 0$ , the asymmetric states remain fully uncoupled from the symmetric states. Using Equation (11), we can now easily find  $|E'_n\rangle$ , noting that  $|E'_0\rangle = |G'\rangle$ . Application of  $H'_r$  to  $|G'\rangle$ , upon normalization, then leads to the result that  $|E'_1\rangle = \sum_{k=1}^N |g'_1 g'_2, \dots, e'_k, \dots, g'_N\rangle/\sqrt{N}$ . This is essentially the same as the well-known first-excitation Dicke state, with the exception that the spatial phases seen by the individual atoms are incorporated in the constituent states  $|g'\rangle$  and  $|e'\rangle$ , as noted before in the context of  $N = 2$ .

It is now easy to see how to generate  $|E'_n\rangle$  for any value of  $n$ , by repeated application of  $H'_r$ , and allowing for the normalization, as prescribed by Equation (11). Specifically,

we get

$$|E'_n\rangle = J(N, n)^{-1/2} \sum_{k=1}^{J(N, n)} P_k |g'^{\otimes(N-n)} e'^{\otimes n}\rangle, \quad (12)$$

where  $J(N, n) \equiv J = \binom{N}{n}$ , and  $P_k$  is the permutation operator [34].

Under the ideal condition being considered here, the ACSs remain fully decoupled from the symmetric set at all times, as noted above. As such, an explicit description of the forms of the ACSs is not necessary for understanding the behavior of the ensemble. However, when we consider non-idealities later, it will be important to understand the form of the ACSs. Therefore, we discuss here how to determine these states explicitly in the ideal case, and a simple modification of this approach will then be used later on for the non-ideal cases, where the ACSs are relevant.

Consider a particular manifold corresponding to the absorption of  $n$  photons. The SCS is  $|E'_n\rangle$ , and there are  $(J-1)$  ACSs, denoted as  $|E'_{n,j}\rangle$  for  $j = 1$  to  $(J-1)$ . To find these states, we consider  $\Phi_{N,n}$ , the Hilbert subspace of dimension  $J$  spanned by the states  $P_k |g'^{\otimes(N-n)} e'^{\otimes n}\rangle$ . The elements of  $\Phi_{N,n}$  are arbitrarily labeled  $\hat{s}_1, \hat{s}_2, \dots, \hat{s}_J$ . The SCS is a particular vector in this Hilbert space, and the ACSs are any set of mutually orthogonal vectors that are all normal to the SCS. Thus, the set of ACSs is not unique, and there are many ways to construct them. The standard procedure for finding such a set of orthonormal vectors is the Gram–Schmidt Orthogonalization (GSO) process. From a geometric point of view, the GSO process can be seen as a set of generalized rotations (with potentially complex angles) in the Hilbert space. Given that the SCS consists of a superposition of the basis vectors with real coefficients, these rotations can be viewed in terms of physical angles for  $N = 2$  and 3, whereas for  $N > 3$ , the angles have to be interpreted in an abstract manner. In order to elucidate our understanding of the ACS's, we first formulate the construction of ACS's for arbitrary  $N$  and  $n$ , by successive rotations of the Hilbert subspace,  $\Phi_{N,n}$ . We then illustrate the application of this model for  $N = 3$  for constructing some explicit version of the ACSs (noting that the  $N = 2$  case has only a single ACS which can be found trivially and has been explained in detail in Section 2).

The elements of  $\Phi_{N,n}$ , labeled  $\hat{s}_1, \hat{s}_2, \dots, \hat{s}_J$ , form the coordinate axes of this Hilbert space. In this picture, we can represent the SCS as  $\mathbf{V} = (\hat{s}_1 + \hat{s}_2 + \dots + \hat{s}_J)/\sqrt{J}$ , a vector that makes an angle,  $\theta = \cos^{-1}(1/\sqrt{J})$  with each of the axes. Thus, to find all the collective states of  $\Phi_{N,n}$ , including the SCS and all the ACS's, we proceed as follows. We start with the original set of coordinate axes:  $\hat{s}_1, \hat{s}_2, \dots, \hat{s}_J$ . We then carry out a set of  $(J-1)$  rotations, producing a new set of coordinate axes that are mutually orthogonal. The rotation angles are chosen to ensure that after the  $(J-1)$  rotations, one of the coordinate axes is parallel to  $\mathbf{V}$  (which

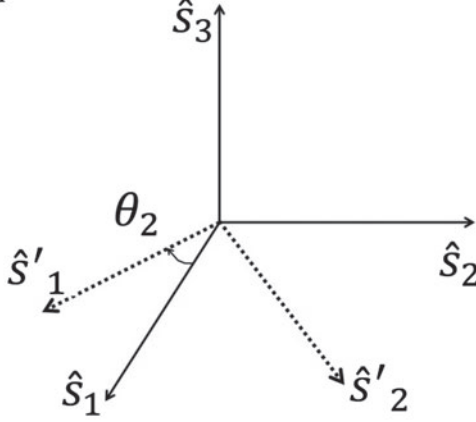
is the SCS), so that the remaining set of coordinate axes can be identified as the ACSs. This is accomplished by carrying out the following steps:

*Step 1* We write  $\mathbf{V}$  as a sum of two terms,  $\mathbf{V}_{12}$  and  $\mathbf{V}_{\text{rest}}$ , where  $\mathbf{V}_{12} = (\hat{s}_1 + \hat{s}_2)/\sqrt{J}$ . Normalization of  $\mathbf{V}_{12}$  gives the unit vector  $\hat{\mathbf{V}}_{12} = (\hat{s}_1 + \hat{s}_2)/\sqrt{2}$ , revealing that it makes an angle  $\cos^{-1}(1/\sqrt{2})$  with  $\hat{s}_1$  and  $\hat{s}_2$ . Therefore, the plane of  $\hat{s}_1$  and  $\hat{s}_2$  must be rotated around the origin by  $\theta_2 = (-\cos^{-1}(1/\sqrt{2}))$  to give  $\hat{s}'_1 = (\hat{s}_1 - \hat{s}_2)/\sqrt{2}$  and  $\hat{s}'_2 = (\hat{s}_1 + \hat{s}_2)/\sqrt{2}$ . Obviously,  $\hat{s}'_2$  is parallel to  $\mathbf{V}_{12}$ . By construction,  $\hat{s}'_1$  is orthogonal to  $\hat{s}'_2$ , and therefore to  $\mathbf{V}_{12}$ . Since  $\mathbf{V}_{\text{rest}}$  does not contain any component in the  $\{\hat{s}_1, \hat{s}_2\}$  plane, it then follows that  $\hat{s}'_1$  is orthogonal to  $\mathbf{V}$ , and is therefore an ACS. For  $N = 2$  described in Sec. 2,  $\hat{s}'_1 = |E'_{1,1}\rangle$  and  $\hat{s}'_2 = |E'_1\rangle$ , and the process stops at this point.

*Step 2* The vector,  $\mathbf{V}$  is rewritten as another sum of two terms,  $\mathbf{V}_{123}$  and  $\mathbf{V}'_{\text{rest}}$ , where  $\mathbf{V}_{123} = (\hat{s}_1 + \hat{s}_2 + \hat{s}_3)/\sqrt{J}$ . Normalization of  $\mathbf{V}_{123}$  gives the unit vector  $\hat{\mathbf{V}}_{123} = (\hat{s}_1 + \hat{s}_2 + \hat{s}_3)/\sqrt{3}$ , showing that it makes an angle  $\cos^{-1}(1/\sqrt{3})$  with  $\hat{s}_1, \hat{s}_2$  and  $\hat{s}_3$ . Since  $\hat{s}'_1$  is orthogonal to  $\mathbf{V}$ , we leave it undisturbed. The plane of  $\hat{s}'_2$  and  $\hat{s}_3$  is rotated around the origin by  $\theta_3 = (-\cos^{-1}(1/\sqrt{3}))$ , resulting in  $\hat{s}''_2 = (\hat{s}_1 + \hat{s}_2 - 2\hat{s}_3)/\sqrt{6}$  and  $\hat{s}'_3 = (\hat{s}_1 + \hat{s}_2 + \hat{s}_3)/\sqrt{3}$ . It is clear that  $\hat{s}''_2$  is parallel to  $\mathbf{V}_{123}$ . By construction,  $\hat{s}''_2$  is orthogonal to  $\hat{s}'_3$ , and therefore, to  $\mathbf{V}_{123}$ . Furthermore, since  $\mathbf{V}'_{\text{rest}}$  does not contain any component in the  $\{\hat{s}_1, \hat{s}_2, \hat{s}_3\}$  plane, it then follows that  $\hat{s}''_2$  is orthogonal to  $\mathbf{V}$ .  $\hat{s}''_2$  is also orthogonal to  $\hat{s}'_1$ , since it is a linear combination of  $\hat{s}'_2$  and  $\hat{s}'_3$ , which are both orthogonal to  $\hat{s}'_1$ . Thus,  $\hat{s}''_2$  is the second ACS. For  $N = 3$  and  $n = 2$ , this is the terminal step, resulting in  $\hat{s}'_1 = |E'_{2,1}\rangle$ ,  $\hat{s}''_2 = |E'_{2,2}\rangle$  and  $\hat{s}'_3 = |E'_2\rangle$ , as shown in Figure 4.

*Step 3*  $\mathbf{V}$  is written again as  $\mathbf{V} = \mathbf{V}_{1234} + \mathbf{V}''_{\text{rest}}$ , where  $\mathbf{V}_{1234} = (\hat{s}_1 + \hat{s}_2 + \hat{s}_3 + \hat{s}_4)/\sqrt{J}$ . Again, normalizing  $\mathbf{V}_{1234}$  gives  $\hat{\mathbf{V}}_{1234} = (\hat{s}_1 + \hat{s}_2 + \hat{s}_3 + \hat{s}_4)/\sqrt{4}$ , showing that it makes an angle  $\cos^{-1}(1/\sqrt{4})$  with  $\hat{s}_1, \hat{s}_2, \hat{s}_3$ , and  $\hat{s}_4$ . As described in Step 2 above,  $\hat{s}'_1$  and  $\hat{s}''_2$  are orthogonal to each other and to  $\mathbf{V}$ , and, therefore, we leave these two undisturbed. To find the vector orthogonal to this pair as well as to  $\mathbf{V}$ , we rotate the plane of  $\hat{s}'_3$  and  $\hat{s}_4$  about the origin by  $\theta_4 = (-\cos^{-1}(1/\sqrt{4}))$ , and derive  $\hat{s}'''_3 = (\hat{s}_1 + \hat{s}_2 + \hat{s}_3 - 3\hat{s}_4)/\sqrt{12}$  and  $\hat{s}'_4 = (\hat{s}_1 + \hat{s}_2 + \hat{s}_3 + \hat{s}_4)/\sqrt{4}$ . Following the same set of arguments presented in Step 2, it is easy to show that  $\hat{s}'''_3$  is orthogonal to  $\hat{s}'_1, \hat{s}''_2$  and  $\mathbf{V}$ . As such, this is the third ACS. For  $N = 4$  and  $n = 1$ , this is the terminal step, resulting in  $\hat{s}'_1 = |E'_{1,1}\rangle$ ,  $\hat{s}''_2 = |E'_{1,2}\rangle$ ,  $\hat{s}'''_3 = |E'_{1,3}\rangle$  and  $\hat{s}'_4 = |E'_1\rangle$ .

Step 1



Step 2

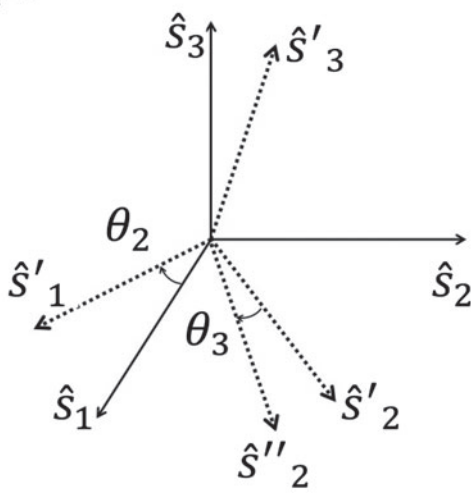


Figure 4. Hilbert subspace rotation of the first excited state of an ensemble of three atoms.

For arbitrary  $N$  and  $n$ , there are  $(J-1)$  such steps to arrive at the Hilbert subspace  $\Phi'_{N,n}$  spanned by  $\hat{s}'_1, \hat{s}''_2, \hat{s}'''_3, \dots, \hat{s}'_J$ , where  $\hat{s}'_j$  is the SCS and the rest are the ACSs. This process can be formalized by the method of matrix rotations considering the column vector formed by the elements of the space  $\Phi_{N,n}$  as follows

$$\mathbf{S} = [\hat{s}_1 \ \hat{s}_2 \ \dots \ \hat{s}_J]^T. \quad (13)$$

The vector,  $\mathbf{S}$  undergoes a series of rotations that transforms it to another vector,  $\mathbf{S}_C$  whose elements are the symmetric and asymmetric collective states for that particular manifold of the ensemble. The first rotation matrix,  $R(2)$ , causes a rotation of  $\mathbf{S}$  in the  $\{\hat{s}_1, \hat{s}_2\}$  plane to form  $\mathbf{S}_2$  whose elements are  $\{\hat{s}'_1, \hat{s}'_2, \hat{s}_3, \dots, \hat{s}_J\}$ . The second rotation matrix,  $R(3)$ , further rotates the vector  $\mathbf{S}_2$  in the  $\{\hat{s}'_2, \hat{s}_3\}$  plane to give  $\mathbf{S}_3$ . This process is continued until the vector,  $\mathbf{S}_J \equiv \mathbf{S}_C$ , is formed by applying  $R(J)$  on  $\mathbf{S}_{J-1}$ . Therefore, the overall process may be expressed as  $\mathbf{S}_C = R_T \mathbf{S}$ , where  $R_T = R(J)R(J-1)\dots R(3)R(2)$ . The  $j$ -th rotation vector is of

the form

$$R(j)_{m,n} = \begin{cases} 1 & \text{for } m = n, m \neq j-1, j \\ \cos \theta_j & \text{for } m = n = j-1, j \\ -\sin \theta_j & \text{for } m = j, n = j-1 \\ \sin \theta_j & \text{for } m = j-1, n = j \\ 0 & \text{otherwise} \end{cases}, \quad (14)$$

where  $\theta_j = \cos^{-1}(1/\sqrt{j})$ , so that  $\cos \theta_j = 1/\sqrt{j}$  and  $\sin \theta_j = \sqrt{(j-1)/j}$ . This matrix represents a simple rotation by an angle of  $(-\theta_j)$  in the plane of  $\hat{s}'_{j-1}$  and  $\hat{s}_j$ . To visualize this, we show below the explicit form of  $R(2)$ ,  $R(3)$ , and  $R(4)$ .

$$R(2) = \begin{bmatrix} \cos \theta_2 & -\sin \theta_2 & 0 & 0 & \dots & 0 \\ \sin \theta_2 & \cos \theta_2 & 0 & 0 & \dots & 0 \\ 0 & 0 & 1 & 0 & \dots & 0 \\ 0 & 0 & 0 & 1 & \dots & 0 \\ \vdots & \vdots & \vdots & \vdots & \ddots & \vdots \\ 0 & 0 & 0 & 0 & \dots & 1 \end{bmatrix},$$

$$\theta_2 = \cos^{-1}(1/\sqrt{2}),$$

$$R(3) = \begin{bmatrix} 1 & 0 & 0 & 0 & \dots & 0 \\ 0 & \cos \theta_3 & -\sin \theta_3 & 0 & \dots & 0 \\ 0 & \sin \theta_3 & \cos \theta_3 & 0 & \dots & 0 \\ 0 & 0 & 0 & 1 & \dots & 0 \\ \vdots & \vdots & \vdots & \vdots & \ddots & \vdots \\ 0 & 0 & 0 & 0 & \dots & 1 \end{bmatrix},$$

$$\theta_3 = \cos^{-1}(1/\sqrt{3}),$$

$$R(4) = \begin{bmatrix} 1 & 0 & 0 & 0 & \dots & 0 \\ 0 & 1 & 0 & 0 & \dots & 0 \\ 0 & 0 & \cos \theta_4 & -\sin \theta_4 & \dots & 0 \\ 0 & 0 & \sin \theta_4 & \cos \theta_4 & \dots & 0 \\ \vdots & \vdots & \vdots & \vdots & \ddots & \vdots \\ 0 & 0 & 0 & 0 & \dots & 1 \end{bmatrix},$$

$$\theta_4 = \cos^{-1}(1/\sqrt{4}). \quad (15)$$

In general, for arbitrary  $N, n$  and therefore  $J$ , the SCS, and ACSs can be expressed as follows

$$|E'_n\rangle = \sum_{l=1}^J \hat{s}_l / \sqrt{J},$$

$$|E'_{n,j}\rangle = \left( \sum_{l=1}^j \hat{s}_l - j\hat{s}_{j+1} \right) / \sqrt{j(j+1)}, \quad (16)$$

where  $j = 1, 2, \dots, n-1$ . Conversely, the original unrotated vectors can be written in terms of the rotated, collective states bases as follows

$$\begin{aligned}\hat{s}_1 &= |E'_n\rangle/\sqrt{J} + \sum_{j=1}^{J-1} |E'_{n,j}\rangle/\sqrt{j(j+1)}, \\ \hat{s}_j &= |E'_n\rangle/\sqrt{J} + \sum_{l=j}^{J-1} |E'_{n,l}\rangle/\sqrt{l(l+1)} \\ &\quad - \sqrt{j-1} |E'_{n,j-1}\rangle/\sqrt{j},\end{aligned}\quad (17)$$

where  $j = 2, \dots, n-1$ . This inversion is useful in illustrating the behavior of the collective states in more complex situations, an example of which will be presented shortly.

In order to get a clearer picture of how the spread in detuning affects the behavior of the ensemble, we consider the simple case of a three-atom ensemble interacting with a laser of uniform profile. Additionally, we assume that the  $i$ -th atom experiences a detuning of  $\delta_i$ . The manifold corresponding to the absorption of *one* photon is spanned by the set  $\Phi_{3,1}$ , whose elements, given by  $|e'_1g'_2g'_3\rangle$ ,  $|g'_1e'_2g'_3\rangle$ , and  $|g'_1g'_2e'_3\rangle$ , are now labeled as  $\hat{s}_1$ ,  $\hat{s}_2$ , and  $\hat{s}_3$ , respectively. The SCS of this manifold, as defined in Equation (16), is given by  $|E'_1\rangle = (\hat{s}_1 + \hat{s}_2 + \hat{s}_3)/\sqrt{3} = (|e'_1g'_2g'_3\rangle + |g'_1e'_2g'_3\rangle + |g'_1g'_2e'_3\rangle)/\sqrt{3}$ . One of the possible ways of forming the set of ACSs is  $|E'_{1,1}\rangle = (\hat{s}_1 - \hat{s}_2)/\sqrt{2} = (|e'_1g'_2g'_3\rangle - |g'_1e'_2g'_3\rangle)/\sqrt{2}$ , and  $|E'_{1,2}\rangle = (\hat{s}_1 + \hat{s}_2 - 2\hat{s}_3)/\sqrt{6} = (|e'_1g'_2g'_3\rangle + |g'_1e'_2g'_3\rangle - 2|g'_1g'_2e'_3\rangle)/\sqrt{6}$ . The action of the ensemble Hamiltonian,  $H'_C = H'_r + H'_l + H'_d$  on  $|E'_1\rangle$ , shows how it experiences an energy shift, and couples with its adjacent states as follows:

$$H'_r |E'_1\rangle/\hbar = \Omega (|e'_1e'_2g'_3\rangle + |e'_1g'_2e'_3\rangle + |g'_1e'_2e'_3\rangle)/\sqrt{3}, \quad (18a)$$

$$H'_l |E'_1\rangle/\hbar = \sqrt{3}\Omega |g'_1g'_2g'_3\rangle/2, \quad (18b)$$

$$\begin{aligned}H'_d |E'_1\rangle/\hbar &= \left( -\delta_1 |e'_1g'_2g'_3\rangle - \delta_2 |g'_1e'_2g'_3\rangle \right. \\ &\quad \left. - \delta_3 |g'_1g'_2e'_3\rangle \right)/\sqrt{3}.\end{aligned}\quad (18c)$$

It can be seen from Equation (16) that Equation (18a) can be written as  $H'_r |E'_1\rangle/\hbar = \Omega |E'_2\rangle$  and Equation (18b) can be written as  $H'_l |E'_1\rangle/\hbar = \sqrt{3}\Omega |G'\rangle/2$ . Furthermore, each term on the right-hand side in Equation (18c) can be written in terms of the relevant SCS and ACSs according to Equation (17):

$$\begin{aligned}H'_d |E'_1\rangle/\hbar &= -\delta_1 \hat{s}_1/\sqrt{3} - \delta_2 \hat{s}_2/\sqrt{3} - \delta_3 \hat{s}_3/\sqrt{3} \\ &\quad - (\delta_1 + \delta_2 + \delta_3) |E'_1\rangle/3 - (\delta_1 - \delta_2) |E'_{1,1}\rangle/\sqrt{6} \\ &\quad - (\delta_1 + \delta_2 - 2\delta_3) |E'_{1,2}\rangle/\sqrt{18}.\end{aligned}\quad (19)$$

The first term in parentheses on the right-hand side of Equation (19) is the energy shift in  $|E'_1\rangle$ . The second and third terms give the coupling strength of  $|E'_1\rangle$  with  $|E'_{1,1}\rangle$  and  $|E'_{1,2}\rangle$ , respectively. In the case that each atom in the ensemble experiences the same detuning due to Doppler shift,

these two terms go to zero, and the ACSs remain uncoupled from the symmetric set.

In the more complex case where each atom in the ensemble experiences a unique Rabi frequency, the raising part of the ensemble Hamiltonian applied to any SCS yields the next higher SCS of that ensemble, as prescribed in Equation (11). To illustrate this, we consider the example of a four-atom ensemble where the raising part of the Hamiltonian is  $H'_r = \sum_{i=1}^4 \hbar\Omega_i |e'_i\rangle\langle g'_i|/2$ . The set of SCSs are therefore, the following:

$$\begin{aligned}|E'_1\rangle &= (\Omega_1 |e'_1g'_2g'_3g'_4\rangle + \Omega_2 |g'_1e'_2g'_3g'_4\rangle + \Omega_3 |g'_1g'_2e'_3g'_4\rangle \\ &\quad + \Omega_4 |g'_1g'_2g'_3e'_4\rangle) \times (\Omega_1^2 + \Omega_2^2 + \Omega_3^2 + \Omega_4^2)^{-1/2} \\ |E'_2\rangle &= (\Omega_1\Omega_2 |e'_1e'_2g'_3g'_4\rangle + \Omega_1\Omega_3 |e'_1g'_2e'_3g'_4\rangle \\ &\quad + \Omega_1\Omega_4 |e'_1g'_2g'_3e'_4\rangle + \Omega_2\Omega_3 |g'_1e'_2e'_3g'_4\rangle \\ &\quad + \Omega_2\Omega_4 |g'_1e'_2g'_3e'_4\rangle + \Omega_3\Omega_4 |g'_1g'_2e'_3e'_4\rangle) ((\Omega_1\Omega_2)^2 \\ &\quad + (\Omega_1\Omega_3)^2 + (\Omega_1\Omega_4)^2 \\ &\quad + (\Omega_2\Omega_3)^2 + (\Omega_2\Omega_4)^2 + (\Omega_3\Omega_4)^2)^{-1/2} \\ |E'_3\rangle &= (\Omega_1\Omega_2\Omega_3 |e'_1e'_2e'_3g'_4\rangle \\ &\quad + \Omega_1\Omega_2\Omega_4 |e'_1e'_2g'_3e'_4\rangle + \Omega_1\Omega_3\Omega_4 |e'_1g'_2e'_3e'_4\rangle \\ &\quad + \Omega_2\Omega_3\Omega_4 |g'_1e'_2e'_3e'_4\rangle) ((\Omega_1\Omega_2\Omega_3)^2 + (\Omega_1\Omega_2\Omega_4)^2 \\ &\quad + (\Omega_1\Omega_3\Omega_4)^2 + (\Omega_2\Omega_3\Omega_4)^2)^{-1/2} \\ |E'_4\rangle &= |e'_1e'_2e'_3e'_4\rangle.\end{aligned}\quad (20)$$

The set of ACSs corresponding to  $|E'_n\rangle$  in the present case of non-uniform Rabi frequency consists of  $(J-1)$  elements that are orthogonal to one another as well as to  $|E'_n\rangle$ . As mentioned above, they can be constructed using the GSO process. The realization of this process as a set of rotations follows a similar set of rules as described above. However, the rotation angles will now depend on the relative amplitudes of all the Rabi frequencies. The details of this process are beyond the scope of the present discussion and will be presented elsewhere.

#### 4. Quantized COM model of ensemble

As mentioned earlier, we have been investigating the use of atomic ensembles for a COSAIN. In a CRAIN, one must take into account the quantum nature of the COM motion. Similarly, for a COSAIN, we must consider the COM motion of the atom quantum mechanically. In doing so, one must consider all the degrees of freedom of the COM. However, for a CRAIN as well as the COSAIN (which is a variant of the CRAIN), only the motion in the direction parallel to the laser beams (which we have chosen to be the  $\mathbf{z}$  direction) has to be quantized. As such, in what follows, we keep our discussion confined to such a scenario.

The  $i$ -th atom is now a Gaussian wave packet formed by the superposition of an infinite number of plane waves, where the  $p$ -th plane wave can exist in two energy states,  $|g_{ip}, \hbar k'_{ip}\rangle$  and  $|e_{ip}, \hbar(k'_{ip} + k)\rangle$ , which differ by a momentum  $\hbar k$ . Since the laser field amplitude is assumed to be

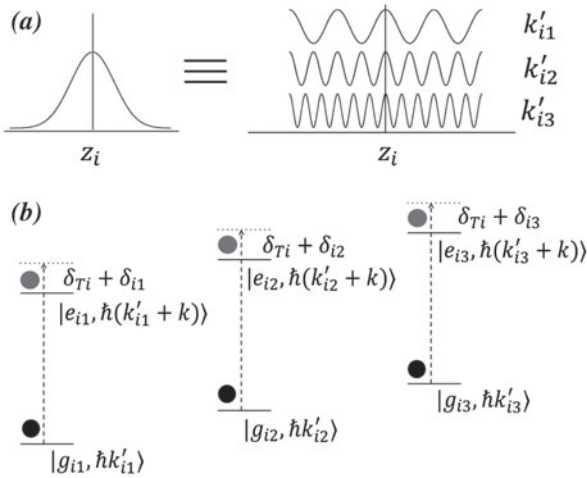


Figure 5. (a) Quantized COM model of an atom, (b) two-level model of each plane wave component.

constant in the **z** direction, the Rabi frequency experienced by each plane wave manifold of the  $i$ -th atom is  $\Omega_i$ . The Doppler shift induced due to the thermal motion of the atoms in the **z** direction ascribes a detuning of  $\delta_{Ti}$  to this atom. As such, the Hamiltonian of the  $p$ -th plane wave of the  $i$ -th atom is

$$H_{ip}/\hbar = \left( \omega_g + \hbar k_{ip}^2/2m \right) |g_{ip}\rangle\langle g_{ip}| + \left( \omega_e + \hbar (k'_{ip} + k)^2/2m \right) |e_{ip}\rangle\langle e_{ip}| + \Omega_i (\exp(i(\omega_{0i}t - \xi_i)) |g_{ip}\rangle\langle e_{ip}| + h.c.)/2. \quad (21)$$

The Schrödinger equation governing the evolution of the state vector of this plane wave,  $|\psi_{ip}\rangle$ , is  $i\hbar\partial|\psi_{ip}\rangle/\partial t = H_{ip}|\psi_{ip}\rangle$ . Similar to the description given in Equations (3) and (4), a unitary transformation,  $Q_{ip}$ , changes  $|\psi_{ip}\rangle$  to  $|\psi'_{ip}\rangle$  such that

$$Q_{ip} = \sum_{j=1}^2 \exp(i(a_{ipj}t + b_{ipj})) |j\rangle\langle j|, \quad (22)$$

where  $a_{ipj}$  and  $b_{ipj}$  are the arbitrary parameters. The Hamiltonian in the new basis vector thus formed is  $H'_{ip} = Q_{ip}H_{ip}Q_{ip}^{-1} - \hbar\dot{Q}_{ip}Q_{ip}^{-1}$ , so that  $i\hbar\partial|\psi'_{ip}\rangle/\partial t = H'_{ip}|\psi'_{ip}\rangle$ . It can be stripped of its time dependence by setting  $a_{ip1} = \omega_g + \hbar k_{ip}^2/2m$  and  $a_{ip2} = \omega_e + \delta_{vi} + \hbar k_{ip}^2/2m$ . For  $b_{ip1} = 0$  and  $b_{ip2} = -\xi_i$ ,  $H'_{ip}$  is rendered independent of any phase factors. In the transformed frame, the Hamiltonian is thus

$$H'_{ip}/\hbar = (-\delta_{vi} + \hbar k^2/2m + \hbar k k'_{ip}/m) |e'_{ip}\rangle\langle e'_{ip}| + \Omega_i (|g'_{ip}\rangle\langle e'_{ip}| + h.c.)/2. \quad (23)$$

Since the atom is a sum of these individual plane waves, it evolves according to the equation that is the sum of the

individual Schrödinger equations,  $i\hbar\partial(\sum_{p=-\infty}^{\infty} |\psi'_{ip}\rangle)/\partial t = \sum_{p=-\infty}^{\infty} H'_{ip} |\psi'_{ip}\rangle$ . In the limit that the Rabi frequency of the  $i$ -th atom is large compared to the Doppler shift due to the COM momentum of each of the constituent plane waves, i.e.  $\Omega_i \gg \hbar k k'_{ip}/m$ , the corresponding Hamiltonians become identical to one another. The resulting evolution equation is then  $i\hbar\partial|\psi'_i\rangle/\partial t = H'_i|\psi'_i\rangle$ , where  $|\psi'_i\rangle = \sum_{p=-\infty}^{\infty} |\psi'_{ip}\rangle$  and  $H'_i = H'_{i1} = H'_{i2}$ , etc. In this regime, the atom's Hamiltonian becomes  $H'_i/\hbar = -\delta_i |e'_i\rangle\langle e'_i| + \Omega_i (|g'_i\rangle\langle e'_i| + h.c.)/2$ , where  $\delta_i = \delta_{vi} - \hbar k^2/2m$ . This is identical to the semiclassical Hamiltonian of the atom where the COM mass degree of freedom of the atom is not considered. Thus, we conclude that, under approximations that are valid for the COSAIN, a semiclassical description of the COM motion of each atom is sufficient. As such, all the results we have derived above regarding the properties of collective state remain valid for the COSAIN.

## 5. Summary

We have investigated the behavior of an ensemble of  $N$  non-interacting, identical atoms excited by a laser with a wavelength of  $\lambda$ . In doing so, we have assumed that the wave functions of the atoms do not overlap with one another, so that quantum statistical properties are not relevant. In general, the  $i$ -th atom sees a Rabi frequency  $\Omega_i$ , an initial position dependent laser phase  $\phi_i$ , and a motion induced Doppler shift of  $\delta_i$ . When  $\Omega_i = \Omega$  and  $\delta_i = \delta$  for all atoms, the system evolves into a superposition of  $(N + 1)$  generalized symmetric collective states, independent of the values of  $\phi_i$ . If  $\phi_i = \phi$  for all atoms, these states simplify to the well-known Dicke collective states. When  $\Omega_i$  or  $\delta_i$  is distinct for each atom, the system evolves into a superposition of symmetric as well as asymmetric collective states. For large values of  $N$ , the number of asymmetric states ( $2^N - (N + 1)$ ) is far larger than that of the symmetric states. For a COSAIN and a COSAC, it is important to understand the behavior of all the collective states under various conditions. In this paper, we have shown how to formulate systematically the properties of all the collective states under various non-idealities, and used this formulation to understand the dynamics thereof. Specifically, for the case where  $\Omega_i = \Omega$  and  $\delta_i = \delta$  for all atoms, we have shown how the amplitudes of each of the generalized collective states can be determined explicitly in a simple manner. For the case where  $\Omega_i$  or  $\delta_i$  is distinct for each atom, we have shown how the symmetric and asymmetric collective states can be treated on the same footing. Furthermore, we have shown that the collective states corresponding to the absorption of a given number of photons can be visualized as an abstract, multi-dimensional rotation in the Hilbert space spanned by the ordered product states of individual atoms. This technique enables one to construct the explicit expression for any asymmetric state of interest. Such

expressions in turn can be used to determine the evolution of such a state in the COSAIN or the COSAC. We have also considered the effect of treating the COM degree of freedom of the atoms quantum mechanically on the description of the collective states. This is particularly relevant for the COSAIN. In particular, we have shown that it is indeed possible to construct a generalized collective state when each atom is assumed to be in a localized wave packet.

## Disclosure statement

No potential conflict of interest was reported by the authors.

## Funding

This work has been supported by the NSF [grant number DGE-0801685], [grant number DMR-1121262]; AFOSR [grant number FA9550-09-1-0652].

## ORCID

Resham Sarkar  <http://orcid.org/0000-0003-3206-1871>

## References

- [1] Bordé, C.J. *Phys. Lett. A* **1989**, *140*, 10–12.
- [2] Gustavson, T.L.; Bouyer, P.; Kasevich, M.A. *Phys. Rev. Lett.* **1997**, *78*, 2046–2049.
- [3] Gustavson, T.L.; Landragin, A.; Kasevich, M.A. *Classical Quantum Gravity* **2000**, *17*, 2385–2398.
- [4] Geiger, R.; Menoret, V.; Stern, G.; Zahzam, N.; Cheinet, P.; Battelier, B.; Villing, A.; Moron, F.; Lours, M.; Bidel, Y.; Bresson, A.; Landragin, A.; Bouyer, P. *Nat. Commun.* **2011**, *2*, 474.
- [5] Stern, G.; Battelier, B.; Geiger, R.; Varoquaux, G.; Villing, A.; Moron, F.; Carraz, O.; Zahzam, N.; Bidel, Y.; Chaibi, W.; Pereira Dos Santos, F.; Bresson, A.; Landragin, A.; Bouyer, P. *Eur. Phys. J. D* **2009**, *53*, 353–357.
- [6] Peters, A.; Chung, K.Y.; Chu, S. *Nature* **1999**, *400*, 849–852.
- [7] Rosi, G.; Sorrentino, F.; Cacciapuoti, L.; Prevedelli, M.; Tino, T.M. *Nature (London)* **2014**, *510*, 518–521.
- [8] Snadden, M.J.; McGuirk, J.M.; Bouyer, P.; Haritos, K.G.; Kasevich, M.A. *Phys. Rev. Lett.* **1998**, *81*, 971–974.
- [9] Müller, H.; Peters, A.; Chu, S. *Nature* **2010**, *463*, 926–929.
- [10] Bouchendira, R.; Cladé, P.; Guellati-Khélifa, S.; Nez, F.; Biraben, F. *Phys. Rev. Lett.* **2011**, *106*, 080801.
- [11] Cadoret, M.; de Mirandes, E.; Cladé, P.; Guellati-Khélifa, S.; Schwob, C.; Nez, F.; Julien, L.; Biraben, F. *Phys. Rev. Lett.* **2008**, *101*, 230801.
- [12] Lan, S.Y.; Kuan, P.-C.; Estey, B.; English, D.; Brown, J.M.; Hohensee, M.A.; Müller, H. *Science* **2013**, *339*, 554–557.
- [13] Sagnac, M.G. *C.R. Acad. Sci.* **1913**, *157*, 708–710.
- [14] Kasevich, M.; Chu, S. *Phys. Rev. Lett.* **1991**, *67*, 181–184.
- [15] Shahriar, M.S.; Pati, G.S.; Tripathi, R.; Gopal, V.; Messall, M.; Salit, K. *Phys. Rev. A* **2007**, *75*, 053807.
- [16] Sarkar, R.; Kim, M.; Fang, R.; Shahriar, M.S. [arxiv.org/abs/1410.7131v2](http://arxiv.org/abs/1410.7131v2).
- [17] Shahriar, S.M.; Hemmer, P.R.; Katz, D.P.; Lee, A.; Prentiss, M.G. *Phys. Rev. A* **1997**, *55*, 2272.
- [18] Shahriar, S.M.; Jheeta, M.; Tan, Y.; Pradhan, P.; Gangat, A. *Opt. Commun.* **2004**, *243*, 183–201.
- [19] Shahriar, S.M.; Pradhan, P.; Tan, Y.; Jheeta, M.; Morzinski, J.; Hemmer, P.R. *J. Opt. Soc. Am. B* **2005**, *22* (7), 1566–1570.
- [20] Dicke, R.H. *Phys. Rev.* **1954**, *93*, 99–110.
- [21] Arechi, F.T.; Courtens, E.; Gilmore, R.; Thomas, H. *Phys. Rev. A* **1972**, *6*, 2211–2237.
- [22] Scully, M.O.; Fry, E.S.; Ooi, C.H.R.; Wódkiewicz, K. *Phys. Rev. Lett.* **2006**, *96*, 010501.
- [23] Kim, M.E.; Sarkar, R.; Fang, R.; Tu, Y.; Shahriar, S.M. [arxiv.org/abs/1410.2268v3](http://arxiv.org/abs/1410.2268v3).
- [24] Hemmer, P.R.; Shahriar, M.S.; Natoli, V.D.; Ezekiel, S. *J. Opt. Soc. Am. B* **1989**, *6*, 1519–1528.
- [25] Hemmer, P.R.; Ontai, G.P.; Ezekiel, S. *J. Opt. Soc. Am. B* **1986**, *3*, 219–230.
- [26] Hemmer, P.R.; Shahriar, M.S.; Lamela-Rivera, H.; Smith, S.P.; Bernacki, B.E.; Ezekiel, S. *J. Opt. Soc. Am. B* **1993**, *10*, 1326–1329.
- [27] Pati, G.S.; Fatemi, F.K.; Shahriar, M.S. *Opt. Express* **2011**, *19*, 22388–22401.
- [28] Ramsey, N.F. *Molecular Beams*; Oxford University Press: New York, 1956.
- [29] Verhaar, B.J.; Gibble, K.; Chu, S. *Phys. Rev. A* **1993**, *48*, R3429–R3432.
- [30] Kitagawa, M.; Ueda, M. *Phys. Rev. A* **1993**, *47*, 5138–5143.
- [31] Hald, J.; Sørensen, J.L.; Schori, C.; Polzik, E.S. *Phys. Rev. Lett.* **1999**, *83*, 1319–1322.
- [32] Kuzmich, A.; Mandel, L.; Bigelow, N.P. *Phys. Rev. Lett.* **2000**, *85*, 1594–1597.
- [33] Hammerer, K.; Sørensen, A.S.; Polzik, E.S. *Rev. Mod. Phys.* **2010**, *82*, 1041–1093.
- [34] Hume, D.B.; Chou, C.W.; Rosenband, T.; Wineland, D.J. *Phys. Rev. A* **2009**, *80*, 052302.

## Appendix 1. Equivalence between Doppler effect induced phase shift and position change induced phase shift

Consider an ideal two-level atom excited by a laser field traveling in the **z** direction, assuming the field amplitude to be uniform in all directions. The atom is modeled as having two energy levels,  $|g\rangle$  and  $|e\rangle$ . For the issue at hand, it is not necessary to consider the radiative decay of  $|e\rangle$ . As such, we assume both of the states to be long-lived. This two-level system is shown in Figure A1(a), where  $\omega_0$  is the frequency of the laser field, assumed to be resonant for a stationary atom. The laser field is assumed to be polarized, arbitrarily, in the **x** direction. As illustrated in Figure A1(b), the atom is initially ( $t = 0$ ) positioned at  $\mathbf{r}_{0i} = x_{0i}\hat{\mathbf{x}} + y_{0i}\hat{\mathbf{y}} + z_{0i}\hat{\mathbf{z}}$  and is moving in the **z** direction with a non-relativistic velocity  $v$ . The electric field at a time  $t$ , in the atom's frame of reference is  $\mathbf{E}(\mathbf{r}, t) = \hat{\mathbf{x}}E_0 \cos(\omega_0 t - kz)$ , where  $z = z_{0i} + vt$ . In the semiclassical model employed here, the Hamiltonian of this atom can be written as  $H = H_{0i} + q\rho \cdot \mathbf{E}$ , where the terms have their usual meanings as given in Section 2. After making the rotating-wave approximation as prescribed in Section 2,  $H$  can be written in the bases of  $|g\rangle$  and  $|e\rangle$  as

$$H/\hbar = \omega_g |g\rangle \langle g| + \omega_e |e\rangle \langle e| + \Omega(\exp(i(\omega_0 t - k(z_{0i} + vt))) |g\rangle \langle e| + h.c.)/2, \quad (A1)$$

where  $\Omega \equiv \langle g | (\mathbf{x} \cdot \rho) | e \rangle E/\hbar = \langle e | (\mathbf{x} \cdot \rho) | g \rangle E/\hbar$ .

The state of this atom,  $|\psi\rangle$ , evolves according to the Schrödinger equation,  $i\hbar\partial|\psi\rangle/\partial t = H|\psi\rangle$ . A unitary transformation,  $Q$ , defined as  $Q = \sum_{j=1}^2 \exp(i(a_j t + b_j)) |j\rangle \langle j|$  changes  $|\psi\rangle$  to  $|\psi'\rangle = Q|\psi\rangle$ , where  $a_j$  and  $b_j$  are the arbitrary parameters. The  $Q$ -transformed Hamiltonian for this state vector is then  $H' = QHQ^{-1} - \hbar\dot{Q}Q^{-1}$ , so that  $i\hbar\partial|\psi'\rangle/\partial t = H'|\psi'\rangle$ .  $H'$  is stripped of its time dependence by setting  $a_1 = \omega_g$  and  $a_2 = \omega_0 + \omega_g = \omega_e - kv$ . Now, setting  $b_1 = 0$ ,  $b_2 = -kz_{0i}$  makes  $H'$  independent

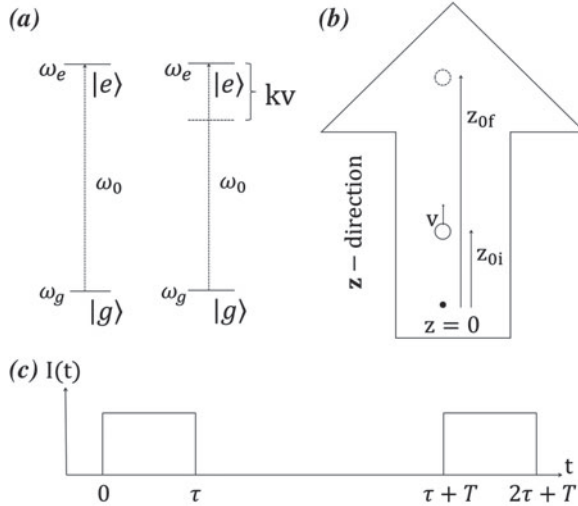


Figure A1. (a) (left) Two-level atom in the lab frame, (right) in the atom's frame of reference, (b) change in the coordinates of the atom over the duration of interaction with the laser pulses, (c) laser beam intensity variation over the duration of interaction.

of any phase factor as well. The  $Q$ -transformed Hamiltonian thus becomes

$$H'/\hbar = kv |e'\rangle\langle e'| + \Omega(|g'\rangle\langle e'| + h.c.)/2. \quad (\text{A2})$$

Therefore, the velocity of the atom induces a net detuning of  $\delta = -kv$ . The new basis vectors,  $|g'\rangle$  and  $|e'\rangle$ , are related to the original basis vectors as  $\exp(-i\omega_g t)|g\rangle$  and  $\exp(-i((\omega_e - kv)t - kz_{0i}))|e\rangle$ , respectively. If the atom is initially in  $c_{g1}(0)|g_i'\rangle + c_{e1}(0)|e_i'\rangle$ , its state after interaction for a time  $t$  is given by Equation (5).

We consider this atom's interaction with two consecutive laser fields separated by a dark zone of duration  $T$ , as illustrated in Figure A1(c). The time of interaction of the atom with each field is such that  $\tau = \pi/2\Omega$ . The atom initially at  $z = z_{0i}$  drifts to  $z = z_{0f}$  by the end of the entire interaction sequence. For the sake of simplicity, we assume that  $kv \ll \Omega$  and that the atom's position does not change appreciably over the duration of the pulse. Starting with the atom in state  $|g\rangle$  at  $t = 0$ , the state of the atom at the end of the first pulse ( $t = \tau$ ) is  $|\psi'\rangle = (|g'\rangle - i|e'\rangle)/\sqrt{2}$ . The  $Q$ -transformed Hamiltonian in the dark zone is given by  $H'_d = kv |e'\rangle\langle e'|$ . At  $t = \tau + T$ , the state of the atom can be expressed as

$$|\psi'\rangle = (|g'\rangle - i \exp(-ikvT)|e'\rangle)/\sqrt{2}. \quad (\text{A3})$$

After the atom's encounter with the second pulse ( $t = 2\tau + T$ ), its quantum state can be written as  $|\psi'\rangle = (1 - \exp(-ikvT))|g'\rangle/2 - i(1 + \exp(-ikvT))|e'\rangle/2$ . In the original bases of  $|g\rangle$  and  $|e\rangle$ , the

final state of the atom at the end of the separated field interaction sequence is given by

$$|\psi\rangle = (1 - \exp(-ikvT)) \exp(-i\omega_g t)|g\rangle/2 - i(1 + \exp(-ikvT)) \exp(-i(\omega_e - kv)t + ikz_{0i})|e\rangle/2. \quad (\text{A4})$$

Now, we consider the same interaction shown in Figure A1(c) in the laboratory frame of reference in which the electric field at any point along the laser's direction of propagation ( $\mathbf{z}$  direction) is given by  $\mathbf{E}(\mathbf{r}, t) = \hat{\mathbf{x}}E_0 \cos(\omega_0 t - kz)$ . Considering that at  $t = 0$ , the atom is positioned at  $z = z_{0i}$ , the Hamiltonian for the first interaction zone is given by  $H_{L1}/\hbar = \omega_g |g\rangle_{LL}\langle g| + \omega_e |e\rangle_{LL}\langle e| + \Omega(\exp(i(\omega_0 t - kz_{0i}))|g\rangle_{LL}\langle e| + h.c.)/2$ , where the subscript  $L$  indicates that this is in the laboratory frame. The state of the atom evolves according to  $i\hbar\partial|\psi\rangle_L/\partial t = H_{L1}|\psi\rangle_L$ . Therefore, the transformation  $Q_1$  to remove time and phase dependence from  $H_{L1}$  is given by  $Q_1 = \exp(i\omega_g t)|1\rangle\langle 1| + \exp(i(\omega_e t - kz_{0i}))|2\rangle\langle 2|$ . The resulting  $Q$ -transformed Hamiltonian in the bases of  $|g'\rangle_L$  and  $|e'\rangle_L$  is  $H'_{L1}/\hbar = (\Omega|g'\rangle_{LL}\langle e'| + h.c.)/2$ . As a result, considering that the atom is in state  $|g'\rangle_L$  at  $t = 0$ , the state of the atom at  $t = \tau$  is  $|\psi'\rangle = (|g'\rangle_L - i|e'\rangle_L)/\sqrt{2}$ .

The dark zone  $Q$ -transformed Hamiltonian,  $H'_{Ld}$ , contains no non-zero elements. Thus, at the end of the dark zone ( $t = \tau + T$ ), the quantum state of the atom remains unaltered. Since the atom has a non-zero velocity,  $v$  along  $\mathbf{z}$  direction, by the end of the dark zone, it will have moved to  $z = z_{0f}$ . As a consequence, the Hamiltonian for the second pulse will be  $H_{L2}/\hbar = \omega_g |g\rangle_{LL}\langle g| + \omega_e |e\rangle_{LL}\langle e| + \Omega(\exp(i(\omega_0 t - kz_{0f}))|g\rangle_{LL}\langle e| + h.c.)/2$ . The  $Q$ -transformation required to make  $H_{L2}$  time and phase factor independent may be written as  $Q_2 = \exp(i\omega_g t)|1\rangle\langle 1| + \exp(i(\omega_e t - kz_{0f}))|2\rangle\langle 2|$  and we define  $|\psi''\rangle_L = Q_2|\psi\rangle_L$ . The new basis states thus formed are  $|g''\rangle_L = \exp(i\omega_g t)|g\rangle_L$  and  $|e''\rangle_L = \exp(i(\omega_e t - kz_{0f}))|e\rangle_L$ . Therefore, the quantum state of the atom at the end of the dark zone ( $t = \tau + T$ ), must now be written in the  $Q_2$ -transformed bases of  $|g''\rangle_L$  and  $|e''\rangle_L$ . As such, we get  $|\psi''\rangle_L = Q_2 Q_1^{-1} |\psi'\rangle_L = (|g''\rangle_L - i \exp(ik(z_{0i} - z_{0f}))|e''\rangle_L)/\sqrt{2}$ . This is the initial condition for the second pulse. At the end of the second pulse,  $t = 2\tau + T$ , the atom's quantum state is, therefore, given by  $|\psi''\rangle_L = (1 - \exp(ik(z_{0i} - z_{0f})))|g''\rangle_L/2 - i(1 + \exp(ik(z_{0i} - z_{0f})))|e''\rangle_L/2$ . Thus, in the original bases of  $|g\rangle_L$  and  $|e\rangle_L$ , the state of the atom is

$$|\psi\rangle_L = (1 - \exp(ik(z_{0i} - z_{0f}))) \exp(-i\omega_g t)|g\rangle_L/2 - i(1 + \exp(ik(z_{0i} - z_{0f}))) \exp(-i\omega_e t + ikz_{0f})|e\rangle_L/2. \quad (\text{A5})$$

Since  $z_{0f} = z_{0i} + vT$ , Equation (A5) is identical to Equation (A4). Thus, when one takes into account the Doppler shift, it is no longer necessary to consider explicitly the fact that the atom sees a different laser phase at different times.

# **$N$ -atom collective-state atomic clock with $\sqrt{N}$ -fold increase in effective frequency and $\sqrt{N}$ -fold reduction in fringe width**

May E. Kim,<sup>1,\*</sup> Resham Sarkar,<sup>1</sup> Renpeng Fang,<sup>1</sup> and Selim M. Shahriar<sup>1,2</sup>

<sup>1</sup>*Department of Physics and Astronomy, Northwestern University, Evanston, Illinois 60208, USA*

<sup>2</sup>*Department of Electrical Engineering and Computer Science, Northwestern University, Evanston, Illinois 60208, USA*

(Received 3 October 2014; revised manuscript received 8 December 2014; published 24 June 2015)

We describe a collective state atomic clock (COSAC) with Ramsey fringes narrowed by a factor of  $\sqrt{N}$  compared to a conventional clock— $N$  being the number of noninteracting atoms—without violating the uncertainty relation. This narrowing is explained as being due to interferences among the collective states, representing an effective  $\sqrt{N}$ -fold increase in the clock frequency, without entanglement. We discuss the experimental inhomogeneities that affect the signal and show that experimental parameters can be adjusted to produce a near ideal signal. The detection process collects fluorescence through stimulated Raman scattering of Stokes photons, which emits photons predominantly in the direction of the probe beam for a high enough optical density. By using a null measurement scheme, in which detection of zero photons corresponds to the system being in a single collective state, we detect the population in a collective state of interest. The quantum and classical noise of the ideal COSAC is still limited by the standard quantum limit and performs only as well as the conventional clock. However, when detection efficiency and collection efficiency are taken into account, the detection scheme of the COSAC increases the quantum efficiency of detection significantly in comparison to a typical conventional clock employing fluorescence detection, yielding a net improvement in stability by as much as a factor of 10.

DOI: [10.1103/PhysRevA.91.063629](https://doi.org/10.1103/PhysRevA.91.063629)

PACS number(s): 03.75.Dg, 06.30.Ft, 32.80.Qk

## I. INTRODUCTION

It is well known that the width of the fringes, observed as a function of the detuning, in a pulsed excitation of an atomic transition, is limited by the inverse of the interaction time. This effect is routinely observed in systems such as microwave or Raman atomic clocks [1–5]. It is also well known that the effective interaction time can be extended by employing Ramsey’s technique of separated field excitations [6]. In that case, the transit time limited linewidth is determined by the inverse of the time delay between the two fields. The temporal profile of the field envelope seen by the atoms is a pair of square pulses, each with a duration  $T_1$ , separated by  $T_2$ . For a conventional clock (CC), the Ramsey technique produces a sync function with a width of  $\sim T_1^{-1}$ , modulated by a sinusoid with a fringe width of  $\sim T_2^{-1}$ , all centered at the carrier frequency.

The width of these fringes can be reduced by making use of entanglement, as demonstrated by Wineland *et al.* using trapped ions [7]. Consider, for example, a situation where the use of entanglement allows one to couple the ground state of three particles to a state where all three particles are in the excited state, representing a collective excitation. This corresponds to an effective increase in the transition frequency by a factor of 3. As such, the detuning for a single atom gets tripled for this collective excitation, so that the width of the Ramsey fringe gets reduced by a factor of 3. However, realizing such a scheme for a large number of particles is beyond the capability of current technology.

Here, we describe a scheme that produces Ramsey fringes that are narrower by a factor of more than  $10^3$  for parameters that are readily accessible, without making use of

entanglement. While the concept can be applied to other types of atomic clocks, as described later, the specific experiment we propose is an optically off-resonant Raman atomic clock using ensembles of  $N$  cold atoms. The clock transition is detected by measuring one of the collective states rather than measuring individual atomic states. The fringes observed as a function of the Raman (i.e., two photon) detuning is found to be  $\sim \sqrt{N}$  times narrower than the transit time limited width that would be seen by measuring individual atomic states, as is the case with the CC. For the current state of the art of trapped atoms, the value of  $N$  can easily exceed  $10^6$ , so that a reduction of fringe width by a factor of more than  $10^3$  is feasible.

The reduction in the width of the fringe, especially by such a large factor, strongly violates the conventional transit time limit of spectroscopic resolution. However, we show, via a detailed analysis of the standard quantum limit and the Heisenberg limit, that, indeed, this violation of the conventional transit-time limit is allowed, and is within the constraint of the more fundamental uncertainty principle of quantum mechanics. We also show that under certain conditions, frequency fluctuation of the collective state atomic clock (COSAC) can be significantly smaller, by as much as a factor of 10, than that for a fluorescence detection based conventional clock employing the same transition and the same atomic flux. The ultranarrow resonances produced in this process may also open up the possibility of exploring novel ways of implementing spin-squeezing techniques for further improvement in clock stability [8–11].

The rest of the paper is organized as follows. In Sec. II, we introduce a single three level atomic system and how it propagates through a Ramsey fringe experiment. In Sec. III, we derive the propagation of a collective state through the same Ramsey fringe experiment, showing mathematically the narrowing of the fringe by  $\sqrt{N}$ . In the subsections, the effects of velocity distribution, field inhomogeneity, spontaneous

\*mekim@u.northwestern.edu

emission, and fluctuation in the number of atoms are discussed. We show that while these effects tend to degrade the signal, these limitations can be circumvented with proper choice of experimental parameters. In Sec. IV, we lay out the scheme for realizing the COSAC experimentally. The detection scheme is fundamentally different from that of the CC since only a single collective state is detected. Because the atoms are in a superposition of collective states at the end of the Ramsey fringe experiment, and the CC detects signal from one level of the (reduced) two level system, such detection scheme collects signal from most of the collective states. In contrast, the heterodyne detection scheme employed for the COSAC ensures that only a single collective state is detected. In Sec. V, the performance of the COSAC is compared to that of the CC by analyzing quantum and classical noise, detector efficiency, and collection efficiency. In Sec. VI, we present the physical interpretation for why the linewidth narrows for a COSAC. We ensure, by proper interpretation of the frequency uncertainty and observation time, that the fundamental quantum limit is not violated. Last, in Sec. VII, we conclude with a summary of the paper.

## II. THREE LEVEL ATOMIC SYSTEM IN RAMSEY FRINGE EXPERIMENT

The optically off-resonant Raman atomic clock employs three hyperfine energy levels in a  $\Lambda$  scheme depicted in Fig. 1(a). The ground states  $|1\rangle$  and  $|2\rangle$  of this atom interact with an excited state  $|3\rangle$  via two coherent electromagnetic light fields of frequencies  $\omega_1$  and  $\omega_2$ , respectively, detuned from resonance by  $\delta_1$  and  $\delta_2$ , respectively. The Hamiltonian after the dipole approximation, rotating wave approximation, and rotating wave transformation can be expressed as [12]

$$H = \frac{\hbar}{2} [(\delta\sigma_{11} - \delta\sigma_{22} - 2\Delta\sigma_{33}) - (\Omega_1\sigma_{13} + \Omega_2\sigma_{23} + \text{H.c.})], \quad (1)$$

where  $\sigma_{\mu\nu} = |\mu\rangle\langle\nu|$ ,  $\delta \equiv \delta_1 - \delta_2$  is the two photon detuning,  $\Delta \equiv (\delta_1 + \delta_2)/2$  is the average detuning, and  $\Omega_{1,2}$  are the Rabi frequencies. Here, we have also assumed a phase transformation applied to the Hamiltonian so that  $\Omega_{1,2}$  are real. We assume next that  $\Delta \gg \Gamma$ ,  $\Omega_1$ , and  $\Omega_2$  (where  $\Gamma$  is the decay rate of state  $|3\rangle$ ) so that the effect of  $\Gamma$  can be neglected, and state  $|3\rangle$  can be eliminated adiabatically [13,14] (in Sec. III, we will consider the residual effect of spontaneous emission). Under these conditions, the Hamiltonian

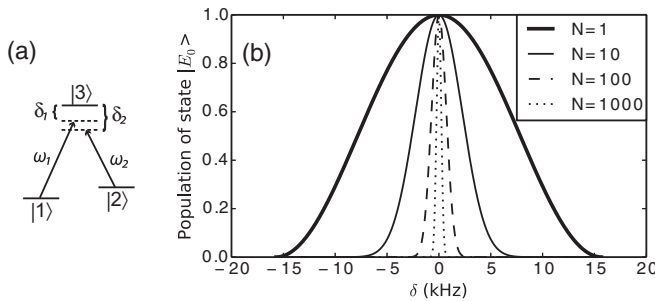


FIG. 1. (a) Three level atomic system. (b) Population of  $|E_N\rangle$  at the end of Ramsey pulse sequence as function of  $\delta$ .

of the reduced two level system can be expressed as  $H_{\text{red}} = (\hbar\delta/2)\sigma_z - (\hbar\Omega/2)\sigma_x$ , where  $\Omega \equiv \Omega_1\Omega_2/2\Delta$  is the Raman Rabi frequency, and  $\sigma_z$  and  $\sigma_x$  are Pauli matrices defined as  $\sigma_z = (\sigma_{11} - \sigma_{22})$  and  $\sigma_x = (\sigma_{12} + \sigma_{21})$ . The quantum state for this system is given by  $|\psi(t' + t)\rangle = W_{\Omega t}^{\delta t}|\psi(t')\rangle$  where  $|\psi(t')\rangle = \tilde{c}_1(t')|1\rangle + \tilde{c}_2(t')|2\rangle$ , and the propagation operator is given by [15]

$$W_{\Omega t}^{\delta t} = e^{i\delta t/2} \begin{pmatrix} \cos \phi - i \frac{\delta}{\Omega'} \sin \phi & -i \frac{\Omega}{\Omega'} \sin \phi \\ -i \frac{\Omega}{\Omega'} \sin \phi & \cos \phi + i \frac{\delta}{\Omega'} \sin \phi \end{pmatrix}, \quad (2)$$

where  $\phi = \Omega't/2$ , and  $\Omega' \equiv \sqrt{\Omega^2 + \delta^2}$  is the generalized Rabi frequency.

When this system is excited by two pulses of duration  $T_1$ , separated in time by  $T_2$ , we have  $\Omega_1(t) \sim \Omega_2(t) = \Omega_0\{U(t) - U(t - T_1) + U[t - (T_1 + T_2)] - U[t - (2T_1 + T_2)]\}$  where  $U(t)$  is the Heaviside step function. When  $\delta \ll \Omega$  and the width of the pulse is chosen to be  $\Omega T_1 = \pi/2$ , each pulse acts on the system as a propagation operator  $W_{\pi/2}^0 = (I - i\sigma_x)/\sqrt{2}$ . While the system is between  $t = T_1$  and  $t = T_1 + T_2$  where no interaction is present, the propagation operator can be expressed as  $W_0^{\delta T_2} = \sigma_{11} + e^{i\delta T_2}\sigma_{22}$ . After passing through the three zones, the state of the atom that was originally in state  $|1\rangle$  is  $|\psi\rangle = W_{\pi/2}^0 W_0^{\delta T_2} W_{\pi/2}^0 |1\rangle = -ie^{i\theta}(\sin \theta |1\rangle + \cos \theta |2\rangle)$  where  $\theta = \delta T_2/2$  is the dephasing angle. The probability of the atom being in state  $|2\rangle$  is  $P_2 \equiv |\langle 2 | \psi \rangle|^2 = (\cos \theta)^2$ .

## III. COLLECTIVE STATE ATOMIC SYSTEM IN RAMSEY FRINGE EXPERIMENT

The discussion can be generalized to  $N$  atoms that are all excited by the same field. We assume that there are no overlaps between the wave functions of the atoms and there is no interaction among them [16]. The evolution of each atom under these assumptions can be described individually, and the total quantum state is simply the outer (tensor) product of individual quantum states [17,18]. However, the interaction can also be described equivalently using a basis of collective states [16,17]. The Hilbert space of  $N$  two level atoms is spanned by  $2^N$  states. Thus, when transformed to the collective state basis, there are also  $2^N$  collective states. For identical Rabi frequencies and resonant frequencies, however, only the generalized symmetric states [17], of which there are only  $(N+1)$ , are relevant, and the rest of the  $(2^N - N - 1)$  states become decoupled. The case where inhomogeneity of the Rabi frequencies and different Doppler shifts experienced by different atoms are taken into account is presented at the end of this section. We also note that if different atoms see different phase factors from the excitation fields, these factors can be absorbed into the definition of the generalized symmetric states [17]. The simplified symmetric states, known as the conventional Dicke states [16], represent the case where it is assumed that the mean separation between the atoms is much less than the wavelength corresponding to the two level transition [which, for the copropagating off resonant Raman excitation, is  $\sim(k_1 - k_2)^{-1}$ ]. While this constraint is not necessary for the concept proposed here [17], it is easier to describe the process initially under this constraint. The observables computed remain correct when this constraint is not met. Some of these Dicke states are as follows:  $|E_0\rangle \equiv |111 \dots 1\rangle$ ,

$|E_1\rangle \equiv \sum_{i=1} |11 \dots 2_i \dots 1\rangle / \sqrt{N}$ ,  $|E_2\rangle \equiv \sum_{i,j \neq i} |11 \dots 2_i \dots 2_j \dots 1\rangle / \sqrt{^N C_2}$ ,  $|E_3\rangle \equiv \sum_{i,j,k} |11 \dots 2_i \dots 2_j \dots 2_k \dots 1\rangle / \sqrt{^N C_3}$ , and  $|E_N\rangle \equiv |222 \dots 2\rangle$  where  $^N C_n = N! / n!(N-n)!$ . For instance,  $|E_2\rangle$  is the Dicke state with two atoms in  $|2\rangle$  and the rest in  $|1\rangle$ . Any two atoms can be in  $|2\rangle$  with equal probability, with  $^N C_2 = N(N-1)/2$  such possible combinations.

The Hamiltonian in the basis of the symmetric collective states is  $H = \sum_{k=0}^N [-k\hbar\delta|E_k\rangle\langle E_k|] + \sum_{k=0}^{N-1} [(\hbar\Omega_{k+1}|E_k\rangle\langle E_{k+1}| + \text{H.c.})]$  where  $\Omega_{k+1} = \sqrt{N-k}$   $\sqrt{k+1}\Omega$  is the Rabi frequency between collective states [16,17]. The states are separated by  $\hbar\delta$  in energy and couple at different rates. For instance,  $\Omega_1 = \Omega_N = \sqrt{N}\Omega$ ,  $\Omega_2 = \Omega_{N-1} = \sqrt{2(N-1)}\Omega$ , etc. The middle states have the strongest coupling rate of  $\Omega_{N/2} = N\Omega$  and the end states couple most weakly.

The final state of the system at the end of the second  $\pi/2$  pulse can be derived by using either the collective state picture or, equivalently, the single atom picture. For a large value of  $N$ , carrying out the calculation in the collective states basis is numerically cumbersome and analytically intractable. However, we can find the state trivially by using the single atom picture and then determining the coefficients of the collective states by simple projection, given the definition of the  $(N+1)$  generalized symmetric collective states. As such, the final state of the system is  $|\psi\rangle = \prod_{i=1}^N (W_{\pi/2}^0 W_0^{\delta T_2} W_{\pi/2}^0)_i |1\rangle_i$ . In the basis of the generalized symmetric collective states, this becomes

$$|\psi\rangle = (-ie^{i\theta})^N \sum_{k=0}^N \sqrt{^N C_k} (\sin \theta)^{N-k} (\cos \theta)^k |\tilde{E}_k\rangle. \quad (3)$$

The population of the state  $|\tilde{E}_N\rangle$  at the end of the separated field experiment is

$$P_N^C \equiv |\langle \tilde{E}_N | \psi \rangle|^2 = (\cos \theta)^{2N}, \quad (4)$$

which is simply  $(P_2)^N$ . This quantity,  $P_N^C$ , represents the probability of finding the whole system in the state  $|E_N\rangle$  whereas  $P_2$  represents the probability of finding each atom in state  $|2\rangle$ . In a conventional experiment, the population of atoms in state  $|2\rangle$  is measured, for example, by collecting fluorescence produced by coupling  $|2\rangle$  to an auxiliary state. The resulting signal is proportional to  $P_2$ , independent of the number of atoms. The experiment that we propose, to be described shortly, produces a signal that is proportional to  $P_N^C$ . When Eq. (4) is plotted for various values of  $N$  [Fig. 1 (b)], it is evident that the linewidth of the fringe as a function of  $\theta$  decreases as  $N$  increases. The value of the linewidth, defined as the full width half maximum (FWHM), is given by  $\Gamma(N) = 2 \arccos(2^{-1/2N})$ . The derivative of  $[\Gamma(1)/\Gamma(N)]^2$  with respect to  $N$ , for large  $N$ , approaches the value of  $0.8899 + O(N^{-3/2})$ , which we have verified with a linear fit to  $[\Gamma(1)/\Gamma(N)]^2$ . To a good approximation,  $\Gamma(N)/\Gamma(1) \approx 1/\sqrt{N}$ . Noting that  $\theta = \delta T_2/2$ ,  $\Gamma(1) \simeq \pi/T_2$  is understood to be the transit time limited linewidth. Then  $\Gamma(N) = \Gamma(1)/\sqrt{N} = \pi/(T_2\sqrt{N})$  is a violation of the transit time limit, which is discussed in Sec. VI, along with the physical interpretation of what occurs in the collective atomic clock system.

### A. Effect of velocity distribution

A two level atomic system  $|\psi\rangle$  interacts with light fields and evolves as  $|\psi(t'+t)\rangle = W_{\Omega t}^{\delta t} |\psi(t')\rangle$ . The two levels in the proposed scheme are, for example, the hyperfine ground states of an alkali-metal atom such as  $^{85}\text{Rb}$ . After the  $\pi/2$ -dark- $\pi/2$  sequence, the system is in state  $|\psi\rangle = W_{\pi/2}^{\delta T_2} W_0^{\delta T_2} W_{\pi/2}^{\delta T_2} |1\rangle$ . Unlike in Sec. II, we here do not make the approximation that  $\delta \ll \Omega$ . Then the signal we expect to see for a single atom is proportional to  $P_2 = |\langle 2 | \psi \rangle|^2 = |\langle 2 | W_{\pi/2}^{\delta T_2} W_0^{\delta T_2} W_{\pi/2}^{\delta T_2} | 1 \rangle|^2$ , and the collective state signal is

$$S_{\text{col}} = \prod_{i=1}^N |\langle 2 | W_{\pi/2}^{\delta T_2} W_0^{\delta T_2} W_{\pi/2}^{\delta T_2} | 1 \rangle|^2 = |\langle 2 | W_{\pi/2}^{\delta T_2} W_0^{\delta T_2} W_{\pi/2}^{\delta T_2} | 1 \rangle|^{2N}. \quad (5)$$

We assume that the density of atoms in the trap is fixed at  $\rho_A = 10^9 \text{ mm}^{-3}$ , so that the width of the atomic ensemble, which has a Gaussian spatial distribution, varies with the number of atoms. With  $N = 2 \times 10^6$  atoms in the trap, the size of the cigar-shaped ensemble is 1 mm in length in the direction of the Raman beams, and  $\sim 50 \mu\text{m}$  in diameter in the other two directions.

When an atom with velocity  $v$  interacts with a field with frequency  $\omega$  propagating in the direction of the atom, the frequency of the field is shifted by  $\delta_D = v\omega/c$ . The Maxwell Boltzmann velocity distribution is  $\rho_{MB}(v, T) = \sqrt{m_a/(2\pi kT)} \exp^{-m_a v^2/(2kT)}$  where  $m_a$  is the atomic mass and  $T$  is the temperature. We assume the temperature to be given by the Doppler cooling limit, so that  $T_{\text{MOT}} = \Gamma_{Rb}\hbar/(2k) = 138 \mu\text{K}$  for  $^{87}\text{Rb}$ . The average velocity is then  $v_{av} \sim 18.3 \text{ cm/s}$ , with a corresponding Doppler shift of  $\delta_{Dav} = 4.18 \text{ Hz}$ . Under these conditions, the signal is

$$S_{\text{Dop}} = \prod_{v'=-5v_{av}}^{5v_{av}} |\langle 2 | W_{\pi/2}^{[\delta+\delta_D(v')]T_2} W_0^{[\delta+\delta_D(v')]T_2} \times W_{\pi/2}^{[\delta+\delta_D(v')]T_2} | 1 \rangle|^{[2\rho_{MB}(v', T_{\text{MOT}})]}, \quad (6)$$

where we take into account velocities that are up to five times the  $v_{av}$ . Plotted in Fig. 2 are the signals  $S_{\text{col}}$  and  $S_{\text{Dop}}$  for various  $N$  values, with  $T_2 = 3 \times 10^{-5} \text{ s}$  and  $\Omega = 5 \times 10^6 \text{ s}^{-1}$ . The Doppler effect decreases the overall signal while having virtually no effect on its width. It decreases exponentially as  $N$  increases. However, for the given choice of temperature and  $N = 2 \times 10^6$ , the reduced signal is  $S_{\text{Dop}} \sim 0.9 S_{\text{col}}$ . Of course, the signal can be improved if the temperature is reduced below the Doppler cooling limit.

### B. Effect of field inhomogeneity

Consider next the effect of the inhomogeneity in the laser field amplitude. We assume that the atomic ensemble has a Gaussian spread with a width of  $\omega_A$ :  $\rho_N(\gamma) = \rho_0 e^{-(\gamma^2/\omega_A^2)}$ . The width considered in this section is in the direction perpendicular to the propagation direction of the Raman beams, since the atoms spread in the propagation direction of the beams see the same fields. Each of the two laser fields that produce the Raman-Rabi excitation is also assumed to have a Gaussian profile with a width of  $\omega_L > \omega_A$ . Since the Raman-Rabi frequency is proportional to the product of the Rabi frequencies for each of these lasers, it follows that the Raman-Rabi frequency is also a Gaussian with a width of

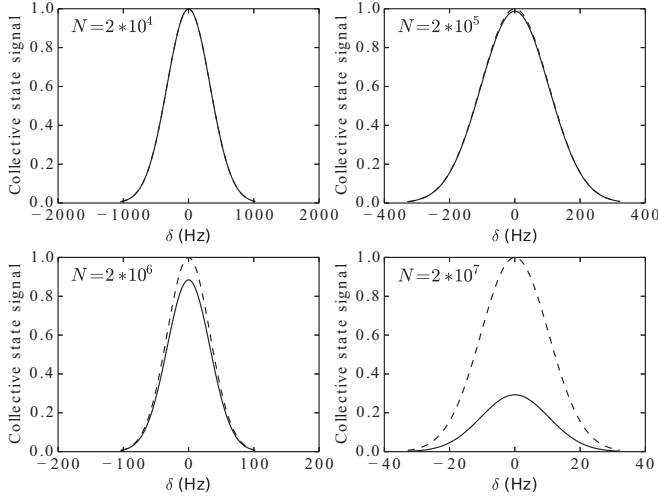


FIG. 2. Collective state signal at the end of the Ramsey field experiment for various numbers of atoms, with parameters  $\Omega = 5 \times 10^5 \text{ s}^{-1}$  and  $T_2 = 3 \times 10^{-5} \text{ s}$ . Plotted are the ideal signal (dashed line)  $S_{\text{col}}$  and the reduced signal (solid line)  $S_{\text{Dop}}$ , where the effect of Doppler shift is taken into account.

$\omega_L$ :  $\Omega(\gamma) = \Omega_0 e^{-(\gamma^2/\omega_L^2)}$ . The peak value of  $\Omega$  (i.e.,  $\Omega_0$ ) is chosen so that the atoms at the center ( $r = 0$ ) experience a perfect  $\pi/2$  pulse for an interaction time of  $T_1$ . Ignoring the effect of the Doppler spread in the velocity, the COSAC signal is then given by

$$S_{\Omega} = \Pi_{r=-w_{rb}}^{w_{rb}} |\langle 2 | W_{\Omega(r)T_1}^{\delta T_2} W_0^{\delta T_2} W_{\Omega(r)T_1}^{\delta T_2} | 1 \rangle|^{2\rho_N(r)}. \quad (7)$$

The signals for various ratios of  $w_L/w_A$  are plotted in Fig. 3 for  $N = 2 \times 10^6$  and density of  $\rho_A = 10^9 \text{ mm}^{-3}$ . The signal affected by the inhomogeneous fields can reach the peak value

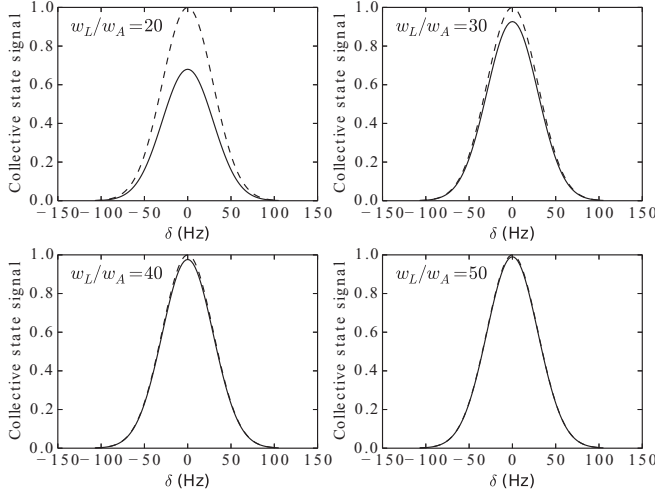


FIG. 3. Collective state signal at the end of the Ramsey field experiment for various Gaussian beam widths.  $N = 2 \times 10^6$  atoms;  $\Omega = 5 \times 10^5 \text{ s}^{-1}$ ;  $T_2 = 3 \times 10^{-5} \text{ s}$ . Plotted are the ideal signal (dashed line)  $S_{\text{col}}$  and the reduced signal (solid line)  $S_{\Omega}$ , when the Gaussian nature of the beam is taken into account. The plots are for various ratios of the widths of the laser field to the atomic ensemble:  $w_L/w_A$ .

of the ideal signal when  $\omega_L/\omega_A = 50$ . Since  $w_A = 50 \mu\text{m}$  in our system,  $w_L = 2.5 \text{ mm}$  for the Raman beams is sufficiently large enough to achieve this goal.

### C. Effect of spontaneous emission

In the analysis of the COSAC, we have used a model in which the intermediate state is adiabatically eliminated. However, the actual population of this state is approximately  $\Omega_1^2/\Delta^2$  with  $\Omega_1 \sim \Omega_2$ . In the time that it takes for a  $\pi = \Omega/T_1 \simeq \Omega_1^2/(2\Delta T_1)$  pulse (or two  $\pi/2$  pulses) to occur, we can estimate that the number of spontaneous emissions that occur per atom is  $(\Omega_1^2/\Delta^2)\Gamma T_1 \simeq 2\pi\Gamma/\Delta$ . For  $\Delta = 200\Gamma$ , this, number is about  $3 \times 10^{-2}$ , and increases by a factor of  $N$  for an ensemble of  $N$  atoms. (Note that there is no enhancement of the rate of spontaneous emission due to superradiant effects, since we are considering a dilute ensemble). As a result, the signal for both the CC and the COSAC would deviate from the ideal one. The actual effect of spontaneous emission on the CC can be taken into account by using the density matrix equation for a three level system. However, in this case, it is not possible to ascribe a well defined quantum state for each atom. This, in turn, makes it impossible to figure out the response of the COSAC, since our analysis for the COSAC is based on using the direct product of the quantum state of each atom. For a large value of  $N$ , it is virtually impossible to develop a manageable density matrix description of the system directly in terms of the collective states. However, it should be possible to evaluate the results of such a density matrix based model for a small value of  $N$  ( $< 10$ , for example). In the near future, we will carry out such a calculation and report the findings.

For the general case of large  $N$ , one must rely on an experiment (which, in this context, can be viewed as an analog computer for simulating this problem) to determine the degree of degradation expected from residual spontaneous emission. It should be noted that the deleterious effect of spontaneous emission, for both the CC and the COSAC, can be suppressed to a large degree by simply increasing the optical detuning while also increasing the laser power. This is the approach used, for example, in reducing the effect of radiation loss of atoms in a far off resonant trap (FORT).

### D. Effect of fluctuation in number of atoms

For both the CC and the COSAC, the signal is collected multiple times and averaged to increase the signal to noise ratio (SNR). However, the number of atoms can fluctuate from shot to shot. When  $N$  fluctuates by  $\Delta N$ , the signal in the CC changes by the same amount while the linewidth does not change. It is easy to see this from the classical signal,  $S_{\text{CC}} = N \cos^2 \theta$ . Changing  $N$  by  $\Delta N$  will change the signal, but the FWHM, which occurs at  $S_{\text{CC}} = N/2$ , will not change. A more thorough approach for expressing the classical and quantum noise of the CC and the COSAC is covered in Sec. V A. In this section, we focus on how the fluctuation in the number of atoms from shot to shot affects the signal of the COSAC.

Figure 4 (left) is the plot of a collective signal with  $N = 2 \times 10^6$ . The dashed red lines represent the case in which  $\Delta N/N = 0.01$ . Increasing the number of atoms by  $\Delta N$  decreases the linewidth, and decreasing the number of atoms by  $\Delta N$  increases the linewidth. However, the peak

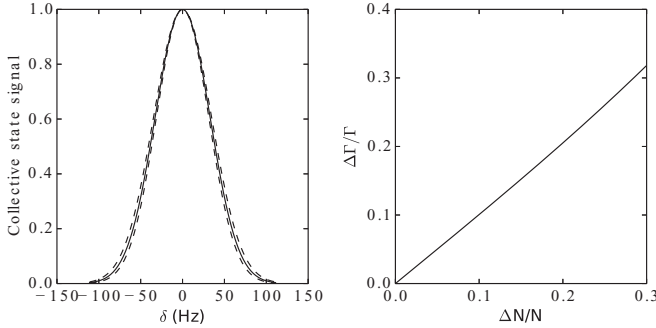


FIG. 4. (left) Collective state signal (solid line) at the end of the Ramsey field experiment for  $N = 2 \times 10^6$  atoms;  $\Omega = 5 \times 10^6 \text{ s}^{-1}$ ;  $T = 3 \times 10^{-5} \text{ s}$ . The dashed curves show the signal for  $N + \Delta N$  (narrower) and  $N - \Delta N$  (wider), where  $\Delta N/N = 0.01$ . (right) Plot of  $\Delta\Gamma/\Gamma$  as a function of  $\Delta N/N$ .

of the signal remains at unity. This is in contrast to the results from velocity distribution and field inhomogeneity. We calculate the change in the COSAC linewidth by noting that its FWHM is approximately  $\Gamma(N) = \Gamma(1)/\sqrt{N}$ . The width of the uncertainty in  $\Gamma(N)$ , as a result of fluctuation in  $N$ , is  $\Delta\Gamma(N) = \Gamma(1)/\sqrt{N - \Delta N} - \Gamma(1)/\sqrt{N + \Delta N}$ , so that the fractional fluctuation is  $\Delta\Gamma(N)/\Gamma(N) = (1 - \Delta N/N)^{-1/2} - (1 + \Delta N/N)^{-1/2} = \Delta N/N + 0.625(\Delta N/N)^3 + O[(\Delta N/N)^7]$ . For small  $\Delta N/N$ , the fractional change in FWHM is  $\Delta\Gamma(N)/\Gamma(N) \simeq \Delta N/N$  to a good approximation. Figure 4 (right) shows this correspondence for  $N = 2 \times 10^6$ . However, the plot is equivalent for any  $N$ , since the fractional change in FWHM is only dependent on  $\Delta N/N$ .

#### IV. EXPERIMENT AND DETECTION SCHEME FOR REALIZING A COSAC

Before proceeding further, we describe the experimental approach that can be used to measure  $P_N^C$ , as summarized in Fig. 5. For concreteness, and without loss of generality, we consider  $^{87}\text{Rb}$  as the atomic species. By making use of the necessary  $D2$  line transitions, we start by trapping atoms in a magneto-optical trap (MOT), and transferring them into a more localized dipole trap, cooled down to the Doppler cooling limit of  $T_D = \hbar\Gamma/(2k_B) = 138 \mu\text{K}$  [19–22]. After capturing about  $2 \times 10^6$  atoms in a cigar-shaped cloud with a diameter of  $\sim w_A = 50 \mu\text{m}$  and length of 1 mm, the atoms are released and optically pumped into the  $|F = 1\rangle$  state by applying a beam that is resonant with the  $5^2S_{1/2}, |F = 2\rangle \rightarrow 5^2P_{3/2}, |F' = 2\rangle$  transition of the rubidium  $D2$  line. Furthermore, a  $\pi$  polarized beam that is resonant with the  $5^2S_{1/2}, |F = 1\rangle \rightarrow 5^2P_{1/2}, |F' = 1\rangle$  transition of the rubidium  $D1$  line is applied, as depicted in Fig. 6. Because the  $|F = 1, m_F = 0\rangle \rightarrow |F' = 1, m_{F'} = 0\rangle$  transition is forbidden for the  $D1$  line, the atoms will finally be pumped into the  $|F = 1, m_F = 0\rangle$  level. It is possible, with the imperfections that are inadvertently present in the system, that there might be some residual atoms left in  $|F = 1, m_F = -1\rangle$  and  $|F = 1, m_F = 1\rangle$ . We avoid the detection of these residual atoms by making use of the fact that the Zeeman shifts of levels in  $|F = 1\rangle$  and  $|F = 2\rangle$  are in opposite directions, which will be discussed in more detail after we outline the null measurement

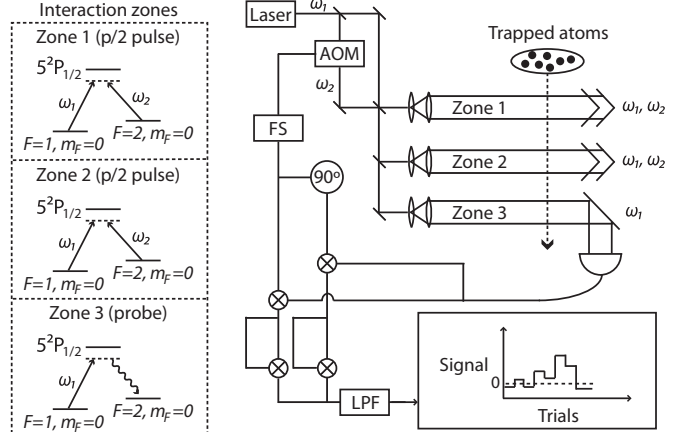


FIG. 5. Ramsey fringe experiment for an ensemble of  $\Lambda$ -type atoms for the detection of collective state  $|E_N\rangle$ . Atoms are released from the trap, and the experiment is performed while they are free falling inside the vacuum chamber. They interact with two  $\pi/2$  Ramsey pulses, which are separated in time by  $T_2$ , and are probed by a probe. The probe induces a unidirectional Raman transition in the atoms while producing Stokes photons in the direction of the detector, given high enough optical density. The combined signal from the probe and emitted Stokes photons are multiplied with the frequency produced by the FS in such a way that the resulting signal will be proportional to the number of Stokes photons detected. Determining the threshold of the zero emission signal, and counting how many trials result in zero emission, the histogram can be built to produce signal in Fig. 1(b).

scheme. Once the initialization of atoms into the  $|F = 1, m_F = 0\rangle$  state is complete, a bias magnetic field of  $\sim 2 \text{ G}$ , generated with a pair of Helmholtz coils, is turned on in the  $\hat{z}$  direction. While the atoms are in free fall, we turn on a pair of copropagating right circularly polarized ( $\sigma_+$ ) Raman beams in the  $\hat{z}$  direction. One of these beams is tuned to be  $\sim 3.417 \text{ GHz}$  red detuned from the  $|F = 1\rangle \rightarrow |F' = 1\rangle$  transition ( $D1$  manifold), and the other is tuned to be  $\sim 3.417 \text{ GHz}$  red detuned from the  $|F = 2\rangle \rightarrow |F' = 1\rangle$  transition ( $D1$  manifold). The second Raman beam is generated from the first one via an acousto-optic modulator (AOM), for example. The AOM is driven by a highly stable frequency synthesizer (FS), which is tuned close to  $\sim 6.835 \text{ GHz}$  corresponding to the

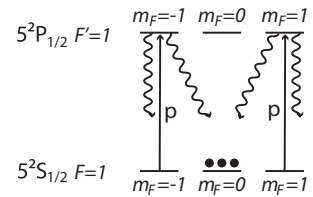


FIG. 6. Initialization of the system involves first optically pumping the atoms into  $|F = 1\rangle$  state by applying a laser field that is resonant with  $5^2S_{1/2}, |F = 2\rangle \rightarrow 5^2P_{3/2}, |F' = 2\rangle$  transition. Afterwards, as is depicted here, a  $\pi$  polarized beam that is resonant with  $5^2S_{1/2}, |F = 1\rangle \rightarrow 5^2P_{1/2}, |F' = 1\rangle$  transition is applied. Because the  $|F = 1, m_F = 0\rangle \rightarrow |F' = 1, m_{F'} = 0\rangle$  transition is forbidden for the  $D1$  line, the atoms are eventually pumped into  $|F = 1, m_F = 0\rangle$ .

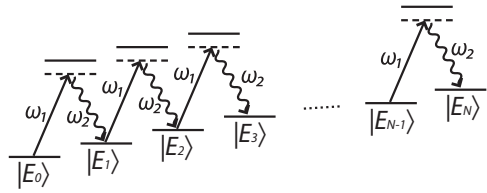


FIG. 7. In the detection zone, we probe the population of state  $|E_N\rangle$  by applying field  $\omega_1$  and detecting Stokes photons produced during the Raman transition. In the bad cavity limit, the atomic system will not reabsorb the photon that has been emitted during the Raman process, such that the transition from  $|E_k\rangle$  to  $|E_{k+1}\rangle$  will occur, but not vice versa.

frequency difference between the  $|F = 1\rangle$  and  $|F = 2\rangle$  states in the  $5^2S_{1/2}$  manifold.

These beams excite off-resonant Raman transitions between  $|F = 1, m_F = m\rangle$  and  $|F = 2, m_F = m\rangle$  levels, for  $m = 1, 0, -1$ . Since the system is initialized in  $|F = 1, m_F = 0\rangle$ , the  $\sigma_+$  Raman transitions through the excited states  $|F' = 1, m_{F'} = 1\rangle$  and  $|F' = 2, m_{F'} = 1\rangle$  couple the initial state to  $|F = 2, m_F = 0\rangle$ . Hence, the energy levels  $|1\rangle$  and  $|2\rangle$  from the previously discussed  $\Lambda$  scheme correspond to hyperfine ground states  $|F = 1, m_F = 0\rangle$  and  $|F = 2, m_F = 0\rangle$ , respectively. The resulting four level system, with the two excited states, can be reduced to a two level system in the same manner as the  $\Lambda$  system by adiabatically eliminating the excited states together. The resulting two level system has a coupling rate that is the sum of the two Raman Rabi frequencies, one involving the  $|F' = 1, m_{F'} = 1\rangle$  state, and the other involving the  $|F' = 2, m_{F'} = 1\rangle$  state. The laser power at  $\omega_1$  and  $\omega_2$  are adjusted to ensure that the light shifts of levels  $|1\rangle$  and  $|2\rangle$  are matched.

In the first interaction zone, the copropagating Raman beams interact with the atomic ensemble for a duration of  $\Omega T_1 = \pi/2$ . After waiting for a time  $T_2$ , chosen such that  $T_2 \gg T_1$ , we pulse the Raman beams again, in place, to interact with the atomic ensemble for another duration  $\Omega T_1 = \pi/2$ . The Raman beams can be pulsed in place as long as the width of the beams is much larger than that of the free-falling, thermally expanding atomic cloud.

After these excitations, we probe the population in one of the collective states,  $|E_N\rangle$ , where all the individual atoms are in state  $|2\rangle$ , by a method of zero photon detection. For illustrative purposes, let us consider first a situation where the atomic ensemble is contained in a single mode cavity with mode volume  $V$ , cavity decay rate  $\gamma_c$ , and wave vector  $k_2 = \omega_2/c$ . The cavity is coupled to the atomic transition  $|2\rangle \rightarrow |3\rangle$  with coupling rate  $g_c = |e\langle r\rangle|E/\hbar$ , where  $|e\langle r\rangle|$  is the dipole moment of the atom and the field of the cavity is  $E = \sqrt{2\hbar\omega_2/(\epsilon_0 V)}$ . If we then send a probe beam, an off-resonant classical laser pulse with frequency  $\omega_1$ , the presence of the cavity will allow Raman transitions to occur between the collective states  $|E_k\rangle$  and  $|E_{k+1}\rangle$  with the coupling rates  $\Omega'_{k+1} = \sqrt{N - k}\sqrt{k + 1}\Omega'$  where  $\Omega' = \Omega_1 g_c/2\Delta$ . The schematic of the interaction is shown in Fig. 7.

In the bad cavity limit where  $\gamma_c \gg \sqrt{N}\Omega'$ , the Raman transitions will still occur. However, the atomic system will not reabsorb the photon that has been emitted during the

process, such that the transition from  $|E_k\rangle$  to  $|E_{k+1}\rangle$  will occur, but not vice versa. The electric field of such a photon is  $E = \sqrt{2\hbar\omega_2/(\epsilon_0 A c \tau)}$ , where  $A$  is the cross sectional area of the atomic ensemble,  $c$  is the speed of light, and  $\tau$  is the duration of the photon. This limit applies in our case, which has no cavity. In this limit, the stimulated Raman scattering is an irreversible process that can be modeled as a decay with an effective decay rate that is singular to each  $|E_j\rangle$  state. The decay rate from state  $|E_1\rangle$  is  $\gamma_0 = 4NL|g_c\Omega_1|^2/(\Delta^2 c) = N\gamma_{sa}$  where  $\gamma_{sa} = 16L\Omega^2/c$  [23] is the decay rate for a single atom. The value of  $g_c$  is given by  $|e\langle r\rangle|E$ . The effective decay rates for the other states can be calculated following the same logic as  $\gamma_j = (j + 1)(N - j)\gamma_{sa}$ .

When photons are scattered through stimulated Raman scattering in the detection process, the resonant optical density (OD) determines the degree to which the emission occurs in the direction of propagation of the probe beam [23]. Specifically, the fraction of photons that are not emitted in the direction of the probe is given by  $1/\text{OD}$ . Thus,  $(1 - 1/\text{OD})$  determines the effective collection efficiency of the detection process. The OD depends on the density of atoms  $n$ , the diameter of the atomic ensemble  $w_A$ , and the resonant scattering cross section  $\sigma \simeq (\lambda/2)^2$ , as  $\rho = \sigma n L$ . For the rubidium-87  $D1$  line wavelength,  $\lambda \sim 795$  nm, and a cigar-shaped trap with  $N = 2 \times 10^6$  atoms, a diameter of  $50 \mu\text{m}$ , and a length of 1 mm, we find that the resonant optical density is  $\rho \sim 300$ . The beam consisting of the probe and the emitted photons is sent to a high speed detector, which produces a dc voltage as well as a signal at the beat frequency of  $\sim 6.835$  GHz. The phase of this beat frequency signal is unknown. As such, the total signal is sent in two different paths, one to be multiplied by the FS signal and another to be multiplied by the FS signal shifted in phase by  $90^\circ$ . Each of these signals is squared, then combined and sent through a low pass filter (LPF) to extract the dc voltage that is proportional to the number of scattered photons. A voltage reading above a predetermined threshold value will indicate the presence of emitted photons during the interrogation period. The interrogation period is set to  $\gamma_0 T = 10$  where  $\gamma_0 = \gamma_{N-1} = N\gamma_{sa}$  is the slowest decay rate, to ensure that even the longest lived state has a chance to decay almost completely. If no photon emission occurs and the voltage reads below the threshold, this indicates that the atoms are all in  $|2\rangle$  and the collective state of the system is  $|E_N\rangle$ . For any other collective state, at least one photon will be emitted. For a given value of  $\delta$ , this process is repeated  $m$  times (where the choice of  $m$  would depend on the temporal granularity of interest). The fraction of events corresponding to detection of no photons would represent the signal for this value of  $\delta$ . The process is now repeated for a different value of  $\delta$ , thus enabling one to produce the clock signal as a function of  $\delta$ . Usual techniques of modulating the detuning and demodulating the signal can be used to produce the error signal for stabilizing the FS, thus realizing the COSAC.

As noted earlier, it is possible that a small fraction of the detected signal might be due to the residual atoms that were not optically pumped to  $|F = 1, m_F = 0\rangle$  initially. The  $\sigma_+$  polarized Raman probe is applied to the  $|F = 1\rangle$  level, and the residual atoms in  $|F = 1, m_F = -1\rangle$  and  $|F = 1, m_F = 1\rangle$  can also see the excitation. However, the bias magnetic field of 2 G lifts the degeneracy of the energy

levels. Moreover, since  $g_F = -1/2$  for  $|F = 1\rangle$  and  $g_F = 1/2$  for  $|F = 2\rangle$ , the energy levels shift in opposite directions such that the Raman signals for the transitions involving  $m_F = -1$  and  $m_F = 1$  are detuned from resonance. Each will be shifted by  $\delta_z = -m(g_{F=2} - g_{F=1})\mu_B B/\hbar = -1.4$  (MHz/G) $m_F B$  where  $B = 2$  G. Therefore, these transitions will not be a part of the detection, which only involves looking at 6.835-GHz beat frequency between the probe and the spontaneously generated photon.

In the particular implementation of the COSAC considered here, we have used off-resonant Raman transition. However, effects such as residual light shifts can limit the stability of such a clock. The ground states can also be coupled directly by using a microwave pulse, which has the advantage of being free from differential light shifts. Thus, the COSAC can also be realized by using a traveling-wave microwave pulse sequence for the separated Ramsey field experiment [24], as long as the detection pulse remains the same. Since the Hamiltonian for light-shift balanced off-resonant Raman excitation, with the excited state eliminated adiabatically, is formally identical to that of microwave excitation [12], the basic behavior of the COSAC would be identical for a microwave version.

## V. PERFORMANCE OF THE COSAC COMPARED TO THAT OF THE CC

In order to compare the performance of the COSAC to that of the comparable CC, we examine the stability of the clocks by investigating the fluctuation that has both quantum-mechanical and classical components, or  $\delta f|_{\text{total}} = (\Delta S_{\text{QM}} + \Delta S_{\text{class}})/(\partial S/\partial f)$ , where  $S(f)$  is the signal and  $f$  is the detuning of the clock away from its center value. Because the signal depends on the frequency, the fluctuations in a clock are not necessarily constant, and there is not a single value of the SNR to compare unless we compare the two clocks at a particular value of the frequency. Instead, the fluctuations must be compared as a function of  $f$  for completeness. In this section, we discuss the quantum fluctuation due to quantum projection noise,  $\Delta P = \sqrt{P(1 - P)}$  [8], where  $P$  is the population of the state to be measured, the classical noise in the long term regime, and the effects of detector efficiency and the collection efficiency. The ratios of the frequency fluctuations in the CC to the frequency fluctuations in the COSAC show that the two clocks perform comparably around the signal at  $f = 0$  if the clocks have perfect collection efficiency. However, the traditional fluorescence detection based clock suffers from collection efficiency issues that the collective clock is immune to. For the CC, a resonant beam probes the clock state, generating spontaneously emitted photons. The collection efficiency of such a system is limited by the solid angle of the detection system. On the other hand, the COSAC collects the fluorescence of photons through coherent Raman scattering, which enables large collection efficiency that can be close to unity for sufficiently high resonant optical density (as noted earlier). As such, for the same number of atoms detected per unit time, the COSAC is expected to perform better than the fluorescence detection based CC by as much as a factor of 10. This is discussed in greater detail in Sec. V C.

### A. Effects of quantum and classical noise

In order for the COSAC to be useful, it must perform at least as well as, or better than, the CC, and for that, we must compare the two clocks' stability in the short term and the long term regimes. The stability of a clock can be measured by investigating the frequency fluctuation that has both quantum-mechanical and classical components. Before comparing the stabilities of the COSAC and the CC, it is instructive first to review briefly the stability of a CC.

For concreteness, we consider an off-resonant Raman-Ramsey clock as the CC. The population of the detected state  $|2\rangle$  at the end of the second pulse is given by  $P_2 = \cos^2(fT_2/2)$ , where  $T_2$  is the separation period of the two  $\pi/2$  pulses and  $f$  is the deviation of the clock frequency away from its ideal value, expressed in radial units (i.e., rad/s rather than Hz). The signal is detected by probing the desired state for a duration of time. If  $\tilde{N}$  is the number of atoms per unit time and  $\tau$  is the interrogation period, the net signal is  $S_{\text{sa}} = \tilde{N}\tau P_2 = \tilde{N}\tau \cos^2(fT_2/2)$ . For the sake of comparison, we allow the number of atoms per trial in the COSAC signal,  $N$ , multiplied by the number of trials  $m$ , to equal  $\tilde{N}\tau$ . Therefore, we can write  $S_{\text{sa}} = mN \cos^2(fT_2/2)$ . The quantum-mechanical variance of this quantity is  $\Delta S_{\text{QM,sa}} = (\sqrt{mN}/2) \sin(fT_2)$ , where the derivation is made by noting that the fluctuations in  $mN$  is  $\sqrt{mN}$  [8], and the projection noise in a single two level atomic system is  $\Delta P_2 = \sqrt{P_2(1 - P_2)}$  [8]. (It should be noted that the fluctuation in  $mN$  is also a manifestation of this projection noise, as discussed in detail in [8].) When the probability of finding the population in this state is unity or nil, the projection noise vanishes; on the other hand, it is largest at  $P_2 = 1/2$ . Calculating the slope from the signal, we find that  $\partial S_{\text{sa}}/\partial f = -[mN/(2\gamma_{\text{sa}})] \sin(fT_2)$ , where  $\gamma_{\text{sa}} = 1/T_2$  is the linewidth.

Assuming perfect quantum efficiency for the detection process, the frequency fluctuation can be written as  $\delta f|_{\text{total}} = |(\Delta S_{\text{QM}} + \Delta S_{\text{class}})/(\partial S/\partial f)|$ , which can be regarded as noise ( $\Delta S$ ), both quantum and classical, over the spectral variation of signal ( $\partial S/\partial f$ ), or SVS. In what follows, we consider first the effect of quantum noise only. Thus, the quantum frequency fluctuation (QFF) for a CC can be expressed as

$$\delta f_{\text{QM,CC}} \equiv \left| \frac{\Delta S_{\text{QM,sa}}}{(\partial S_{\text{sa}}/\partial f)} \right| = \frac{\gamma_{\text{sa}}}{\sqrt{mN}}. \quad (8)$$

It should be noted that while both  $\Delta S_{\text{QM}}$  and  $(\partial S/\partial f)$  depend on  $f$ , their ratio is a constant, which is merely an accident due to the fact that the signal is sinusoidal. However, this accidental cancellation has led to an apparently simple perception of the QFF as being simply the ratio of the linewidth ( $\gamma_{\text{sa}}$ ) to the SNR, where the SNR is understood to be  $\sqrt{mN}$ . This expression for the SNR, in turn, follows from thinking about the signal as being  $S' = mN$  and noise  $N'$  as being  $\sqrt{mN}$ , so that  $\text{SNR} \equiv S'/N' = \sqrt{mN}$ . However, it should be clear from the discussion above that the signal is not given by  $mN$ , and noise is not given by  $\sqrt{mN}$ ; rather, they both depend on  $f$ .

In cases where frequency fluctuation is not a constant (as will be the case for the COSAC), we can no longer measure the stability of the clock in terms of a constant  $\gamma/\text{SNR}$ . Instead, it is necessary to carry out the full calculation of the frequency

fluctuation as a function of frequency. Thus, we will adopt the convention that the net frequency fluctuation  $\delta f$  should be thought of as the *ratio of the noise to the SVS*. This approach should be adopted universally for all metrological devices. Of course, for devices where the relevant quantity is not the frequency, the definition should be adapted accordingly. For example, in an interferometer that measures phase, the relevant quantity can be expressed as follows: net phase fluctuation is the *ratio of the noise to the angular variation of signal (AVS)*.

Following this convention, we can now examine the net frequency fluctuation of the COSAC and compare it to that of the CC. We will first compare their quantum fluctuations, which is relevant in the short term regime, and then the classical fluctuations, which dominates the long term regime. The collective state signal for  $m$  trials is  $S_{\text{col}} = mP_N^C = m \cos^{2N}(fT_2/2)$  and the projection noise is  $\Delta P_N^C = \sqrt{P_N^C(1-P_N^C)}$  for a single trial and  $\Delta P_N^C = \sqrt{m} \sqrt{P_N^C(1-P_N^C)}$  for  $m$  trials, so that the total quantum-mechanical noise in the signal is

$$\Delta S_{\text{QM,col}} = \sqrt{m} \cos^N(fT_2/2) \sqrt{1 - \cos^{2N}(fT_2/2)} \quad (9)$$

and the SVS is

$$\partial S_{\text{col}}/\partial f = -(mN/\gamma_{\text{sa}}) \sin(fT_2/2) \cos^{2N-1}(fT_2/2). \quad (10)$$

Therefore, the frequency fluctuation in the COSAC due solely to quantum noise can be expressed as

$$\delta f_{\text{QM,COSAC}} = \left| \frac{\gamma_{\text{sa}}}{N\sqrt{m}} \sqrt{\frac{1-P_N^C}{P_N^C}} \cot\left(\frac{fT_2}{2}\right) \right|, \quad (11)$$

where  $P_N^C$  is a function of  $f$ . Thus, unlike in the case of the CC, the frequency fluctuation is not a constant, and depends strongly on  $f$ .

We consider first the limiting case of  $f \rightarrow 0$ . Using Taylor expansion, it is easy to see that

$$\delta f_{\text{QM,COSAC}} \simeq \frac{\gamma_{\text{sa}}}{\sqrt{mN}}, \quad (12)$$

which is the same as that of the CC, given in Eq. (8). This can be understood physically by noting that while the fringe width becomes much narrower for the COSAC, the SNR also decreases due to the fact that a single observation is made for all  $N$  atoms in a given trial.

The QFF for the COSAC, given in Eq. (11), is smallest as  $f \rightarrow 0$  and increases as  $f$  moves away from resonance. The ratio of the QFF for the CC, given in Eq. (8), to that of the COSAC, given in Eq. (11), is plotted as a function of  $f$  in Fig. 8 (left) for  $T_2 = 10^{-4}$  s,  $m = 1000$ , and  $N = 2 \times 10^6$ . Here, the vertical bars indicate the FWHM of the COSAC signal. It is clear from this plot that the QFF for the COSAC increases significantly as we move away from resonance. However, since a servo will keep the value of  $f$  confined to be close to zero, the frequency stability of the COSAC, under quantum noise limited operation, should be very close to that of the CC, assuming that all the other factors remain the same.

The classical frequency fluctuation (CFF),  $\delta f|_{\text{class}} = \Delta S_{\text{class}}/(\partial S/\partial f)$ , is the limiting factor in the long term stability. While the quantum fluctuation is dominated by quantum projection noise, the classical noise is dominated by noise in the electronics employed to generate the clock signal. Since

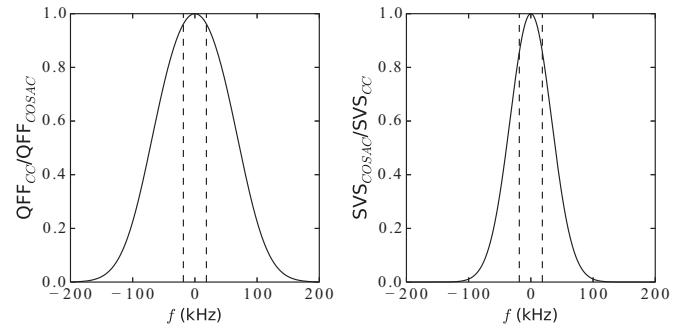


FIG. 8. Left: Ratio of the QFF in the CC to the QFF in the COSAC, for  $T_2 = 3 \times 10^{-5}$  s,  $m = 1000$ , and  $N = 2 \times 10^6$ . It should be noted that the fluctuation in the CC is independent of  $f$  while that of the COSAC varies significantly with  $f$ . Right: Ratio of the SVS of the COSAC to the SVS of the CC for  $T_2 = 3 \times 10^{-5}$  s,  $m = 1000$ , and  $N = 2 \times 10^6$ . The dashed vertical lines in the plots show where the  $\text{FWHM}_{\text{col}}$  are.

the pieces of equipment used in the development of both the COSAC and CC suffer from similar noise issues, the variance  $\Delta S$  is expected to be of the same order of magnitude for both clocks. On the other hand, the SVS,  $(\partial S/\partial f)$ , is not the same, as was shown previously. The ratio of the SVS of the COSAC to the SVS of the CC is

$$\frac{\partial S_{\text{col}}/\partial f}{\partial S_{\text{sa}}/\partial f} = \frac{\cos^{2N}\left(\frac{fT_2}{2}\right)}{\cos^2\left(\frac{fT_2}{2}\right)} = \frac{P_N^C}{P_2} \quad (13)$$

and is plotted in Fig. 8 (right). With  $\Delta S_{\text{class,col}} \sim \Delta S_{\text{class,sa}}$ , the ratio of the CFF of the COSAC to the CFF of the CC can be written

$$\frac{\delta f_{\text{class,COSAC}}}{\delta f_{\text{class,CC}}} \simeq \frac{\cos^2\left(\frac{fT_2}{2}\right)}{\cos^{2N}\left(\frac{fT_2}{2}\right)}. \quad (14)$$

Similar to the ratio of the two clocks in QFF, Eq. (14) is smallest as  $f \rightarrow 0$  and increases as  $f$  moves away from resonance. Thus, with respect to both quantum and classical sources of noise, the COSAC must be operated near  $f \simeq 0$  for optimal performance.

We have investigated the effects of quantum and classical noise by deriving the expression for fluctuation in frequency. However, as was shown in the first section, the signal is also a function of other experimental variables; and in general, the fluctuations in any of these can be expressed as

$$\delta A \equiv \left| \frac{\Delta S_{\text{QM}}(A) + \Delta S_{\text{class}}(A)}{\partial S(A)/\partial A} \right|, \quad (15)$$

where  $A$  is the variable whose fluctuation is of interest, and the signal  $S$  is expressed in terms of  $A$ .

## B. Effect of detector efficiency

We recall briefly that in the COSAC detection scheme, a laser with a frequency corresponding to one leg of the Raman transition interacts with the atoms, which are in the quantum state  $|\psi\rangle = c_N|E_N\rangle + \sum_{j=0}^{N-1} c_j|E_j\rangle$ . Interaction between this field, the atoms, and the free space vacuum modes on the other leg would lead to production of photons unless  $c_N = 1$  and  $c_j = 0$  for all  $j$ . These photons are detected using a

heterodyning technique, as described previously. The voltage output of the heterodyning system is proportional to the amplitude of the electric field corresponding to the photons.

In general, one or more photons are produced as  $|E_j\rangle$  decays to  $|E_{j+1}\rangle$  and subsequent states. The time needed for these photons to be produced depends on the vacuum and probe field induced Raman transition rates between  $|E_j\rangle$  and  $|E_{j+1}\rangle$ . If one assumes perfect efficiency for detecting each of these photons, and waits for a time long compared to the inverse of the weakest of these transition rates, then the detection of no photons implies that the system is in state  $|E_N\rangle$ . In practice, we can choose a small threshold voltage at the output of the heterodyning system as an indicator of null detection. Thus, any signal below this threshold would be viewed as detection of the quantum system in the  $|E_N\rangle$  state, and all signals above this threshold would be discarded. The number of events below this threshold for  $m$  trials carried out with all the parameters of the experiment unchanged is the derived signal for the COSAC. After collecting data for all the values of detuning that are of interest, the result would ideally yield the plot of the COSAC signal  $S_{\text{col}} = |c_N|^2$ , averaged over  $m$  trials. However, with a fractional detector efficiency and finite detection period, the signal would deviate from the ideal result.

Consider first the effect of the detection period. Given the decay rate of the off-resonant Raman process,  $\gamma_j = (j+1)(N-j)\gamma_{\text{sa}}$  as described previously, the probability that  $|E_j\rangle$  will produce zero photons during the measurement period  $\tau$  is  $P_{0,j} = e^{-\gamma_j\tau}$ . Thus, the total probability of zero photon emission (which should vanish ideally for any  $c_j \neq 0$ ) is given by  $P_0 = \sum_{j=0}^{N-1} |c_j|^2 e^{-\gamma_j\tau}$ . The collective state signal  $S_{\text{col}}$  is the total probability of finding zero photons during  $\tau$ , and can be expressed as  $S_{\text{col}} = |c_N|^2 + \sum_{j=0}^{N-1} |c_j|^2 e^{-\gamma_j\tau}$ . Noting that  $\gamma_N = 0$ , we can rewrite this compactly as  $S_{\text{col}} = \sum_{j=0}^N |c_j|^2 e^{-\gamma_j\tau}$ . The lower and upper bounds of  $S_{\text{col}}$  can be established by considering the strongest and the weakest effective decay rates. The strongest decay rate occurs for the middle state,  $\gamma_{N/2} = (N/2)(N/2+1) \approx (N^2/4)\gamma_{\text{sa}}$ , where  $N \gg 1$  approximation has been made. With the substitution of the largest decay rate for each  $|E_j\rangle$  into the equation for  $S_{\text{col}}$ , the lower bound is set by

$$S_{\text{LB}} = |c_N|^2 + (1 - |c_N|^2) e^{-(N^2/4)\gamma_{\text{sa}}\tau}. \quad (16)$$

Likewise, with the substitution of the weakest decay rate for each  $|E_j\rangle$ ,  $\gamma_0 = \gamma_{N-1} = N\gamma_{\text{sa}}$ , into  $S_{\text{col}}$ , the upper bound is set by

$$S_{\text{UB}} = |c_N|^2 + (1 - |c_N|^2) e^{-N\gamma_{\text{sa}}\tau}. \quad (17)$$

The signal produced in time  $\tau$  will then lie somewhere between the lower and the upper bounds.

Consider next the effect of nonideal detection efficiency of the heterodyning scheme. To be concrete, let us define as  $\eta$  the efficiency of detecting a single photon. In practice, this parameter will depend on a combination of factors, including the quantum efficiency of the high-speed photodetector and the overlap between the probe laser mode and the mode of the emitted photon, as well as the resonant optical depth of the ensemble, as discussed earlier. For the COSAC, it should be noted that we are interested in knowing only whether one or more photons have been detected, and not in the actual number

of photons. When more photons are emitted, the detector will have a better chance of observing a nonzero signal, and hence distinguish zero photon emission from the rest with more certainty. For example, if three photons are emitted during the interrogation time, then four different outcomes are possible:

- (i) all three photons are detected, with probability  $\eta^3$ ;
- (ii) two of the photons are detected, with probability  $\eta^2(1-\eta)$ ; this can occur for any two of the photons, so the multiplicity is 3;
- (iii) one photon is detected, with probability  $\eta(1-\eta)^2$  and multiplicity of 3;
- (iv) no photons are detected, with probability  $\epsilon^3$  where  $\epsilon \equiv 1 - \eta$ .

The sum of these probabilities is 1. The probability that at least one photon is detected is thus  $(1 - \epsilon^3)$ . For any state  $j \neq N$ , the probability of detecting at least one photon is therefore  $(1 - \epsilon^{N-j})$ .

Moreover, we must also consider how the effective detection efficiency is influenced by the fact that the collective states decay at different rates. Specifically, the  $j$ th level for  $j < N$  might produce  $N - j$  photons,  $N - j - 1$  photons, down to no photons, depending on the length of the measurement time and the effective decay rate. If the system is in the state  $|E_{N-3}\rangle$ , for example, it can produce up to three photons but with probabilities that change over the course of the detection period. For a given time  $\tau$ ,  $|E_{N-3}\rangle$  evolves into a sum of the states  $|E_{N-3}\rangle \rightarrow \sum_{k=N-3}^N a_{jk}(\tau) |E_k\rangle$ , where the coefficient  $a_{jk}(\tau)$  depends on the effective decay rate that is specific to each state, and changes as the states evolve in time. The detector efficiency can be inserted to show the true probability of detecting a nonzero signal, keeping in mind that no photon is produced if the ensemble remains in state  $|E_{N-3}\rangle$ , one photon is produced via evolution of the ensemble to state  $|E_{N-2}\rangle$ , and so on. Then the probability of at least one photon being produced during a period of  $\tau$  is

$$P_{N-3} = \sum_{k=N-3}^N (1 - \epsilon^{k-N+3}) |\alpha_{jk}(\tau)|^2. \quad (18)$$

Thus, the total probability of detecting at least one photon is

$$P = \sum_{j=0}^{N-1} |c_j|^2 \sum_{k=j}^N (1 - \epsilon^{k-j}) |\alpha_{jk}(\tau)|^2. \quad (19)$$

The probability of seeing no photon is

$$S_{\text{col}} = 1 - P = 1 - \sum_{j=0}^{N-1} |c_j|^2 \sum_{k=j}^N (1 - \epsilon^{k-j}) |\alpha_{jk}(\tau)|^2. \quad (20)$$

The numerical analysis for a large number of atoms is tedious and scales as at least  $(N-1)!$  for the COSAC. However, we can take the worst case scenario to serve as the upper bound for the signal. The worst case occurs when only a single photon is produced as a result of  $|E_j\rangle$  decaying to only the  $|E_{j+1}\rangle$  state, so that the index of the second summation stops at  $k = j+1$ . In this case, we can write  $|\alpha_{j,j+1}(\tau)| = (1 - e^{-\gamma_j\tau})$  and the signal becomes

$$S_{\text{col}} = |c_N|^2 + \epsilon(1 - |c_N|^2) + \eta \sum_{j=0}^{N-1} |c_j|^2 e^{-\gamma_j\tau}. \quad (21)$$

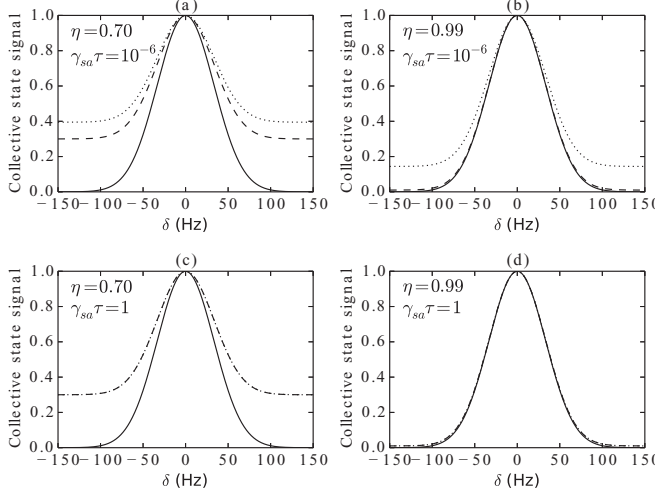


FIG. 9. Plot of the ideal signal (solid line), the upper bound (dotted line), and the lower bound (dashed line) for  $N = 2 \times 10^6$ ,  $T_2 = 3 \times 10^{-4}$  s, and  $\gamma_{\text{sa}} = 10^4$  s $^{-1}$ . Note that in (c) and (d), the upper and lower bounds are virtually indistinguishable.

Now, using the approach we employed in arriving at Eqs. (16) and (17), we now consider the strongest and the weakest decay rates for single-photon production to arrive at the lower and upper bounds of the zero-photon count signal:

$$S_{\text{LB}} = 1 - \eta(1 - |c_N|^2)(1 - e^{-(N^2/4)\gamma_{\text{sa}}\tau}), \quad (22)$$

$$S_{\text{UB}} = 1 - \eta(1 - |c_N|^2)(1 - e^{-N\gamma_{\text{sa}}\tau}). \quad (23)$$

Plots in Fig. 9 are of the ideal signal (under infinite detection time and  $\eta = 1$ ), the lower bound, and the upper bound for various values of  $\tau$  and  $\eta$  for  $N = 2 \times 10^6$ ,  $T_2 = 3 \times 10^{-5}$  s, and  $\gamma_{\text{sa}} = 10^4$  s $^{-1}$ . As can be seen, the detector efficiency and measurement time do not affect the peak value of the amplitude. As the signal trails off for nonzero detuning, however, the difference increases. The decrease in  $\eta$  affects both  $S_{\text{UB}}$  and  $S_{\text{LB}}$  similarly, whereas the effect of the decrease in  $\tau$  is more evident in  $S_{\text{UB}}$ . With the given parameters, the interrogation period of  $\tau = 10^{-4}$  s and detector efficiency of  $\eta = 0.99$  yields an almost ideal signal. A somewhat lower value of  $\eta$  (e.g., 0.70) still yields a signal that is nearly ideal near zero detuning, which is the desired operating regime for the COSAC, as pointed out earlier.

If we set  $\gamma_{\text{sa}}\tau = 1$ , the signal depends on  $\eta$  as

$$S_{\text{col}} \simeq 1 - \eta[1 - \cos^{2N}(fT_2/2)] \quad (24)$$

for large  $N$  and  $m = 1$ . Hence, we can calculate the QFF for the COSAC to see how it depends on the detector efficiency, and how it compares to the CC. For the CC, it is straightforward to show that with  $S_{\text{sa}} = \eta N \cos^2(fT_2/2)$ , the quantum-mechanical noise in the signal is  $\Delta S_{\text{sa}} = \sqrt{\eta N} \cos(fT_2/2) \sin(fT_2/2)$  and the SVS is  $|\partial S_{\text{sa}}/\partial \delta| = (\eta N/\gamma_{\text{sa}}) \cos(fT_2/2) \sin(fT_2/2)$ , so that the QFF is  $\delta f_{\text{QM,CC}} = \gamma_{\text{sa}}/\sqrt{\eta N}$ . It is also straightforward to calculate the QFF for the COSAC. The total quantum-mechanical noise in the COSAC signal in Eq. (24) is

$$\Delta S_{\text{QM,col}} = \sqrt{\eta} \cos^N(fT_2/2) \sqrt{1 - \cos^{2N}(fT_2/2)} \quad (25)$$

and the SVS is

$$\partial S_{\text{col}}/\partial f = -(\eta N/\gamma_{\text{sa}}) \sin(fT_2/2) \cos^{2N-1}(fT_2/2). \quad (26)$$

Thus, the QFF in the COSAC is

$$\delta f_{\text{QM,COSAC}} = \left| \frac{\gamma_{\text{sa}}}{N\sqrt{\eta}} \sqrt{\frac{1 - P_N^C}{P_N^C}} \cot\left(\frac{fT_2}{2}\right) \right|, \quad (27)$$

which approaches  $\gamma_{\text{sa}}/\sqrt{\eta N}$  as  $f \rightarrow 0$ . Assuming that the detector efficiencies of the COSAC and the CC can be essentially the same, they do not affect the ratio of the two QFFs.

### C. Effect of collection efficiency

We consider next the effect of the collection efficiency  $\beta$ . The signal, for both the COSAC and CC, is directly proportional to  $\beta$ . Thus, it is easy to see, using Eqs. (8) and (11), that

$$\begin{aligned} \zeta &\equiv \frac{\delta f_{\text{QM,COSAC}}}{\delta f_{\text{QM,CC}}} \\ &= \left[ \frac{1}{\sqrt{N}} \sqrt{\frac{1 - P_N^C}{P_N^C}} \cot\left(\frac{fT_2}{2}\right) \right] \sqrt{\frac{\beta_{\text{CC}}}{\beta_{\text{COSAC}}}}, \end{aligned} \quad (28)$$

where  $\beta_{\text{CC}}$  ( $\beta_{\text{COSAC}}$ ) is the collection efficiency of the CC (COSAC).

As noted above, the quantity written in the square brackets in Eq. (28) approaches unity as  $f \rightarrow 0$ . Thus, in this limit, we see that the ratio of the QFF for the COSAC to that of the CC would depend on the ratio of the collection efficiencies of the detection processes. As discussed previously, for a high enough resonant optical density ( $10^3$  in the example we are considering) the coherent stimulated Raman scattering based detection method used for the COSAC process has a collection efficiency that is close to unity, or  $\beta_{\text{COSAC}} \simeq 1$ . As for the CC, the fluorescence is typically collected from the spontaneous emission process, which emits photons in a dipolar radiation pattern. We can estimate typical values of  $\beta_{\text{CC}}$  by considering, for example, a CC that makes use of cold atoms released from a MOT. For a lens placed at a distance of 5 cm, with a diameter of 2.5 cm, ignoring the dipolar pattern of radiation for simplicity, and assuming it to be uniform in all directions, this system yields a value of  $\beta_{\text{CC}} \simeq r^2/(4d^2) = 1/16$  corresponding to  $\zeta \sim 0.25$ . In a typical CC, various geometric constraints make it difficult to achieve a value of  $\beta_{\text{CC}}$  much larger than this. In fact, in cases where the total volume occupied by the CC has to be constrained in order to meet the user requirements, the value of  $\beta_{\text{CC}}$  is typically 1%, which would correspond to  $\zeta \sim 0.1$ . Thus, the near unity collection efficiency of the COSAC can lead to an improvement of the clock stability by as much as a factor of 10, compared to a typical CC that makes use of fluorescence detection.

Absorption is another way of detecting the signal in a CC. However, many practical issues must be taken into account if absorbtion is to be used. First, the fluctuation in the clock frequency is affected by additional noise contributed by the laser used in absorbtion. Let us assume that the observation time window is  $\tau$ , and the number of photons in the probe beam, before absorbtion, is  $N_P$ , and the probe is in a coherent state. We also assume that the number of atoms passing

through the detection process in this time window is  $N_A$ , and the linewidth of the resonance is  $\Gamma$ . If the detection process produces an absorption by a fraction of  $\alpha$  (i.e.,  $\alpha = 1$  represents perfect absorption of the laser beam), and the detector has a quantum efficiency of  $\eta$ , then the resulting fluctuation in the clock frequency can be expressed as

$$\delta\omega_{\text{ABS}} = \Gamma \left( \frac{1}{\sqrt{\eta\alpha N_A}} + \frac{1}{\sqrt{\eta\alpha N_P}} \right). \quad (29)$$

Here, the first term inside the parentheses represents the quantum projection noise of the atoms, and the second term represents the shot noise of the photons (which can be thought of as the quantum projection noise of photons). The validity of this expression can be easily established by considering various limits. Consider first the ideal case where  $\xi \equiv \eta\alpha = 1$ . For  $N_P \gg N_A$ , the additional noise from the laser can be neglected, and we get the fundamental noise limit due to the quantum projection noise of atoms. On the other hand, if  $N_A \gg N_P$ , the quantum projection noise from the atoms can be neglected, and the process is limited by the shot noise of the laser. In general, the parameter  $\xi$  represents the overall quantum efficiency of the detection process. The corresponding expression for detection via fluorescence is  $\delta\omega_{\text{FLU}} = \Gamma(\eta\rho N_A)^{-1/2}$ , where again  $\eta$  is the quantum efficiency of the detector, and  $\rho$  is the fraction of fluorescence falling on the detector.

The contribution from the second term in Eq. (29) shows that the intensity of the laser beam used in absorption must be made strong enough in order to make the effect of this term negligible compared to the first term. However, since the absorption process is nonlinear and saturates for a strong laser beam, increasing the laser intensity often decreases the effective value of  $\alpha$ . For example, consider an ensemble of  $2 \times 10^6$  atoms with a linear resonant optical density of 300, which can be realized (as we have shown above) for an ensemble confined to a cigar-shaped ensemble with a diameter  $\sim 50 \mu\text{m}$ . For a weak probe, the value of  $\alpha$  is unity. However, as the probe power is increased, the value of  $\alpha$  decreases dramatically. This can be seen by considering a situation where the value of  $N_P$  is  $10^9$ , for example. Since the atomic transition used for absorption is not closed (i.e., not cyclic), the ensemble can only absorb a number of photons that is of the order of  $2 \times 10^6$ . Thus, the maximum value of  $\alpha$  would be only about 0.002. Furthermore, if the area of the laser beam ( $A_L$ ) is much larger than the area of the atomic ensemble ( $A_A$ ), then the value of  $\alpha$  can never exceed the value of  $A_A/A_L$ . We are not aware of any publication reporting a cold atom clock that makes use of absorption for detecting the atoms, possibly because of these constraints and considerations. Nonetheless, as a matter of principle, an absorption process can certainly be used to reduce the quantum frequency fluctuation below what is observed in fluorescence detection systems, under proper choice of parameters.

## VI. PHYSICAL INTERPRETATION OF LINewidth REDUCTION AND ITS RELEVANCE TO THE TRANSIT TIME LIMIT

As we have shown, the fact that the linewidth in a COSAC is narrower by a factor of  $\sqrt{N}$  can be proven mathematically. However, it is instructive to discuss the physical mechanism

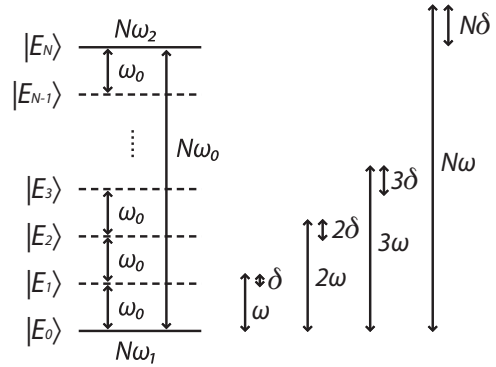


FIG. 10. Collective state energy levels, separated by  $\omega_0$ , are excited by a field of frequency  $\omega$ . All the states from  $|E_0\rangle$  to  $|E_N\rangle$  are excited, and participate in producing an effective clock transition frequency proportional to  $\sqrt{N}$ .

that leads to this narrowing. Furthermore, it is also important to address the issue of why the violation of the conventional notion of the transit time limit does not contradict the fundamental laws of quantum mechanics.

### A. Physical interpretation of line narrowing

We consider a simple picture of an oscillator and a probe in order to understand the physical explanation as to why the linewidth of a COSAC narrows by  $\sqrt{N}$ . A clock is essentially an oscillator oscillating at some frequency  $\omega$ . In order to ascertain that the oscillator has not drifted, the oscillator frequency is mapped into light and interacts with a two level atom, with the ground state  $|1\rangle$  and the excited state  $|2\rangle$ , and a transition frequency  $\omega_0$ . If  $\omega$  does not match  $\omega_0$ , an error signal proportional to  $\delta = \omega - \omega_0$  is produced to correct for the difference. Now consider for a moment that we can create a two state superposition of  $N$  atoms such that they are all either in the ground state or the excited state. In other words,  $|\psi\rangle = C_0|E_0\rangle + C_N|E_N\rangle$  where  $|E_0\rangle = |111\dots11\rangle$  and  $|E_N\rangle = |222\dots22\rangle$ . The energy difference between these two states is  $N\omega_0$ . The oscillator frequency is still  $\omega$ , but when a light field with  $N$  photons is compared with such a two level system, the difference in energy is  $N\delta = N\omega - N\omega_0$ . If it were possible to produce an error signal that is proportional to this energy difference without degrading the effective signal-to-noise ratio (or, more accurately, the ratio of noise to the SVS, as discussed in Sec. V A), the resulting clock would be  $N$ -fold more accurate. This is functionally equivalent to the clock transition frequency being enhanced by a factor of  $N$ .

However, this clean two level superposition of collective states is virtually impossible to achieve with a collection of  $N$  noninteracting atoms and a single field since there is no electric dipole moment to excite the  $|E_N\rangle$  state directly from the  $|E_0\rangle$  state. What occurs instead is that all the states between these get excited as well, as illustrated in Fig. 10. If we consider only the excitations from state  $|E_0\rangle$ , there are  $N$  possible transitions that can occur, so that the error signal includes the set of all the possible detunings,  $\delta, 2\delta, 3\delta, \dots, N\delta$ . In other words, there are effectively  $N$  different sensors running at the same time. All the other states also act as sensors as they interact with the others. It turns out, as we have proven mathematically in Sec. III, that the error signal becomes proportional to  $\sqrt{N}\delta$ , corresponding to

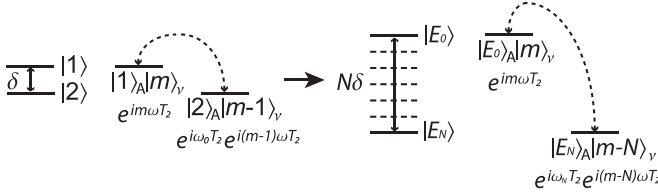


FIG. 11. Ramsey fringe experiment of a two level atom, in the Jaynes-Cummings model, involves states  $|1\rangle_A|m\rangle_v$  and  $|2\rangle_A|m-1\rangle_v$ , where the state with subscript  $A$  represents the atomic state, and subscript  $v$  represents the Ramsey field. The phase difference of the two levels at the end of the experiment is  $e^{i\delta T_2}$ , and the signal produced would oscillate at frequency  $\delta$ ; if a two level system existed in which the ground state were the collective state  $|E_0\rangle_A|m\rangle_v$  and the excited state were the collective state  $|E_N\rangle_A|m-N\rangle_v$ , the phase accumulation between the two states at the end of the Ramsey fringe experiment would be  $e^{iN\delta T_2}$ , and the oscillation frequency would be  $N\delta$ .

an effective detuning of  $\sqrt{N}\delta$ . This is functionally equivalent to the clock transition frequency being enhanced by a factor of  $\sqrt{N}$ .

In the Ramsey fringe experiment, the error signal that is generated occurs as a result of the phase difference between the interacting states. A detailed picture can be viewed in Fig. 11. Consider first a single two level atom, initially in state  $|1\rangle_A$ , going through the Ramsey fields. In the Jaynes-Cummings model, when a field with  $m$  photons interacts with an atom, the  $\pi/2$  pulse will produce the quantum state  $|\psi\rangle = |1\rangle_A|m\rangle_v - i|2\rangle_A|m-1\rangle_v$ . The energy of state  $|2\rangle_A|m-1\rangle_v$  is lower than that of state  $|1\rangle_A|m\rangle_v$  by  $\hbar\delta$ . In the second zone, these two composite states evolve freely for a time  $T_2$  and accumulate different phases. State  $|1\rangle_A$ , with energy 0 remains the same, whereas  $|2\rangle_A$  with energy  $\omega_0$  evolves as  $e^{i\omega_0 T_2}$ . The field with  $m$  photons evolve as  $e^{i m \omega T_2}$  whereas the field with  $m-1$  photons evolve as  $e^{i(m-1)\omega T_2}$ . Thus, the quantum state of the total system at the end of the dark zone is

$$|\psi\rangle = e^{i\omega_0 T_2} |1\rangle_A|m\rangle_v - i e^{i\omega_0 T_2} e^{i(m-1)\omega T_2} |2\rangle_A|m-1\rangle_v. \quad (30)$$

The net accumulated phase difference in the two states is  $e^{i\delta T_2}$ . The third zone where another  $\pi/2$  pulse occurs produces interference between the two states, so that when interrogation occurs, the signal produced is in the form of Ramsey fringes that oscillate at frequency  $\delta$ . Therefore, the energy difference between the two composite states determines the oscillation frequency of the Ramsey fringes. Alternatively, if one were to plot the signal as a function of the dark zone time  $T_2$ , the width of the fringe is given by the inverse of this energy difference. If the same calculation is carried out now for a two state system where the ground state is  $|E_0\rangle_A|m\rangle_v$  and the excited state is  $|E_N\rangle_A|m-N\rangle_v$ , where  $|E_0\rangle_A$  and  $|E_N\rangle_A$  are the collective states of  $N$  atoms, then the energy difference is  $N\delta$  and the width of the fringe as a function of  $T_2$  would be  $1/(N\delta)$  and the width of the Ramsey fringe as a function of  $\delta$  will be  $(T_2^{-1}/N)$ .

As mentioned earlier, such a two level system of collective states for a large value of  $N$  is virtually impossible to realize for noninteracting atoms. Instead, for  $N$  atoms, the first Ramsey zone produces a superposition of all the states from  $|E_0\rangle_A$

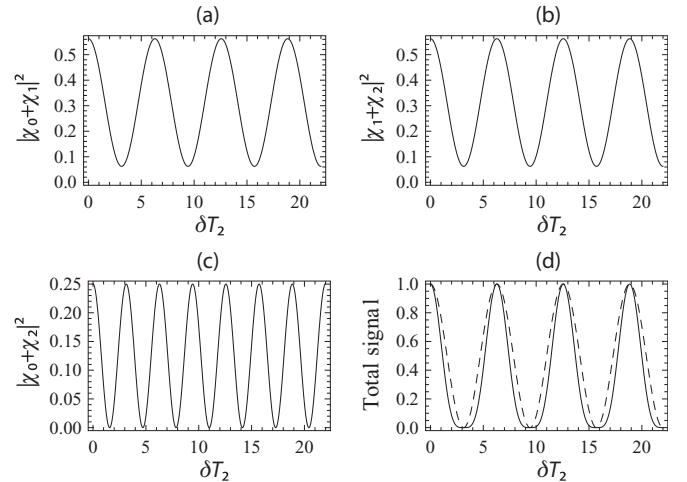


FIG. 12. In a two atom ensemble, each of the three collective states interfere with one another to produce different Ramsey fringes (a)–(c). The overall envelope is not drawn. The sum of these interferences gives the narrowing of the fringe linewidth as seen in (d). In (d), the dotted curve represents the signal from a single atom and the solid curve the signal from two atoms for comparison.

to  $|E_N\rangle_A$ . In the second zone, each of the collective states  $|E_k\rangle_A$  accumulates a phase factor of  $e^{i(\delta T_2)k}$  with respect to the state  $|E_0\rangle_A$ . When the atoms pass through the third zone, each of these collective states interferes with one another and contributes to the final state  $|E_2\rangle$  by amount  $\chi_0 = 1/4$ ,  $\chi_1 = e^{i\delta T}/2$ , and  $\chi_2 = e^{2i\delta T}/4$  respectively. The total signal is  $S_{\text{col}} = |\langle E_2 | E_2 \rangle|^2 = \cos^4(\delta T_2/2)$ . This comes about because  $S_{\text{col}} = |\chi_0 + \chi_1 + \chi_2|^2 = |\chi_0 + \chi_1|^2 + |\chi_1 + \chi_2|^2 + |\chi_0 + \chi_2|^2 - (\chi_0^2 + \chi_1^2 + \chi_2^2)$ . In other words, it is as though  $|E_0\rangle$  and  $|E_1\rangle$  interfered together to produce Ramsey fringes at frequency  $\delta$ ,  $|E_1\rangle$  and  $|E_2\rangle$  interfered together to produce Ramsey fringes at frequency  $\delta$ , and  $|E_0\rangle$  and  $|E_2\rangle$  interfered together to produce Ramsey fringes at frequency  $2\delta$ ; the signal observed is the addition of all these Ramsey fringes minus an overall factor (see Fig. 12), which is due to the fact that the actual process is a simultaneous interference between the three states.

We have verified this interpretation explicitly for two atoms. The collective states in this case are (where the subscript  $A$  has been dropped)  $|E_0\rangle$ ,  $|E_1\rangle$ , and  $|E_2\rangle$ . After they accumulate different phases in the second zone, each of them contributes to the final state  $|E_2\rangle$  by amount  $\chi_0 = 1/4$ ,  $\chi_1 = e^{i\delta T}/2$ , and  $\chi_2 = e^{2i\delta T}/4$  respectively. The total signal is  $S_{\text{col}} = |\langle E_2 | E_2 \rangle|^2 = \cos^4(\delta T_2/2)$ . This comes about because  $S_{\text{col}} = |\chi_0 + \chi_1 + \chi_2|^2 = |\chi_0 + \chi_1|^2 + |\chi_1 + \chi_2|^2 + |\chi_0 + \chi_2|^2 - (\chi_0^2 + \chi_1^2 + \chi_2^2)$ . In other words, it is as though  $|E_0\rangle$  and  $|E_1\rangle$  interfered together to produce Ramsey fringes at frequency  $\delta$ ,  $|E_1\rangle$  and  $|E_2\rangle$  interfered together to produce Ramsey fringes at frequency  $\delta$ , and  $|E_0\rangle$  and  $|E_2\rangle$  interfered together to produce Ramsey fringes at frequency  $2\delta$ ; the signal observed is the addition of all these Ramsey fringes minus an overall factor (see Fig. 12), which is due to the fact that the actual process is a simultaneous interference between the three states.

## B. Violation of the conventional notion of the transit time limit

The narrowing of the COSAC fringe as given by  $\Gamma(N) = \Gamma(1)/\sqrt{N} = \pi/(T_2\sqrt{N})$  violates the conventional transit time limit, which constrains the fringe width to be at least  $\sim 1/T_2$ . This is a manifestation of the uncertainty relation  $\Delta f \Delta t \geq 1$ , which apparently follows from the Heisenberg uncertainty principle of  $\Delta E \Delta t \geq \hbar$ . However, when we properly define  $\Delta f$  as the uncertainty in the fringe width—in the case of the Ramsey technique considered here—and  $\Delta t$  as the total observation time, we can derive the uncertainty relations

more systematically and show that despite the fact that the conventional transit time limit is violated, the Heisenberg uncertainty principle is not violated.

First, consider a single atom that undergoes the Ramsey fringe experiment. The uncertainty in the fringe width is  $\Delta f = (1/T_2)$ , where  $T_2$  is the separation period between the two  $\pi/2$  pulses. When the experiment is repeated  $m$  times, it is as though the separation period expands  $m$ -fold, so that the effective observation time is in fact  $\Delta t = mT_2$ , and the uncertainty in the fringe width is  $\Delta f = (1/T_2)/\sqrt{m}$  in the standard quantum limit (SQL) and  $\Delta f = (1/T_2)/m$  in the Heisenberg limit (HL). Hence, the product  $\Delta f \Delta t$  yields  $\sqrt{m}$  in the SQL and 1 in the HL. Note that as  $m \rightarrow 1$ , the SQL approaches the HL, which is the more fundamental limit.

Next, consider  $N$  atoms in the same Ramsey fringe experiment during a single trial. Since each atom, in its individual state, is considered separately from the rest, having  $N$  atoms is equivalent to running  $N$  trials simultaneously. The effective observation time in this case is  $\Delta t = NT_2$ , and the uncertainties in the fringe width are  $\Delta f = (1/T_2)/\sqrt{N}$  in the SQL and  $\Delta f = (1/T_2)/N$  in the HL. Moreover, if the experiment is repeated  $m$  times, the effective observation time increases to  $\Delta t = mNT_2$ , and the uncertainties in the fringe width are  $\Delta f = (1/T_2)/\sqrt{mN}$  in the SQL and  $\Delta f = (1/T_2)/(mN)$  in the HL. Thus, we find that the uncertainty relations for  $N$  atoms and  $m$  trials are  $\Delta f \Delta t = \sqrt{mN}$  in the SQL and  $\Delta f \Delta t = 1$  in the HL.

Consider next the COSAC case, containing  $N$  atoms, and repeated  $m$  times. As we have shown in Sec. V, the frequency

fluctuation in the COSAC is  $\Delta f = 1/(T_2\sqrt{mN})$  for ideal detection efficiency. It may not be obvious what the effective observation time is for this case. However, given the fact that, under ideal detection efficiency, the COSAC is equivalent to the case of  $N$  atoms repeated  $m$  times, we are led to conclude that the effective observation time is  $\Delta t = T_2mN$ . As such, we get  $\Delta f \Delta t = \sqrt{mN}$ , which is the SQL in this case. In the HL, we could get  $\Delta f \Delta t = 1$ . Thus, we see that when the frequency uncertainty and the observation times are interpreted properly, the COSAC signal does not violate the fundamental quantum limit.

## VII. CONCLUSION

We have described an atomic clock with a significant reduction in the Ramsey fringe linewidth, by a factor of  $\sqrt{N}$ , by measuring the amplitude of a collective state with a heterodyne detection scheme. We have shown that the reduction occurs due to multipath interference among the collective states, and does not violate the fundamental quantum limit. The performance of the COSAC has been compared to that of the CC by analyzing quantum and classical fluctuations in frequency. When the effects of detector efficiency and collection efficiency are considered, it can be seen that the COSAC may perform ten times better than a typical CC employing fluorescence detection.

## ACKNOWLEDGMENTS

This work has been supported by NSF Grants No. DGE-0801685 and No. DMR-1121262, and AFOSR Grant No. FA9550-09-1-0652.

---

[1] M. Niering, R. Holzwarth, J. Reichert, P. Pokasov, Th Udem, M. Weitz, T. W. Hänsch, P. Lemonde, G. Santarelli, M. Abgrall, P. Laurent, C. Salomon, and A. Clairon, *Phys. Rev. Lett.* **84**, 5496 (2000).

[2] G. Santarelli, P. Laurent, P. Lemonde, A. Clairon, A. G. Mann, S. Chang, A. N. Luiten, and C. Salomon, *Phys. Rev. Lett.* **82**, 4619 (1999).

[3] E. Arimondo, *Prog. Opt.* **35**, 257 (1996).

[4] F.-X. Esnault, E. Blanshan, E. N. Ivanov, R. E. Scholten, J. Kitching, and E. A. Donley, *Phys. Rev. A* **88**, 042120 (2013).

[5] G. Wilpers, T. Binnewies, C. Degenhardt, U. Sterr, J. Helmcke, and F. Riehle, *Phys. Rev. Lett.* **89**, 230801 (2002).

[6] N. F. Ramsey, *Phys. Rev.* **78**, 695 (1950).

[7] P. O. Schmidt, T. Rosenband, C. Langer, W. Itano, J. Bergquist, and D. Wineland, *Science* **309**, 749 (2005).

[8] W. M. Itano, J. C. Bergquist, J. J. Bollinger, J. M. Gilligan, D. J. Heinzen, F. L. Moore, M. G. Raizen, and D. J. Wineland, *Phys. Rev. A* **47**, 3554 (1993).

[9] M. Kitagawa and M. Ueda, *Phys. Rev. A* **47**, 5138 (1993).

[10] J. Hald, J. L. Sørensen, C. Schori, and E. S. Polzik, *Phys. Rev. Lett.* **83**, 1319 (1999).

[11] A. Kuzmich, L. Mandel, and N. P. Bigelow, *Phys. Rev. Lett.* **85**, 1594 (2000).

[12] S. M. Shahriar, P. R. Hemmer, D. P. Katz, A. Lee, and M. G. Prentiss, *Phys. Rev. A* **55**, 2272 (1997).

[13] P. Hemmer, M. Shahriar, V. Natoli, and S. Ezekiel, *J. Opt. Soc. Am. B* **6**, 1519 (1989).

[14] M. Kasevich and S. Chu, *Phys. Rev. Lett.* **67**, 181 (1991).

[15] M. O. Scully and M. S. Zubairy, *Quantum Optics* (Cambridge University Press, Cambridge, England, 1997).

[16] R. Dicke, *Phys. Rev.* **93**, 99 (1954).

[17] R. Sarkar, M. E. Kim, R. Fang, Y. Tu, and M. S. Shahriar, *J. Mod. Opt.* (2015), doi: 10.1080/09500340.2015.1033026.

[18] F. Arecchi, E. Courtens, R. Gilmore, and H. Thomas, *Phys. Rev. A* **6**, 2211 (1972).

[19] C. Foot, *Atomic Physics* (Oxford University Press, New York, 2008).

[20] W. Ketterle and N. J. Van Druten, *Adv. At. Mol. Opt. Phys.* **37**, 181 (1996).

[21] K. Kowalski, V. C. Long, K. D. Xuan, M. Główz, B. Nguyen Huy, and J. Szonert, *Comput. Meth. Sci. Technol. Spec.* **SI2**, 115 (2010).

[22] J. D. Miller, R. A. Cline, and D. J. Heinzen, *Phys. Rev. A* **47**, R4567 (1993).

[23] L.-M. Duan, M. Lukin, J. I. Cirac, and P. Zoller, *Nature (London)* **414**, 413 (2001).

[24] P. R. Hemmer, M. S. Shahriar, M. G. Prentiss, D. P. Katz, K. Berggren, J. Mervis, and N. P. Bigelow, *Phys. Rev. Lett.* **68**, 3148 (1992).

# N-atom collective-state atomic interferometer with ultrahigh Compton frequency and ultrashort de Broglie wavelength, with $\sqrt{N}$ reduction in fringe width

Resham Sarkar,<sup>1,\*</sup> May E. Kim,<sup>1</sup> Renpeng Fang,<sup>1</sup> and Selim M. Shahriar<sup>1,2</sup>

<sup>1</sup>Department of Physics and Astronomy, Northwestern University, 2145 Sheridan Road, Evanston, Illinois 60208, USA

<sup>2</sup>Department of EECS, Northwestern University, 2145 Sheridan Road, Evanston, Illinois 60208, USA

(Received 17 December 2014; published 7 December 2015)

We describe a collective-state atomic interferometer (COSAIN) with the signal fringe as a function of phase difference or rotation narrowed by  $\sqrt{N}$  compared to a conventional interferometer,  $N$  being the number of atoms, without entanglement. This effect arises from the interferences among collective states, and is a manifestation of interference at a Compton frequency of  $10 \times 10^{30}$  Hz, or a de Broglie wavelength of 4.5 femtometer, for  $N = 10^6$  and  $v = 1$  m/s. The population of the collective state of interest is detected by a null measurement scheme, in which an event corresponding to detection of zero photons corresponds to the system being in that particular collective state. The signal is detected by collecting fluorescence through stimulated Raman scattering of Stokes photons, which are emitted predominantly against the direction of the probe beam, for a high enough resonant optical density. The sensitivity of the ideal COSAIN is found to be given by the standard quantum limit. However, when detection efficiency and collection efficiency are taken into account, the detection scheme of the COSAIN increases the quantum efficiency of detection significantly in comparison to a typical conventional Raman atomic interferometer employing fluorescence detection, yielding a net improvement in stability by as much as a factor of 10. We discuss how the inhomogeneities arising from the nonuniformity in experimental parameters affect the COSAIN signal. We also describe an alternate experimental scheme to enhance resonant optical density in a COSAIN by using cross-linearly polarized counterpropagating Raman beams.

DOI: [10.1103/PhysRevA.92.063612](https://doi.org/10.1103/PhysRevA.92.063612)

PACS number(s): 37.25.+k, 03.75.Dg, 06.30.Gv

## I. INTRODUCTION

Matter-wave interferometry is a potent technology in metrology. Atom interferometers have been demonstrated as gyroscopes and accelerometers [1,2], gravity gradiometers [3,4], matter-wave clocks [5], and may lead to a more accurate measurement of the fine-structure constant [6,7]. They also form testbeds for measuring Newton's gravitational constant [8], gravitational red-shift [9], and for testing universality of free fall [10].

The building block of a conventional Raman atom interferometer (CRAIN) is a three-level atom, with two metastable states  $|g, p_z=0\rangle \equiv |g, 0\rangle$  and  $|e, p_z=\hbar(k_1+k_2)\rangle \equiv |e, \hbar k\rangle$  and an excited state  $|a, p_z=\hbar k_1\rangle \equiv |a, \hbar k_1\rangle$  coupled by two counterpropagating beams, with a single-photon detuning  $\delta$  [Fig. 1(a)]. One of the beams, with Rabi frequency  $\Omega_1$ , couples  $|g, 0\rangle$  to  $|a, \hbar k_1\rangle$ , while the other beam, with Rabi frequency  $\Omega_2$ , couples  $|a, \hbar k_1\rangle$  to  $|e, \hbar k\rangle$ . For  $\delta \gg \Omega_1, \Omega_2$ , the interaction can be described as an effective two-level system excited by an effective traveling wave with a momentum  $\hbar k = \hbar(k_1+k_2)$ , with a Rabi frequency  $\Omega = \Omega_1 \Omega_2 / 2\delta$  [Fig. 1(b)] [11]. We assume that  $\delta \gg \Gamma$ , where  $\Gamma$  is the decay rate of  $|a\rangle$ , so that the effect of  $\Gamma$  can be neglected. Under a sequence of  $\pi/2$ - $\pi$ - $\pi/2$  pulses [Fig. 1(c)], the wave packet first separates into two components, then gets redirected, and finally recombines to produce an interference which is sensitive to any phase difference  $\Delta\phi$  between the two paths. The amplitude of  $|g\rangle$  at the end varies as  $\cos^2(\Delta\phi/2)$  [12,13].

A CRAIN of this type can be realized by employing an atomic beam with a continuous flux, or by employing pulses of atoms pushed out periodically from a magneto-optic trap

(MOT). The behavior of the CRAIN is essentially the same in both modes if the number of atoms interrogated in a given time window is the same. However, as we will describe later, the collective-state atomic interferometer (COSAIN) must operate in the latter (pulsed) mode. Thus, for proper comparison we will assume, in the rest of the paper, that the CRAIN is operated in the pulsed mode.

The phase difference induced due to rotation at the rate of  $\Omega_G$  along an axis normal to the area  $\Theta$  of the interferometer is given by  $\Delta\phi = 4\pi \Theta m \Omega_G / \hbar$ ,  $m$  being the atomic mass [13,14]. This expression can be derived by two different methods. In the first method, the path difference of the two counterpropagating waves is multiplied by  $2\pi/\lambda_{dB}$ , where  $\lambda_{dB}$  is the de Broglie wavelength, to get the phase difference. The second method invokes the relativistic addition of velocities to find the time lag  $\Delta T = 2\Theta \Omega_G / c^2$  in the arrival of the two branches of the wave,  $c$  being the speed of light.  $\Delta\phi$  is then the product of  $\Delta T$  and the wave frequency. For the CRAIN, this frequency is the Compton frequency of the atom  $\omega_C = \gamma mc^2/\hbar \approx mc^2/\hbar$ , where the relativistic time-dilation factor  $\gamma$  is close to unity for nonrelativistic velocities. These approaches are equivalent due to the fact that  $\lambda_{dB}$  is the laboratory-frame manifestation of the  $\omega_C$  induced phase variation in the rest frame of the atom [5,15–17]. To explain this without loss of generality, let us consider the direction of the velocity of the particle as  $\hat{x}$ . For nonrelativistic velocities, mixing between the spinors can be ignored, and the phase factor of a positive-energy spinor, in the rest frame of the particle, is given simply as  $\exp(-i\phi)$ , where  $\phi = \omega_C \tau$  with  $\tau$  being the proper time. The phase  $\phi$  is a Lorentz-invariant parameter, and can in general be written as a contraction between the position four-vector  $x^\mu$  and momentum four-vector  $\hbar k^\mu$ :  $\phi = k_\mu x^\mu$ . In the rest frame of the particle, the position four-vector is  $x^\mu = \{c\tau, 0, 0, 0\}$

\*rsarkar@u.northwestern.edu

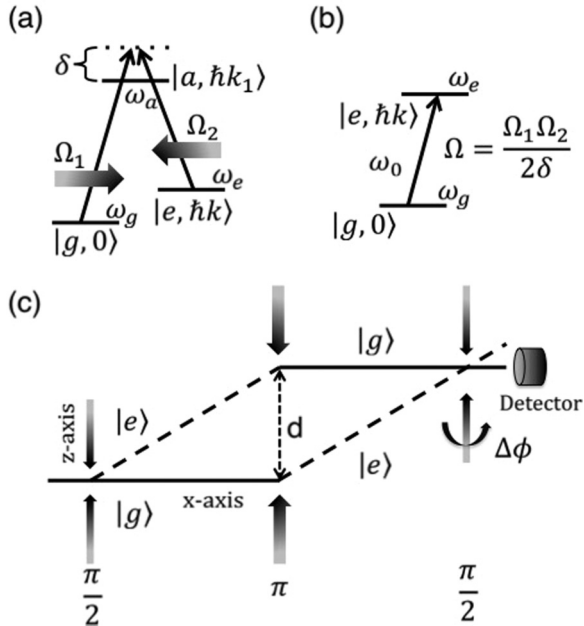


FIG. 1. (a) A three-level atom. (b) An equivalent reduced two-level atom model. (c) A CRAIN produced via  $\pi/2-\pi-\pi/2$  sequence of excitation.

and the momentum four-vector is  $\hbar k^\mu = \hbar\{\omega_C/c, 0, 0, 0\}$ . In the laboratory frame, the position four-vector is, by definition,  $x^\mu = \{ct, 0, 0, 0\}$ , and application of Lorentz transform shows that the momentum four-vector is  $\hbar k^\mu = \hbar\{\omega'_C/c, k_{dB}, 0, 0\}$ , where  $k_{dB} = \gamma m V/\hbar = 2\pi/\lambda_{dB}$  and the phase factor becomes  $\phi = \omega'_C t - k_{dB}x$ . Again, in the nonrelativistic limit,  $\gamma \approx 1$  and we get  $\lambda_{dB} \approx 2\pi\hbar/mV$ . Thus, the de Broglie wavelength is simply the laboratory-frame manifestation of the phase variation in the rest frame due to the Compton frequency.

The dependence of  $\Delta\phi$  on  $\omega_C$  has motivated matter-wave interferometry with large molecules. To date, the largest molecule used has a mass of  $\sim 10\,000$  atomic-mass units [18], corresponding to the mass of  $\sim 75$   $^{133}\text{Cs}$  atoms. These interferometers, based on the Talbot effect, are not suited for rotation sensing. Furthermore, for interferometry with much larger particles it would be necessary to use gratings with spacings too small to be realized with existing technologies. Additionally, effects such as van der Waals interaction would become dominant for such gratings. Here, we propose an experiment that would reveal evidence of matter-wave interference where a collection of  $N$  noninteracting, unentangled atoms act as a *single* particle. For  $^{87}\text{Rb}$  and  $N = 10^6$ ,  $\omega_C$  is  $\sim 10 \times 10^{30}$  Hz, and  $\lambda_{dB}$  is  $\sim 4.5$  femtometer at a velocity of 1 m/s. Furthermore, it can improve the phase measurement ability by a factor of as much as 10. This type of matter-wave interferometry may also open up new opportunities for sensitive measurement of gravitational red-shift [9] or matter-wave clocks [5]. It may also serve as a testbed for macroscopic quantum decoherence due to gravitational red-shift [19].

Consider an assembly of  $N$  identical noninteracting atoms, subjected to the  $\pi/2-\pi-\pi/2$  sequence. If we imagine a situation where the ground state  $|E_0\rangle \equiv |g_1, g_2, \dots, g_N\rangle$  is coupled, directly and only, to the state where all the atoms are in the excited state  $|E_N\rangle \equiv |e_1, e_2, \dots, e_N\rangle$ , the resulting ensemble

interferometer would experience a phase difference  $\Delta\phi_{EI} = N\Delta\phi$ . However, existing technology does not enable such an excitation. Even if one were to use a pure Fock state of  $N' > N$  photons, the ensemble would evolve into a superposition of  $(N+1)$  symmetric collective states  $|E_n\rangle |N'-n\rangle$ , where  $|N'-n\rangle$  is a state of the field with  $(N'-n)$  photons, and  $|E_n\rangle = J(N,n)^{-1/2} \sum_{k=1}^{J(N,n)} P_k |g^{\otimes(N-n)} e^{\otimes n}\rangle$ , where  $J(N,n) \equiv \binom{N}{n}$ ,  $P_k$  is the permutation operator, and  $n = 0, 1, 2, \dots, N$  [20]. Since a laser is a superposition of many Fock states, the evolution of this system under laser excitation would produce a seemingly intractable superposition of these collective states. Modeling the laser field as a semiclassical one also does not simplify the picture much [21–24]. However, we show here that, by measuring the quantum state of a single collective state, it is possible to determine the effect of the interference among all the collective states, and describe how such a measurement can be done. Choosing this collective state to be one of the two extremal states (i.e.,  $|E_0\rangle$  or  $|E_N\rangle$ ) also makes it possible to calculate this signal easily since the state of the whole system can be described as the tensor product of individual atomic states. We show that the fringe width is reduced by a factor of  $\sqrt{N}$ , without using entanglement. For the current state of the art, the value of  $N$  can easily exceed  $10^6$ , so that a reduction of fringe width by a factor of more than  $10^3$  is feasible. We also show that the phase fluctuation of the COSAIN can be significantly smaller, by as much as a factor of 10, than that for a conventional interferometer employing the same transition and the same atomic flux. The extremely narrow resonances produced in the COSAIN may also help advance the field of spin squeezing [25–28], which in turn is useful for approaching the Heisenberg limit in precision metrology. Recently, we have also proposed a collective-state atomic clock, which employs the principle of collective excitation of atomic ensemble, and exhibits a similar narrowing in signal fringe [29].

In this paper, we discuss the various aspects of the collective-state atomic interferometer. The rest of the paper is arranged in the following way: In Sec. II, we describe the theory of the working principle of a COSAIN. We also describe the physical phenomenon behind the narrowing of the signal fringes. Section III gives an account of the various parameter inhomogeneities that affect the signal amplitude and width. Section IV details the description of the COSAIN experiment, also including a discussion of the role of the optical density of the ensemble. We also propose an alternate experimental scheme to achieve a higher value of effective optical density in Sec. V. In Sec. VI, we analyze the performance of the COSAIN as compared to that of the CRAIN. We consider the effect of quantum and classical noise, detector efficiency, and collection efficiency.

## II. DESCRIPTION OF THE COSAIN

Consider an ensemble of  $N$  noninteracting atoms of the kind described above [21], with the  $i$ th atom in its ground state  $|g_i\rangle$ . The ensemble is assumed to be initially situated at  $(x=0, z=0)$  and traveling along the  $\mathbf{x}$  direction with a velocity  $v$ . The ensemble undergoes the same  $\pi/2-\pi-\pi/2$  sequence as described for the CRAIN. Assuming resonant excitation, the Hamiltonian of the  $i$ th atom after the rotating-wave transformation is  $H_i = \Omega_i |g_i\rangle \langle e_i|/2 + \text{c.c.}$  [22], where

$\Omega_i$  is the Rabi frequency of the  $i$ th atom. Here, a phase transformation on the Hamiltonian has also been applied to render  $\Omega_i$  real. For the sake of simplicity and brevity, we consider only the case where the intensity profile of the beams is rectangular, so that  $\Omega_i = \Omega$ . In a real experiment, the Rabi frequency of each atom depends on its position relative to the Gaussian distribution of the beam intensity profile. Due to the nonzero temperature of the trapped atoms, they also experience Doppler shift arising from thermal motion. A detailed description of the effect of these inhomogeneities on the COSAIN signal is presented in Sec. III.

A  $\pi/2$  pulse of duration  $\tau$  is applied to the ensemble at  $t = 0$ , following which each atom is in state  $|\psi_i(\tau)\rangle = (|g_i\rangle - i|e_i\rangle)/\sqrt{2}$ . After the first dark zone of duration of  $T_d$ , the component of the atom in state  $|e_i\rangle$  drifts to  $(x = vT_d, z = \hbar k T_d/m)$ . The state  $|g_i\rangle$  continues along the  $\mathbf{x}$  direction. We label the trajectories taken by  $|g_i\rangle$  and  $|e_i\rangle$  as  $A$  and  $B$ , respectively. The state of an atom at  $t = \tau + T_d$  is  $|\psi_i(\tau + T_d)\rangle = |\psi_i(\tau + T_d)\rangle_A + |\psi_i(\tau + T_d)\rangle_B$ , where  $|\psi_i(\tau + T_d)\rangle_A = |g_i\rangle/\sqrt{2}$  and  $|\psi_i(\tau + T_d)\rangle_B = -i|e_i\rangle/\sqrt{2}$ . At the end of this zone, a  $\pi$  pulse causes the state  $|g_i\rangle$  to evolve into  $|e_i\rangle$  and vice versa. The state at the end of this pulse is  $|\psi_i(3\tau + T_d)\rangle = |\psi_i(3\tau + T_d)\rangle_A + |\psi_i(3\tau + T_d)\rangle_B$ , such that  $|\psi_i(3\tau + T_d)\rangle_A = -i|e_i\rangle/\sqrt{2}$  and  $|\psi_i(3\tau + T_d)\rangle_B = -|g_i\rangle/\sqrt{2}$ . Following the second dark zone of duration  $T_d$ , the two trajectories converge, as shown in Fig. 1(c), and  $|\psi_i(3\tau + 2T_d)\rangle = |\psi_i(3\tau + T_d)\rangle$ . At  $t = 3\tau + 2T_d$ , a third pulse of duration  $\tau$  is applied to the atoms. If a phase difference of  $\Delta\phi$  is introduced between the paths, the state of the atom at the end of the last  $\pi/2$  pulse is  $|\psi_i(4\tau + 2T_d)\rangle = |\psi_i(4\tau + 2T_d)\rangle_A + |\psi_i(4\tau + 2T_d)\rangle_B$ , where  $|\psi_i(4\tau + 2T_d)\rangle_A = -i[-i \exp(-i\Delta\phi)|g_i\rangle + |e_i\rangle]/2$  and  $|\psi_i(4\tau + 2T_d)\rangle_B = -[|g_i\rangle - i \exp(i\Delta\phi)|e_i\rangle]/2$ . This phase difference can occur, for example, due to a rotation of the entire system about the  $y$  direction.

The final fringe pattern is the result of the interference of the states from the two trajectories. This is observed by measuring the probability of finding the atom in either of the two states. The signal as a measure of the amplitude of  $|g\rangle$  is therefore,  $S_{\text{CRAIN}} = |[1 + \exp(-i\Delta\phi)]/2|^2 = \cos^2(\Delta\phi/2)$ . We note now that the state  $|\Psi\rangle$  of the ensemble is the direct product of its constituent atoms:  $|\Psi\rangle = \prod_{i=1}^N |\psi_i\rangle$  [22,23]. The signal of the COSAIN is a measurement of any of the arising collective states. We choose to measure the state  $|E_0\rangle$ , so that the resulting signal is the probability of finding all the atoms of the ensemble simultaneously in  $|g\rangle$ . This choice of state will be explained later on when we discuss the detection system of the COSAIN. The signal of the COSAIN is thus the product of the signals from the constituent atoms  $S_{\text{COSAIN}} = \prod_{i=1}^N S_{\text{CRAIN}} = \cos^{2N}(\Delta\phi/2)$ . The fringe linewidth as a function of  $\Delta\phi$  decreases with increasing  $N$ . We define this linewidth as the full width at half maximum (FWHM) of the signal fringe  $\varrho(N) = 2 \cos^{-1}(2^{-1/2N})$ . We have verified that  $\varrho(1)/\varrho(N) \approx \sqrt{N}$ .

#### Physical interpretation of fringe narrowing

The narrowing of the signal fringes in a COSAIN can be understood by considering the physical properties of the collective excitations. If the ensemble in the ground state

interacts with a single photon of momentum  $\hbar k$ , it will oscillate between  $|E_0, 0\rangle \leftrightarrow |E_1, \hbar k\rangle$ . Consequently, it will exhibit collective behavior such that its center of mass recoils with a velocity in the  $\mathbf{z}$  direction equal to  $\hbar k/Nm$ . Thus, this ensemble can be viewed as a single entity with a mass of  $Nm$ , and a Compton frequency  $\omega_C$  that is  $N$  times that of a single atom, despite no interaction between the atoms. Conversely, the ensemble can be viewed as having a  $\lambda_{dB}$  of  $h/Nmv$  that is  $N$  times lower than that of a single atom, where  $v$  is the magnitude of its total velocity (e.g., a constant velocity in the  $\mathbf{x}$  direction that is much larger than the velocity in the  $\mathbf{z}$  direction due to the recoil). In the ideal case of uniform Rabi frequencies and no Doppler shift related detunings, the first  $\pi/2$  pulse splits the ensemble into a superposition of  $N + 1$  symmetric collective states (we have shown the corresponding interpretation of the other, more general cases in Ref. [22]). The state  $|E_n\rangle$  receives a recoil of  $n\hbar k$  due to the first  $\pi/2$  pulse and is deflected in the  $\mathbf{z}$  direction by  $n\hbar k T_d/Nm$  by the end of the first dark zone, making an angle  $\theta_n = \tan^{-1}(n\hbar k/Nmv)$  with the  $\mathbf{x}$  axis. We label the path taken by this state as path  $n$ . The subsequent  $\pi$  pulse causes  $|E_n\rangle$  to evolve to  $|E_{N-n}\rangle$ . This results in the deflection of the trajectory of the states so that all the  $N + 1$  trajectories converge by the end of the second dark zone. The third pulse causes each of the  $N + 1$  states to split further. The resulting COSAIN is, thus,  $J(N + 1, 2)$  collective interferometers operating simultaneously. Of these, there are  $x$  interferometers of area  $(N - x + 1)\Theta/N$ , producing signal fringe amplitudes equaling  $\cos^2[(N - x + 1)\Delta\phi/2]$ , where  $x$  assumes values  $1, 2, \dots, N$ . The interference between these sinusoidal fringes results in the narrowing of the total fringe width. In what follows, we illustrate the physical mechanism behind this narrowing by considering first the role of Compton frequency in a CRAIN. We then extend this analysis to an ensemble of  $N$  atoms to describe the phenomenon of narrowing in the COSAIN.

We consider the product state of the atom and a Fock state with  $N'$  photons denoted by  $|N'\rangle$  or with  $N' - 1$  photons denoted by  $|N' - 1\rangle$ . Thus, at  $t = 0$ , the atom photon system is assumed to be in the state  $|g\rangle|N'\rangle \equiv |g, N'\rangle$ . The atom-field interaction couples it to the state  $|e\rangle|N' - 1\rangle \equiv |e, N' - 1\rangle$ , as illustrated in Fig. 2(a). We assume that the photon energy  $\hbar\omega$  exactly matches the energy difference between the atomic internal states  $|e\rangle$  and  $|g\rangle$ . We define the dressed frequency of the atom-photon system as  $\omega_{PA}$ , which is a constant, for all possible states of the system. If we define  $\omega_{C,e} = m_e c^2/\hbar$  as the Compton frequency of the excited atom, where  $m_e = m_g + \hbar\omega/c^2$  is the rest mass of the excited atom, and  $m_g = m$  is the rest mass of the atom in the ground state, then we have  $\omega_{PA} = m_e c^2/\hbar + (N' - 1)\omega = m_g c^2/\hbar + N'\omega$ . The Compton frequency of the atom in the ground state is  $\omega_{C,g} = m_g c^2/\hbar$ . The effect of temporal phase accumulation on the system during an interval  $\Delta t$ , if the system is in an arbitrary superposition of  $|g\rangle$  and  $|e\rangle$ , i.e.,  $c_g|g\rangle + c_e|e\rangle$  at the start of the interval, will be  $\exp(-i\omega_{PA}\Delta t)(c_g|g, N'\rangle + c_e|e, N' - 1\rangle)$ . Thus, after the first  $\pi/2$  pulse of a time duration  $\tau$ , the quantum state of the system is  $\exp(\omega_{PA}\tau)(|g, N'\rangle_A - i|e, N' - 1\rangle_B)/\sqrt{2}$ , where the subscripts  $A$  and  $B$  indicate the lower and upper trajectories of the interferometer, respectively. This is followed by a dark zone of duration  $T_d$  at

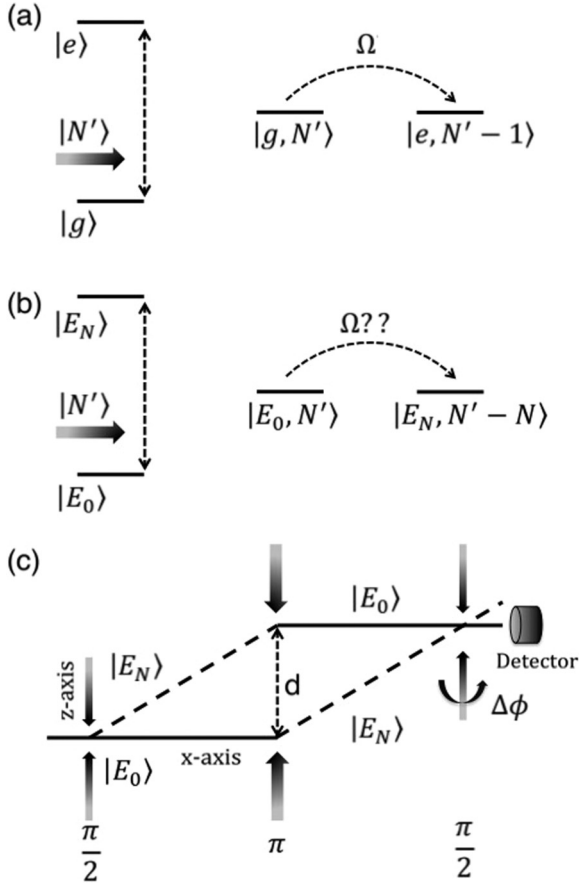


FIG. 2. (a) Single atom coupled to an  $N'$ -photon state, (b)  $N$ -atom ensemble coupled to an  $N'$ -photon state, (c) ensemble interferometer formed by splitting and recombining of  $|E_0\rangle$  and  $|E_N\rangle$ .

the end of which the quantum state of the system is  $\exp[-i\omega_{PA}(\tau + T_d)](|g,N'\rangle_A - i|e,N' - 1\rangle_B)/\sqrt{2}$ . A  $\pi$  pulse is applied at the end of the first dark zone, and therefore at  $t = 3\tau + T_d$ , the quantum state of the system is  $|\psi(3\tau + T_d)\rangle = |\psi(3\tau + T_d)\rangle_A + |\psi(3\tau + T_d)\rangle_B$ , where  $|\psi(3\tau + T_d)\rangle_A = -i \exp[-i\omega_{PA}(3\tau + T_d)]|e,N' - 1\rangle/\sqrt{2}$  and  $|\psi(3\tau + T_d)\rangle_B = -\exp[-i\omega_{PA}(3\tau + T_d)]|g,N'\rangle/\sqrt{2}$ . At this point, the second dark zone begins, at the end of which the state of the system can be written as  $|\psi(3\tau + 2T_d)\rangle = |\psi(3\tau + 2T_d)\rangle_A + |\psi(3\tau + 2T_d)\rangle_B$ , where  $|\psi(3\tau + 2T_d)\rangle_A = -i \exp[-i\omega_{PA}(3\tau + 2T_d)]|e,N' - 1\rangle/\sqrt{2}$  and  $|\psi(3\tau + 2T_d)\rangle_B = -\exp[-i\omega_{PA}(3\tau + 2T_d)]|g,N'\rangle/\sqrt{2}$ . Finally, the last  $\pi/2$  pulse causes each of the arms to further split into  $|g,N'\rangle$  and  $|e,N' - 1\rangle$ , so that the state of the system at  $t = 4\tau + 2T_d$  is given by  $|\psi(4\tau + 2T_d)\rangle = |\psi(4\tau + 2T_d)\rangle_A + |\psi(4\tau + 2T_d)\rangle_B$ , where

$$|\psi(4\tau + 2T_d)\rangle_A = \frac{-i}{2} \exp[-i\omega_{PA}(4\tau + 2T_d)] \times (-i|g,N'\rangle + |e,N' - 1\rangle),$$

$$|\psi(4\tau + 2T_d)\rangle_B = \frac{-1}{2} \exp[-i\omega_{PA}(4\tau + 2T_d)] \times (|g,N'\rangle - i|e,N' - 1\rangle). \quad (1)$$

The two arms, thus, yield identical proportions of  $|g,N'\rangle$  and  $|e,N' - 1\rangle$ . The probability of finding the atom in the ground state, which is the signal for the CRAIN, is therefore  $S_{\text{CRAIN}} = 1$ . However, if the entire system is rotating at the rate  $\Omega_G$  about an axis perpendicular to the area carved by the interferometer, a time delay  $\Delta T$  is introduced between the two paths. To consider its effect on the signal of the CRAIN, we note that the state of the system at  $t = 3\tau + 2T_d$  is such that

$$|\psi(3\tau + 2T_d)\rangle_A = \frac{-i}{\sqrt{2}} \exp[-i\omega_{PA}(3\tau + 2T_d)] \times \exp[i(\omega_{C,g} + \omega_{C,e})\Delta T/4] |e,N' - 1\rangle,$$

$$|\psi(3\tau + 2T_d)\rangle_B = \frac{-1}{\sqrt{2}} \exp[-i\omega_{PA}(3\tau + 2T_d)] \times \exp[-i(\omega_{C,e} + \omega_{C,g})\Delta T/4] |g,N'\rangle. \quad (2)$$

Finally, the state of the system due to rotation at the end of the  $\pi/2$ -dark- $\pi$ -dark- $\pi/2$  sequence is such that

$$|\psi(4\tau + 2T_d)\rangle_A = \frac{-i}{2} \exp[-i\omega_{PA}(4\tau + 2T_d)] \times \exp(i\omega_{C,\text{avg}}\Delta T/2) (-i|g,N'\rangle + |e,N' - 1\rangle),$$

$$|\psi(4\tau + 2T_d)\rangle_B = \frac{-1}{2} \exp[-i\omega_{PA}(4\tau + 2T_d)] \times \exp(-i\omega_{C,\text{avg}}\Delta T/2) (|g,N'\rangle - i|e,N' - 1\rangle), \quad (3)$$

where  $\omega_{C,\text{avg}} = (\omega_{C,g} + \omega_{C,e})/2$ . The probability of finding the atom in the ground state, which is the signal for the CRAIN, is therefore given by  $S_{\text{CRAIN}} = \cos^2(\Delta\phi/2)$ , where  $\Delta\phi = \omega_{C,\text{avg}}\Delta T$ . From the special relativistic addition of velocities along the two trajectories, the time delay is found to be  $\Delta T = 2\theta\Omega_G/c^2$ , where  $\theta$  is the area enclosed by the CRAIN [16]. In a real experiment, one makes use of a laser, which is a coherent state, and not a Fock state. However, when the mean photon number in the laser is very large, the excitation is akin to what we described here. In effect, the laser in this limit can be viewed effectively as a Fock state with a photon number equaling the mean photon number in the laser. This is the semiclassical approximation, where the quantum state of the field is assumed to remain unchanged (and thus factorized) independent of the state of the atom.

Next, we consider an ensemble of  $N$  such two-level atoms that are independent and noninteracting. Furthermore, we consider the product state of this ensemble and a Fock state of  $N'$  photon as described above. Initially, all the atoms are in the state  $|g\rangle$ , so that the state of the ensemble-photon system is  $|E_0\rangle|N'\rangle \equiv |E_0,N'\rangle$ , where  $|E_0\rangle = |g_1, g_2, \dots, g_N\rangle$ . Now, let us imagine a scenario (which is impossible in practice) that the state  $|E_0,N'\rangle$  is directly coupled to the state  $|E_N,N' - N\rangle$  via the exchange of  $N$  photons between the states, where  $|E_N\rangle = |e_1, e_2, \dots, e_N\rangle$  as illustrated in Fig. 2(b). Such a process can be used to realize an atomic interferometer in a manner analogous to the CRAIN, as illustrated in Fig. 2(c). The area enclosed in this case would be the same as that for a CRAIN. However, the average Compton frequency will now be  $N\omega_{C,\text{avg}}$  (and the

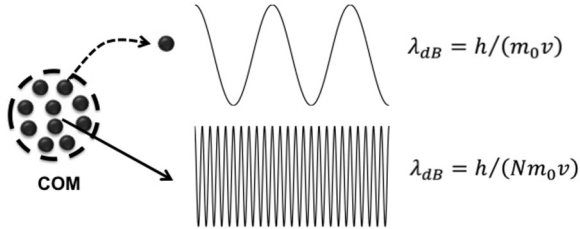


FIG. 3.  $\lambda_{dB}$  of an  $^{87}\text{Rb}$  atom moving at a constant velocity of 1 m/s is 4.56 nm. In the rest frame of the atom, its characteristic Compton frequency is  $1.96(10^{25} \text{ Hz})$ . A cluster of  $10^6$  such atoms will exhibit the characteristics of a single entity of mass that is  $1 \times 10^6$  times that of a single  $^{87}\text{Rb}$  atom. Therefore,  $\lambda_{dB}$  will be  $4.56(10^{-15} \text{ m})$  and Compton frequency is  $1.96(10^{31} \text{ Hz})$ .

de Broglie wavelength will be  $\lambda_{dB, \text{single atom}}/N$ , so that the signal given by the population of state  $|E_0\rangle$  measured at the end, will be  $S_{\text{ensemble}} = \cos^2(N\Delta\phi/2)$ , where  $\Delta\phi$  is the phase shift experienced by a CRAIN for the same amount of rotation.

However, since the electric dipole moment for a superposition of  $|E_0\rangle$  and  $|E_N\rangle$  vanishes, there is no way to realize the type of excitation envisioned above. Instead, when excited by a Fock state of  $N'(> N)$  photons, this ensemble unfolds into a superposition of  $(N+1)$  symmetric collective states given by  $|E_n\rangle |N'-n\rangle$ , where  $|N'-n\rangle$  is a state of the field with  $(N'-n)$  photons and  $|E_n\rangle = J(N,n)^{-1/2} \sum_{k=1}^{J(N,n)} P_k |g^{\otimes(N-n)} e^{\otimes n}\rangle$ ,  $J(N,n) = \binom{N}{n}$ ,  $P_k$  is the permutation operator, and  $n = 0, 1, 2, \dots, N$  [20]. The state  $|E_n\rangle$  has a momentum of  $n\hbar k$  in the direction of the beam since it has absorbed  $n$  photons. Thus, it will exhibit collective behavior such that its center of mass (COM) recoils with a velocity equal to  $n\hbar k/Nm$ . As such, an ensemble in such a state can be viewed as a single entity with a mass of  $Nm$  and a Compton frequency  $\omega_C$  that is  $N$  times that of a single constituent atom, despite no interaction between the atoms. Conversely, the ensemble can also be viewed as having a de Broglie wavelength  $\lambda_{dB} = h/Nmv$  that is  $N$  times smaller than that of a single atom, where  $v$  is the magnitude of the total velocity (e.g., a constant velocity in the  $\mathbf{x}$  direction that is much larger than the recoil velocity). This is illustrated schematically in Fig. 3.

Some of these states and their relevant couplings are illustrated in Fig. 4. For example, state  $|E_0, N'\rangle$  is coupled to the state  $|E_1, N'-1\rangle$  at the rate of  $\sqrt{N}\Omega_{N'}$ , where  $\Omega_{N'} = \sqrt{N'}\Omega_0$ , with  $\Omega_0$  being the single-photon Rabi frequency (for exciting a single atom) and the  $\sqrt{N}$  factor results from the collective enhancement of coupling. If the excitation is carried out by a laser field where the mean photon number is much larger than  $N$ , then we can make a semiclassical approximation that  $\Omega_{N'} \cong \Omega_{N'-1} \cong \dots \cong \Omega_{N'-N} \equiv \Omega$ . Furthermore, the quantum state of the laser remains unchanged (and thus

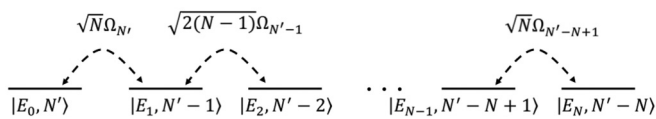


FIG. 4. Coupling between an  $N$ -atom ensemble symmetric collective states and  $N'$  photons.

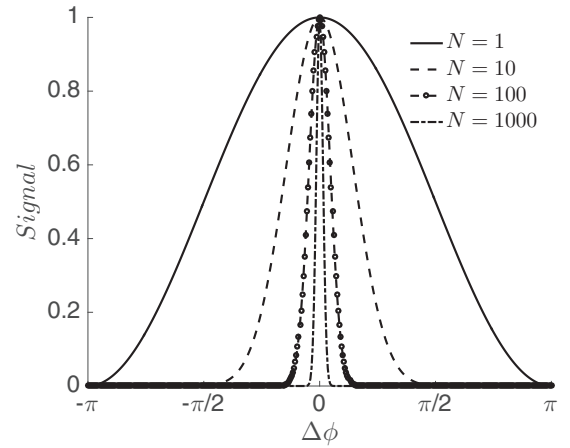


FIG. 5. Measurement of the COSAIN signal (amplitude of  $|E_0\rangle$ ) shows a narrowing of the fringe width such that the ratio  $\varrho(1)/\varrho(N)$  increases with  $\sqrt{N}$ .

factorized) independent of the state of the ensemble. The Compton frequency of the state  $|E_n\rangle$  is given by  $\omega_{C,E_n} = m_{E_n}c^2/\hbar$ , where  $m_{E_n} = m_{E0} + n\hbar\omega/c^2$  is the rest mass of the ensemble in state  $|E_n\rangle$ , and  $m_{E0} = Nm$  is the rest mass of the ensemble in state  $|E_0\rangle$ . Thus, the dressed frequency of the ensemble-photon system  $\omega_{PE}$ , which is a constant for all possible states of the system can be written as  $\omega_{PE}(N, N') = m_{E_n}c^2/\hbar + (N'-n)\omega = m_{E0}c^2/\hbar + N'\omega$ .

In the absence of an effective detuning, the COSAIN is based on the coherent splitting and recombining of all of these symmetric collective states. The signal of the COSAIN is, thus, the product of the signals of the constituent CRAIN's that work simultaneously, resulting in the narrowing of the signal fringes. The fringe linewidth, defined as the full width at half maximum (FWHM) of the signal fringe is given by  $\varrho(N) = 2\cos^{-1}(2^{-1/2N})$ . It is evident from Fig. 5 that the  $\varrho(N)$  decreases with increasing  $N$ . To illustrate the mechanism behind the COSAIN more transparently, we now consider the simplest ensemble: an assembly of two atoms of the kind described above and  $N'$  photons. At  $t = 0$ , the ensemble-photons system is assumed to be in the state  $|E_0, N'\rangle$ . The atom-field interaction couples it to the state  $|E_1, N'-1\rangle$ , which in turn is coupled to the state  $|E_2, N'-2\rangle$ . Following the notations of the  $\pi/2$ -dark- $\pi$ -dark- $\pi/2$  sequence established for the CRAIN, the state of the ensemble after the first  $\pi/2$  pulse is  $|\Psi(\tau)\rangle = \exp(-i\omega_{PE}\tau)(|E_0, N'\rangle_A - i\sqrt{2}|E_1, N'-1\rangle_B - |E_2, N'-2\rangle_C)/2$ , where  $\omega_{PE} \equiv \omega_{PE}(2, N')$  and the subscripts  $A$ ,  $B$ , and  $C$  denote the lower, middle, and upper trajectories of the interferometer, respectively, as shown in Fig. 6. This is followed by a dark zone of duration  $T_d$ , at the end of which the state of the ensemble is  $|\Psi(\tau + T_d)\rangle = \exp(-i\omega_{PE}T_d)|\Psi(\tau)\rangle$ . The component  $|E_1, N'-1\rangle_B$  is displaced by  $\hbar k T_d/2m$  along the  $\mathbf{z}$  axis since it has absorbed the recoil from one photon ( $\hbar k$ ), and it has a mass of  $2(m_{C,g} + m_{C,e}) \approx 2m$ . Similarly,  $|E_2, N'-2\rangle$  is displaced by  $\hbar k T_d/m$  along the  $\mathbf{z}$  axis since it has absorbed recoils from two photons ( $2\hbar k$ ), and it has a mass of  $2m_{C,e} \approx 2m$ . At  $t = \tau + T_d$ , the system interacts with the  $\pi$  pulse (of duration  $2\tau$ ) which causes the transition  $|E_0, N'\rangle \leftrightarrow |E_2, N'-2\rangle$ . The state  $|E_1, N'-1\rangle$ , however, only picks up a phase due to the  $\pi$  interaction, and its trajectory remains

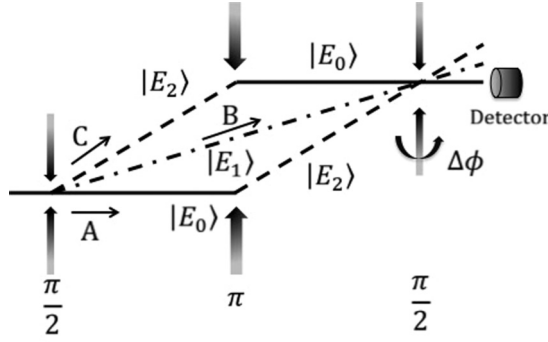


FIG. 6. Illustration of a two-atom COSAIN depicting the state trajectories.

unchanged. Explicitly, the state of the system at the end of the  $\pi$  pulse is  $|\Psi(3\tau + T_d)\rangle = |\Psi(3\tau + T_d)\rangle_A + |\Psi(3\tau + T_d)\rangle_B + |\Psi(3\tau + T_d)\rangle_C$ , where

$$\begin{aligned} |\Psi(3\tau + T_d)\rangle_A &= -\frac{1}{2} \exp[-i\omega_{PE}(3\tau + T_d)] |E_2, N' - 2\rangle, \\ |\Psi(3\tau + T_d)\rangle_B &= -\frac{1}{\sqrt{2}} \exp[-i\omega_{PE}(3\tau + T_d)] |E_1, N' - 1\rangle, \\ |\Psi(3\tau + T_d)\rangle_C &= \frac{1}{2} \exp[-i\omega_{PE}(3\tau + T_d)] |E_0, N'\rangle. \end{aligned} \quad (4)$$

At the end of this pulse, the system passes through a second dark zone of duration  $T_d$ , which causes the state of the system to become  $|\Psi(3\tau + 2T_d)\rangle = |\Psi(3\tau + 2T_d)\rangle_A + |\Psi(3\tau + 2T_d)\rangle_B + |\Psi(3\tau + 2T_d)\rangle_C$ , where  $|\Psi(3\tau + 2T_d)\rangle_A = \exp(-i\omega_{PE}T_d) |\Psi(3\tau + T_d)\rangle_A$ ,  $|\Psi(3\tau + 2T_d)\rangle_B = \exp(-i\omega_{PE}T_d) |\Psi(3\tau + T_d)\rangle_B$ , and  $|\Psi(3\tau + 2T_d)\rangle_C = \exp(-i\omega_{PE}T_d) |\Psi(3\tau + T_d)\rangle_C$ . By the end of this dark zone, the three trajectories converge and a last  $\pi/2$  pulse is applied which causes each of the trajectories to further split as follows:

$$\begin{aligned} |\Psi\rangle_A &= \frac{-1}{4} \exp[-i\omega_{PE}(4\tau + 2T_d)] (-|E_0, N'\rangle \\ &\quad - i\sqrt{2} |E_1, N' - 1\rangle + |E_2, N' - 2\rangle), \\ |\Psi\rangle_B &= \frac{1}{2} \exp[-i\omega_{PE}(4\tau + 2T_d)] (|E_0, N'\rangle + |E_2, N' - 2\rangle), \\ |\Psi\rangle_C &= \frac{1}{4} \exp[-i\omega_{PE}(4\tau + 2T_d)] (|E_0, N'\rangle \\ &\quad - i\sqrt{2} |E_1, N' - 1\rangle - |E_2, N' - 2\rangle). \end{aligned} \quad (5)$$

The signal of the COSAIN is the probability of finding the ensemble in any of the collective states. We choose to measure the probability of  $|E_0, N'\rangle$ . The probability of finding the ensemble in state  $|E_0, N'\rangle$  is, therefore,  $S_{\text{COSAIN}} = 1$ . However, as explained above for the case of the CRAIN, if the entire system is rotating at the rate  $\Omega_G$  about an axis perpendicular to the area carved by the interferometer, a time delay is introduced between the paths. This time delay depends only on the area enclosed and the rate of rotation, as noted earlier. Let us assume that the delay between the paths  $C$  and  $A$ , which forms the  $A-C$  loop, is  $\Delta T$ . Therefore, the delay between paths  $B$  and  $A$  which forms the  $A-B$  loop will be  $\Delta T/2$ . Similarly, the delay between paths  $C$  and  $B$ , which forms the  $B-C$  loop, will also be  $\Delta T/2$ . Since only the relative delay between two paths matter, we assume, for simplicity, that there is no delay on path  $B$ . Thus, just before

the final  $\pi/2$  pulse, we can write the quantum states of these paths under rotation as  $|\Psi\rangle_{BR} = |\Psi(3\tau + 2T_d)\rangle_B$ ,  $|\Psi\rangle_{AR} = \exp[i(\omega_{C,E0} + \omega_{C,E2})\Delta T/4] |\Psi(3\tau + 2T_d)\rangle_A$ , and  $|\Psi\rangle_{CR} = \exp[-i(\omega_{C,E2} + \omega_{C,E0})\Delta T/4] |\Psi(3\tau + 2T_d)\rangle_C$ . The last  $\pi/2$  pulse causes each of these components to further split so that the state of the system at the end of the  $\pi/2$ -dark- $\pi$ -dark- $\pi/2$  sequence is

$$\begin{aligned} |\Psi\rangle_{AR} &= \frac{-1}{4} \exp[-i\omega_{PE}(4\tau + 2T_d)] \\ &\quad \times \exp[i(\omega_{C,E0} + \omega_{C,E2})\Delta T/4] \\ &\quad \times (-|E_0, N'\rangle - i\sqrt{2} |E_1, N' - 1\rangle + |E_2, N' - 2\rangle), \\ |\Psi\rangle_{BR} &= \frac{1}{2} \exp[-i\omega_{PE}(4\tau + 2T_d)] (|E_0, N'\rangle + |E_2, N' - 2\rangle), \\ |\Psi\rangle_{CR} &= \frac{1}{4} \exp[-i\omega_{PE}(4\tau + 2T_d)] \\ &\quad \times \exp[-i(\omega_{C,E2} + \omega_{C,E0})\Delta T/4] \\ &\quad \times (|E_0, N'\rangle - i\sqrt{2} |E_1, N' - 1\rangle - |E_2, N' - 2\rangle). \end{aligned} \quad (6)$$

The signal of the COSAIN can, thus, be viewed as the aggregation of interference patterns due to three independent CRAIN's working simultaneously, i.e., those formed by paths  $A-B$ ,  $B-C$ , and  $A-C$ . To illustrate this, we denote the component of  $|E_0, N'\rangle$  in paths  $A$ ,  $B$ , and  $C$  as  $\chi_A$ ,  $\chi_B$ , and  $\chi_C$ , respectively. The interferometers formed by  $A-B$  and  $B-C$  are identical. The measurement of the amplitude of  $|E_0, N'\rangle$  from each of these interferometers is given by  $S_{A-B} = S_{B-C} = |\chi_A + \chi_B|^2 = |\chi_B + \chi_C|^2 = 3/16 + \cos^2(\omega_{C,\text{avg}}\Delta T/2)/4$ . This corresponds to a CRAIN that is operating with an atom of average Compton frequency  $\omega_{C,\text{avg}}$ . The interferometer formed by  $A-C$  yields the signal value  $S_{A-C} = |\chi_A + \chi_C|^2 = \cos^2(\omega_{C,\text{avg}}\Delta T)/4$ , behaving analogously to a CRAIN formed by an atom of average Compton frequency  $2\omega_{C,\text{avg}}$ . The total COSAIN

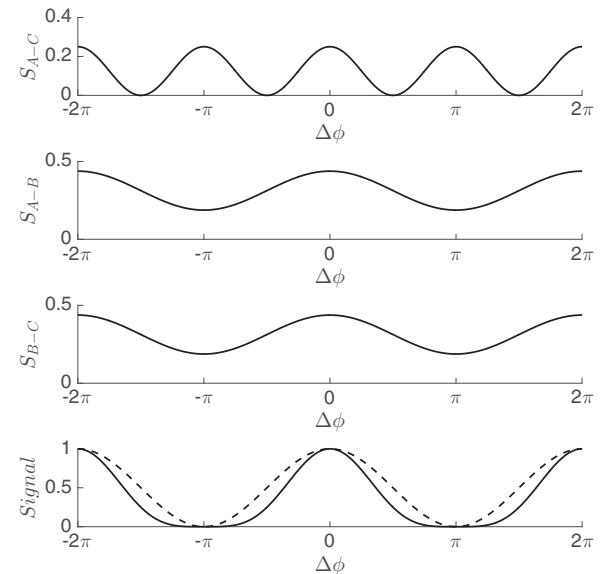


FIG. 7. Signals derived from the interferometers formed by trajectories  $A-C$ ,  $A-B$ , and  $B-C$ . The bottom panel shows the signal of CRAIN (broken line) to the signal of a two-atom COSAIN (solid line).

signal arises due to the interference of the component of  $|E_0, N'\rangle$  from the three paths  $S_{\text{COSAIN}} = |\chi_A + \chi_B + \chi_C|^2 = \cos^4(\omega_{C,\text{avg}} \Delta T/2)$ , as shown in Fig. 7. This is reconciled by the fact that  $|\chi_A + \chi_B + \chi_C|^2 = |\chi_A + \chi_B|^2 + |\chi_B + \chi_C|^2 + |\chi_A + \chi_C|^2 - (|\chi_A|^2 + |\chi_B|^2 + |\chi_C|^2)$ . The collective atomic recoil laser (CARL) mechanism is similar to this concept presented here, in the sense that no interaction between atoms is needed [30,31]. On the other hand, the Dicke phase transition pertains to the BEC regime, and is not closely related to what is being presented here [32].

### III. PARAMETER INHOMOGENEITIES AFFECTING SIGNAL

In this section, we present a detailed description of the effect of inhomogeneity in Rabi frequency and Doppler shift on the signal of a COSAIN. These inhomogeneities put significant constraints on the ensemble size, temperature of the trapped atoms, and the intensity profile and size of the laser beams. The manifestations of these effects can be analyzed by considering an ensemble of  $N$  identical noninteracting and independent atoms of the type described in Sec. II. A laser beam propagating along the  $\mathbf{z}$  axis will impart a momentum  $\hbar k$  to an atom upon absorption of recoil from a single photon, driving it to a superposition of the states  $|g_i, 0\rangle$  and  $|e_i, \hbar k\rangle$ , with the amplitude of each state depending on the intensity of the laser beam and the time of interaction. The field amplitude of the laser beams is assumed to be of Gaussian profile in  $\mathbf{x}$  and  $\mathbf{y}$  directions, and constant in the  $\mathbf{z}$  direction. At  $t = 0$ , the position of the  $i$ th atom is given by  $\mathbf{r} = x_i \hat{\mathbf{x}} + y_i \hat{\mathbf{y}} + z_i \hat{\mathbf{z}}$ . Due to the thermal motion of the atoms, each atom experiences a different Doppler shift and, therefore, a different effective laser frequency  $\omega_{0i}$ . The net consequence of this is that the  $i$ th atom picks up a detuning of  $\delta_i = k \mathbf{v}_{iz}$ , where  $\mathbf{v}_{iz}$  denotes the atom's velocity in the  $\mathbf{z}$  direction. Furthermore, each atom sees a different electric field  $\mathbf{E}_i = \hat{\mathbf{x}} E_0 \exp[-(x_i^2 + y_i^2)/2\sigma_L^2] \cos(\omega_{0i}t - kz_i)$ , due to the finite extent of the ensemble. Here,  $\sigma_L$  represents the width of the laser beam in the transverse directions. Therefore, the Rabi frequency experienced by the  $i$ th atom is given by  $\Omega_i = \Omega_0 \exp[-(x^2 + y^2)/2\sigma_L^2]$ , where  $\Omega_0 \equiv \langle g_i | (\mathbf{x} \cdot \rho_i) | e_i \rangle E_0 / \hbar = \langle e_i | (\mathbf{x} \cdot \rho_i) | g_i \rangle E_0 / \hbar$  and  $\rho_i$  is the position of the electron with respect to the nucleus.

In the electric dipole approximation, the Hamiltonian for the  $i$ th atom can be written as  $H_i = |\mathbf{p}_i|^2/2m + H_{0i} + q \rho_i \cdot \mathbf{E}_i$ , where  $H_{0i}$  is the internal energy of the atom,  $q$  is the electronic charge,  $m$  is the mass of the atom, and  $\mathbf{p}_i$  is the momentum of the  $i$ th atom. The COM motion kinetic energy term can be expressed as  $|\mathbf{p}_i|^2/2m = |\mathbf{p}_{iz}|^2/2m + |\mathbf{p}_{i\perp}|^2/2m$ , where  $\mathbf{p}_{iz}$  is the momentum in the  $\mathbf{z}$  direction, and  $\mathbf{p}_{i\perp}$  is the momentum in a direction perpendicular to  $\mathbf{z}$ . Consider first the effect of the second term:  $|\mathbf{p}_{i\perp}|^2/2m$ . In a typical experimental scenario, this accounts for the motion of the atom, typically at a large velocity, in the  $\mathbf{x}$  direction (see Fig. 1), acquired, for example by the initial push imparted to the trapped atoms before they enter the first interaction zone. Thus, any variation in this due to a velocity spread within the ensemble can be ignored, and this term can be treated as an overall constant energy which can be subtracted from the Hamiltonian. Consider next the first term:  $|\mathbf{p}_{iz}|^2/2m$ .

This term shows that the state  $|g, \mathbf{p}_{iz}\rangle$  coupled to  $|e, \mathbf{p}_{iz} + \hbar k\rangle$  by the laser differs in energy by  $(\hbar k v_{iz} + \hbar^2 k^2/2m)$ , where the first term is the Doppler shift and the second term is the recoil energy which is a constant for all atoms, and can be subtracted from the Hamiltonian. Thus, after subtraction of constant terms, the net effect of the kinetic energy term is to account for the Doppler shift. Finally, as we have shown in detail in Ref. [22], a fully quantum mechanical description of the COM motion (e.g., by keeping track explicitly of the momentum of the atoms in the  $|g\rangle$  and  $|e\rangle$  states) is not essential in describing the collective states in the limit where the Rabi frequency of the  $i$ th atom  $\Omega_i$  is large compared to the Doppler shift due to the COM motion. This regime is valid for the COSAIN, and, therefore, a semiclassical description of the COM motion of each atom suffices for the case at hand. Upon making the rotating-wave approximation,  $H_i$  can then be expressed in the bases of  $|g_i\rangle$  and  $|e_i\rangle$  as  $H_i/\hbar = \omega_g |g_i\rangle \langle g_i| + \omega_e |e_i\rangle \langle e_i| + \Omega_i \{\exp[i(\omega_{0i}t - kz_i)] |g_i\rangle \langle e_i| + \text{H.c.}\}/2$ , where  $\omega_e$  includes the Doppler shift. Performing the rotating-wave transformation and removing any phase factors causes the transformation  $H_i \rightarrow H'_i$ , such that  $H'_i/\hbar = -\delta_i |e'_i\rangle \langle e'_i| + \Omega_i (|g'_i\rangle \langle e'_i| + \text{H.c.})/2$ . The new basis vectors  $|g'_i\rangle$  and  $|e'_i\rangle$  are related to the original basis vectors as  $\exp(-i\omega_g t) |g_i\rangle$  and  $\exp\{-i[(\omega_e + \delta_i)t - kz_i]\} |e_i\rangle$ , respectively. Assuming that the  $i$ th atom is initially in the state  $c_{gi}(0) |g'_i\rangle + c_{ei}(0) |e'_i\rangle$ , its quantum state can be written as

$$|\psi'_i\rangle = e^{i\delta_i t/2} \left\{ \left[ c_{gi}(0) \cos\left(\frac{\Omega'_i t}{2}\right) - i \frac{c_{gi}(0)\delta_i + c_{ei}(0)\Omega_i}{\Omega'_i} \sin\left(\frac{\Omega'_i t}{2}\right) \right] |g'_i\rangle + \left[ -i \frac{c_{gi}(0)\Omega_i - c_{ei}(0)\delta_i}{\Omega'_i} \sin\left(\frac{\Omega'_i t}{2}\right) + c_{ei}(0) \cos\left(\frac{\Omega'_i t}{2}\right) \right] |e'_i\rangle \right\}, \quad (7)$$

where  $\Omega'_i = \sqrt{\Omega_i^2 + \delta_i^2}$  is the effective coupling frequency of this atom. The relative separation of the atoms along the direction of propagation of the laser beam has no effect on the fidelity of the collective states that can be attained by the ensemble [22]. For the purpose of the present discussion, we stay in the bases of  $|g'_i\rangle$  and  $|e'_i\rangle$ .

At  $t = 0$ , the first pulse of duration  $\tau$  is applied to the atoms so that  $\Omega_0\tau = \pi/2$ . The state of the  $i$ th atom following this interaction can be written as  $|\psi'_i(\tau)\rangle = c_{gi}(\tau) |g'_i\rangle_A + c_{ei}(\tau) |e'_i\rangle_B$ , where  $c_{gi}(\tau) = \exp(i\delta_i\tau/2) [\cos(\Omega'_i\tau/2) - i\delta_i \sin(\Omega'_i\tau/2)/\Omega'_i]$  and  $c_{ei}(\tau) = \exp(i\delta_i\tau/2) [-i\Omega_i \sin(\Omega'_i\tau/2)/\Omega'_i]$ . The subscripts  $A$  and  $B$  denote the lower and upper arms of the interferometer trajectory. The ensuing dark zone lasts for a duration  $T_d$  wherein the atoms are left to drift freely so that at  $t = \tau + T_d$ , the COM of state  $|e'_i\rangle$  is separated from that of state  $|g'_i\rangle$  by  $d = \hbar k T_d / m$ . During this dark zone where no atom-light interaction is taking place, the portion of the atom in state  $|e'_i\rangle$  picks up a phase due to detuning, making the state of the atom at the end of this pulse  $|\psi'_i(\tau + T_d)\rangle = c_{gi}(\tau + T_d) |g'_i\rangle_A + c_{ei}(\tau + T_d) |e'_i\rangle_B$ , where  $c_{gi}(\tau + T_d) = c_{gi}(\tau)$  and  $c_{ei}(\tau + T_d) = \exp(i\delta_i T_d) c_{ei}(\tau)$ . At

this point, a second pulse of duration  $2\tau$  ( $\pi$  pulse) is applied to atoms, and each trajectory undergoes further splitting, as shown in Fig. 1. The  $\pi$  pulse can, in principle, be perfect only for one group of atoms, such as those with  $\delta = 0$ . For all other atoms, the pulse duration will differ slightly from  $\pi$ . As a result, for example, the  $|e'_i\rangle$  state will not fully evolve into the  $|g'_i\rangle$  state, and a residual amount will stay in the  $|e'_i\rangle$  state. In the regime where  $\Omega_i \gg \delta_i$  for all  $i$ , the effect of these residual components can be safely ignored. Under this approximation, the state of the atom is given by  $|\psi'_i(3\tau + T_d)\rangle = c_{ei}(3\tau + T_d)|e'_i\rangle_A + c_{gi}(3\tau + T_d)|g'_i\rangle_B$ , where  $c_{ei}(3\tau + T_d) = \exp(i\delta_i\tau)c_{gi}(\tau + T_d)[-i\Omega_i \sin(\Omega'_i\tau)/\Omega'_i]$  and  $c_{gi}(3\tau + T_d) = \exp(i\delta_i\tau)c_{ei}(\tau + T_d)[-i\Omega_i \sin(\Omega'_i\tau)/\Omega'_i]$ . Following the  $\pi$  pulse, the atoms are further set adrift in another dark zone of duration  $T_d$ , where the component of the atom following trajectory  $A$  picks up a phase due to detuning. The net effect of this is that  $|\psi'_i(3\tau + 2T_d)\rangle = c_{ei}(3\tau + 2T_d)|e'_i\rangle_A + c_{gi}(3\tau + 2T_d)|g'_i\rangle_B$ , where  $c_{ei}(3\tau + 2T_d) = \exp(i\delta_i T_d)c_{ei}(3\tau + T_d)$  and  $c_{gi}(3\tau + 2T_d) = c_{ei}(3\tau + T_d)$ . By the end of this dark zone, the two trajectories converge and a third pulse of duration  $\tau$  is applied to the atoms. Therefore, the state of the atom at  $t = 4\tau + 2T_d$  is  $|\psi'_i(4\tau + 2T_d)\rangle = [c_{gi}(4\tau + 2T_d)_A|g'_i\rangle + c_{ei}(4\tau + 2T_d)_A|e'_i\rangle] + [c_{gi}(4\tau + 2T_d)_B|g'_i\rangle + c_{ei}(4\tau + 2T_d)_B|e'_i\rangle]$ , where  $c_{gi}(4\tau + 2T_d)_A = \exp(i\delta_i\tau/2)c_{ei}(3\tau + 2T_d)[-i\Omega_i \sin(\Omega'_i\tau/2)/\Omega'_i]$ ,  $c_{ei}(4\tau + 2T_d)_A = \exp(i\delta_i\tau/2)c_{ei}(3\tau + 2T_d)[\cos(\Omega'_i\tau/2) + i\delta_i \sin(\Omega'_i\tau/2)/\Omega'_i]$ ,  $c_{gi}(4\tau + 2T_d)_B = \exp(i\delta_i\tau/2)c_{gi}(3\tau + 2T_d)[\cos(\Omega'_i\tau/2) - i\delta_i \sin(\Omega'_i\tau/2)/\Omega'_i]$ , and  $c_{ei}(4\tau + 2T_d)_B = \exp(i\delta_i\tau/2)c_{gi}(3\tau + 2T_d)[-i\Omega_i \sin(\Omega'_i\tau/2)/\Omega'_i]$ .

The signal of the CRAIN formed by the  $i$ th atom is the measurement of the amplitude of state  $|g'_i\rangle$  at the end of the  $\pi/2$ -dark- $\pi$ -dark- $\pi/2$  sequence due to the interference of the components from the two paths. Since the two arms yield identical proportions of both  $|g'_i\rangle$  and  $|e'_i\rangle$ , i.e.,  $c_{gi}(4\tau + 2T_d)_A = c_{gi}(4\tau + 2T_d)_B$  and  $c_{ei}(4\tau + 2T_d)_A = -c_{ei}(4\tau + 2T_d)_B$ , the signal of the CRAIN formed is  $S_{\text{CRAIN},i} = \alpha_i$ , where  $\alpha_i = |2c_{gi}(4\tau + 2T_d)_A|^2 \leq 1$ . Since the signal of a COSAIN is the product of the signals of the individual CRAIN's formed by the constituent atoms in the ensemble [22], the signal of the resulting COSAIN is, consequently,  $S_{\text{COSAIN}} = \prod_i^N S_{\text{CRAIN},i} = \prod_i^N \alpha_i$ . However, if a phase difference is introduced between the two paths, the signal of the CRAIN's and thus the COSAIN will depend on it additionally. Assuming that an external phase  $\Delta\phi$  is introduced to the path  $A$  of the interferometer, the quantum state of the atom at  $t = 4\tau + 2T_d$  is given by  $|\psi'_i(4\tau + 2T_d)\rangle = \exp(i\Delta\phi)[c_{gi}(4\tau + 2T_d)_A|g'_i\rangle + c_{ei}(4\tau + 2T_d)_A|e'_i\rangle] + [c_{gi}(4\tau + 2T_d)_B|g'_i\rangle + c_{ei}(4\tau + 2T_d)_B|e'_i\rangle]$ . The amplitude of  $|g'_i\rangle$  will, thus, be  $S_{\text{CRAIN},i} = |1 + \exp(-i\Delta\phi)|^2\alpha_i = 4\alpha_i \cos^2(\Delta\phi/2)$ . In the case where  $\Omega_i \gg \delta_i$ ,  $\alpha_i = \frac{1}{4}$  and the signal shows the well-known  $\cos^2(\Delta\phi/2)$  dependence. The resulting COSAIN signal is, therefore,  $S_{\text{COSAIN}} = \prod_i^N 4\alpha_i \cos^2(\Delta\phi/2)$ . In the ideal situation where each atom sees the same Rabi frequency due to a uniform beam profile and there is no effective detuning experienced by the atoms,  $\alpha_i = \frac{1}{4}$  and the signal at the end of the interferometer sequence is given by  $S_{\text{COSAIN}} = \cos^{2N}(\Delta\phi/2)$ . This corresponds to the narrowing of the signal fringe by a factor proportional to  $\sqrt{N}$  as compared to the signal in a CRAIN.

In the more practical situation relevant for experimental conditions,  $\Omega_i$  and  $\delta_i$  for each atom are determined by the laser beam intensity profile, and atom trap size and temperature, as described above. To illustrate the effect of these parameters, we assume that the atoms are first cooled down using a magneto-optic trap arrangement. The trapped atoms are then held in a cigar-shaped dipole trap to further cool them down via evaporative cooling. The density of atoms in the trap is assumed to follow a Gaussian spatial distribution so that its length in the longitudinal direction is  $\xi_L$ , and its width in the transverse direction is  $\xi_T$ .

### A. Effect of velocity distribution

The Maxwell-Boltzmann velocity distribution of the ensemble is  $f_{MB}(v, T_{MB}) = \sqrt{m/2\pi k_B T_{MB}} \times \exp(-mv^2/2\pi k_B T_{MB})$ , where  $T_{MB}$  is the temperature of the trap and  $k_B$  is the Boltzmann constant. Since the ensemble undergoes interaction with a pair of counterpropagating laser beams, the Doppler shift observed by the  $i$ th atom  $\delta_i = (k_1 + k_2)v_i$  cannot be neglected compared to the Raman-Rabi frequency experienced by it. Thus, at nonzero ensemble temperatures, the signal contribution from each atom is significantly lower than the maximum amplitude possible. The signal peak value falls sharply with increasing  $N$  as illustrated in Fig. 8(a). It is also evident from Fig. 8(b) that the signal of a COSAIN varies significantly as a function of the temperature.

### B. Effect of intensity profile of laser beams

Next, we consider the effect of the Gaussian spatial distribution of the Raman beams on the COSAIN. Assuming that the beam waist size is  $w$ , the Raman Rabi frequency experienced by the  $i$ th atom of the ensemble is  $\Omega_i = \Omega_0 \exp(-2r^2/w^2)$ . Here,  $\Omega_0$  is the peak value of the Raman Rabi frequency and  $r$  is the radial distance of the  $i$ th atom from the center of the beam. We consider that the average temperature of the trapped atoms is  $T_{MB} = 0.5 \mu\text{K}$  and the peak value of the beam intensity is  $15 \text{ mW/mm}^2$  so that  $\Omega_0 = 1.9 \times 10^7 \text{ rad/s}$ . Figure 9 shows the variation of the peak value of the  $S_{\text{COSAIN}}$  with increasing value of  $\varsigma = w/\xi_T$ .

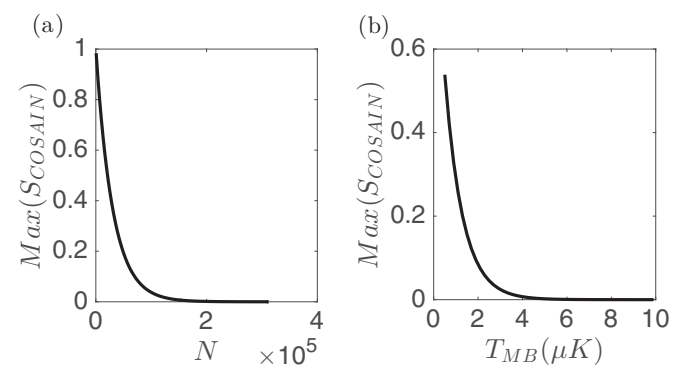


FIG. 8. (a) Variation of signal peak value with  $N$  at  $0.5 \mu\text{K}$  average temperature and rectangular intensity profile beams at  $\Omega = 1.9 \times 10^7 \text{ s}^{-1}$ . (b) Variation of signal peak value with trap temperature for  $N \approx 1.9 \times 10^4$ .

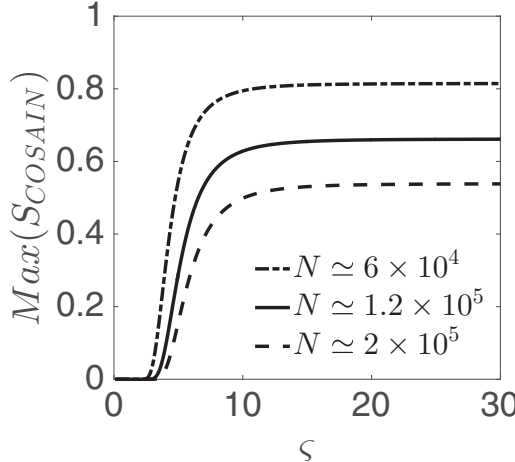


FIG. 9. Variation of the peak value of the  $S_{\text{COSAIN}}$  with increasing MOT size to beam waist ratio at  $T_{MB} = 0.5 \mu\text{K}$  for different values of  $N$ .

### C. Effect of spontaneous emission

In our analysis of the COSAIN, we have employed a model of a three-level atom where the intermediate state ( $|a, \hbar k_1\rangle$ ) is adiabatically eliminated to reduce the system to an equivalent two-level model. However, the actual population of this state is approximately  $\Omega^2/\delta^2$ , with  $\Omega = \Omega_1 = \Omega_2$ . In the time that it takes for a  $2\pi$  pulse ( $\pi/2$ - $\pi$ - $\pi/2$  sequence sans the dark zones), we can estimate that the number of spontaneous emissions that occur per atom is  $2(\Omega^2/\delta^2)\tau\Gamma \simeq 4\pi\Gamma/\delta$ . For  $\delta = 200\Gamma$ , this number is about  $6.3 \times 10^{-2}$  and increases by a factor of  $N$  for an ensemble of  $N$  atoms. Note that there is no enhancement in the rate of spontaneous emission due to superradiant effects since we are considering a dilute ensemble. Consequently, the signal for both the CRAIN and the COSAIN would deviate from the ideal one. The effect of spontaneous emission on the CRAIN can be taken into account by using the density matrix equation for a three-level system. However, in this case, it is not possible to ascribe a well-defined quantum state for each atom. This, in turn, makes it difficult to figure out the response of the COSAIN since our analysis for the COSAIN is based on using the direct product of the quantum state of each atom. For a large value of  $N$ , it is virtually impossible to develop a manageable density matrix description of the system directly in terms of the collective states. However, it should be possible to evaluate the results of such a density matrix based model for a small value of  $N$  ( $< 10$ , for example). This calculation is a subject of our future work.

For the general case of large  $N$ , one must rely on an experiment (which, in this context, can be viewed as an analog computer for simulating this problem) to determine the degree of degradation expected from residual spontaneous emission. It should be noted that the detrimental effect of spontaneous emission, for both the CRAIN and the COSAIN, can be suppressed to a large degree by simply increasing the optical detuning while also increasing the laser power. This is the approach used, for example, in reducing the effect of radiation loss of atoms in a far-off resonant trap (FORT).

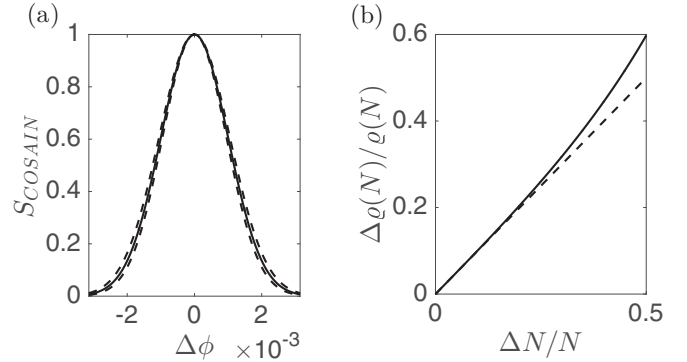


FIG. 10. (a)  $S_{\text{COSAIN}}$  for  $N = 2 \times 10^5$ . (b) Plot of  $\Delta\varrho/\varrho$  as a function of  $\Delta N/N$ .

### D. Effect of fluctuation in number of atoms

In both the CRAIN and the COSAIN, the signal is collected multiple times and averaged to increase the signal-to-noise ratio (SNR). The number of atoms in the ensemble can vary in each run. In the CRAIN, a fluctuation of  $\Delta N$  in  $N$  is reflected in the signal amplitude by the same amount while the linewidth does not change. This can be easily deduced from the fact that  $S_{\text{CRAIN}} = N \cos^2(\Delta/2)$ . Replacing  $N$  by  $\Delta N$  will change the signal. However, the FWHM which occurs at  $S_{\text{CRAIN}} = N/2$  will not change. More details on the classical and quantum noise in the CRAIN and the COSAIN are given in Sec. VI A. In this section, we discuss how the fluctuation in the number of atoms in every run of the experiment affects the signal of the COSAIN.

The signal of the COSAIN due to a fluctuation of  $\Delta N$  in  $N$  is given by  $S_{\text{COSAIN}} = \cos(\Delta\phi/2)^{2(N \pm \Delta N)}$ . Figure 10(a) shows plot of a COSAIN signal with  $N = 2 \times 10^5$ . The broken lines represent the case where  $\Delta N/N = 0.1$ . As is evident from the above discussion, the linewidth increases (decreases) with decreasing (increasing)  $\Delta N$ . However, the peak of the signal remains at unity, as opposed to the effect of inhomogeneity of field and velocity distribution. The signal linewidth of the COSAIN is approximately  $\varrho(N) = \varrho(1)/\sqrt{N}$ . A fluctuation of  $\Delta N$  in  $N$  is reflected in the linewidth uncertainty as  $\Delta\varrho(N) = \varrho(1)[(N - \Delta N)^{-1/2} - (N + \Delta N)^{-1/2}]$ . The fractional fluctuation is, therefore,  $\Delta\varrho(N)/\varrho(N) \simeq (1 - \Delta N/N)^{-1/2} - (1 + \Delta N/N)^{-1/2} = \Delta N/N + 0.625(\Delta N/N)^3 + 0.492(\Delta N/N)^5 + O[(\Delta N/N)^6]$ . This relation is depicted in Fig. 9(b) by the broken line. For small  $\Delta N/N$ , the fractional change in FWHM is  $\Delta\varrho(N)/\varrho(N) \simeq \Delta N/N$  to a good approximation, as shown by the solid line in Fig. 10(b).

## IV. DETAILS OF PROPOSED EXPERIMENT

In order to illustrate the complete picture of the proposed experiment, we consider  $^{87}\text{Rb}$  as the atomic species as an example. We assume a scenario where the atoms will be evaporatively cooled to a temperature of about  $2 \mu\text{K}$ , in a dipole force trap [33] and then released. The Raman pulses will be applied while these atoms are falling under gravity. Each Raman pulse will consist of a pair of counterpropagating, right circularly polarized ( $\sigma_+$ ) beams. One of these beams is red detuned from the  $F=1 \rightarrow F'=1$  transition in the  $D1$

manifold by  $\sim 1.5$  GHz, and the other one is red detuned by the same amount from  $F=2 \rightarrow F'=1$  transition, also in the  $D1$  manifold. The second Raman beam is generated from the first one by a modulator which is driven by an ultrastable frequency synthesizer (FS) tuned to 6.834 682 610 9 GHz. We assume that the atoms are initially in the  $F=1, m_F=0$  state.

Thus, the states  $|g\rangle$  and  $|e\rangle$  in Fig. 1(a) would correspond to the hyperfine ground states  $F=1, m_F=0$  and  $F=2, m_F=0$ , respectively. The Raman transitions occur via the excited states  $F'=1, m_{F'}=1$  and  $F'=2, m_{F'}=1$ . The resulting four-level system can be reduced to a two-level system in the same way as that for the  $\Lambda$  system by adiabatically eliminating the excited states together. The resulting system has a coupling rate that is the sum of the two Raman Rabi frequencies. The laser intensities are adjusted to ensure that the light shifts of  $|g\rangle$  and  $|e\rangle$  are matched.

At the end of the  $\pi/2-\pi-\pi/2$  sequence, a probe beam is applied to measure the amplitude of one of the collective states, via the method of zero-photon detection. To explain this, we revert to the three-level model of the atom, and first consider a situation where the atomic ensemble is contained in a single-mode cavity with volume mode  $V$ , cavity decay rate  $\gamma_c$ , resonant at  $\omega_1$ . The cavity is coupled to the transition  $|a\rangle \rightarrow |g\rangle$  with coupling rate  $g_c = |e\langle r\rangle|E/\hbar$ , where  $|e\langle r\rangle|$  is the dipole moment of the atom and  $E = \sqrt{2\hbar\omega_1/\epsilon_0 V}$ . If an off-resonant classical laser pulse of frequency  $\omega_2$  is applied, the cavity causes Raman transitions to occur between the collective states  $|E_n\rangle$  and  $|E_{n-1}\rangle$  with the coupling rates  $\Omega'_n = \sqrt{N-n+1}\sqrt{n}\Omega'$ , where  $\Omega' = \Omega_2 g_c/2\Delta$ . This is illustrated in Fig. 11(a).

In the bad cavity limit ( $\gamma_c \gg \sqrt{N}\Omega'$ ), the Raman transitions will still occur. However, the system will not reabsorb the emitted photon, i.e., the transition from  $|E_n\rangle$  to  $|E_{n-1}\rangle$  will occur, but not vice versa. The field of such a photon is  $E = \sqrt{2\hbar\omega_1/\epsilon_0 \mathcal{A}cT}$ , where  $\mathcal{A}$  is the cross-sectional area of the ensemble and  $T$  the interaction time [34]. This limit applies here since there is no cavity, so that the stimulated Raman scattering is an irreversible process that can be modeled as a decay with an effective decay rate that is unique to each  $|E_n\rangle$ . The decay rate from  $|E_N\rangle$  is  $\gamma_N = 4NL|g_c\Omega_2|^2/\Delta^2c = N\gamma_{sa}$ , where  $\gamma_{sa} = 16L\Omega'^2/c$  [35], and that for  $|E_n\rangle$  is  $\gamma_n = n(N+1-n)\gamma_{sa}$ .

The read beam is extracted from the source and is passed through a 99:1 ( $R/T$ : the ratio of the intensity reflectivity  $R$  to the intensity transmittivity  $T$ ) nonpolarizing beam splitter  $B1$  before hitting the ensemble. The probability of counterpropagating photons emitted from this interaction is determined by the resonant optical density of the ensemble. The direction of signal emission and the role of optical density are discussed further in Sec. IV. The emitted photons pass through  $B1$  and, subsequently, through a half-wave plate. The emitted photons and the probe beam are recombined by another 99:1 beam splitter  $B2$  and sent to a high-speed detector, which generates a dc voltage along with a signal at the beat frequency  $\sim 6.834$  GHz with an unknown phase. This signal is bifurcated and one part is multiplied by the FS signal, while the other is multiplied by the FS signal phase shifted by  $90^\circ$ . The signals are then squared before being combined and sent through a low-pass filter (LPF) to derive the dc voltage. This dc voltage is proportional to the number of scattered photons. A lower limit

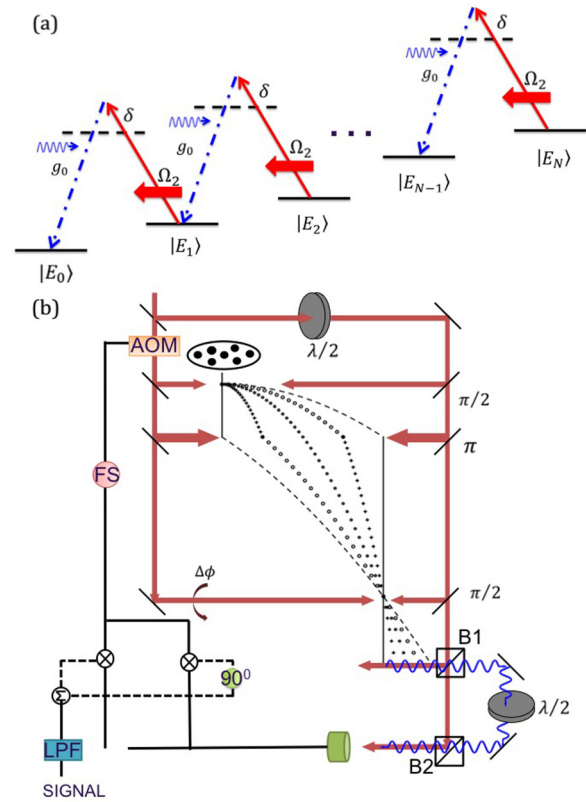


FIG. 11. (Color online) (a) Interaction between the collective states in the bad cavity limit. (b) Atomic interferometer experiment for an ensemble of  $\Lambda$ -type atoms for detecting state  $|E_0\rangle$ .

is set for the voltage reading and any values recorded above it will indicate the presence of emitted photons. The duration of the probe beam is set at  $\gamma_N T = 10$ , where  $\gamma_N = N\gamma_{sa}$  is the slowest decay rate, to ensure that even the longest-lived state is allowed to decay almost completely. If no photon is emitted, the voltage will read below the limit, indicating that the ensemble is in state  $|E_0\rangle$ . If the ensemble is in any other collective state, at least one photon will be emitted. This process is repeated  $\mathcal{M}$  times for a given value of  $\Delta\phi$ . The fraction of events where no photons are detected will correspond to the signal for this value of  $\Delta\phi$ . This process is then repeated for several values of  $\Delta\phi$ , producing the signal fringe for a COSAIN. The experimental scheme is illustrated in Fig. 11(b).

### Role of optical density

In this paper, we have assumed that the ensemble is cigar shaped. This particular choice of configuration is made to achieve the optimum optical density required for realizing the detection scheme discussed above. Consider a four-wave mixing process where three laser beams with wave vectors  $\vec{k}_1$ ,  $\vec{k}_2$ , and  $\vec{k}_3$  interact with a nonlinear medium. The process can be viewed as the scattering of the  $\vec{k}_3$  beam, for example, off the grating formed by the interference between the  $\vec{k}_1$  and  $\vec{k}_2$  beams. Efficient phase matching (which is akin to Bragg matching) then requires that the generated beam with a wave vector  $\vec{k}_4$  will satisfy the condition that  $\vec{k}_1 + \vec{k}_2 = \vec{k}_3 + \vec{k}_4$ . The

detection process for the COSAIN can be viewed as a time-delayed four-wave mixing process. The coherence induced in the ensemble has a spatial variation (i.e., a phase grating) proportional to  $\exp[i(\vec{k}_1 + \vec{k}_2)]$ . In the detection zone, we apply a readout field with a wave vector  $\vec{k}_3 = \vec{k}_2$ . Thus, the scattering field will have a wave vector  $\vec{k}_4 = \vec{k}_1$ . This implied that the photon would be scattered in the direction opposite to that of the probe.

In such a scattering process, the fraction of photon that would be scattered in directions other than the direction dictated by exact phase matching is determined by the resonant optical density of the ensemble, which is given by  $\rho = \sigma n \xi_L$  [34]. Here,  $\sigma \simeq (\lambda/2)^2$  is the resonant scattering cross section,  $n$  is the density, and  $\xi_L$  is the interaction length. The fraction of the signal captured by the detector would then be  $(\rho - 1)/\rho$ . This effect can be incorporated in the detector quantum efficiency by writing it as  $\eta = \eta_0(\rho - 1)/\rho$ , where  $\eta_0$  is the ideal quantum efficiency of the detector.

The proposed detection scheme demands that  $\rho \geq 75$ , so that at least 98% of the emitted photons are captured, assuming an ideal detector. As discussed in Sec. III A, the signal amplitude falls exponentially with increasing ensemble temperature, and  $N$ . However, the ensemble must not reach the vicinity of critical density at low temperatures. Considering these factors, we choose  $N = 2.6 \times 10^4$ ,  $\xi_L = 1$  mm, and  $\xi_T = 10 \mu\text{m}$ , deriving  $\rho = 78.45$  for the  $D1$  manifold of  $^{87}\text{Rb}$ .

## V. ALTERNATE EXPERIMENTAL SCHEME

The limitation on cooling the ensemble to reduce the effects of Doppler shift restricts the number of atoms. In turn, this restricts the optical density that can be achieved for an ensemble undergoing the COSAIN sequence. Here, we discuss an alternate experimental scheme that raises the effective optical density of the ensemble. In this scheme, each atom is modeled as a four-level system, as shown in Fig. 12(a). The metastable states  $|g\rangle$  and  $|e\rangle$  are coupled via two intermediate states  $|a\rangle$  and  $|b\rangle$ . This four-level system can be reduced to an effective three-level system in the  $\Lambda$  configuration. Each Raman pulse will consist of a pair of  $s$ -polarized and  $p$ -polarized beams, applied in counterpropagating directions. We assume that the  $s$ -polarized beam is moving in the  $+z$  direction, and thus, can be represented as  $\mathbf{E}_s = (\hat{\sigma}^+ \tilde{E}_{s0} + \hat{\sigma}^- \tilde{E}_{s0}) \cos(\omega_s t - k_s z) = \hat{\mathbf{s}} E_{s0} \cos(\omega_s t - k_s z)$ . Similarly, the  $p$ -polarized beam is moving in the  $-z$  direction, and thus, can be represented as  $\mathbf{E}_p = (\hat{\sigma}^+ \tilde{E}_{p0} - \hat{\sigma}^- \tilde{E}_{p0}) \cos(\omega_p t + k_p z) = \hat{\mathbf{p}} E_{p0} \exp(i\pi/2) \cos(\omega_p t - k_p z)$ . Here,  $\omega_s$  and  $\omega_p$  are the laser frequencies, and  $E_{s0}$  and  $E_{p0}$  are the amplitudes of the electric field of each laser beam. After making the rotating-wave approximation and rotating-wave transformation, the atom-laser interaction Hamiltonian elements are  $\langle g | \hat{\rho} \cdot \hat{\sigma}^+ \tilde{E}_{s0} | a \rangle$ ,  $\langle g | \hat{\rho} \cdot \hat{\sigma}^- \tilde{E}_{s0} | b \rangle$ ,  $\langle e | \hat{\rho} \cdot \hat{\sigma}^+ \tilde{E}_{p0} | a \rangle$ ,  $\langle e | -\hat{\rho} \cdot \hat{\sigma}^- \tilde{E}_{p0} | b \rangle$ , and the corresponding complex conjugates. Here,  $\hat{\rho} = x\hat{\mathbf{x}} + y\hat{\mathbf{y}} + z\hat{\mathbf{z}} = \rho_{\sigma^+} \hat{\sigma}^+ + \rho_{\sigma^-} \hat{\sigma}^- + z\hat{\mathbf{z}}$ . The Hamiltonian can be further simplified to  $H = \rho_{ga} \tilde{E}_{s0} |g\rangle \langle a| + \rho_{gb} \tilde{E}_{s0} |g\rangle \langle b| + \rho_{ea} \tilde{E}_{p0} |e\rangle \langle a| - \rho_{eb} \tilde{E}_{p0} |e\rangle \langle b| + \text{c.c.}$

For concreteness, we use the  $D1$  line of  $^{87}\text{Rb}$  to illustrate the mechanism behind this scheme. Thus, the states  $|g\rangle$  and  $|e\rangle$  in the left part of Fig. 12(a) would

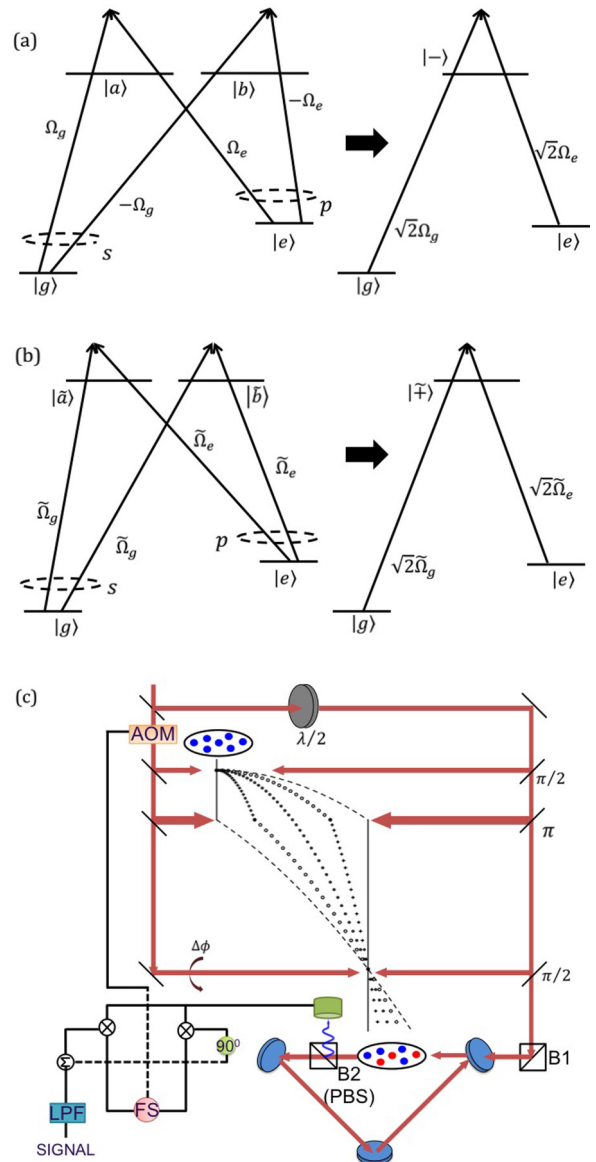


FIG. 12. (Color online) (a) Raman transitions between  $|g \equiv F = 1, m_F = 0\rangle$  and  $|e \equiv F = 2, m_F = 0\rangle$  via  $|a \equiv F' = 1, m_{F'} = -1\rangle$  and  $|b \equiv F' = 1, m_{F'} = 1\rangle$ , (b) Raman transitions between  $|g \equiv F = 1, m_F = 0\rangle$  and  $|e \equiv F = 2, m_F = 0\rangle$  via  $|\tilde{a} \equiv F' = 2, m_{F'} = -1\rangle$  and  $|\tilde{b} \equiv F' = 2, m_{F'} = 1\rangle$ , (c) Alternate experimental scheme to increase the resonant optical density of the ensemble by introducing a ring cavity in the detection zone.

correspond to the hyperfine ground states  $F = 1, m_F = 0$  and  $F = 2, m_F = 0$ , respectively. The Raman transitions occur via the excited states  $|a \equiv F' = 1, m_{F'} = -1\rangle$  and  $|b \equiv F' = 1, m_{F'} = 1\rangle$ . For this particular choice of levels,  $\rho_{ga} = -\rho_{gb} = \rho_{ea} = \rho_{eb} = |\rho_0|$ ,  $|\rho_0 \tilde{E}_{s0}| = \hbar \Omega_g/2$ , and  $|\rho_0 \tilde{E}_{p0}| = \hbar \Omega_e/2$ . The atom-laser interaction Hamiltonian in this case is, therefore,  $H = \hbar(\Omega_g |g\rangle \langle a| - \Omega_g |g\rangle \langle b| + \Omega_e |e\rangle \langle a| - \Omega_e |e\rangle \langle b|)/2 + \text{c.c.}$  This four-level system can be reduced to an equivalent three-level model by rotating the  $\{|a\rangle, |b\rangle\}$  Hilbert sub-space by  $\pi/4$ . The reduced Hamiltonian  $H_{\text{red}}$  is given by  $H_{\text{red}} = \hbar(\Omega_g |g\rangle \langle -| + \Omega_e |e\rangle \langle -|)/\sqrt{2} + \text{c.c.}$ , where  $|-\rangle = (|a\rangle - |b\rangle)/\sqrt{2}$ , as illustrated in the right part of Fig. 12(a). The  $D1$  line

of  $^{87}\text{Rb}$  is also coupled via  $|\tilde{a} \equiv F' = 2, m_{F'} = -1\rangle$  and  $|\tilde{b} \equiv F' = 2, m_{F'} = 1\rangle$ . In this case,  $-\rho_{g\tilde{a}} = -\rho_{g\tilde{b}} = -\rho_{e\tilde{a}} = \rho_{e\tilde{b}} = |\tilde{\rho}_0|$ ,  $|\tilde{\rho}_0 \tilde{E}_{s0}| = \hbar\tilde{\Omega}_g/2$ , and  $|\tilde{\rho}_0 \tilde{E}_{p0}| = \hbar\tilde{\Omega}_e/2$ . Thus, the Hamiltonian is  $\tilde{H} = -\hbar(\tilde{\Omega}_g |g\rangle \langle \tilde{a}| + \tilde{\Omega}_g |g\rangle \langle \tilde{b}| + \tilde{\Omega}_e |e\rangle \langle \tilde{a}| + \tilde{\Omega}_e |e\rangle \langle \tilde{b}|)/2 + \text{c.c.}$  The reduced equivalent three-level Hamiltonian is  $\tilde{H}_{\text{red}} = \hbar(\tilde{\Omega}_g |g\rangle \langle \tilde{+}| + \tilde{\Omega}_e |e\rangle \langle \tilde{+}|)/\sqrt{2} + \text{c.c.}$ , where  $|\tilde{+}\rangle = (|\tilde{a}\rangle + |\tilde{b}\rangle)/\sqrt{2}$ . These transitions are shown in the Fig. 12(b). Thus, the system is equivalent to two  $\Lambda$  systems, each with a different common mode detuning. Adiabatic elimination of the  $|\langle -\rangle$  and the  $|\langle \tilde{+}\rangle$  states would produce the effective two-level transition between  $|g\rangle$  and  $|e\rangle$ , just as in the case of excitations with circularly polarized fields described earlier.

At the end of the  $\pi/2$ -dark- $\pi$ -dark- $\pi/2$  sequence, the ensemble is introduced into a ring cavity of finesse  $\mathcal{F}$ . The read beam is extracted from the  $p$ -polarized beam and enters the cavity through port  $P1$ , as illustrated in Fig. 12(c). The scattered photons, which will be  $s$  polarized, are extracted with a polarizing beam splitter  $B2$ . Note that this type of extraction is not possible if the interferometer were to be realized with circularly polarized beams. The repeated interaction of the ensemble with the read beam increases the effective resonant optical density of the ensemble to  $\mathcal{F}\rho/\pi$ . Since the ensemble is falling under gravity through the course of the experiment, the cavity mode size must be reasonably large to accommodate this motion. We assume that the length of the first dark zone is 1 cm, and that the distance between the last  $\pi/2$  pulse and the read beam is also 1 cm. The duration of the read beam,  $T$  is set at  $\gamma_N T = 10$ , where  $\gamma_N = N\gamma_{\text{sa}}$  is the slowest decay rate, to ensure that even the longest-lived state is allowed to decay completely. It can be shown that for  $N = 2.6 \times 10^4$ ,  $T \simeq 3.3$  ms, so that the distance traveled by the ensemble during the interrogation period is  $\simeq 3.3$  mm. The cavity mode size must be at least twice as much as this distance.

## VI. PERFORMANCE OF THE COSAIN COMPARED TO THAT OF THE CRAIN

In order to compare the performance of the COSAIN to that of the CRAIN, we analyze the stability of the phase difference measured by them by investigating the fluctuation that has both quantum mechanical and classical components, i.e.,  $\delta\Delta\phi|_{\text{total}} = (\Delta S_{QM} + \Delta S_{\text{classical}})/|\partial S/\partial\Delta\phi|$ , where  $S(\Delta\phi)$  is the signal. Since the signal depends on the phase, the fluctuation is not necessarily constant. Therefore, there is no unique value of signal-to-noise ratio (SNR) to compare unless the COSAIN and the CRAIN are compared at a particular value of the phase difference. Thus, the fluctuations must be compared as a function of  $\Delta\phi$ . In Sec. VI A, we discuss in detail the quantum fluctuation due to quantum projection noise  $\Delta P = \sqrt{P(1 - P)}$  [36], where  $P$  is the population of the state being measured, and the classical noise in the long-term regime. Since the measure of the signal depends on counting zero photon events, the efficiency of the high-speed detector affects the signal amplitude and width. In Sec. VI B, we discuss the effect of the detector efficiency on the COSAIN signal. In Sec. VI C, we discuss the collection efficiency of the COSAIN as a measure of its performance as compared to the CRAIN. The CRAIN suffers from imperfect collection efficiency due

to the latter's dependence on experimental geometry. On the other hand, the collection efficiency of the COSAIN is close to unity owing to the fact that the fluorescence of photons is collected through coherent Raman scattering. As a result, for the same number of atoms detected per unit time, the COSAIN is expected to outperform the CRAIN by as much as a factor of 10.

### A. Effect of quantum and classical noise

For the COSAIN to be a useful device for practical metrology, it must outperform the CRAIN. To explore this, we compare their stability in the short-term and the long-term regimes. The stability of an interferometer is determined by the fluctuations in  $\Delta\phi$  that have both quantum mechanical and classical components. The phase difference  $\Delta\phi$  (expressed in radians) is proportional to the rate of rotation of the gyroscope  $\Omega_G$  (see Sec. II). Thus,  $\Delta\phi = \mu\Omega_G$ , where  $\mu$  depends on the area of the interferometer and mass of the single atom.

In the CRAIN described above, the signal is a measure of the probability of finding the atom in state  $|g\rangle$ ,  $P_g = \cos^2(\mu\Omega_G/2)$ . The signal is detected by probing the desired state for a duration of time. If  $\tilde{N}$  is the number of atoms per unit time and  $T$  is the interrogation period, then the net signal is  $S_{\text{CRAIN}} = \tilde{N}TP_g$ . For comparison, we set the number of atoms per trial in the COSAIN  $N$ , multiplied by the number of trials  $M$ , to equal  $\tilde{N}T$ . Therefore,  $S_{\text{CRAIN}} = MN\cos^2(\mu\Omega_G/2)$ . Since the fluctuation in  $MN$  is  $\sqrt{MN}$ , the quantum mechanical variance of the signal is  $\Delta(S_{\text{CRAIN},QM}) = \sqrt{MN}\sin(\mu\Omega_G)/2$  since the projection noise in a single two-level atomic system is  $\Delta S_{\text{CRAIN}} = \sqrt{P_g(1 - P_g)}$  [36]. In the case where the probability of finding the atom in  $|g\rangle$  is 0 or 1, the projection noise vanishes. On the other hand, the projection noise is at its peak value when  $P_g = \frac{1}{2}$ . The slope of the signal is, therefore,  $\partial S_{\text{CRAIN}}/\partial\Omega_G = -MN\sin(\mu\Omega_G)/(2\gamma_{\text{sa}})$ , where  $\gamma_{\text{sa}} = 1/2\mu$  is the linewidth. Assuming ideal quantum efficiency of the detection process, the fluctuation in the rate of rotation can be written as  $\delta\Omega_G|_{\text{total}} = |\Delta S_{QM} + \Delta S_{\text{classical}}|/|\partial S_{\text{CRAIN}}/\partial\Omega_G|$ , which may be considered as noise ( $\Delta S$ ), over the rotational variation of signal (RVS) which is  $(\partial S_{\text{CRAIN}}/\partial\Omega_G)$ . In the following text, we consider first the effect of quantum noise. The quantum rotation-rate fluctuation (QRF) for a CRAIN may be written as

$$\delta\Omega_G|_{QM,\text{CRAIN}} = \left| \frac{\Delta S_{QM}}{(\partial S_{\text{CRAIN}}/\partial\Omega_G)} \right| = \frac{\gamma_{\text{sa}}}{\sqrt{MN}}. \quad (8)$$

It is, thus, merely a coincidence that the QRF turns out to be constant in a CRAIN. Contrary to popular perception, the QRF of an interferometer is, therefore, not fundamentally the linewidth divided by the SNR. It should be evident from the above discussion that the signal is not given by  $MN$ , and the noise is not given by  $\sqrt{MN}$ . Instead, they both depend on  $\Omega_G$ .

In devices where the QRF is not a constant, as we will show for a COSAIN, it is thus imperative that we carry out an analysis of the QRF in a manner analogous to the analysis for the CRAIN shown above. Thus, we will adopt the approach that the net rotation-rate fluctuation  $\delta\Omega_G$  should be thought of as the ratio of the noise to the RVS. This approach should be adopted universally for all metrological devices. Of course, for devices where the relevant quantity is not the rotation rate,

the definition should be adapted accordingly. For example, in a clock that measures frequency, the relevant quantity can be expressed as follows: net frequency fluctuation is the ratio of the noise to the spectral variation of signal (SVS).

Following this approach, we calculate the net rotation-rate fluctuation of the COSAIN and compare it to that of the CRAIN. We will first calculate the quantum fluctuation which is relevant in the short-term regime, and then the classical fluctuation, which dominates in the long-term regime. The signal of a COSAIN for  $M$  trials is  $S_{\text{COSAIN}} = M P_{E0} = M \cos^{2N}(\mu\Omega_G/2)$ , and the projection noise is  $\Delta P_{E0} = \sqrt{P_{E0}(1 - P_{E0})}$  for a single trial, so that  $\Delta P_{E0} = \sqrt{M} \sqrt{P_{E0}(1 - P_{E0})}$  for  $M$  trials. Thus, the total quantum mechanical noise in the signal is

$$\Delta P_{E0} = \sqrt{M} \cos^N(\mu\Omega_G/2) \sqrt{1 - \cos^{2N}(\mu\Omega_G/2)}, \quad (9)$$

and the RVS is

$$\partial S_{\text{COSAIN}}/\partial\Omega_G = -MN \cos^{2N-1}(\mu\Omega_G/2) \sin(\mu\Omega_G/2)/\gamma_{\text{sa}}. \quad (10)$$

Therefore, the QRF in the COSAIN is given by

$$\delta\Omega_{G(QM,\text{COSAIN})} = \frac{\gamma_{\text{sa}}}{N\sqrt{M}} \frac{\sqrt{\sec^{2N}(\mu\Omega_G/2) - 1}}{\tan(\mu\Omega_G/2)}. \quad (11)$$

Thus, unlike the CRAIN, the phase fluctuation in a COSAIN is not constant and depends on  $\Omega_G$  and, thus, on  $\Delta\phi$ . We consider first the limiting case of  $\Omega_G \rightarrow 0$ . Using Taylor expansion, it is evident that  $\delta\Omega_{G(QM,\text{COSAIN})} = \gamma_{\text{sa}}/\sqrt{MN}$ , which is the same as that of a CRAIN. This can be understood physically by noting that while the fringe width becomes much narrower for the COSAIN, the SNR also decreases due to the fact that a single observation is made for all  $N$  atoms in a given trial. The QRF for the COSAIN, given in Eq. (11), is smallest as  $\Omega_G \rightarrow 0$  and increases as  $\Omega_G$  moves away from zero. The ratio of the QRF for the CRAIN to that of the COSAIN is plotted as a function of  $\Omega_G$  in the left side of Fig. 13 for  $M = 1000$  and  $N = 10^4$ . Here, the vertical bars indicate the FWHM of the COSAIN signal. It is clear from this plot that the QRF for the COSAIN increases significantly as we move away from resonance. However, since a servo will keep the value of  $\Omega_G$

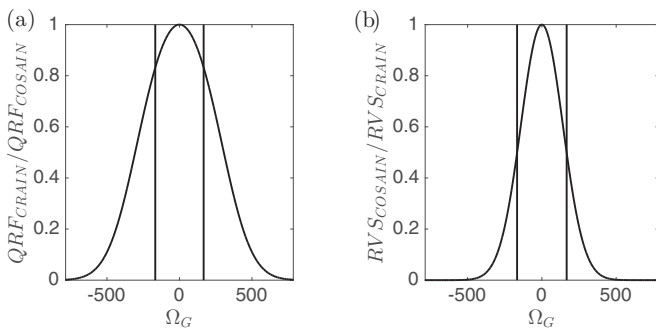


FIG. 13. (Left) Ratio of the QRF in the CRAIN to the QRF in the COSAIN, for  $M = 1000$  and  $N = 10^4$ . It should be noted that the fluctuation in the CRAIN is independent of  $\Omega_G$  while that of the COSAIN varies significantly with it. (Right) Ratio of the RVS of the COSAIN to the RVS of the CRAIN for  $M = 1000$  and  $N = 10^4$ . The vertical lines in the plots show where the FWHM of  $S_{\text{CRAIN}}$  are.

confined to be close to zero, the phase stability of the COSAIN, under quantum noise limited operation, should be very close to that of the CRAIN, assuming that all the other factors remain the same.

The classical rotation-rate fluctuation (CRF)  $\delta\Omega_G|_{\text{classical}} = \Delta S_{\text{classical}}/(\partial S/\partial\Omega_G)$  is the limiting factor in the long-term stability. While the quantum fluctuation is dominated by quantum projection noise, the classical noise is dominated by noise in the electronic and the mechanical components employed to generate the interferometer signal. Since the pieces of equipment used in the development of both the COSAIN and CRAIN suffer from similar noise issues, the variance  $\Delta S$  is expected to be of the same order of magnitude for both interferometers. On the other hand, the RVS ( $\partial S/\partial\Omega_G$ ) is not the same, as was shown previously. The ratio of the RVS of the COSAIN to the RVS of the CRAIN is

$$\frac{\partial S_{\text{COSAIN}}/\partial\Omega_G}{\partial S_{\text{CRAIN}}/\partial\Omega_G} = \frac{\cos^{2N}(\mu\Omega_G/2)}{\cos^2(\mu\Omega_G/2)} = \frac{P_{E0}}{P_g}, \quad (12)$$

and is plotted in Fig. 8 (right). With  $\Delta S_{\text{classical,COSAIN}} \sim \Delta S_{\text{classical,CRAIN}}$ , the ratio of the CRF of the COSAIN to that of the CRAIN can be written as

$$\frac{\delta\Omega_{G(\text{classical,COSAIN})}}{\delta\Omega_{G(\text{classical,CRAIN})}} \sim \frac{\cos^2(\mu\Omega_G/2)}{\cos^{2N}(\mu\Omega_G/2)}. \quad (13)$$

Similar to the ratio of the two interferometers in QRF, Eq. (13) is smallest as  $\Delta\phi \rightarrow 0$  and increases as  $\Delta\phi$  moves away from resonance. Thus, with respect to both quantum and classical sources of noise, the COSAIN must be operated near  $\Delta\phi \simeq 0$  for optimal performance.

## B. Effect of detector efficiency

The key aspect of the COSAIN is the measurement of the amplitude of  $|E_0\rangle$ , which indicates that each of the atoms in the ensemble is individually in  $|g\rangle$ . The probe beam is applied to the ensemble, which is in the quantum state  $|\Psi\rangle = c_0 |E_0\rangle + \sum_{n=1}^N |E_n\rangle$ . Interaction between the probe beam, the ensemble, and the free-space vacuum modes on the other leg would lead to production of photons unless  $c_0 = 1$  and  $c_n = 0$  for all  $n$ . These photons are detected using a heterodyning technique, as described in Sec. II. The voltage output of the heterodyning system is proportional to the amplitude of the electric field corresponding to the photons.

In general, one or more photons are produced as  $|E_n\rangle$  decays to  $|E_{n-1}\rangle$  and subsequent states. The time needed for these photons to be produced depends in the vacuum and probe field induced Raman transition rates between  $|E_n\rangle$  and  $|E_{n-1}\rangle$ . If we assume perfect efficiency for detecting each of these photons, and wait for a time long compared to the inverse of the weakest of these transition rates, then the detection of no photons implies that the system is in state  $|E_0\rangle$ . In practical experimental conditions, we can choose a small threshold voltage at the output of the heterodyning system as an indicator of null detection. Thus, any signal below this threshold would be viewed as detection of the quantum system in the  $|E_0\rangle$  state, and all signals above this threshold would be discarded. The number of events below this threshold for  $M$  trials carried out with all the parameters of the experiment unchanged, is the derived signal for the COSAIN. After collecting data for all

the values of  $\Delta\phi$  that are of interest, the result would ideally yield the plot of the COSAIN signal  $S_{\text{COSAIN}} = |c_0|^2$ , averaged over  $\mathcal{M}$  trials. However, with a fractional detector efficiency and finite detection period, the signal would deviate from the ideal result.

Consider first the effect of the detection period. Given the decay rate of the off-resonant Raman process  $\gamma_n = n(N + 1 - n)\gamma_{\text{sa}}$ , the probability that  $|E_n\rangle$  will produce zero photons during the measurement period  $T$  is  $P_{0,n} = e^{-\gamma_n T}$ . Thus, the total probability of zero-photon emission (which should vanish ideally for any  $c_n \neq 0$ ) is given by  $P_0 = \sum_{n=1}^N |c_n|^2 e^{-\gamma_n T}$ . The COSAIN signal  $S_{\text{COSAIN}}$  is the total probability of finding zero photons during  $T$ , and can be expressed as  $S_{\text{COSAIN}} = |c_0|^2 + \sum_{n=1}^N |c_n|^2 e^{-\gamma_n T}$ . Noting that  $\gamma_0 = 0$ , we can rewrite this as  $S_{\text{COSAIN}} = \sum_{n=0}^N |c_n|^2 e^{-\gamma_n T}$ . The lower and upper bounds of  $S_{\text{COSAIN}}$  can be established by considering the strongest and the weakest effective decay rates. The strongest decay rate occurs for the middle state  $\gamma_{N/2} = (N/2)(N/2 + 1)\gamma_{\text{sa}} \approx (N^2/4)\gamma_{\text{sa}}$ , where  $N \gg 1$  approximation has been made. With the substitution of the largest decay rate for each  $|E_n\rangle$  into the equation for  $S_{\text{COSAIN}}$ , the lower bound is set by

$$P_L = |c_0|^2 + (1 - |c_0|^2) \exp(-N^2\gamma_{\text{sa}}T/4). \quad (14)$$

On the other hand, the weakest decay rate is exhibited when  $n = N$ , making the upper bound on the signal

$$P_U = |c_0|^2 + (1 - |c_0|^2) \exp(-N\gamma_{\text{sa}}T). \quad (15)$$

The signal of the COSAIN  $S_{\text{COSAIN}}$  produced in time  $T$  will lie somewhere between  $P_L$  and  $P_U$ .

Consider next the effect of the nonideal detection efficiency of the heterodyning scheme. For concreteness, we define  $\eta$  as the efficiency of detecting a single photon. In practice, this parameter will depend on a combination of factors, including the quantum efficiency of the high-speed photon detector and the overlap between the probe laser mode and the mode of the emitted photon. For the present experiment, we are only interested in knowing whether at least one photon is detected, and not in the actual number of photons. When more photons are emitted, the detector will have a better chance of observing a nonzero signal, and hence distinguish dark counts from the rest with more certainty. For example, if three photons are emitted in time  $T$ , then four different outcomes are possible:

- (i) All three photons are detected, with probability  $\eta^3$ .
- (ii) Two of the photons are detected with probability  $\eta^2(1 - \eta)$ ; this can occur for any two of the photons, so the multiplicity is 3.
- (iii) One photon is detected, with probability  $\eta(1 - \eta)^2$  and multiplicity of 3.
- (iv) No photons are detected, with probability  $\epsilon^3 \equiv (1 - \eta)^3$ .

The sum of these probabilities is 1. The probability that at least one photon is detected is thus  $(1 - \epsilon^3)$ . For any state  $n \neq 0$ , the probability of detecting at least one photon is, therefore,  $(1 - \epsilon^n)$ .

Moreover, we must also consider how the effective detection efficiency is influenced by the fact that the collective states decay at different rates. Specifically, the  $n$  level for  $n > 0$  might produce  $N - n$  photons,  $N - n - 1$  photons, down to zero photons, depending on the length of the measurement time and

the effective decay rate. If the system is in  $|E_3\rangle$ , for example, it can produce up to three photons but with probabilities that change over  $T$ . For a given time  $T$ ,  $|E_3\rangle$  evolves into a sum of the states  $|E_3\rangle \rightarrow \sum_{k=0}^3 a_{n,k}(T) |E_k\rangle$ , where the coefficient  $a_{n,k}(T)$  depends on the effective decay rate that is specific to each state, and changes as the states evolve in time. Thus, the probability of detecting at least one photon is

$$P = \sum_{n=1}^{N-1} |c_n|^2 \sum_{k=n}^N (1 - \epsilon^{k-n}) |a_{n,k}(T)|^2. \quad (16)$$

Therefore, the probability of detecting no photon is

$$S_{\text{COSAIN}} = 1 - P = 1 - \sum_{n=1}^{N-1} |c_n|^2 \sum_{k=n}^N (1 - \epsilon^{k-n}) |a_{n,k}(T)|^2. \quad (17)$$

The numerical analysis for a large number of atoms is tedious and scales as at least  $(N - 1)!$  for the COSAIN. However, we can take the worst case scenario to serve as the upper bound for the signal. The worst case occurs when only a single photon is produced as a result of  $|E_n\rangle$  decaying to only the  $|E_{n-1}\rangle$  state, so that the index of the second summation stops at  $k = n - 1$ . In this case, we can write  $|a_{n,n-1}(T)| = (1 - e^{-\gamma_n T})$  and the signal becomes

$$S_{\text{COSAIN}} = |c_0|^2 + \epsilon(1 - |c_0|^2) + \eta \sum_{n=1}^N |c_n|^2 e^{-\gamma_n T}. \quad (18)$$

Using the approach we employed in arriving at Eqs. (14) and (15), we now consider the strongest and the weakest decay rates for single-photon production to arrive at the lower and upper bounds of the zero-photon count signal:

$$P_L = 1 - \eta(1 - |c_0|^2)(1 - e^{-N^2\gamma_{\text{sa}}T/4}), \quad (19)$$

$$P_U = 1 - \eta(1 - |c_0|^2)(1 - e^{-N\gamma_{\text{sa}}T}). \quad (20)$$

Figure 14 shows the plot of the ideal  $S_{\text{COSAIN}}$   $P_L$  and  $P_U$  over a variation in  $\Delta\phi$  for different values of detector efficiencies and detection times for  $N = 10\,000$ . It can be seen from the plots that the upper and lower bounds on the signal coincide with the ideal signal in the vicinity of  $\Delta\phi \rightarrow 0$ . For a larger size of the ensemble, a longer detection time ensures that the gap between the bounds decreases and that they are closer to the ideal signal.

If we set  $\gamma_{\text{sa}}T = 1$ , the signal depends on  $\eta$  as

$$S_{\text{COSAIN}} \simeq 1 - \eta[1 - \cos^{2N}(\Delta\phi/2)] \quad (21)$$

for large  $N$  and  $\mathcal{M} = 1$ . Hence, we can calculate the QRF for the COSAIN to see how it depends on the detector efficiency, and how it compares to the CRAIN. For the CRAIN, it is straightforward to show that with  $S_{\text{CRAIN}} = \eta N \cos^2(\Delta\phi/2)$ , the quantum mechanical noise in the signal is  $\Delta S_{\text{CRAIN}} = \sqrt{\eta N} \cos(\Delta\phi/2) \sin(\Delta\phi/2)$  and the RVS is  $|\partial S_{\text{CRAIN}}/\partial \Omega_G| = (\eta N/\gamma_{\text{sa}}) \cos(\Delta\phi/2) \sin(\Delta\phi/2)$ , so that the QRF is  $\delta\Omega_{G(QM,\text{CRAIN})} = \gamma_{\text{sa}}/\sqrt{\eta N}$ . It is also straightforward to calculate the QRF of the COSAIN. The total quantum mechanical noise in the COSAIN signal in Eq. (21) is

$$\Delta S_{QM,\text{COSAIN}} = \eta \cos^N(\Delta\phi/2) \sqrt{1 - \cos^{2N}(\Delta\phi/2)}, \quad (22)$$

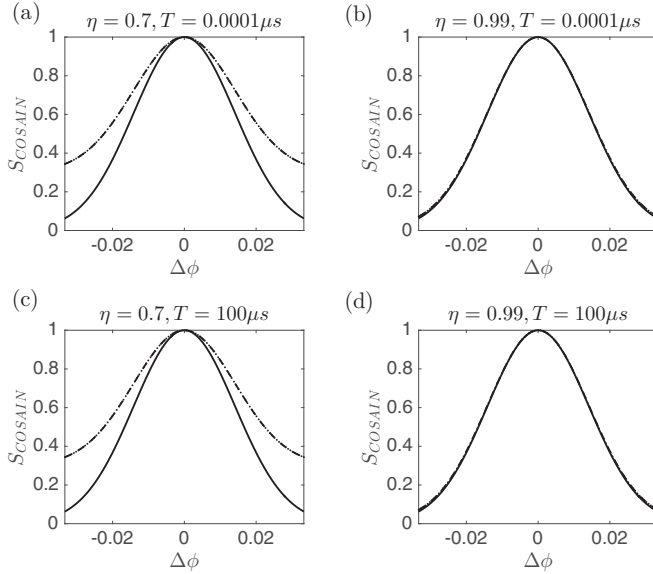


FIG. 14. Plot of ideal signal (solid line), the upper bound (broken line), the lower bound (dotted line) for different detection times  $T$  and detector efficiencies  $\eta$  for  $N = 10\,000$ .

and the RVS is

$$\partial S_{\text{COSAIN}} / \partial \Omega_G = -(\eta N / \gamma_{\text{sa}}) \sin(\Delta\phi/2) \cos^{2N-1}(\Delta\phi/2). \quad (23)$$

Thus, the QRF of the COSAIN is

$$\Omega_{G(QM, \text{COSAIN})} = \left| \frac{\gamma_{\text{sa}}}{N\sqrt{\eta}} \frac{\sqrt{1 - \cos^{2N}(\mu\Omega_G/2)}}{\cos^{N-1}(\mu\Omega_G/2) \sin(\mu\Omega_G/2)} \right| \quad (24)$$

which approaches  $\gamma_{\text{sa}}/\sqrt{\eta N}$  as  $\Omega_G \rightarrow 0$ . Assuming that the detector efficiencies of the COSAIN and the CRAIN can be essentially the same, they do not affect the ratio of the two QRF's.

### C. Effect of collection efficiency

We consider next the effect of collection efficiency  $\beta$  on the COSAIN and compare it to that of the CRAIN. The signal for both the COSAIN and the CRAIN is directly proportional to  $\beta$ . From Eqs. (8) and (11), it is easy to show that

$$\zeta \equiv \frac{\Omega_{G(QM, \text{COSAIN})}}{\Omega_{G(QM, \text{CRAIN})}} = \frac{\sqrt{\sec^{2N}(\mu\Omega_G/2) - 1}}{\sqrt{N} \tan(\mu\Omega_G/2)} \sqrt{\frac{\beta_{\text{CRAIN}}}{\beta_{\text{COSAIN}}}}, \quad (25)$$

where  $\beta_{\text{CRAIN}}$  ( $\beta_{\text{COSAIN}}$ ) is the collection efficiency of the CRAIN (COSAIN).

As  $\Omega_G \rightarrow 0$ , the quantity in the square brackets in Eq. (25) approaches unity. Therefore, in this limit  $\zeta$ , the ratio of the QRF of the COSAIN to that of the CRAIN would depend on the ratio of the collection efficiencies of the detection process. The coherent stimulated Raman scattering based detection method used for the COSAIN process has a collection efficiency that is close to unity, i.e.,  $\beta_{\text{COSAIN}} \simeq 1$ . In the case of the CRAIN,

the fluorescence is collected from the spontaneous emission process, which emits photons in a dipolar radiation pattern. The  $\beta_{\text{CRAIN}}$  can be quantified by analyzing the detection method, for example, of a CRAIN that makes use of cold atoms released from a MOT. For a lens placed at a distance of  $r = 5$  cm, with a diameter of  $d = 2.5$  cm, ignoring the dipolar pattern of radiation for simplicity, and assuming it to be uniform in all directions, this system yields a value of  $\beta_{\text{CRAIN}} \simeq d^2/4r^2 = \frac{1}{16}$  corresponding to  $\zeta \sim 0.25$ . In a typical CRAIN, various geometric constraints make it difficult to achieve a value of  $\beta_{\text{CRAIN}}$  much larger than this. In practice, in cases where the total volume occupied by the CRAIN has to be constrained in order to meet the user requirements, the value of  $\beta_{\text{CRAIN}}$  is typically 1%, which would correspond to  $\zeta \sim 0.1$ . Thus, the near-unity collection efficiency of the COSAIN can lead to an improvement of the interferometer stability by as much as a factor of 10.

Another method of detecting signal in a CRAIN is absorption. However, the use of absorption warrants the consideration of many practical issues. The fluctuation in  $\Delta\phi$  is affected by additional noise contributed by the laser used in absorption. Let us assume that the observation time is  $T$ , and the number of photons in the probe beam before absorption is  $N_P$ , and that the probe is in a coherent state. Furthermore, we assume that the number of atoms passing through the detection process within this time is  $N_A$ , and the linewidth of resonance is  $\Gamma$ . If the detection process produces an absorption by a fraction of  $\kappa$  (i.e.,  $\kappa = 1$  represents perfect absorption of the laser beam), and the detector has a quantum efficiency of  $\eta$ , then the resulting fluctuation in  $\Delta\phi$  can be expressed as

$$\delta\Delta\phi_{\text{abs}} = \Gamma \left( \frac{1}{\sqrt{\eta\kappa N_A}} + \frac{1}{\sqrt{\eta\kappa N_P}} \right), \quad (26)$$

where the first term inside the parentheses represents the quantum projection noise of the atoms, and the second term represents the shot noise of the photons (which can be regarded as the quantum projection noise of photons). The validity of this expression can be easily verified by considering various limits. Consider first the ideal case where  $\varepsilon \equiv \eta\kappa = 1$ . For  $N_P \gg N_A$ , the additional noise from the laser can be neglected, and we get the fundamental noise limit due to the quantum projection noise of the atoms. On the other hand, if  $N_P \ll N_A$ , the quantum projection noise from the atoms can be neglected, and the process is limited by the shot noise of the laser. In general, the parameter  $\varepsilon$  represents the overall quantum efficiency of the detection process. The corresponding expression for detection via fluorescence is  $\delta\Delta\phi_F = \gamma/\sqrt{\eta\rho N_A}$ , where  $\rho$  is the fraction of fluorescence hitting the detector.

The contribution from the second term in Eq. (26) shows that the intensity of the laser beam used in absorption must be made strong enough in order to make the effect of this term negligible compared to the first term. However, since the absorption process is nonlinear and saturates for a strong laser beam, increasing the laser intensity often decreases the effective value of  $\kappa$ . For example, consider an ensemble of  $2 \times 10^6$  atoms with a linear optical density of 300, which can be realized (as we have shown above) for an ensemble confined to a cigar-shaped ensemble. For a weak probe, the value of  $\kappa$  is unity. However, as the probe power is increased, the value

of  $\kappa$  decreases dramatically. This can be seen by considering a situation where the value of  $N_P$  is  $10^9$ , for example. Since the atomic transition used for absorption is not closed (i.e., not cyclic), the ensemble can only absorb a number of photons that are of the order of  $2 \times 10^6$ . Thus, the maximum value of  $\kappa$  would be only about 0.002. Furthermore, if the area of the laser beam ( $\pi w^2$ ) is much larger than the area of the atomic ensemble ( $\pi \xi_T^2$ ), then the value of  $\kappa$  can never exceed the value of  $\xi_T^2/w^2$ . We are not aware of any publication reporting a cold-atom interferometer that makes use of absorption for detecting the atoms, possibly because of these constraints and considerations. Nonetheless, as a matter of principle, an absorption process can certainly be used to reduce the quantum frequency fluctuation below what is observed in fluorescence detection systems, under proper choice of parameters.

## VII. SUMMARY

In this paper, we have described a collective-state atomic interferometer (COSAIN) with  $N$  noninteracting, independent atoms in an ensemble. We have shown that the signal fringes are narrowed by  $\sqrt{N}$  compared to a conventional interferometer, without entanglement. This effect is a result of the interference among collective states, and is a manifestation of interference at a Compton frequency of  $10 \times 10^{30}$  Hz, or a de Broglie wavelength of 4.5 femtometer, for  $N = 10^6$  and  $v = 1$  m/s. The essence of the COSAIN is the detection of a collective state, rather than individual atomic states. For a suitably chosen collective state, this is accomplished via a null detection scheme, wherein the detection of zero photons

corresponds to the system being in this collective state. We have presented a heterodyne detection scheme for measuring this signal. In this scheme, the signal is detected by collecting fluorescence through stimulated Raman scattering of Stokes photons, which are emitted predominantly against the direction of the probe beam, for a high enough resonant optical density. We have shown that the fringe width reduction occurs due to the interference of the multiple paths among the collective states, and does not violate the fundamental quantum limit. We have also proposed an excitation scheme, applicable to both a conventional Raman atomic interferometer (CRAIN) as well to the COSAIN, wherein the counterpropagating beams are cross-linearly polarized. For the COSAIN, this scheme enables an enhancement of the effective resonant optical density by placing a cavity around the atoms in the detection zone. We have analyzed in detail the effect of various inhomogeneities, arising from the nonuniformity in experimental parameters, on the COSAIN signal, and used this analysis to identify a suitable choice of parameters for realizing a COSAIN. The performance of the COSAIN has been compared to that of the conventional Raman atomic interferometer (CRAIN) by analyzing quantum and classical fluctuations in frequency. When the effects of detector efficiency and collection efficiency are considered, it can be seen that the COSAIN may perform 10 times better than a CRAIN employing fluorescence detection.

## ACKNOWLEDGMENT

This work has been supported by the NSF Grants No. DGE-0801685 and No. DMR-1121262, and AFOSR Grant No. FA9550-09-1-0652.

---

[1] T. L. Gustavson, P. Bouyer, and M. A. Kasevich, *Phys. Rev. Lett.* **78**, 2046 (1997).

[2] B. Canuel, F. Leduc, D. Holleville, A. Gauguet, J. Fils, A. Virdis, A. Clairon, N. Dimarcq, C. J. Borde, A. Landragin, and P. Bouyer, *Phys. Rev. Lett.* **97**, 010402 (2006).

[3] A. Peters, K. Y. Chung, and S. Chu, *Nature (London)* **400**, 849 (1999).

[4] M. J. Snadden, J. M. McGuirk, P. Bouyer, K. G. Haritos, and M. A. Kasevich, *Phys. Rev. Lett.* **81**, 971 (1998).

[5] S.-Y. Lan *et al.*, *Science* **339**, 554 (2013).

[6] R. Bouchendira, P. Cladé, S. Guellati-Khélifa, F. Nez, and F. Biraben, *Phys. Rev. Lett.* **106**, 080801 (2011); *Ann. Phys. (Berlin)* **525**, 484 (2013).

[7] M. Cadoret, E. de Mirandes, P. Cladé, S. Guellati-Khélifa, C. Schwob, F. Nez, L. Julien, and F. Biraben, *Phys. Rev. Lett.* **101**, 230801 (2008).

[8] J. B. Fixler *et al.*, *Science* **315**, 74 (2007); G. Lamporesi, A. Bertoldi, I. Cacciapuoti, M. Prevedelli, and G. M. Tino, *Phys. Rev. Lett.* **100**, 050801 (2008).

[9] H. Müller, A. Peters, and S. Chu, *Nature (London)* **463**, 926 (2010).

[10] R. Geiger *et al.*, *Nat. Commun.* **2**, 474 (2011).

[11] M. S. Shahriar, M. Jheeta, Y. Tan, P. Pradhan, and A. Gangat, *Opt. Commun.* **243**, 183 (2004).

[12] M. Kasevich and S. Chu, *Phys. Rev. Lett.* **67**, 181 (1991).

[13] C. J. Bordé, *Phys. Lett. A* **140**, 10 (1989).

[14] F. Riehle, Th. Kisters, A. Witte, J. Helmcke, and Ch. J. Bordé, *Phys. Rev. Lett.* **67**, 177 (1991).

[15] M. O. Scully and J. P. Dowling, *Phys. Rev. A* **48**, 3186 (1993).

[16] G. B. Malykin, *Phys. Usp.* **43**, 1229 (2000).

[17] L. De Broglie, Ph.D. thesis, University of Paris, 1924.

[18] S. Eibenberger, S. Gerlich, M. Arndt, M. Mayor, and J. Tüxen, *Phys. Chem. Chem. Phys.* **15**, 14696 (2013).

[19] I. Pikovski, M. Zych, F. Costa, and Č. Brukner, *Nat. Phys.* **11**, 668 (2015).

[20] D. B. Hume, C. W. Chou, T. Rosenband, and D. J. Wineland, *Phys. Rev. A* **80**, 052302 (2009).

[21] R. H. Dicke, *Phys. Rev.* **93**, 99 (1954).

[22] R. Sarkar, M. E. Kim, R. Fang, Y. Tu, and S. M. Shahriar, *J. Mod. Opt.* **62**, 1253 (2015).

[23] F. T. Arecchi, E. Courtens, R. Gilmore, and H. Thomas, *Phys. Rev. A* **6**, 2211 (1972).

[24] M. O. Scully, E. S. Fry, C. H. Raymond Ooi, and K. Wódkiewicz, *Phys. Rev. Lett.* **96**, 010501 (2006).

[25] M. Kitagawa and M. Ueda, *Phys. Rev. A* **47**, 5138 (1993).

[26] J. Hald, J. L. Sørensen, C. Schori, and E. S. Polzik, *Phys. Rev. Lett.* **83**, 1319 (1999).

- [27] A. Kuzmich, L. Mandel, and N. P. Bigelow, *Phys. Rev. Lett.* **85**, 1594 (2000).
- [28] K. Hammerer, A. S. Sorensen, and E. S. Polzik, *Rev. Mod. Phys.* **82**, 1041 (2010).
- [29] M. E. Kim, R. Sarkar, R. Fang, and S. M. Shahriar, *Phys. Rev. A* **91**, 063629 (2015).
- [30] R. Bonifacio, L. De Salvo, L. M. Narducci, and E. J. D'Angelo, *Phys. Rev. A* **50**, 1716 (1994).
- [31] P. R. Hemmer, N. P. Bigelow, D. P. Katz, M. S. Shahriar, L. DeSalvo, and R. Bonifacio, *Phys. Rev. Lett.* **77**, 1468 (1996)
- [32] K. Baumann, C. Guerlin, F. Brennecke, and T. Esslinger, *Nature (London)* **464**, 1301 (2010).
- [33] A. J. Olson, R. J. Niffenegger, and Y. P. Chen, *Phys. Rev. A* **87**, 053613 (2013).
- [34] L. M. Duan, M. D. Lukin, J. I. Cirac, and P. Zoller, *Nature (London)* **414**, 413 (2001).
- [35] C. W. Gardiner and P. Zoller, *Quantum Noise* (Springer, Berlin, 1999).
- [36] W. M. Itano, J. C. Bergquist, J. J. Bollinger, J. M. Gilligan, D. J. Heinzen, F. L. Moore, M. G. Raizen, and D. J. Wineland, *Phys. Rev. A* **47**, 3554 (1993).

# Quantum noise limits in white-light-cavity-enhanced gravitational wave detectors

Minchuan Zhou,<sup>1</sup> Zifan Zhou,<sup>2</sup> and Selim M. Shahriar<sup>1,2,\*</sup>

<sup>1</sup>*Department of Physics and Astronomy, Northwestern University, 2145 Sheridan Road, Evanston, Illinois 60208, USA*

<sup>2</sup>*Department of EECS, Northwestern University, 2145 Sheridan Road, Evanston, Illinois 60208, USA*  
(Received 7 December 2014; published 6 October 2015)

Previously, we had proposed a gravitational wave detector that incorporates the white-light-cavity (WLC) effect using a compound cavity for signal recycling (CC-SR). Here, we first use an idealized model for the negative dispersion medium (NDM) and use the so-called Caves model for a phase-insensitive linear amplifier to account for the quantum noise (QN) contributed by the NDM, in order to determine the upper bound of the enhancement in the sensitivity-bandwidth product. We calculate the quantum noise limited sensitivity curves for the CC-SR design, and find that the broadening of sensitivity predicted by the classical analysis is also present in these curves, but is somewhat reduced. Furthermore, we find that the curves always stay above the standard quantum limit. To circumvent this limitation, we modify the dispersion to compensate the nonlinear phase variation produced by the optomechanical resonance effects. We find that the upper bound of the factor by which the sensitivity-bandwidth product is increased, compared to the highest-sensitivity result predicted by Bunanno and Chen [Phys. Rev. D 64, 042006 (2001)], is  $\sim 14$ . We also present a simpler scheme (WLC-SR), where a dispersion medium is inserted into the SR cavity. For this scheme, we found the upper bound of the enhancement factor to be  $\sim 18$ . We then consider an explicit system for realizing the NDM, which makes use of five energy levels in M configuration to produce gain, accompanied by electromagnetically induced transparency (the GEIT system). For this explicit system, we employ the rigorous approach based on Master Equation to compute the QN contributed by the NDM, thus enabling us to determine the enhancement in the sensitivity-bandwidth product definitively rather than the upper bound thereof. Specifically, we identify a set of parameters for which the sensitivity-bandwidth product is enhanced by a factor of 17.66.

DOI: 10.1103/PhysRevD.92.082002

PACS numbers: 04.80.Nn, 03.65.Ta, 42.50.Dv, 95.55.Ym

## I. INTRODUCTION

Gravitational waves (GWs) modulate space-time, and for a specific polarization of GW, the modulations along two perpendicular axes are exactly out of phase [1]. Thus, the geometric configuration of a Michelson interferometer makes it a natural candidate for a GW detector. Under conditions where the excess noise is actively suppressed sufficiently, the performance of the detector is limited by quantum noise (QN), consisting of photon shot noise and radiation pressure noise [2]. For the first-generation Laser Interferometer Gravitational Wave Observatory (LIGO), where these two kinds of noises are uncorrelated, the Heisenberg uncertainty principle sets a standard quantum limit (SQL) for the minimum detectable gravitational wave signal [3]. The Advanced LIGO (aLIGO) uses a combination of improved techniques. Along with power recycling (PR) and a higher-power laser source, the aLIGO will employ signal recycling (SR) [4]. There are two special modes of operation corresponding to specific choices of reflectivity ( $r_{\text{SR}}$ ) of the SR mirror ( $M_{\text{SR}}$ ) and length of the SR cavity (SRC) formed ( $L_{\text{SRC}}$ ) (Fig. 1) [5]: extreme signal

recycling mode (narrowband operation) when  $r_{\text{SR}}$  is high and  $\varphi_{\text{SRC}} = k_c L_{\text{SRC}} (\text{mod } 2\pi) = 0$ , and extreme signal extraction mode (broadband operation) when  $r_{\text{SR}}$  is low and  $\varphi_{\text{SRC}} = \pi/2$  [4,6]. In both cases, the QN is above the SQL, since the correlation between shot noise and radiation pressure noise is still zero. However, under modes when  $\varphi_{\text{SRC}} \neq 0$  or  $\pi/2$ , a dynamical correlation between the two kinds of noises is created by  $M_{\text{SR}}$ . As a result, the QN can beat the SQL by roughly a factor of 2 over a small frequency range [7]. The dips in the noise curves correspond to optomechanical (OM) resonances [8]. The reflectivity  $r_{\text{SR}}$  can be increased to create steeper dips with decreasing width. As we know, the GW signal is usually a chirp signal, with the frequency of interest  $10 \text{ Hz} \sim 10^3 \text{ Hz}$ . Thus, the narrow frequency range of these dips may be too small for many types of sources.

A white light cavity (WLC) [9,10,11] is an optical cavity with a high buildup factor yet a broad response. Previously, we proposed a scheme (Fig. 8 in Ref. [9]) for using the WLC effect to broaden the response of a GW detector without a reduction in sensitivity. In this design, which can be adapted to the aLIGO design relatively simply and noninvasively, we replace the conventional SR mirror with a compound cavity (CC) consisting of two mirrors and a

\*shahriar@northwestern.edu

negative dispersion medium (NDM). In what follows, we will refer to this as the CC-SR (compound cavity–signal recycling) design, which will be reviewed briefly in Sec. II. When the dispersion is tuned to a critical value, the transmission window gets broadened significantly, without a reduction in the transmissivity. We have experimentally demonstrated a WLC in rubidium [11], and we have also explored a candidate system for producing this effect at the working wavelength for aLIGO [12].

The analysis presented in Ref. [9] for the CC-SR design did not take into account the effect of the QN. In this paper, we first augment this analysis in order to determine the QN-limited sensitivity of this architecture, using the two-photon formalism of Ref. [13], and an extension of the method employed in Refs. [7] and [14]. We then modify the dispersion of the medium to compensate for the nonlinear phase variation induced by the OM effects. We also propose an alternative and simpler design (WLC-SR), where a dispersive medium with critically tuned dispersion is inserted in the SRC to achieve the phase compensation required by the OM resonance, and we analyze its QN-limited sensitivity. We present different cases where either a negative or positive dispersion medium (PDM) is used to cancel the phase variation, depending on the center frequency of the dispersion.

Since the QN predicted by the Caves model [15] is always less than or equal to that predicted by the ME model, initially we choose to consider an idealized NDM and make use of the Caves model in order to determine an upper bound of the degree of enhancement in the sensitivity-bandwidth product. The effect of the QN from the NDM is then included via a frequency-dependent gain/loss factor in the medium by taking into account an explicit model for the NDM. However, this model makes some assumptions that may not necessarily hold for some systems. To be more exact, we then use the Master Equation (ME) approach to calculate the QN from the NDM, which is established in Ref. [16], for a five-level, M-configuration Gain-EIT (GEIT) system for realizing the NDM.

The remainder of this paper is organized as follows: Section II describes in detail the CC-SR design, considering an explicit model for the dispersive medium, and analyzes the classical frequency response. Section III discusses the QN modeling with and without the excess QN from the dispersive medium taken into account, where the Caves model is used. Section IV discusses the effect of the NDM on the noise density curves in the CC-SR and also introduces a modification to the dispersion in order to achieve a broad region below the SQL. Section V introduces the WLC-SR configuration, exhibiting a broad sub-SQL region. In Sec. VI, we consider the GEIT system as the NDM and use the ME to calculate the QN from the GEIT system. We conclude in Sec. VII with a summary of our results and future plans. In the Appendix, we summarize the abbreviations used in the paper.

## II. CC-SR DESIGN AND ITS CLASSICAL RESPONSE

### A. CC-SR design

The Michelson interferometer with arm cavities and dual recycling is depicted in Fig. 1, referred to as the SR configuration. The interferometer is biased so that Port A is the bright port and Port B is the dark port [17]. Here the power recycling (PR) mirror ( $M_{PR}$ ) in Port A and each of the front mirrors ( $M_1$ ) form a PR cavity (PRC) with a length  $L_{PRC}$  tuned so that it is a highly reflective compound mirror at the carrier frequency. The carrier light then resonates in the cavity established by each of the end mirrors ( $M_2$ ) and the PRC. The net effect of  $M_{PR}$  is to increase the effective power inside the two arms. In our analysis, we do not consider  $M_{PR}$  explicitly [7,14]. Instead, we assume that a power much higher by a factor given by the finesse of the PRC than the laser output is entering the interferometer.  $M_{SR}$  is inserted in Port B after the beam splitter and before the detector, forming an SRC with each of  $M_1$ . One of the sidebands produced by a monochromatic GW resonates in the cavity formed by  $M_2$  and the SRC, thus producing an enhanced sensitivity around the resonant frequency with some bandwidth. In the homodyne detection scheme [18], the output from the interferometer is mixed with a local oscillator (LO) (which is produced by passing a piece of the carrier field through a phase shifter) at the beam splitter, and then detected with two photodetectors (PDs). The two

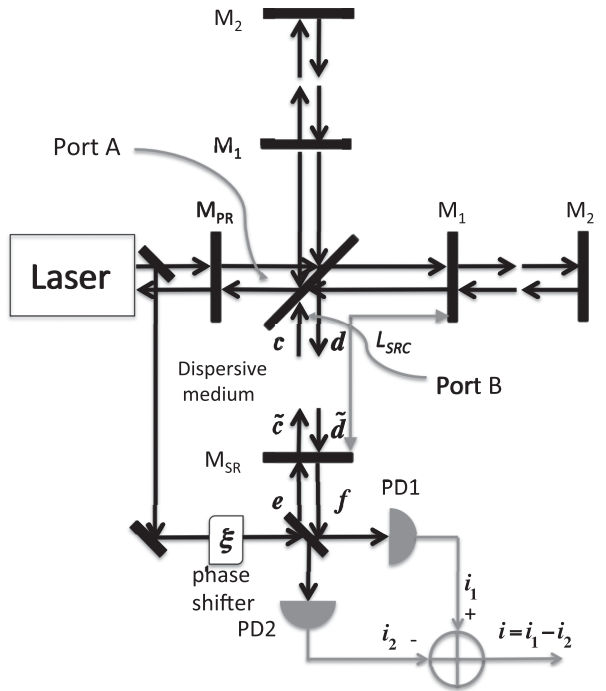


FIG. 1. Michelson interferometer with arm cavities and dual recycling (referred to as SR configuration) with homodyne detection.

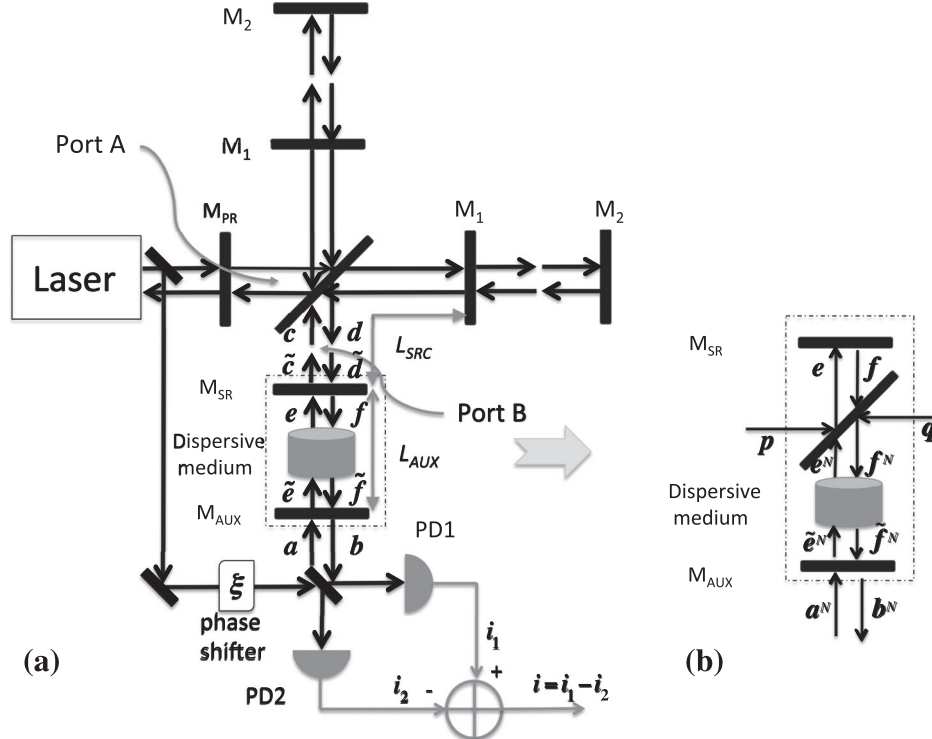


FIG. 2. (a) CC-SR design. In the dot-dashed box is the CC for SR, formed by the original SR mirror ( $M_{SR}$ ) with a modified reflectivity matching that of  $M_1$ ,  $M_{AUX}$  and an NDM, replacing the single SR mirror. (b) Schematic view of the CC with excess QN from the NDM modeled by inserting a beam splitter with power reflectivity  $R_{BS}$  and power transmissivity  $T_{BS}$ . Here  $p$  and  $q$  are the vacuum noises that leak into the system.

resulting photocurrents  $i_{1,2}$  are subtracted to obtain the final signal  $i$ .

In the CC-SR design, summarized in Fig. 2, we modify the above configuration as follows: First, the reflectivity of  $M_{SR}$  is changed to a value that matches the same for  $M_1$ . Next, we reduce the length of the SRC ( $L_{SRC}$ ) by a factor of 20 (to  $\sim 0.5$  m), and tune it to be an integer multiple of the carrier wavelength. Under this condition, the transmissivity of the SRC becomes close to unity for a rather large range of frequencies around the carrier frequency. Thus, effectively, the SRC disappears for the range of GW sidebands we are interested in. Then we add an auxiliary mirror ( $M_{AUX}$ ) for SR and operate at the detuned mode where one of the sidebands resonates. To achieve a high degree of sensitivity, the reflectivity of  $M_{AUX}$  is chosen to be fairly high, as a result of which the finesse of the cavity formed by  $M_{AUX}$  and  $M_2$  is very large, and the bandwidth of the sensitivity is narrowed. To compensate for this, we insert, between  $M_{SR}$  and  $M_{AUX}$ , a medium with a critically tuned negative dispersion. Then  $M_{AUX}$ ,  $M_2$  and the NDM form a WLC. When the dispersion is tuned to the condition where the wavelength becomes independent of frequency over some bandwidth, the transmission profile of the cavity becomes much broader than that for the empty cavity. Thus, a broad bandwidth of the detector can be achieved while keeping the high degree of sensitivity.

The dispersion is designed such that the round-trip phase  $\vartheta_{rt}$  gained by the light for any frequency is constant for a band around the resonant frequency  $\omega_{res}$ . For a dispersive medium with index of refraction  $n(\omega)$  and length  $l$  placed into a cavity of length  $L$ , the round-trip phase can be expressed in general as

$$\vartheta_{rt} = 2k(L - l) + 2n(\omega)kl + \vartheta_{ref}, \quad (1)$$

where  $\vartheta_{ref}$  is the phase from reflection, and  $k$  is the free space wave number. The WLC condition is satisfied if

$$\left. \frac{d\vartheta_{rt}}{d\omega} \right|_{\omega_{res}} = 0. \quad (2)$$

Assuming  $n(\omega_{res}) = 1$ , the condition above is equivalent to

$$\left. \frac{dn}{d\omega} \right|_{\omega_{res}} = -\frac{L}{l} \frac{1}{\omega_{res}}, \quad (3)$$

corresponding to a group index  $n_g = 1 - L/l$ . When the NDM fills up the whole cavity ( $L = l$ ), this condition corresponds to a vanishing group index.

We first use an idealized model for the NDM. We will consider a more explicit model when we take into account the additional QN later. We assume that the NDM has a

transmission profile which is given by a narrow band dip on top of a much broader gain [19]. The real and imaginary parts of the susceptibility  $\chi \equiv \chi' + i\chi''$  are as follows:

$$\chi'' = -\frac{G_e \Gamma_e^2}{\vartheta_e} + \frac{G_i \Gamma_i^2}{\vartheta_i}, \quad (4)$$

$$\chi' = \frac{2G_e(\omega - \omega_c)\Gamma_e}{\vartheta_e} - \frac{2G_i(\omega - \omega_c)\Gamma_i}{\vartheta_i}, \quad (5)$$

where  $\omega_c$  is the center frequency of the dispersion, and  $\vartheta_k = 2\Omega_k^2 + \Gamma_k^2 + 4(\omega - \omega_c)^2$  ( $k = e$  or  $i$ ). Here “ $e$ ” stands for the broad gain and “ $i$ ” for the narrow dip. We use two parameters  $\xi_k = \vartheta_k^2/(\hbar^2 \Gamma_k)$  to define the Rabi frequencies  $\Omega_k^2 \equiv \Gamma_k E^2 \xi_k$  and the gain parameters  $G_k = \hbar N_k \xi_k / \epsilon_0$  [19]. The complex index of refraction is then  $n_c = \sqrt{1 + \chi} \approx 1 + \chi'/2 + i\chi''/2$ . Thus, the total propagation phase in the cavity is  $\varphi_{\text{NDM}} = (1 + \chi'/2)kl_{\text{CAV}} \pmod{2\pi}$ , and the gain/loss factor is given by  $g = \exp(-\chi' kl_{\text{CAV}}/2)$ , where  $l_{\text{CAV}}$  is the length of the cavity. The gain factor is greater (less) than unity for  $\chi'' > 0$  ( $\chi'' < 0$ ). In the limit of vanishing Rabi frequencies ( $\Omega_k \rightarrow 0$ ), the bandwidths of the profiles are given by

$\Gamma_k$ , which are chosen to be  $\Gamma_e/2\pi = 0.8$  MHz and  $\Gamma_i = 10^3 \Gamma_e$ , with the other parameters chosen to satisfy the WLC condition of Eq. (3).

## B. Classical frequency response

We have considered classically the frequency response of the GW detector in Ref. [9]. The propagation of the light at the frequency  $\omega_0$  under the influence of a GW at the frequency  $\Omega$  induces sidebands at frequencies  $\omega_0 \pm \Omega$  [9,14]. Using the complex representation of the electromagnetic field, the total field at Port B is  $\tilde{E}_\pm = E_\pm e^{i(\omega_0 \pm \Omega)t}$  for the component at frequency  $\omega_0 \pm \Omega$ . At the beam splitter the output  $\tilde{E}_{\text{out}} = \tilde{E}_+ + \tilde{E}_-$  mixes with a small amount of the carrier frequency light  $\tilde{E}_L = E_L e^{i(\omega_0 t + \eta)}$ , and the beat signal is [9]

$$\delta I = \tilde{E}_L \tilde{E}_+^* + \tilde{E}_L^* \tilde{E}_+ + \tilde{E}_L \tilde{E}_-^* + \tilde{E}_L^* \tilde{E}_-, \quad (6)$$

which can be written in the form

$$\delta I = P \cos[\Omega(t - L/c)] + Q \sin[\Omega(t - L/c)], \quad (7)$$

where

$$P = P_+ + P_-, \quad (8)$$

$$P_\pm = 2E_0 E_L B \frac{\zeta_\pm [r_2 r_{S\pm} \cos(2k_\pm L - \phi_{rS\pm} + \phi_{tS\pm} + \phi_C) - \cos(\phi_{tS\pm} + \phi_C)]}{1 + F'_{S\pm} \sin^2(k_\pm L_S - \phi_{rS\pm}/2)}, \quad (9)$$

$$Q_\pm = \mp 2E_0 E_L B \frac{\zeta_\pm [-r_2 r_{S\pm} \sin(2k_\pm L - \phi_{rS\pm} + \phi_{tS\pm} + \phi_C) + \sin(\phi_{tS\pm} + \phi_C)]}{1 + F'_{S\pm} \sin^2(k_\pm L_S - \phi_{rS\pm}/2)}. \quad (10)$$

The magnitude of the signal is given by  $|\delta I| = \sqrt{P^2 + Q^2}$ . Here  $r_{S\pm} e^{i\phi_{rS\pm}}$  and  $t_{S\pm} e^{i\phi_{tS\pm}}$  are the reflectivity and transmissivity, respectively, of the compound mirror  $M_S$  composed of  $M_1$ ,  $M_{\text{SR}}$  and  $M_{\text{AUX}}$  at the frequency  $\omega_0 \pm \Omega$ , and  $k_\pm = (\omega_0 \pm \Omega)/c$  is the wave number. The two arm cavities are identical and of length  $L$ .  $L_S$  is the distance from  $M_S$  to  $M_2$ , which in the case of the CC-SR is the same as  $L$ . The relevant parameters are defined as

$$F'_{S\pm} = \frac{4r_{S\pm} r_2}{(1 - r_{S\pm} r_2)^2}, \quad F'_C = \frac{4r_1 r_2}{(1 - r_1 r_2)^2}, \quad (11)$$

$$\zeta_\pm = \frac{t_1 t_{S\pm} r_2 \hbar \omega_0 \sin(\Omega L/c)}{\Omega (1 - r_1 r)^2 (1 - r_2 r_{S\pm})^2}, \quad (12)$$

$$B e^{i\phi_B} = \frac{e^{-2ik_c L} - r_1 r_2}{1 + F'_C \sin^2(k_c L)},$$

$$\phi_C = -2k_c L - \eta + \phi_B - \pi/2. \quad (13)$$

When the NDM is inserted,  $k_\pm L_S$  needs to be changed to  $n(\omega_0 \pm \Omega)k_\pm L_S$  in the equations above.

In Fig. 3, we illustrate the effect of the WLC on the frequency response of the GW detector, which shows  $|\delta I|$

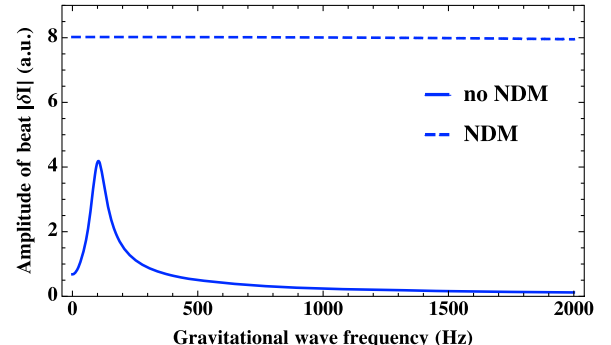


FIG. 3 (color online). Response functions for the CC-SR design with  $R_{\text{AUX}} = 99\%$ , both with (plotted in red) and without (plotted in blue) the NDM inserted.

TABLE I. Values used in plotting Fig. 3.

$k_c = 2\pi/(1064 \times 10^{-9}) \text{ m}^{-1}$	$L = 2\pi(3.75446 \times 10^9)/k_c \approx 4 \text{ km}$
$\omega_0 = k_c c \approx 1.77 \times 10^{15} \text{ Hz}$	$L_{\text{SRC}} = 2\pi(0.47 \times 10^6)/k_c \approx 0.50 \text{ m}$
$t_{\text{SR}} = t_1 \approx 0.183, t_2 = 0$	$k_{\text{res}} = k_c + \gamma/c$
$t_{\text{AUX}} = 0.1$	$L_{\text{AUX}} = -L + 2\pi(7.51 \times 10^9)/(2k_{\text{res}}) \approx 0.57 \text{ m}$

as a function of  $\Omega$  with  $R_{\text{AUX}} = 99\%$ , with the values of the other parameters being as shown in Table I. We assumed that  $M_2$  is totally reflective ( $r_2 = 1$  and  $t_2 = 0$ ), while  $M_1$  has reflectivity  $r_1$  and transmissivity  $t_1$ . The reflectivity and transmissivity, respectively, are  $r_{\text{SR}}$  and  $t_{\text{SR}}$  for  $M_{\text{SR}}$ , and  $r_{\text{AUX}}$  and  $t_{\text{AUX}}$  for  $M_{\text{AUX}}$ . Without the NDM, when the length  $L_{\text{AUX}}$  is chosen so that the sideband at  $\omega_{\text{res}} = \omega_0 + \gamma$  is resonant in the cavity formed by  $M_{\text{AUX}}$  and  $M_2$ , the response curve is peaked at  $\Omega = \gamma$ , with  $P_+$  and  $Q_+$  contributing most to  $|\delta I|$ , and  $P_-$  and  $Q_-$  being negligible, since only one of the sidebands (in this case it is the positive sideband at  $\omega_0 + \gamma$ ) is on resonance. Adding the NDM, which has its dispersion centered at  $\omega_{\text{res}}$  and the shape tailored according to Eq. (3), broadens the response curve with the amplitude being twice as large as that in the case without the NDM. However, the discussion above did not take into account the OM effects that modify the resonance condition, and, as will be shown in Sec. IV, the QN-limited sensitivity curves show significant broadening but remain above the SQL.

We note here that the results shown in Fig. 3 do not take into account enhancement of the sidebands due to the (spectrally varying) gain from the NDM. If this were to be considered, the enhancement in sensitivity would be even larger. However, as is well known now, the sensitivity profile obtained through such a semiclassical analysis is essentially irrelevant. What matters instead is the minimum detectable GW strain amplitude when the effects of QN and the OM resonance are taken into account. Thus, the results we derive later in this paper by taking the effects of QN (including those due to the gain of the NDM) and the OM effects are the more relevant ones.

### III. NOISE MODELING

Following the two-photon formalism developed by Caves and Schumaker [13], Kimble *et al.* have derived the input-output relations for a Michelson interferometer [14], and Buonanno and Chen have derived the input-output relation for an SR interferometer [7]. With the same formalism, we here develop the input-output relation for the CC-SR scheme. For simplicity, we consider first only the dispersive property of the NDM, and do not take into account the QN resulting from the gain spectrum. This is then followed by a more complete analysis where both the effects of the dispersion and the gain due to the NDM on the QN are taken into account.

#### A. Input-output relation

We make the following assumptions: First, the length of the arm cavities  $L$  oscillates at a frequency  $\sim 1 \text{ Hz}$  [20], around an equilibrium position where the laser frequency resonates (this effect in the final signal can be filtered by a high-frequency pass, thus the mirrors can be considered as still effectively). Second, the mirrors and beam splitters are lossless and infinitely thin. We describe the light with a time-dependent electric field, at fixed locations along the optical axis [14]. The laser as a carrier field enters the interferometer at the bright port with intensity  $I_0$  and frequency  $\omega_0$ . The GW with a frequency  $\Omega$  will interact with the carrier field to create sidebands at  $\omega_0 \pm \Omega$  [9,14]. We denote the usual annihilation and creation operators for a photon at frequency  $\omega$  by  $a(\omega)$  and  $a^\dagger(\omega)$ . The amplitudes of the two-photon modes are defined as [13]

$$a_1(\Omega) = a(\omega_0 + \Omega) \sqrt{\frac{\omega_0 + \Omega}{2\omega_0}} + a^\dagger(\omega_0 - \Omega) \sqrt{\frac{\omega_0 - \Omega}{2\omega_0}}, \quad (14a)$$

$$a_2(\Omega) = -ia(\omega_0 + \Omega) \sqrt{\frac{\omega_0 + \Omega}{2\omega_0}} + ia^\dagger(\omega_0 - \Omega) \sqrt{\frac{\omega_0 - \Omega}{2\omega_0}}. \quad (14b)$$

$a_j(\Omega)$  ( $j = 1, 2$ ) operates on two photons at frequencies  $\omega_0 \pm \Omega$  simultaneously. If we ignore the terms proportional to  $\Omega/\omega_0$  ( $\Omega/\omega_0 \ll 1$ ), the commutation relations are [13]

$$[a_1(\Omega), a_2^\dagger(\Omega')] = -[a_2(\Omega), a_1^\dagger(\Omega')] = 2\pi i \delta(\Omega - \Omega'),$$

$$[a_j(\Omega), a_j(\Omega')] = 0 = [a_j(\Omega), a_j^\dagger(\Omega')], \quad j = 1, 2. \quad (15)$$

The electric field  $E_a$  can then be expressed as a linear combination of two quadratures  $E_{a1}$  and  $E_{a2}$ :

$$E_a(t) = E_{a1}(t) \cos(\omega_0 t) + E_{a2}(t) \sin(\omega_0 t), \quad (16)$$

$$E_{aj}(t) = \sqrt{\frac{4\pi\hbar\omega_0}{\mathcal{A}c}} \int_0^{+\infty} [a_j(\Omega) e^{-i\Omega t} + a_j^\dagger(\Omega) e^{i\Omega t}] \frac{d\Omega}{2\pi},$$

$$j = 1, 2, \quad (17)$$

where  $\mathcal{A}$  is the effective cross-section area of the laser. For convenience, we use a vector  $\mathbf{a}(\Omega) = (a_1(\Omega), a_2(\Omega))^T$  to

represent  $E_a$  in the latter context. In order to establish the basic notation, we start by considering the simpler case, corresponding to the original LIGO, where there is no SR mirror, and the input field at Port A has a classical carrier field assumed to be only in the first quadrature. At Port B, the quadrature amplitudes for the input field are  $\mathbf{c}(\Omega)$ , and those for the output are  $\mathbf{d}(\Omega)$ . Following the method in Ref. [14], we derive the relations between  $\mathbf{c}(\Omega)$  and  $\mathbf{d}(\Omega)$ :

$$\mathbf{d}(\Omega) = A(\Omega)\mathbf{c}(\Omega) + \mathbf{B}(\Omega)\tilde{h}(\Omega), \quad (18)$$

where  $A(\Omega)$  is a  $2 \times 2$  matrix and  $\mathbf{B}(\Omega)$  is a two-dimensional column vector with elements

$$\begin{aligned} A_{11} = A_{22} &= \frac{e^{2i\Omega L/c} - r_1}{1 - r_1 e^{2i\Omega L/c}}, \quad A_{12} = 0, \\ A_{21} &= -\frac{I_0}{I_{\text{SQL}}} \frac{8L^2\gamma^4}{\Omega^2 c^2} \frac{e^{i\Omega L/c}}{(1 - r_1 e^{2i\Omega L/c})^2}, \end{aligned} \quad (19a)$$

$$\begin{aligned} B_1 &= 0, \quad B_2 = \sqrt{\frac{I_0}{I_{\text{SQL}}}} \frac{4L\gamma^2}{\Omega c} \frac{e^{i\Omega L/c}}{1 - r_1 e^{2i\Omega L/c}}, \\ \tilde{h}(\Omega) &= \frac{h(\Omega)}{h_{\text{SQL}}(\Omega)}. \end{aligned} \quad (19b)$$

Here  $\gamma = t_1^2 c / (4L) = 2\pi \times 100$  Hz is the half-bandwidth of the arm cavities [14];  $m = 40$  kg is the mass of the

mirrors;  $I_{\text{SQL}} = mL^2\gamma^4/(4\omega_0) = 1.4 \times 10^4$  W is the input light power for which the shot noise equals the radiation pressure noise at  $\Omega = \gamma$ ; and  $h_{\text{SQL}}(\Omega)$  is the SQL for  $h(\Omega)$ , which is the Fourier transform of the dimensionless GW signal  $h(t) = \Delta L(t)/L$  [14]:

$$h_{\text{SQL}}(\Omega) = \sqrt{\frac{8\hbar}{m\Omega^2 L^2}}. \quad (20)$$

Under the assumptions that  $\Omega L/c \ll 1$  and  $t_1 \ll 1$ , we have  $e^{i\Omega L/c} \approx 1 + i\Omega L/c$  and  $r_1 \approx 1 - t_1^2/2$ . This yields  $A_{11} = A_{22} \approx e^{2i\beta(\Omega)}$  and  $A_{21} \approx -\mathcal{K}(\Omega)e^{2i\beta(\Omega)}$ , where  $\beta(\Omega) = \arctan(\Omega/\gamma)$  and  $\mathcal{K}(\Omega) = 2I_0\gamma^4/[I_{\text{SQL}}\Omega^2(\Omega^2 + \gamma^2)]$ , same as the results in Ref. [14].

Free-space propagation of the field operator is represented by a rotation of the vector  $\mathbf{a}(\Omega)$  with a phase shift [7]. For instance, if  $\tilde{\mathbf{a}}(\Omega)$  is the field after propagating a distance of  $L$ , then  $\tilde{\mathbf{a}}(\Omega) = \mathcal{R}(\varphi, \Phi)\mathbf{a}(\Omega)$ , where

$$\mathcal{R}(\varphi, \Phi) = e^{i\Phi} \begin{pmatrix} \cos \varphi & -\sin \varphi \\ \sin \varphi & \cos \varphi \end{pmatrix}, \quad (21)$$

with the phases  $\varphi = \omega_0 L/c (\text{mod } 2\pi)$  and  $\Phi = \Omega L/c (\text{mod } 2\pi)$ . If the light travels through a dispersive medium with index of refraction  $n(\omega)$ , the matrix becomes

$$\mathcal{R}_n(\varphi, \Phi) = \frac{1}{2} \begin{pmatrix} e^{in(\omega_0 + \Omega)(\varphi + \Phi)} + e^{-in(\omega_0 - \Omega)(\varphi - \Phi)} & i[e^{in(\omega_0 + \Omega)(\varphi + \Phi)} - e^{-in(\omega_0 - \Omega)(\varphi - \Phi)}] \\ -i[e^{in(\omega_0 + \Omega)(\varphi + \Phi)} - e^{-in(\omega_0 - \Omega)(\varphi - \Phi)}] & e^{in(\omega_0 + \Omega)(\varphi + \Phi)} + e^{-in(\omega_0 - \Omega)(\varphi - \Phi)} \end{pmatrix}. \quad (22)$$

Since only one of the sidebands is at resonance and contributes to the output, and the contribution of the other sideband is negligible, as argued in Sec. II B, we make the approximation in the above equation that  $n(\omega_0 + \Omega) \approx n(\omega_0 - \Omega)$  when designing the dispersion [we will also show the results using the exact matrix in Eq. (22) in the analysis later], and thus Eq. (22) becomes

$$\mathcal{R}_n(\varphi, \Phi) = e^{in(\omega_0 + \Omega)\Phi} \begin{pmatrix} \cos[n(\omega_0 + \Omega)\varphi] & -\sin[n(\omega_0 + \Omega)\varphi] \\ \sin[n(\omega_0 + \Omega)\varphi] & \cos[n(\omega_0 + \Omega)\varphi] \end{pmatrix}. \quad (23)$$

Now we add a CC for SR, which is composed of  $M_{\text{SR}}$ ,  $M_{\text{AUX}}$  and an NDM, and assume that the distance from the beam splitter to  $M_1$  is negligible compared to  $L_{\text{SRC}}$ . As shown in Fig. 2,  $\tilde{\mathbf{c}}(\Omega)$  and  $\mathbf{d}(\Omega)$  denote the fields just before  $M_{\text{SR}}$ , while  $\mathbf{e}(\Omega)$  and  $\mathbf{f}(\Omega)$  denote the fields immediately after  $M_{\text{SR}}$ ;  $\tilde{\mathbf{e}}(\Omega)$  and  $\tilde{\mathbf{f}}(\Omega)$  denote the fields before  $M_{\text{AUX}}$ , while  $\mathbf{a}(\Omega)$  and  $\mathbf{b}(\Omega)$  denote the fields immediately after  $M_{\text{AUX}}$ . We define the rotation operators for propagation through  $L_{\text{SRC}}$  and  $L_{\text{AUX}}$  as  $\mathcal{R}(\varphi_{\text{SRC}}, \Phi_{\text{SRC}}) = \mathcal{R}_{\text{SRC}}$  and  $\mathcal{R}_n(\varphi_{\text{AUX}}, \Phi_{\text{AUX}}) = \mathcal{R}_{\text{AUX}}$ , with  $\varphi_{\text{SRC}} = \omega_0 L_{\text{SRC}}/c (\text{mod } 2\pi)$ ,  $\Phi_{\text{SRC}} = \Omega L_{\text{SRC}}/c (\text{mod } 2\pi)$ ,  $\varphi_{\text{AUX}} = \omega_0 L_{\text{AUX}}/c (\text{mod } 2\pi)$ , and  $\Phi_{\text{AUX}} = \Omega L_{\text{AUX}}/c (\text{mod } 2\pi)$ . Here we assume that the NDM fills up the whole CC. The effect

of the spectrally varying gain profile of the NDM will add additional QN. We will take this into account later on. For now, we ignore the effect of this gain [Fig. 2(a)]. In that case, we have the following relation:

$$\begin{aligned} \mathbf{c}(\Omega) &= \mathcal{R}_{\text{SRC}} \tilde{\mathbf{c}}(\Omega), & \tilde{\mathbf{d}}(\Omega) &= \mathcal{R}_{\text{SRC}} \mathbf{d}(\Omega), \\ \mathbf{e}(\Omega) &= \mathcal{R}_{\text{AUX}} \tilde{\mathbf{e}}(\Omega), & \tilde{\mathbf{f}}(\Omega) &= \mathcal{R}_{\text{AUX}} \mathbf{f}(\Omega), \end{aligned} \quad (24a)$$

$$\begin{aligned} \tilde{\mathbf{c}}(\Omega) &= t_{\text{SR}} \mathbf{e}(\Omega) + r_{\text{SR}} \tilde{\mathbf{d}}(\Omega), \\ \mathbf{f}(\Omega) &= -r_{\text{SR}} \mathbf{e}(\Omega) + t_{\text{SR}} \tilde{\mathbf{d}}(\Omega), \end{aligned} \quad (24b)$$

$$\begin{aligned}\tilde{\mathbf{e}}(\Omega) &= t_{\text{AUX}}\mathbf{a}(\Omega) + r_{\text{AUX}}\tilde{\mathbf{f}}(\Omega), \\ \mathbf{b}(\Omega) &= -r_{\text{AUX}}\mathbf{a}(\Omega) + t_{\text{AUX}}\tilde{\mathbf{f}}(\Omega).\end{aligned}\quad (24\text{c})$$

Solving the system of Eq. (18) and Eqs. (24a)–(24c) gives the following input-output relation:

$$\mathbf{b}(\Omega) = X(\Omega)\mathbf{a}(\Omega) + Y(\Omega)\tilde{\mathbf{h}}(\Omega), \quad (25)$$

where

$$U(\Omega) = t_{\text{SR}}^2 \mathcal{R}_{\text{SRC}} A(\Omega) [\mathcal{R}_{\text{SRC}}^{-1} - r_{\text{SR}} \mathcal{R}_{\text{SRC}} A(\Omega)]^{-1} - r_{\text{SR}} I, \quad (26\text{a})$$

$$\begin{aligned}\mathbf{V}(\Omega) &= t_{\text{SR}} r_{\text{SR}} \mathcal{R}_{\text{SRC}} A(\Omega) [\mathcal{R}_{\text{SRC}}^{-1} - r_{\text{SR}} \mathcal{R}_{\text{SRC}} A(\Omega)]^{-1} \mathcal{R}_{\text{SRC}} \\ &\quad \times \mathbf{B}(\Omega) + t_{\text{SR}} \mathcal{R}_{\text{SRC}} \mathbf{B}(\Omega),\end{aligned}\quad (26\text{b})$$

$$\begin{aligned}X(\Omega) &= t_{\text{AUX}}^2 \mathcal{R}_{\text{AUX}} U(\Omega) [\mathcal{R}_{\text{AUX}}^{-1} - r_{\text{AUX}} \mathcal{R}_{\text{AUX}} U(\Omega)]^{-1} \\ &\quad - r_{\text{AUX}} I,\end{aligned}\quad (26\text{c})$$

$$\begin{aligned}\mathbf{Y}(\Omega) &= t_{\text{AUX}} r_{\text{AUX}} \mathcal{R}_{\text{AUX}} U(\Omega) [\mathcal{R}_{\text{AUX}}^{-1} - r_{\text{AUX}} \mathcal{R}_{\text{AUX}} U(\Omega)]^{-1} \\ &\quad \times \mathcal{R}_{\text{AUX}} \mathbf{V}(\Omega) + t_{\text{AUX}} \mathcal{R}_{\text{AUX}} \mathbf{V}(\Omega).\end{aligned}\quad (26\text{d})$$

Here  $I$  is a  $2 \times 2$  identity matrix, and  $A(\Omega)$  and  $\mathbf{B}(\Omega)$  are as defined in Eqs. (19a) and (19b). It is confirmed that  $X_{ij}$  has a common phase factor and  $|\text{Det}(X)| = 1$ , so  $b_j(\Omega)$  ( $j = 1, 2$ ) follows the same commutation relations as  $a_j(\Omega)$  in Eq. (13). The relation for the SR configuration can be recovered by setting  $r_{\text{AUX}} = 0$  and  $L_{\text{AUX}} = 0$ . In that case, we get  $\mathbf{f}(\Omega) = \mathbf{b}(\Omega)$  and  $\mathbf{e}(\Omega) = \mathbf{c}(\Omega)$ . It should be noted that unlike in LIGO, where the GW signal  $h(\Omega)$  only appears in the second quadrature of the output,  $h(\Omega)$  now appears in both quadratures for SR (due to the presence of  $M_{\text{SR}}$ ) and for CC-SR (due to the presence of  $M_{\text{SR}}$  and  $M_{\text{AUX}}$ ).

## B. Noise spectral density

At the beam splitter, the output  $E_b(t) = E_{b1}(t) \cos(\omega_0 t) + E_{b2}(t) \sin(\omega_0 t)$  mixes with  $E(t) = E_L \cos(\omega_0 t - \xi)$ . The resulting photocurrents are then

$$\begin{aligned}i_1(t) &\propto \overline{|E(t) + E_b(t)|^2} \\ &= \frac{1}{2} E_L^2 + \frac{1}{2} E_{b1}^2 + \frac{1}{2} E_{b2}^2 + E_L E_{b1}(t) \cos(\xi) \\ &\quad + E_L E_{b2}(t) \sin(\xi),\end{aligned}\quad (27\text{a})$$

$$\begin{aligned}i_2(t) &\propto \overline{|E(t) - E_b(t)|^2} \\ &= \frac{1}{2} E_L^2 + \frac{1}{2} E_{b1}^2 + \frac{1}{2} E_{b2}^2 - E_L E_{b1}(t) \cos(\xi) \\ &\quad - E_L E_{b2}(t) \sin(\xi),\end{aligned}\quad (27\text{b})$$

where the horizontal bar indicates an averaging over a period much longer than  $\omega_0^{-1}$ . We detect the difference of  $i_{1,2}$ :

$$i(t) = i_1(t) - i_2(t) = 2E_L E_{b\xi}, \quad (28)$$

where we have defined

$$E_{b\xi}(\Omega) = E_{b1}(\Omega) \cos(\xi) + E_{b2}(\Omega) \sin(\xi), \quad (29)$$

which can also be expressed as

$$E_{b\xi}(\Omega) = \sqrt{\frac{4\pi\hbar\omega_0}{Ac}} \int_0^{+\infty} [b_\xi(\Omega) e^{-i\Omega t} + b_\xi^\dagger(\Omega) e^{-i\Omega t}] \frac{d\Omega}{2\pi}, \quad (30)$$

where

$$b_\xi(\Omega) = b_1(\Omega) \cos(\xi) + b_2(\Omega) \sin(\xi). \quad (31)$$

The output  $b_\xi(\Omega)$  consists of the signal component  $\langle b_\xi(\Omega) \rangle$  and the noise component  $\Delta b_\xi(\Omega)$ :

$$\langle b_\xi(\Omega) \rangle = [Y_1(\Omega) \cos(\xi) + Y_2(\Omega) \sin(\xi)] \frac{h}{h_{\text{SQL}}}, \quad (32)$$

$$\begin{aligned}\Delta b_\xi(\Omega) &= [X_{11} \sin(\xi) + X_{21} \cos(\xi)] a_1 \\ &\quad + [X_{12} \sin(\xi) + X_{22} \cos(\xi)] a_2.\end{aligned}\quad (33)$$

The noise in the gravitational-wave signal  $h$  at frequency  $\Omega$  is related to the noise in the output  $b_\xi(\Omega)$  via a transfer function

$$\Delta h(\Omega) = \frac{h_{\text{SQL}}(\Omega)}{Y_1(\Omega) \cos(\xi) + Y_2(\Omega) \sin(\xi)} \Delta b_\xi(\Omega). \quad (34)$$

Using the definition of spectral density [13]

$$\begin{aligned}2\pi\delta(\Omega - \Omega') S_h(\Omega) &= \langle in | \Delta h(\Omega) \Delta h^\dagger(\Omega') \\ &\quad + \Delta h^\dagger(\Omega') \Delta h(\Omega) | in \rangle,\end{aligned}\quad (35)$$

and the fact that the input of the detector at the dark port is in the vacuum state  $|in\rangle = |0_a\rangle$ , we derive the noise spectral density for the GW signal  $h(\Omega)$ :

$$S_h^\xi(\Omega) \equiv h_n^2(\Omega) = h_{\text{SQL}}^2(\Omega) \frac{|X_{11} \sin(\xi) + X_{21} \cos(\xi)|^2 + |X_{12} \sin(\xi) + X_{22} \cos(\xi)|^2}{|Y_1 \sin(\xi) + Y_2 \cos(\xi)|^2}. \quad (36)$$

### C. Inclusion of the QN from the NDM

In addition to the QN we have considered above, we must take into account the excess QN resulting from the NDM used for WLC. Specifically, this QN results from the fact that the NDM, in addition to providing dispersion, also amplifies or attenuates the signal. Physically, the noise associated in the amplification or attenuation is due to the spontaneous emission of photons that must accompany such a process. In deriving the QN from the NDM, we note first that the NDM is a phase-insensitive linear amplifier. For such an amplifier, it is in general possible to evaluate the QN by using the approach developed by Caves [15]. However, this model may not necessarily apply to complex systems. We have recently developed a rigorous approach based on Master Equation (ME) to determine QN in arbitrary complex atomic systems [16]. We have applied this approach to several different atomic systems, and compared the results to those predicted by the Caves model. We found that in most cases the Caves model is inadequate. However, we also found several examples where the prediction of the Caves model agrees with that of the ME approach. Furthermore, we found that the QN predicted by the Caves model is always less than or equal to what is predicted by the ME approach. In general, use of the ME approach is tedious and cumbersome. Thus, in this paper, we do not use the ME approach until Sec. VI, which contains the final findings of this paper, based on an explicit system for realizing the NDM. In the other sections, we make use of the simple Caves model in order to determine the upper bound of the enhancement in the sensitivity-bandwidth product achievable under various combinations of configurations and dispersion profiles. We do note, however, that in the result presented in Sec. V A, where we consider a positive dispersion medium (PDM) as the phase compensator, the prediction based on using the Caves model would be the same as that made using the ME model. This is because the PDM is generated by using an electromagnetically induced transparency (EIT) process employing a  $\Lambda$ -type three-level system, for which the Caves model agrees exactly with the ME approach, as shown in Ref. [16].

The Caves model can be described as follows. We define a factor  $g$  as the intensity gain or loss factor of the dispersive medium:

$$g = \exp[-\chi''(\omega_0 + \Omega)kL_{\text{AUX}}]. \quad (37)$$

Generally, to account for the noise from a phase-insensitive linear amplifier, a vacuum field  $\mathbf{v}(\Omega)$  is added after propagating through the medium:

$$\mathbf{y}^*(\Omega) = \sqrt{g}\mathbf{y}(\Omega) + \sqrt{g-1}\mathbf{v}^\dagger(\Omega), \quad g > 1, \quad (38)$$

while for the case of an attenuator,

$$\mathbf{y}^*(\Omega) = \sqrt{g}\mathbf{y}(\Omega) + \sqrt{1-g}\mathbf{v}(\Omega), \quad g < 1, \quad (39)$$

where  $\mathbf{y}(\mathbf{y}^*)$  is the field operator before (after) propagating through the medium. Here  $\mathbf{v}^\dagger$  and  $\mathbf{v}$  are used so that the commutation relations for  $\mathbf{y}$  are maintained for  $\mathbf{y}^*$ . Note also that in keeping with the approximation  $n(\omega_0 + \Omega) \approx n(\omega_0 - \Omega)$  in Eq. (23), we approximate here  $g(\omega_0 + \Omega) \approx g(\omega_0 - \Omega)$ , which we will call later the single-sideband approximation (SSA). The exact results without the SSA are shown later.

For a general model that works both for gain and loss, we model the QN by placing inside the WLC a beam splitter (BS) that has a power reflectivity of  $R_{\text{BS}}$  and power transmissivity of  $T_{\text{BS}}$ , from which the vacuum fields can leak into the system from the outside. We define

$$T_{\text{BS}}(\Omega) = g, \quad R_{\text{BS}}(\Omega) = |1 - T_{\text{BS}}(\Omega)|, \quad (40)$$

and we write

$$\mathbf{y}^*(\Omega) = \sqrt{T_{\text{BS}}}\mathbf{y}(\Omega) + \sqrt{R_{\text{BS}}}\mathbf{v}(\Omega). \quad (41)$$

We have confirmed that the results for the QN curves using Eq. (41) are consistent with those achieved with Eqs. (38) and (39). For the case in the CC-SR scheme, as illustrated in Fig. 2(b), we assume that the distance from the inserted BS to  $M_{\text{SR}}$  is negligible, and represent the field operators just after the beam splitter as  $\mathbf{e}^N(\Omega)$  and  $\mathbf{f}^N(\Omega)$  and the vacuum fields as  $\mathbf{p}(\Omega)$  and  $\mathbf{q}(\Omega)$ . We have the following relationships:

$$\begin{aligned} \mathbf{e}^N(\Omega) &= \mathcal{R}_{\text{AUX}}\tilde{\mathbf{e}}^N(\Omega), \\ \tilde{\mathbf{f}}^N(\Omega) &= \mathcal{R}_{\text{AUX}}\mathbf{f}^N(\Omega), \end{aligned} \quad (42a)$$

$$\begin{aligned} \mathbf{e}(\Omega) &= \sqrt{T_{\text{BS}}}\mathbf{e}^N(\Omega) + \sqrt{R_{\text{BS}}}\mathbf{p}(\Omega), \\ \mathbf{f}^N(\Omega) &= \sqrt{T_{\text{BS}}}\mathbf{f}^N(\Omega) - \sqrt{R_{\text{BS}}}\mathbf{q}(\Omega). \end{aligned} \quad (42b)$$

The final input-output relations in Eqs. (25), (26c) and (26d) are then modified as

$$\begin{aligned} \mathbf{b}^N(\Omega) &= X^N(\Omega)\mathbf{a}^N(\Omega) + Y^N(\Omega)\tilde{\mathbf{h}}(\Omega) \\ &\quad + P^N(\Omega)\mathbf{p}(\Omega) + Q^N(\Omega)\mathbf{q}'(\Omega), \end{aligned} \quad (43)$$

$$\begin{aligned} \mathbf{q}'(\Omega) &= \mathcal{R}_{\text{AUX}} \mathbf{q}(\Omega), \\ W(\Omega) &= [(\sqrt{T_{\text{BS}}} \mathcal{R}_{\text{AUX}})^{-1} - r_{\text{AUX}} \sqrt{T_{\text{BS}}} \mathcal{R}_{\text{AUX}} U(\Omega)]^{-1}, \end{aligned} \quad (44\text{a})$$

$$X^N(\Omega) = t_{\text{AUX}}^2 \sqrt{T_{\text{BS}}} \mathcal{R}_{\text{AUX}} U(\Omega) W(\Omega) - r_{\text{AUX}} I, \quad (44\text{b})$$

$$\begin{aligned} \mathbf{Y}^N(\Omega) &= t_{\text{AUX}} r_{\text{AUX}} T_{\text{BS}} \mathcal{R}_{\text{AUX}} U(\Omega) W(\Omega) \mathcal{R}_{\text{AUX}} V(\Omega) \\ &\quad + t_{\text{AUX}} \sqrt{T_{\text{BS}}} \mathcal{R}_{\text{AUX}} V(\Omega), \end{aligned} \quad (44\text{c})$$

$$P^N(\Omega) = t_{\text{AUX}} \sqrt{R_{\text{BS}}} \mathcal{R}_{\text{AUX}} U(\Omega) W(\Omega) \mathcal{R}_{\text{AUX}}^{-1}, \quad (44\text{d})$$

$$\begin{aligned} Q^N(\Omega) &= -t_{\text{AUX}} r_{\text{AUX}} \sqrt{T_{\text{BS}} R_{\text{BS}}} \mathcal{R}_{\text{AUX}} U(\Omega) W(\Omega) \\ &\quad - t_{\text{AUX}} \sqrt{R_{\text{BS}}} I. \end{aligned} \quad (44\text{e})$$

Here the superscript “ $N$ ” stands for including the QN from the NDM. The noise spectral density of the CC-SR considering the excess noise from the WLC is then

$$S_h^N(\Omega) = \frac{h_{\text{SQL}}^2(\Omega)}{|Y_1 \sin(\xi) + Y_2 \cos(\xi)|^2} \begin{bmatrix} |X_{11}^N \sin(\xi) + X_{21}^N \cos(\xi)|^2 + |X_{12}^N \sin(\xi) + X_{22}^N \cos(\xi)|^2 \\ + |P_{11}^N \sin(\xi) + P_{21}^N \cos(\xi)|^2 + |P_{12}^N \sin(\xi) + P_{22}^N \cos(\xi)|^2 \\ + |Q_{11}^N \sin(\xi) + Q_{21}^N \cos(\xi)|^2 + |Q_{12}^N \sin(\xi) + Q_{22}^N \cos(\xi)|^2 \end{bmatrix}. \quad (45)$$

Without the SSA, the numbers  $\sqrt{T_{\text{BS}}}$  and  $\sqrt{R_{\text{BS}}}$  in the above equations are replaced by matrices:

$$\mathbf{t}_n = \frac{1}{2} \begin{pmatrix} \sqrt{T_{\text{BS}}(\omega_0 + \Omega)} + \sqrt{T_{\text{BS}}(\omega_0 - \Omega)} & \sqrt{T_{\text{BS}}(\omega_0 + \Omega)} - \sqrt{T_{\text{BS}}(\omega_0 - \Omega)} \\ \sqrt{T_{\text{BS}}(\omega_0 + \Omega)} - \sqrt{T_{\text{BS}}(\omega_0 - \Omega)} & \sqrt{T_{\text{BS}}(\omega_0 + \Omega)} + \sqrt{T_{\text{BS}}(\omega_0 - \Omega)} \end{pmatrix}, \quad (46)$$

$$\mathbf{r}_n = \frac{1}{2} \begin{pmatrix} \sqrt{R_{\text{BS}}(\omega_0 + \Omega)} + \sqrt{R_{\text{BS}}(\omega_0 - \Omega)} & \sqrt{R_{\text{BS}}(\omega_0 + \Omega)} - \sqrt{R_{\text{BS}}(\omega_0 - \Omega)} \\ \sqrt{R_{\text{BS}}(\omega_0 + \Omega)} - \sqrt{R_{\text{BS}}(\omega_0 - \Omega)} & \sqrt{R_{\text{BS}}(\omega_0 + \Omega)} + \sqrt{R_{\text{BS}}(\omega_0 - \Omega)} \end{pmatrix}, \quad (47)$$

and the input-output relations are then

$$\mathbf{b}^N(\Omega) = X^N(\Omega) \mathbf{a}^N(\Omega) + \mathbf{Y}^N(\Omega) \tilde{h}(\Omega) + P^N(\Omega) \mathbf{p}(\Omega) + Q^N(\Omega) \mathbf{q}(\Omega), \quad (48)$$

$$W(\Omega) = [(\mathbf{t}_n \mathcal{R}_{\text{AUX}})^{-1} - r_{\text{AUX}} \mathcal{R}_{\text{AUX}} \mathbf{t}_n U]^{-1}, \quad (49\text{a})$$

$$X^N(\Omega) = t_{\text{AUX}}^2 \mathcal{R}_{\text{AUX}} \mathbf{t}_n U(\Omega) W(\Omega) - r_{\text{AUX}} I, \quad (49\text{b})$$

$$\mathbf{Y}^N(\Omega) = t_{\text{AUX}} r_{\text{AUX}} \mathbf{t}_n \mathcal{R}_{\text{AUX}} U(\Omega) W(\Omega) \mathcal{R}_{\text{AUX}} \mathbf{t}_n V(\Omega) + t_{\text{AUX}} \mathcal{R}_{\text{AUX}} \mathbf{t}_n V(\Omega), \quad (49\text{c})$$

$$P^N(\Omega) = t_{\text{AUX}} \mathcal{R}_{\text{AUX}} \mathbf{t}_n U(\Omega) W(\Omega) \mathcal{R}_{\text{AUX}}^{-1} \mathbf{t}_n^{-1} \mathbf{r}_n, \quad (49\text{d})$$

$$Q^N(\Omega) = -t_{\text{AUX}} r_{\text{AUX}} \mathcal{R}_{\text{AUX}} \mathbf{t}_n U(\Omega) W(\Omega) \mathcal{R}_{\text{AUX}} \mathbf{r}_n - t_{\text{AUX}} \mathcal{R}_{\text{AUX}} \mathbf{r}_n. \quad (49\text{e})$$

#### IV. NOISE DENSITY CURVES FOR THE CC-SR CONFIGURATION

Assuming the GW detector is working at  $I_0 = I_{\text{SQL}}$ , we plot  $h_n(\Omega)/h_{\text{SQL}}(\gamma)$  for two quadratures  $b_1$  ( $\xi = \pi/2$ ) and  $b_2$  ( $\xi = 0$ ). The noise curves for the SR configuration are plotted as red solid (dashed) for  $b_1$  ( $b_2$ ) in Fig. 4 [both (a) and (b)], generated by using the approximation  $\Omega L/c \ll 1$  and  $t_1 \ll 1$  in Eqs. (19a)–(19b), and setting  $r_{\text{AUX}} = 0$  and  $L_{\text{AUX}} = 0$  in Eqs. (26c)–(26d), in agreement with the results in Ref. [7]. The corresponding noise curves for the CC-SR configuration of Fig. 2, but *without the NDM*, are shown by green solid (dashed) lines for the  $b_1$  ( $b_2$ )

quadrature, for two different values of  $R_{\text{AUX}}$  ( $\equiv r_{\text{AUX}}^2$ ): 99% in Fig. 4(a) and 99.5% in Fig. 4(b). Both curves have a minimum at around  $\Omega_c/(2\pi) = 127$  Hz; this value is determined by the choice of  $L_{\text{AUX}}$ . As can be seen, use of a higher reflectivity  $M_{\text{AUX}}$  reduces the QN at the minimum (i.e., increases sensitivity) but narrows the width of the resonance dip.

Next, we show the noise curves for the CC-SR configuration of Fig. 2, in the presence of the NDM and under the SSA, but without taking into account the QN from the NDM. The  $b_1$  ( $b_2$ ) quadrature is shown as the black solid (dashed) lines in Fig. 4, again for two different values of  $R_{\text{AUX}}$ . As expected, the addition of the NDM causes the

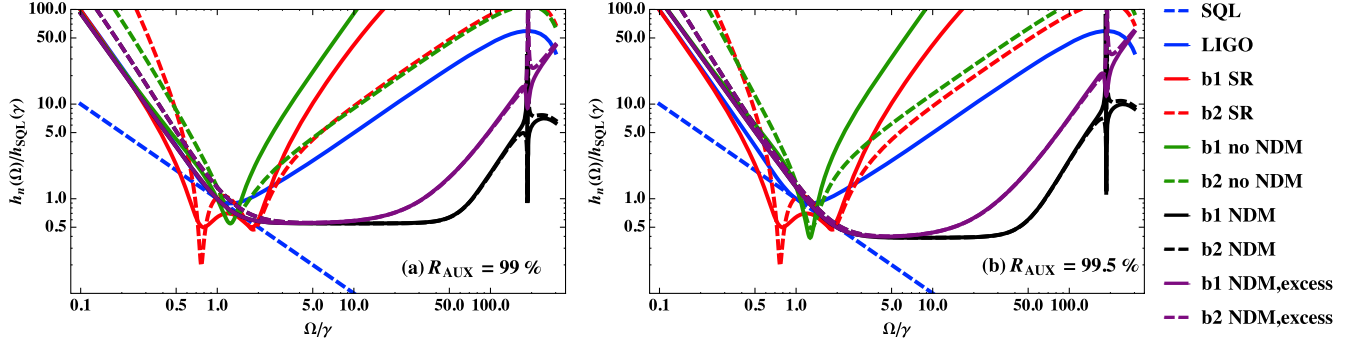


FIG. 4 (color online). Log-log plots of  $h_n(\Omega)/h_{\text{SQL}}(\gamma)$  versus  $\Omega/\gamma$  for the two quadratures  $b_1$  and  $b_2$ , for the CC-SR configuration when (a)  $R_{\text{AUX}} = 99\%$  and (b)  $R_{\text{AUX}} = 99.5\%$ , with (without) the NDM are shown in black (green) under the SSA. The noise curves considering the QN from the NDM are shown in purple. The noise curves for  $b_{1,2}$  in the SR configuration with  $R_{\text{SR}} = 81\%$ ,  $\varphi_{\text{SRC}} = \pi/2 - 0.47$  and  $\Phi_{\text{SRC}} = 0$ , are shown as the red curves. The noise curve for LIGO and the SQL line are plotted in blue.

WLC effect, thus broadening the dips significantly, covering the range from  $\sim 100$  Hz to  $\sim 5000$  Hz without considering the excess QN from the NDM, for  $R_{\text{AUX}} = 99\%$ , without reducing sensitivity. This is consistent with the result for the classical response of the CC-SR presented in Sec. II B. For the higher value of  $R_{\text{AUX}} = 99.5\%$ , we also see a significant broadening ( $\sim 200$  Hz to  $\sim 4000$  Hz), again without a reduction in sensitivity. When the excess QN from the NDM is taken into account, the noise curves get narrower, as shown in purple. When the SSA is relaxed, the results are shown in black in Figs. 5(a) and 5(b) for the two values of  $R_{\text{AUX}}$  above. We find that the noise curves for  $b_1$  change a lot, while those for  $b_2$  are modified slightly with a narrower width and higher sensitivity. The noise curve for  $b_2$  when  $R_{\text{AUX}} = 99\%$  is highly broadened with the introduction of the WLC [plotted as the purple dashed line in Fig. 5(a)]. Even though the curves remain above the SQL, this broadening is a very important result [21] and may prove useful in the aLIGO, since the noise floor in the current design is above the SQL anyway [7]. The fact that the noise floor remains above the SQL when the QN from the NDM is taken into account is not a fundamental constraint. As we will show soon, when the dispersion profile of the NDM is tailored to take into account the effect of OM resonance, it is possible to get the sensitivity well below the SQL.

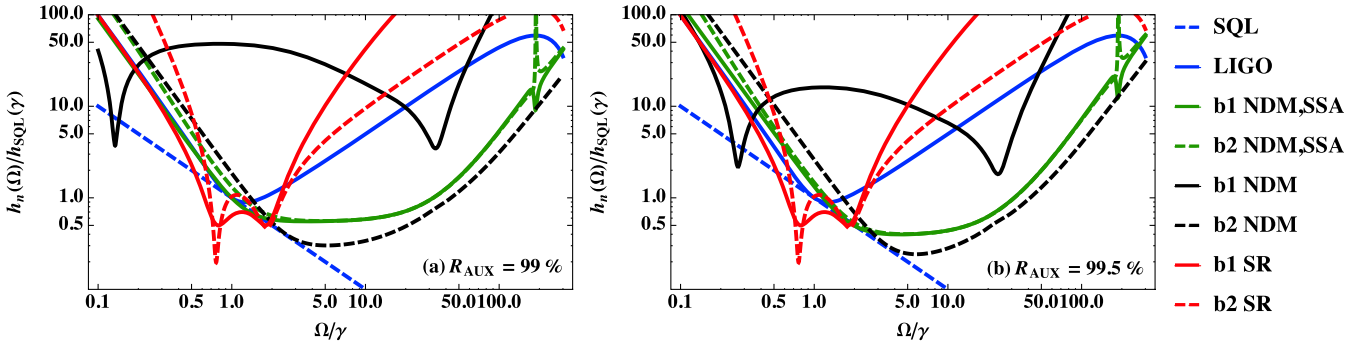


FIG. 5 (color online). Log-log plots of  $h_n(\Omega)/h_{\text{SQL}}(\gamma)$  versus  $\Omega/\gamma$  for the two quadratures  $b_1$  and  $b_2$ , for the CC-SR configuration when (a)  $R_{\text{AUX}} = 99\%$  and (b)  $R_{\text{AUX}} = 99.5\%$ , with and without the SSA.

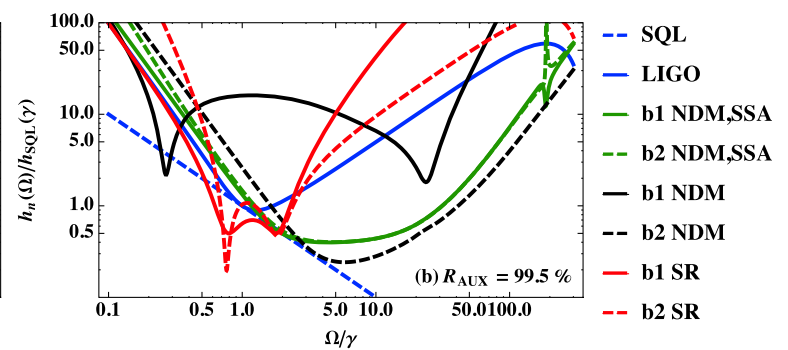
In the SR configuration, the OM resonance dips are induced by the phase  $\varphi_{\text{SRC}}$  gained from reflection off the SRC. It is shown in Ref. [7] that the position of the dips in the noise curves with a high  $r_{\text{SR}}$  agrees well with the resonances of the closed system ( $r_{\text{SR}} = 1$ ) with no GW signal [ $h(\Omega) = 0$ ]. We follow the method in Ref. [7] to evaluate the free oscillation modes for the closed system. Similarly to the quantum-field operators for the two quadrature fields, we consider a classical field  $\mathbf{E}$  consisting of two quadrature components  $E_1$  and  $E_2$ , i.e.,  $\mathbf{E}(\Omega) = (E_1(\Omega), E_2(\Omega))^T$ .  $\mathbf{E}$  enters Port B and returns as  $\mathbf{E}'$  after propagating through the two arms. At resonance,  $\mathbf{E}'$  propagates round-trip in the SRC and returns in phase with  $\mathbf{E}$ . As a result we find

$$[A(\Omega) - \mathcal{R}_{\text{SRC}}^{-2}]E(\Omega) = \mathbf{0}, \quad (50)$$

where  $A(\Omega)$  is as defined in Eqs. (18) and (19a), and  $\mathcal{R}_{\text{SRC}}$  is as defined in the paragraph preceding Eq. (24a). Therefore, the characteristic equation for this system is

$$|A(\Omega) - \mathcal{R}_{\text{SRC}}^{-2}| = 0. \quad (51)$$

The solution of this equation yields the eigenvalue  $\varphi_{\text{SRC}}$  (denoted by  $\varphi_{\text{SRC}}^0$ ) in the limit  $\Omega L_{\text{SRC}}/c \ll \pi$ , so that



$\Phi_{\text{SRC}} \approx 0$ . As is discussed in Sec. II, only one of the two sidebands will be on resonance for a specific choice of  $\varphi_{\text{SRC}}$ , and whether the plus- or minus-sideband is on resonance depends on the value of  $\varphi_{\text{SRC}}$ . Therefore, the phase shift experienced by a beam inside the arm cavities upon reflection from the SRC can be expressed as

$$\vartheta_{\text{SRC}} = \text{Arg} \left( \frac{t_1^2 r_{\text{SR}} e^{2i\varphi_{\text{SRC}}^0}}{1 + r_1 r_{\text{SR}} e^{2i\varphi_{\text{SRC}}^0}} + r_1 \right). \quad (52)$$

While we derived Eq. (52) for the limit  $r_{\text{SR}} = 1$ , the equation is still valid for a large value of  $r_{\text{SR}}$ , as discussed in Ref. [7].

In the CC-SR the SRC is tuned to resonance of the carrier wavelength and effectively disappears for the range of GW sidebands of interest. Therefore, the frequency-dependent phase  $\vartheta_{\text{SRC}}$  can be effectively achieved by round-trip propagation in the cavity of length  $L_{\text{AUX}}$  with a dispersive medium, i.e.,  $2(1 + \chi'/2)kL_{\text{AUX}}(\text{mod } 2\pi) = \vartheta_{\text{SRC}}$ . The dispersion is centered around the sideband in OM resonance in the same system but without the dispersive medium, whose frequency is determined by  $L_{\text{AUX}}$ . However, the exact dispersion required by Eq. (52) is hard to achieve, and we first use the Lorentzian model described by Eqs. (4) and (5) as an approximation to Eq. (52) for a certain range of frequencies.

The results for the QN-limited sensitivity using an NDM are plotted in Fig. 6, where the OM resonance is located at  $\omega_c = \omega_0 - \Omega_c$  [ $\Omega_c/(2\pi) = 236.3$  Hz] without the NDM for a specifically chosen  $L_{\text{AUX}}$ , and the dispersion is centered at  $\omega_c$ . When  $R_{\text{AUX}} = 99.9\%$ , the QN curves (shown as black curves) show a sub-SQL region around  $\omega_c$ . Here the parameters for the NDM are chosen so that at the center of the dispersion  $\omega_c$ , the gain is exactly zero, that is  $\chi''(\omega_c) = 0$  and  $g(\omega_c) = 1$  [here  $\Gamma_e/(2\pi) \approx 400$  Hz]. The minimum of the noise is  $\sim 0.18 h_{\text{SQL}}(\gamma)$ , and the bandwidth of the sub-SQL region is  $\sim 50$  Hz. Compared with the curve in the SR configuration with the highest

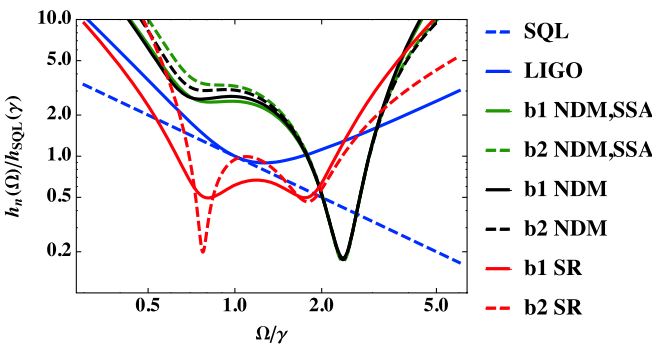


FIG. 6 (color online). Log-log plots of  $h_n(\Omega)/h_{\text{SQL}}(\gamma)$  versus  $\Omega/\gamma$  for the CC-SR scheme with a modified dispersion of the NDM centered at  $\omega_c = \omega_0 - \Omega_c$  [ $\Omega_c/(2\pi) = 236.3$  Hz]. The plots with (green) and without (black) the SSA are shown for comparison.

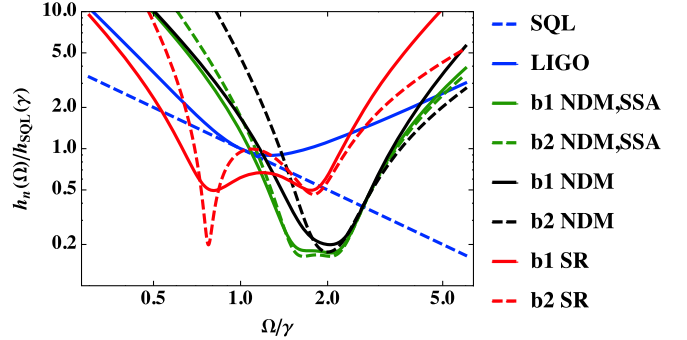


FIG. 7 (color online). Log-log plots of  $h_n(\Omega)/h_{\text{SQL}}(\gamma)$  versus  $\Omega/\gamma$  for the CC-SR scheme with a modified dispersion of the NDM centered at  $\omega_c = \omega_0 - \Omega_c$  [ $\Omega_c/(2\pi) = 200$  Hz].

sensitivity, which occurs for the second quadrature  $b_2$  (plotted as a dashed red line), the minimum is comparable while the bandwidth is much larger, resulting in an improvement in sensitivity-bandwidth product by a factor of  $\sim 7$ . We also show the results with the SSA in green as a comparison. We see that the SSA causes only a slight modification in the QN curves in this case.

In order to achieve a broader sub-SQL region, we center the dispersion at  $\omega_c = \omega_0 - \Omega_c$  [ $\Omega_c/(2\pi) = 200$  Hz] and tailor it according to Eq. (52).  $L_{\text{AUX}}$  is also modified so that the OM resonance without the NDM is moved to the new  $\omega_c$ . The QN curves with  $R_{\text{AUX}} = 99.9\%$  under the SSA are shown in green in Fig. 7 [here  $\Gamma_e/(2\pi) \approx 16$  kHz], which exhibits a sub-SQL region of  $\sim 100$  Hz in width around  $\omega_c$ , with the minimum beating the SQL by a factor of 5. Without the SSA, the curves are plotted in black, exhibiting a sub-SQL region somewhat narrower than the case with SSA. The QN curves for both quadratures show resonance dips around  $\Omega_c$ , and the dip for  $b_1$  is broader but shallower than that for  $b_2$ . If we compare the dip for  $b_1$  in this case with the highest sensitivity dip (corresponding to  $b_2$ ) in the SR case, we see that the sensitivity-bandwidth product is enhanced by a factor of  $\sim 14$ .

## V. WLC-SR CONFIGURATION

In the preceding section, we have shown that it is indeed possible to broaden the QN-limited response without a reduction in sensitivity. However, the degree of broadening is significantly smaller than the same found in the classical response. To overcome this limitation of broadening, we consider next an alternative scheme, simpler than the CC-SR, where we insert a dispersive medium in the SRC in aLIGO [Fig. 8(a)], with the propagation phase in the SRC approximating the eigenvalues  $\varphi_{\text{SRC}}^0$  determined by Eq. (51). We set  $L_{\text{SRC}}$  to  $\sim 10$  m and assume that the dispersive medium fills up the whole SR cavity. The QN can be calculated by taking  $r_{\text{AUX}} = 0$  and  $L_{\text{AUX}} = 0$ , and  $\mathcal{R}_n(\varphi_{\text{SRC}}, \Phi_{\text{SRC}}) = \mathcal{R}_{\text{SRC}}$  in Eqs. (25), (26a)–(26d), while the QN including the QN from the dispersive medium can be calculated using the method in Sec. III C [see Fig. 8(b)].

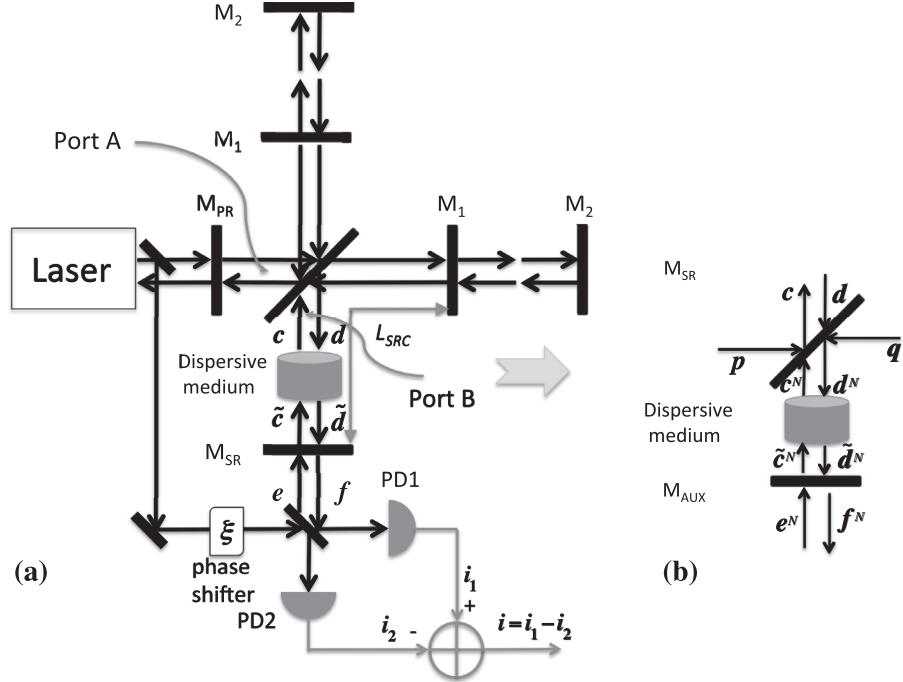


FIG. 8. (a) WLC-SR design. A dispersive medium is inserted in the SRC to achieve a broader sub-SQL dip. (b) Schematic view of the SR cavity with excess QN modeled by inserting a beam splitter with power reflectivity  $R_{BS}$  and power transmissivity  $T_{BS}$ . Here  $\mathbf{p}$  and  $\mathbf{q}$  are the vacuum noises that leak into the system.

### A. Phase compensation using a positive dispersion medium

As a direct comparison to the SR scheme in Ref. [7], where there is an OM resonance at  $\omega_c = \omega_0 - \Omega_c$  [ $\Omega_c/(2\pi) = 77.5$  Hz], we first choose  $L_{SRC}$  so that the OM resonance condition is satisfied at  $\omega_c$  and center the dispersion there. A careful inspection of the frequency dependence of the phase  $\varphi_{SRC}^0$  shows that in order to compensate for it, one must make use of positive dispersion. Of course, the concept of using a WLC to broaden the response of a cavity has traditionally been based on the use of negative dispersion, due to the nature of the round-trip phase in a conventional cavity. However, as we see here, for a more complex system, this general notion does not necessarily hold. For the PDM we need to use

here, we model the dispersion as a narrow transparency peak on top of a broader absorption dip, opposite to the NDM described in Eqs. (4) and (5). In the limit of vanishing Rabi frequencies ( $\Omega_k \rightarrow 0$ ),  $\chi'$  and  $\chi''$  of the PDM necessary to achieve the phase  $\varphi_{SRC}^0$  are plotted in Fig. 9, with the parameters chosen such that at the center of the dispersion  $\chi''(\omega_c) = 0$  and  $g(\omega_c) = 1$ . The PDM can be realized, for example, via EIT. It is shown in Ref. [16] that the QN of the  $\Lambda$ -type EIT system can be correctly described by the single-channel Caves model. The QN-limited sensitivity with the QN from the PDM is shown in Fig. 10. When the power reflectivity of  $M_{SR}$  is  $R_{SR} = 81\%$  (same as the SR case), the sensitivity curve for  $b_2$  under the SSA [plotted as dashed green lines in Fig. 10(a)] exhibits a sub-SQL region 3 times broader than that for  $b_2$  in the case of an empty SRC

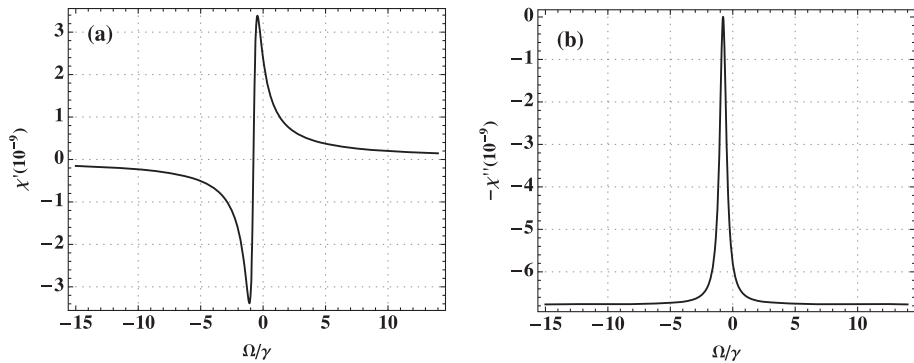


FIG. 9. Plots of (a)  $\chi'$  and (b)  $-\chi''$  versus  $\Omega/\gamma$  for the PDM used in plotting Fig. 10.

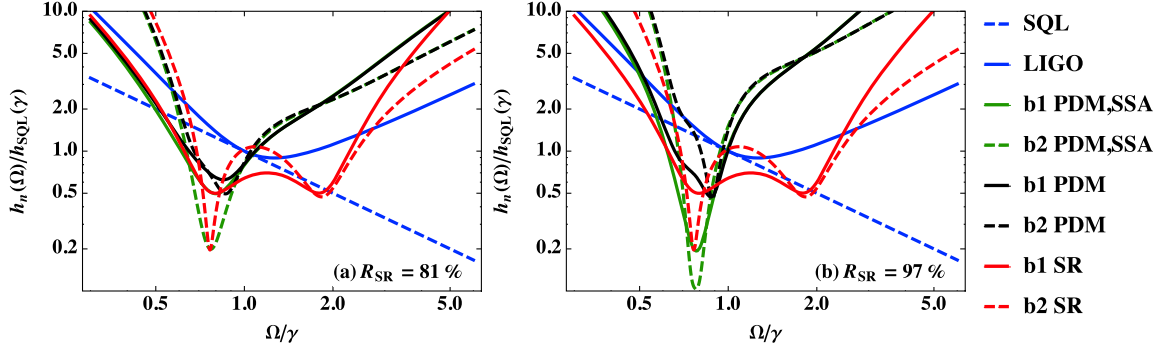


FIG. 10 (color online). Log-log plot of  $h_n(\Omega)/h_{\text{SQL}}(\gamma)$  versus  $\Omega/\gamma$  in the WLC-SR configuration with a tailored positive dispersion centered at  $\omega_c = \omega_0 - \Omega_c$  [ $\Omega_c/(2\pi) = 77.5$  Hz] when (a)  $R_{\text{SR}} = 81\%$  and (b)  $R_{\text{SR}} = 97\%$ .

(plotted as a red dashed line) without decrease in sensitivity. When  $R_{\text{SR}} = 97\%$  [Fig. 10(b)], the sensitivity increases. The minimum value for the second quadrature  $b_2$  decreases by a factor of 2 with a loss in the bandwidth, and the curve for the first quadrature  $b_1$  is lowered to about the same level as that for  $b_2$  in the SR case. Without the SSA, the QN curves are shown in black. In this case, however, the QN is lifted up to  $\sim 0.5h_{\text{SQL}}(\gamma)$  for both  $R_{\text{SR}} = 81\%$  and  $97\%$ , and there is no improvement in the sensitivity-bandwidth product.

### B. Phase compensation using a negative dispersion medium

We next consider a case where the dispersion is centered at a higher frequency. For this case, an NDM has to be used, whose  $\chi'$  and  $\chi''$  are plotted in Fig. 11 for  $\Omega_c/(2\pi) = 200$  Hz [here  $\Gamma_e/(2\pi) \approx 16$  kHz]. The results for the QN-limited sensitivity curves are shown in Fig. 12. Here  $L_{\text{SRC}}$  is changed so that the OM resonance of the system without the dispersive medium is at  $\omega_c = \omega_0 - \Omega_c$ . We choose the parameters for the dispersion such that  $\chi''(\omega_c) = 0$  and  $g(\omega_c) = 1$ . Under the SSA, the noise curves exhibit a rather broad sub-SQL region of a bandwidth around 140 Hz with its minimum  $\sim 5.5$  times smaller than  $h_{\text{SQL}}(\gamma)$  when  $R_{\text{SR}} = 97\%$ . We also show in Fig. 12 that when the SSA is removed, the results remain almost unchanged with the valley  $\sim 5$  Hz narrower in width. To

summarize, the sensitivity-bandwidth product is enhanced by nearly a factor of 18 compared to the highest sensitivity result (for  $b_2$ ) in the SR scheme.

### C. Lasing condition

When the gain medium is introduced, one potential issue is that the system might start lasing. Consider the cavity composed by  $M_{\text{SR}}$  and the arm cavity as a compound mirror  $M_{12}$ , which entails an effective quality factor  $Q_c = 3.8 \times 10^{13}$ . Since the OM effects modify the resonance position to  $\omega_0 - \Omega_c$  [ $\Omega_c/(2\pi) = 200$  Hz] in the system in the case shown above in Sec. V B, we alter the length  $L_{\text{SRC}}$  so that the semiclassical resonance of the cavity is located at  $\omega_0 - \Omega_c$ . In steady state, the phase and amplitude of the field inside the cavity satisfy a set of self-consistent equations [19]:

$$\begin{aligned} & \left(1 + \frac{1}{2}\chi'(E, \omega)\right) \frac{\omega}{c} 2L_{\text{SRC}} + \vartheta_{12}(\omega) \\ &= \frac{\omega_{\text{res}}}{c} 2L_{\text{SRC}} + \vartheta_{12}(\omega_{\text{res}}), \end{aligned} \quad (53)$$

$$\chi''(E, \omega) = -1/Q_c. \quad (54)$$

where  $\vartheta_{12}$  is the frequency-dependent phase that the field gains from reflecting off  $M_{12}$ ,  $\omega$  is the lasing frequency, and  $\omega_{\text{res}} = 2\pi f_{\text{res}}$  is the resonant frequency of the cavity in the

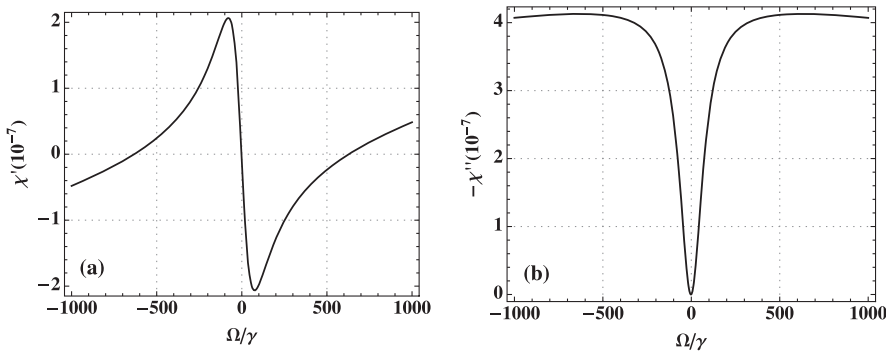


FIG. 11. Plots of (a)  $\chi'$  and (b)  $-\chi''$  versus  $\Omega/\gamma$  for the NDM used in plotting Fig. 12.

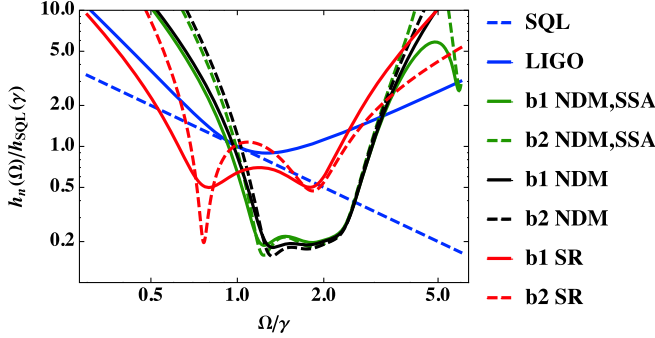


FIG. 12 (color online). Log-log plot of  $h_n(\Omega)/h_{SQL}(\gamma)$  versus  $\Omega/\gamma$  in the WLC-SR configuration with a tailored negative dispersion centered around  $\omega_0 - \Omega_c$  ( $\Omega_c/(2\pi) = 200$  Hz). The noise curves when  $R_{SR} = 97\%$  without (with) the SSA are plotted in black (green).

absence of the medium. For the PDM with  $\chi''(\omega_c) = 0$ ,  $\chi''$  is always positive for all frequencies, therefore the system is always below the lasing threshold. For the NDM, the boundaries of the lasing range can be solved by setting  $E = 0$  ( $\Omega_k = 0$ ) in Eq. (4) and plugging the resulting value of  $\chi''$  into Eq. (54). For frequencies  $f_{-1} < f < f_1$ ,  $f < f_{-2}$  or  $f_2 < \omega$  ( $f_{\pm 1} = f_{res} \pm 2.0$  Hz,  $f_{\pm 2} = f_{res} \pm 2.0 \times 10^9$  Hz, as shown in Fig. 13), the gain cannot compensate for the cavity loss, so that  $E = 0$ ; otherwise Eq. (54) is satisfied, from which we can solve for  $E(f)$  as a function of frequency  $f = \omega/(2\pi)$ . It can be seen that the frequency  $\omega$  that satisfies Eq. (53) falls within the range  $f_{-1} < f < f_1$ , where the gain is below lasing threshold and  $E = 0$ . Thus, we find that lasing will not occur in this system.

## VI. CONSIDERATION OF AN EXPLICIT SYSTEM FOR THE NDM AND MORE EXACT CONSIDERATION OF THE QN

As we have discussed briefly earlier in the paper, the Caves model makes some assumptions that may not necessarily hold for some systems. In Ref. [16], we have carried out a comprehensive and systematic analysis in

order to determine whether the noise in a particular system can be predicted correctly by using the Caves model. Specifically, we have used a Master Equation (ME) approach to determine the noise spectrum for a range of excitations, involving two or more energy levels, under conditions that may yield gain or attenuation. For each case, we have then computed the noise spectrum using the Caves model. In some cases, we have found these models to agree with each other. In other cases, we have shown that the details of the process must be considered to compute the noise using the ME while the Caves model cannot be used. This is true, for example, in a composite system where an inverted two-level transition produces gain, while a non-inverted two-level system produces absorption, with the gain exactly canceling the absorption at a particular probe frequency. While a naive, single-channel Caves model would imply no noise at this frequency, the ME result predicts a noise that is substantial at this frequency. We have also shown that in a  $\Lambda$ -type EIT (electromagnetically induced transparency) system where, in the steady state, the atoms are in a so-called dark-state, representing a superposition of metastable ground states, and no population in excited states, the single-channel Caves model yields the correct result. Such a system occurs, for example, in a  $\Lambda$ -type EIT (electromagnetically induced transparency) system. Inspired by EIT, we have shown that it is also possible to produce such an EIT system where the steady state is essentially a dark state, in a five-level transition which produces a broad gain away from the EIT condition. This configuration, which we call a Gain-EIT (GEIT) system, can be tailored to produce the negative dispersion necessary for realizing the WLC effect. Here, we first describe this GEIT system briefly before considering its application as the NDM in the WLC-SR configuration. More details about this system can be found in Ref. [16].

The GEIT system is shown schematically in Fig. 14. It is a five-level M system, where the transitions  $|1\rangle - |4\rangle$ ,  $|2\rangle - |4\rangle$  and  $|3\rangle - |5\rangle$  are coupled by the pump fields  $\Omega_1$ ,  $\Omega_2$  and  $\Omega_4$ , respectively, while the transition  $|2\rangle - |5\rangle$  is coupled by the probe field  $\Omega_3$ . We assume that  $\delta_i$  ( $i = 1, 2$ ) is chosen to

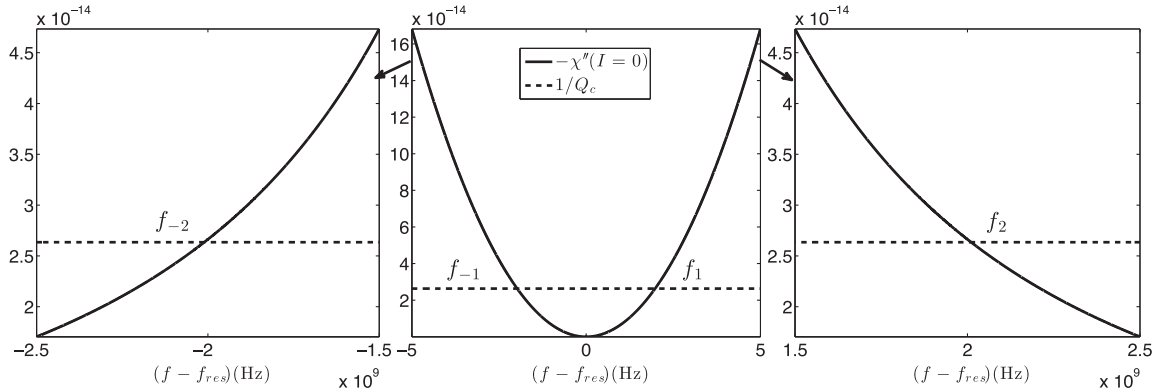


FIG. 13. Illustration of the lasing ranges.

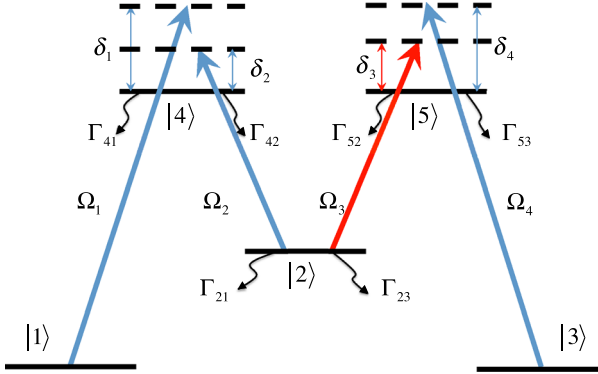


FIG. 14 (color online). Schematic illustration of the five-level GEIT system.

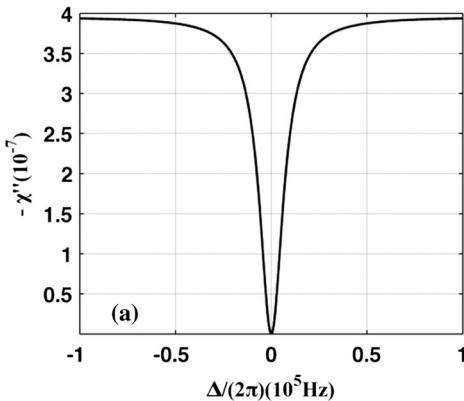
balance the differential light shift experienced by levels  $|1\rangle$  ( $\Omega_1^2/(4\delta_1)$ ) and  $|2\rangle$  ( $\Omega_2^2/(4\delta_2) + \Omega_3^2/(4\delta_3)$ ), so that the left leg of the M system composed by  $|1\rangle - |4\rangle - |2\rangle$  is resonant. For the other leg,  $|2\rangle - |5\rangle - |3\rangle$ , we define  $\delta_3 = \delta_{30} + \Delta$ , where  $\Delta = 0$  corresponds to the condition where the differential light shift experienced by levels  $|3\rangle$  ( $\Omega_4^2/(4\delta_4)$ ) and  $|2\rangle$  ( $\Omega_2^2/(4\delta_2) + \Omega_3^2/(4\delta_3)$ ) is balanced.

We consider the case when  $\gamma/(2\pi) = 6\text{MHz}$ ,  $\Omega_1 = \gamma$ ,  $\Omega_2 = 10^2\gamma$ ,  $\Omega_3 = 10^{-6}\gamma$ ,  $\Omega_4 = 10^{-1}\gamma$ , and  $\delta_1 \approx \delta_2 \approx \delta_3 \approx \delta_4 \approx 10^3\gamma$ . We show in Fig. 15(a) that a transmission profile with a dip on top of a broad gain peak is produced, and the negative dispersion is plotted in Fig. 15(b). We have also verified that the gain remains linear (i.e., independent of the amplitude of  $\Omega_3$ ) as the amplitude of  $\Omega_3$  approaches a vanishing value.

To evaluate the QN using the result from the ME model [16], we need to make use of the equations

$$\mathbf{y}^*(\Omega) = \sqrt{g}\mathbf{y}(\Omega) + X_1\mathbf{v}_1^\dagger(\Omega) + X_2\mathbf{v}_2(\Omega), \quad (55)$$

$$X_1 = \sqrt{(g-1)\frac{G_1}{G_1-G_2}}, \quad X_2 = \sqrt{(g-1)\frac{G_2}{G_1-G_2}}, \quad (56)$$



instead of Eqs. (40) and (41), where  $\mathbf{v}_1^\dagger$  and  $\mathbf{v}_2$  are vacuum fields that account for the additional noise. Here,  $G_1$  and  $G_2$  are the contributions of the amplification and attenuation, respectively, to the net gain  $g = \exp(G_1 - G_2)$ , which are proportional to  $\mathcal{A}$  and  $\mathcal{B}$  in Ref. [16]. The values of  $\mathcal{A}$  and  $\mathcal{B}$  are calculated from solving the master equation of the GEIT system.

Using the results from the ME model and Eqs. (55) and (56), we can calculate the QN-limited sensitivity. We show in Fig. 16 that the sensitivity curves using the GEIT with the parameters same as in Fig. 15 are very similar to the noise curves we plot in Fig. 12. The curves remain well below the SQL, and they have an enhancement of sensitivity-bandwidth product by a factor of 16.55 compared to the curve in the SR configuration with the highest sensitivity. As a comparison, we show in Fig. 17 the sensitivity curves for the first quadrature, when the QN from the NDM is taken into account using the ME approach and the Caves model, respectively. In this case, the results predicted by these models differ by less than 0.2%, and the difference is not noticeable. Similar agreement is seen for the second quadrature as well (not shown).

Using a different set of parameters for the GEIT system with the susceptibilities plotted in Fig. 18, we are able to achieve an even higher enhancement, 17.66, in the sensitivity-bandwidth product. The QN-limited sensitivity curves are shown in Fig. 19. In this case, the sensitivity predicted by the Caves model differs significantly from the result determined by the ME approach. At the bottom of the sensitivity curves, the difference is about 13%. Therefore, in general, the QN must be calculated by the ME approach only. Finally, it can be shown that lasing will not occur in this GEIT system by carrying out an analysis similar to what is described in Sec. V C. Thus, the predicted enhancement in sensitivity, as shown in Fig. 19, is not invalidated by any potential instability due to lasing.

It should be possible to demonstrate the five-level GEIT system using sublevels in alkali atoms such as Rb. However, current LIGO operates at the wavelength of

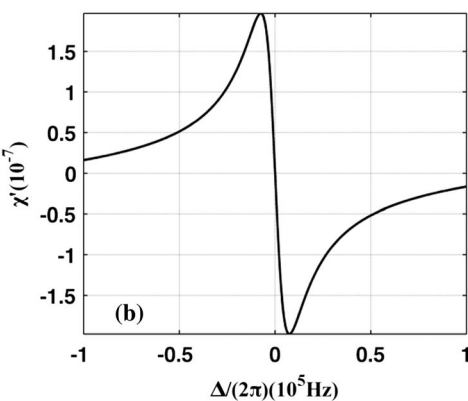


FIG. 15. Plots of (a)  $-\chi''$  and (b)  $\chi'$  versus  $\Delta/2\pi$  for the GEIT system in Fig. 14. Here,  $\gamma/(2\pi) = 6\text{ MHz}$ ,  $\Gamma_{41} = \Gamma_{42} = \Gamma_{52} = \Gamma_{53} = \Gamma_{21} = \Gamma_{23} = \gamma/2$ ,  $\delta_1 \approx \delta_2 \approx \delta_3 \approx \delta_4 \approx 10^3\gamma$ ,  $\Omega_1 = \gamma$ ,  $\Omega_2 = 10^2\gamma$ ,  $\Omega_3 = 10^{-6}\gamma$  and  $\Omega_4 = 10^{-1}\gamma$ .

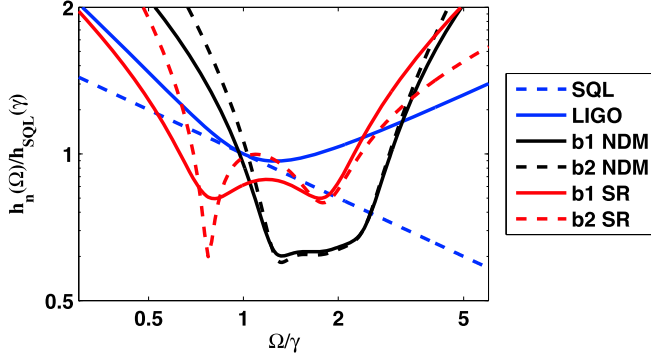


FIG. 16 (color online). Log-log plot of  $h_n(\Omega)/h_{SQL}(\gamma)$  versus  $\Omega/\gamma$  in the WLC-SR using the GEIT system with the parameters in Fig. 15 as the NDM.

1064 nm. We have not yet been able to identify a set of atomic transitions that can be used to realize the GEIT system at this wavelength. It is certainly possible that the operating wavelength of the next-generation LIGO would be chosen to coincide with an alkali atom transition, thus

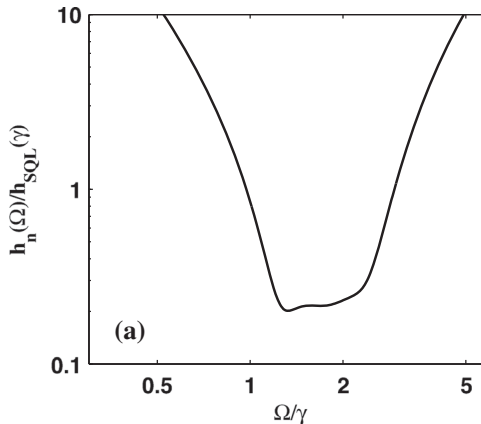


FIG. 17. Log-log plot of  $h_n(\Omega)/h_{SQL}(\gamma)$  versus  $\Omega/\gamma$  in the WLC-SR using the GEIT system with the parameters in Fig. 15 as the NDM. Then QN from the NDM is taken into account using (a) the ME approach and (b) the Caves model.

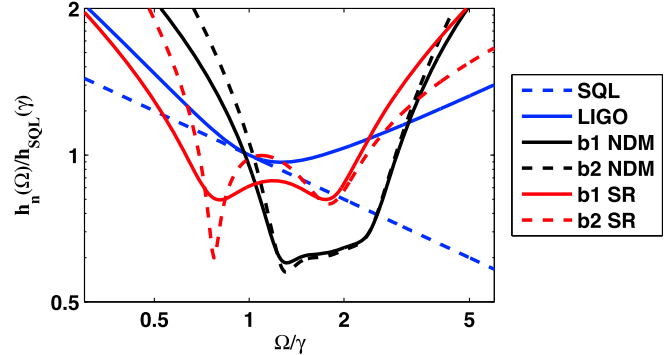


FIG. 19 (color online). Log-log plot of  $h_n(\Omega)/h_{SQL}(\gamma)$  versus  $\Omega/\gamma$  in the WLC-SR using the GEIT system with the parameters in Fig. 18 as the NDM.

making it possible to implement rather easily the WLC-SR configuration using the GEIT system. For the current wavelength of 1064 nm, one possible scheme for realizing the GEIT involves making use of a set of coupled fiber resonators, along with amplification induced, for example,

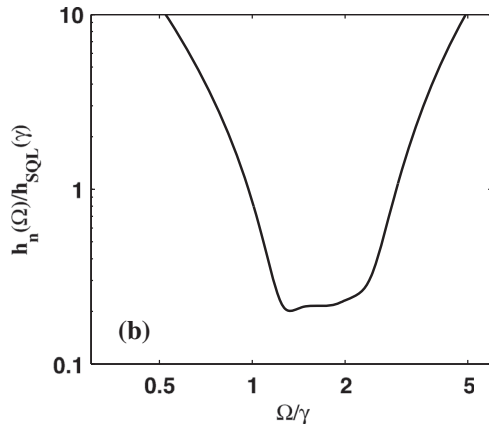


FIG. 18. Plots of (a)  $-\chi''$  and (b)  $\chi'$  versus  $\Delta/2\pi$  for the GEIT system in Fig. 14. Here,  $\gamma/(2\pi) = 6 \text{ MHz}$ ,  $\Gamma_{41} = \Gamma_{42} = \Gamma_{52} = \Gamma_{53} = \gamma/2$ ,  $\Gamma_{21} = \Gamma_{23} \approx 2.02 \times 10^{-3} \gamma$ ,  $\delta_1 \approx \delta_2 \approx \delta_3 \approx \delta_4 \approx 10^3 \gamma$ ,  $\Omega_1 = \gamma$ ,  $\Omega_2 = 10^2 \gamma$ ,  $\Omega_3 = 10^{-6} \gamma$  and  $\Omega_4 = 10^{-1} \gamma$ .

via stimulated Brillouin scattering [22]. Conventional EIT has already been demonstrated in coupled fiber resonators [23]. Work is currently in progress to devise the GEIT scheme using this approach and analyze the QN properties of such a system.

## VII. CONCLUSION

We have derived the QN density curves that show minimum detectable GW amplitudes for the CC-SR scheme (Fig. 2) and the WLC-SR scheme (Fig. 8), following the two-photon formalism [13]. We first take the QN from the NDM into account using the single-channel Caves model to determine an upper bound of the degree of enhancement in the sensitivity-bandwidth product. In the CC-SR GW detector, the conventional SR mirror is replaced by a CC containing an NDM. We have carried out a detailed QN analysis for various choices of parameters, taking into account all possible sources of QN, including the QN due to the NDM, under the assumption that all excess noise is suppressed below the QN. In keeping with our previous proposal, we first considered the case where the negative dispersion is centered at the semiclassical resonance frequency at which the maximum sideband amplitude is generated in the absence of the NDM, without taking into account the OM effects. In this case, even if the QN from the NDM is taken into account, the QN-limited sensitivity curves exhibit a significant broadening. Although the curves remain above the SQL, this result is of considerable significance, since the current noise in the aLIGO design does not allow operating in the sub-SQL region. We then modify the spectral profile of the dispersion so that it is centered at a different, optimally chosen, frequency  $\omega_0 - \Omega_c$  [ $\Omega_c/(2\pi) = 200$  Hz], which is the position of the OM resonance for the chosen  $L_{\text{AUX}}$ , and the shape of the dispersion curve is tailored to compensate for the nonlinear phase variation induced by the OM effects. Under these conditions, the noise curves fall significantly below the SQL with its minimum beating  $h_{\text{SQL}}(\gamma)$  by a factor of 5, while retaining a broad bandwidth  $\sim 120$  Hz. This represents an upper bound of  $\sim 14$  for the factor by which the sensitivity-bandwidth product is increased, compared with the highest sensitivity quadrature ( $b_2$ ) in the SR design [7]. We also considered an alternative, simpler WLC-SR design, which adds an NDM or a PDM in front of the conventional SR mirror in the SR configuration, depending on where the dispersion is centered. The nearly Lorentzian dispersion is tailored to compensate, as closely as possible, the nonlinear phase variation produced by the OM resonance. At the center of dispersion, which is the OM resonance frequency for the chosen SRC length  $L_{\text{SRC}}$ ,

shifted from the semiclassical resonance frequency mentioned above, the QN due to the dispersive medium is minimal but increases away from this point. After optimization of the various parameters, we have identified conditions using an NDM with  $\Omega_c/(2\pi) = 200$  Hz, under which the noise curves beat the SQL by a factor of 5.5. This represents an upper bound of  $\sim 18$  for the factor by which the sensitivity-bandwidth product is increased, compared with the highest sensitivity quadrature ( $b_2$ ) in the SR design [7]. Finally, we consider an explicit system for realizing the NDM, which is a five-level, M-configuration GEIT system. For this system, we use a rigorous approach, based on Master Equations [16] to calculate the QN from the NDM, so that the resulting prediction about the enhancement in the sensitivity-bandwidth product is definitive, and not simply an upper bound. Using the GEIT system as the NDM in the WLC-SR, we can get an enhancement of the sensitivity-bandwidth product by a factor of 17.66. Further investigation will focus on identifying practical schemes for implementing this concept.

## ACKNOWLEDGMENTS

This work was supported by DARPA through the Slow Light program under Grant No. FA9550-07-C-0030, and by AFOSR under Grants No. FA9550-10-1-0228 and No. FA9550-09-1-0652.

## APPENDIX: ABBREVIATIONS

Abbr.	Description	Abbr.	Description
aLIGO	Advanced LIGO	OM	Optomechanical
AUX	Auxiliary	PD	Photodetector
CC	Compound cavity	PDM	Positive dispersion medium
EIT	Electromagnetically induced transparency	PR	Power recycling
		PRC	Power recycling cavity
GEIT	Gain-EIT	QN	Quantum noise
GW	Gravitational wave	SQL	Standard quantum limit
LIGO	Laser Interferometer Gravitational Wave Observatory	SR	Signal recycling
		SRC	Signal recycling cavity
LO	Local oscillator	SSA	Single sideband approximation
ME	Master Equation		
NDM	Negative dispersion medium	WLC	White light cavity

- [1] J. B. Hartle, *Gravity: An Introduction to Einstein's General Relativity* (Addison-Wesley, Reading, MA, 2003).
- [2] A. Buonanno and Y. Chen, *Classical Quantum Gravity* **18**, L95 (2001).
- [3] K. S. Thorne, *Three Hundred Years of Gravitation*, edited by S. W. Hawking and W. Israel, (Cambridge University Press, Cambridge, England, 1987).
- [4] J. Mizuno, K. A. Strain, P. G. Nelson, J. M. Chen, R. Schilling, A. Rudiger, W. Winkler, and K. Danzmann, *Phys. Lett. A* **175**, 273 (1993).
- [5] K. A. Strain *et al.*, *Appl. Opt.* **42**, 1244 (2003).
- [6] R. Abbott *et al.* (LIGO), LIGO Note No. T070247-01, 2008.
- [7] A. Buonanno and Y. Chen, *Phys. Rev. D* **64**, 042006 (2001).
- [8] A. Buonanno and Y. Chen, *Phys. Rev. D* **65**, 042001 (2002).
- [9] M. Salit and M. S. Shahriar, *J. Opt.* **12**, 104014 (2010).
- [10] R. H. Rinkleff and A. Wicht, *Phys. Scr.* **T118**, 85 (2005); A. Wicht, R. H. Rinkleff, L. S. Molella, and K. Danzmann, *Phys. Rev. A* **66**, 063815 (2002); A. Rocco, A. Wicht, R. H. Rinkleff, and K. Danzmann, *Phys. Rev. A* **66**, 053804 (2002); A. Wicht, M. Muller, R. H. Rinkleff, A. Rocco, and K. Danzmann, *Opt. Commun.* **179**, 107 (2000); A. Wicht, K. Danzmann, M. Fleischhauer, M. Scully, G. Müller, and R. H. Rinkleff, *Opt. Commun.* **134**, 431 (1997); M. Salit, G. S. Pati, K. Salit, and M. S. Shahriar, *J. Mod. Opt.* **54**, 2425 (2007).
- [11] G. S. Pati, M. Salit, K. Salit, and M. S. Shahriar, *Phys. Rev. Lett.* **99**, 133601 (2007).
- [12] H. N. Yum, M. Salit, G. S. Pati, S. Tseng, P. R. Hemmer, and M. S. Shahriar, *Opt. Express* **16**, 20448 (2008).
- [13] C. M. Caves and B. L. Schumaker, *Phys. Rev. A* **31**, 3068 (1985); B. L. Schumaker and C. M. Caves, *Phys. Rev. A* **31**, 3093 (1985).
- [14] H. J. Kimble, Yu. Levin, A. B. Matsko, K. S. Thorne, and S. P. Vyatchanin, *Phys. Rev. D* **65**, 022002 (2001).
- [15] C. M. Caves, *Phys. Rev. D* **26**, 1817 (1982); Y. Yamamoto and H. A. Haus, *Rev. Mod. Phys.* **58**, 1001 (1986); M. O. Scully and M. S. Zubairy, *Quantum optics* (Cambridge University Press, Cambridge, England, 1997), Chap. 15.
- [16] M. Zhou, Z. Zhou, and S. M. Shahriar, [arXiv:1507.02251](https://arxiv.org/abs/1507.02251).
- [17] E. D. Black and R. N. Gutenkunst, *Am. J. Phys.* **71**, 365 (2003).
- [18] S. P. Vyatchanin and A. B. Matsko, *JETP* **77**, 218 (1993); S. P. Vyatchanin and E. A. Zubova, *Phys. Lett. A* **201**, 269 (1995); T. T. Fricke, Ph.D. thesis, Louisiana State University, 2011.
- [19] H. N. Yum, M. Salit, J. Yablon, K. Salit, Y. Wang, and M. S. Shahriar, *Opt. Express* **18**, 17658 (2010).
- [20] V. B. Braginsky, M. L. Gorodetsky, F. Ya. Khalili, A. B. Matsko, K. S. Thorne, and S. P. Vyatchanin, *Phys. Rev. D* **67**, 082001 (2003).
- [21] Y. Chen (private communication).
- [22] H. N. Yum, J. Scheuer, M. Salit, P. R. Hemmer, and M. S. Shahriar, *J. Lightwave Technol.* **31**, 3865 (2013).
- [23] Q. F. Xu, S. Sandhu, M. L. Povinelli, J. Shakya, S. H. Fan, and M. Lipson, *Phys. Rev. Lett.* **96**, 123901 (2006); L. Maleki, A. B. Matsko, A. A. Savchenkov, and V. S. Ilchenko, *Opt. Lett.* **29**, 626 (2004); Q. F. Xu, P. Dong, and M. Lipson, *Nat. Phys.* **3**, 406 (2007); J. Scheuer, A. A. Sukhorukov, and Y. S. Kivshar, *Opt. Lett.* **35**, 3712 (2010).

## Evolution of an $N$ -level system via automated vectorization of the Liouville equations and application to optically controlled polarization rotation

M.S. Shahriar<sup>a,b\*</sup>, Ye Wang<sup>a</sup>, Subramanian Krishnamurthy<sup>a</sup>, Y. Tu<sup>a</sup>, G.S. Pati<sup>c</sup> and S. Tseng<sup>a</sup>

<sup>a</sup>Department of EECS, Northwestern University, Evanston, IL 60208, USA; <sup>b</sup>Department of Physics and Astronomy, Northwestern University, Evanston, IL 60208, USA; <sup>c</sup>Department of Physics & Pre-Engineering, Delaware State University, DE 19901, USA

(Received 23 August 2013; accepted 8 November 2013)

The Liouville equation governing the evolution of the density matrix for an atomic/molecular system is expressed in terms of a commutator between the density matrix and the Hamiltonian, along with terms that account for decay and redistribution. To find solutions of this equation, it is convenient first to reformulate the Liouville equation by defining a vector corresponding to the elements of the density operator, and determining the corresponding time-evolution matrix. For a system of  $N$  energy levels, the size of the evolution matrix is  $N^2 \times N^2$ . When  $N$  is very large, evaluating the elements of these matrices becomes very cumbersome. We describe a novel algorithm that can produce the evolution matrix in an automated fashion for an arbitrary value of  $N$ . As a non-trivial example, we apply this algorithm to a 15-level atomic system used for producing optically controlled polarization rotation. We also point out how such a code can be extended for use in an atomic system with arbitrary number of energy levels.

**Keywords:** optically controlled birefringence; multi-level coherent process; novel computational algorithm

### 1. Introduction

For some situations in atomic and molecular physics, it is necessary to consider a system with many energy levels, such as excitation involving many hyperfine levels and/or Zeeman sublevels. The Liouville equation that describes the evolution of the density matrix is expressed in terms of a commutator between the density matrix and the Hamiltonian, as well as additional terms that account for decay and redistribution [1–4]. To find solutions to this equation in steady state or as a function of time, it is convenient first to reformulate the Liouville equation by defining a vector corresponding to the elements of the density operator, and determining the corresponding time evolution matrix. To find the steady-state solution in a closed system, it is also necessary to eliminate one of the diagonal elements of the density matrix from these equations, because of redundancy. For a system of  $N$  atoms, the size of the evolution matrix is  $N^2 \times N^2$ , and the size of the reduced matrix is  $(N^2 - 1) \times (N^2 - 1)$ . When  $N$  is very large, evaluating the elements of these matrices becomes very cumbersome. In this paper, we describe an algorithm that can produce the evolution matrix in an automated fashion, for an arbitrary value of  $N$ . We then apply this algorithm to a 15-level atomic system used for producing optically controlled polarization rotation.

The paper is organized as follows. In Section 2, we introduce the algorithm, using a two-level system as an example. In Section 3, we verify the algorithm with a common three-level Raman system, and also show how

to generate a time-independent Hamiltonian for any system by inspection alone. In Section 4, we show how to generalize this to a system with arbitrary number of levels. In Section 5, we use this algorithm to solve a 15-level atomic system used for producing optically controlled polarization rotation. In the appendices, we include explicit Matlab codes for two-, three-, and 15-level systems and also a non-intuitive, but faster computational method for our algorithm.

### 2. A two-level system

To illustrate the basic idea behind the algorithm, we first consider the simplest case: a two-level system of atoms excited by a monochromatic field [3], as illustrated in Figure 1. Here,  $\hbar\omega_1$  and  $\hbar\omega_2$  are the energies of levels  $|1\rangle$  and  $|2\rangle$ , and  $\omega$  is the frequency of the laser, with a Rabi frequency of  $\Omega_0$  [5].

The Hamiltonian, under electric dipole and rotating wave approximations, is given by

$$\mathcal{H} = \hbar \begin{pmatrix} \omega_1 & \frac{\Omega_0 e^{i(\omega t - kz_0 + \phi)}}{2} \\ \frac{\Omega_0}{2} e^{-i(\omega t - kz_0 + \phi)} & \omega_2 \end{pmatrix}, \quad (1)$$

where  $k$  is the wavenumber of the laser,  $z_0$  is the position of the atom, and  $\phi$  is the phase of the field. Without loss of generality, we set  $z_0 = 0$  and  $\phi = 0$  in what follows. The corresponding two-level state vector for each atom is

\*Corresponding author. Email: [shahriar@northwestern.edu](mailto:shahriar@northwestern.edu)

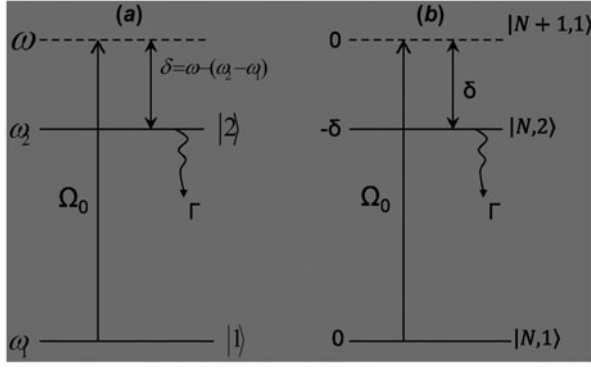


Figure 1. Schematic diagram showing a two-level system. (a) Two-level system with eigenvectors  $|1\rangle$  and  $|2\rangle$ ; (b) considering photon numbers, where  $|N,1\rangle$  and  $|N+1,1\rangle$  have the same energy, and the energy difference between  $|N+1,1\rangle$  and  $|N,2\rangle$  is  $\hbar\delta$ .

$$|\psi\rangle = \begin{bmatrix} C_1(t) \\ C_2(t) \end{bmatrix}, \quad (2)$$

which obeys the Schrödinger equation

$$i\hbar \frac{\partial |\psi\rangle}{\partial t} = \mathcal{H}|\psi\rangle. \quad (3)$$

To simplify the calculation, we convert the equations to the rotating wave frame by carrying out the following transformation into an interaction picture:

$$|\tilde{\psi}\rangle \equiv \begin{bmatrix} \tilde{C}_1(t) \\ \tilde{C}_2(t) \end{bmatrix} = R|\psi\rangle, \quad (4a)$$

where

$$R = \begin{bmatrix} e^{i\omega_1 t} & 0 \\ 0 & e^{i\omega_2 t} \end{bmatrix}. \quad (4b)$$

The Schrödinger equation now can be written as

$$i\hbar \frac{\partial |\tilde{\psi}\rangle}{\partial t} = \tilde{\mathcal{H}}|\tilde{\psi}\rangle, \quad (5a)$$

where

$$\tilde{\mathcal{H}} = \hbar \begin{pmatrix} 0 & \frac{\Omega_0}{2} \\ \frac{\Omega_0}{2} & -\delta \end{pmatrix}, \quad (5b)$$

$$\delta = \omega - (\omega_2 - \omega_1). \quad (5c)$$

The time-independent Hamiltonian shown in Equation (5b) can also be derived easily without any algebraic manipulation. To see how, consider the diagram shown in Figure 1(b), where we have added the number of photons as a quantum number in designating the quantum states. Thus, for example,  $|N,1\rangle$  represents a joint quantum system where the number of photons in the laser field is  $N$ , and the atom is in state 1, and so on. Of course, a laser, being in a coherent state, is a linear

superposition of number states, with a mean photon number  $\langle N \rangle$ , assumed to be much larger than unity. In the presence of such a field, the interaction takes place between near-degenerate states, namely  $|N,2\rangle$  and  $|N+1,1\rangle$ , for example, with a coupling rate of  $\Omega_0/2$ , where  $\Omega_N \propto \sqrt{N}$ . Since the mean value of  $N$  is assumed to be very large, and much larger than its variance, one can assume the mean value of  $\Omega_N$ , defined as  $\Omega_0$ , to be proportional to  $\sqrt{N}$ . Under this approximation, we see that the coupling between any neighboring, near-degenerate pair of states is  $\Omega_0$ , and the energies of these states differ by  $\delta$ . If we choose the energy of  $|N+1,1\rangle$  to be 0, arbitrarily, then the energy of  $|N,2\rangle$  is  $-\hbar\delta$ . The interaction is contained within a given manifold, so that a difference in energy (by  $\hbar\omega$ ) between neighboring manifold is of no consequence in determining the evolution. These considerations directly lead to the Hamiltonian of Equation (5b). For a system involving more than two levels, a similar observation can be employed to write down the time-independent Hamiltonian by inspection, as we will show later.

The decay of the excited state amplitude, at the rate of  $\Gamma/2$ , can be taken into account by adding a complex term to the Hamiltonian, as follows:

$$\tilde{\mathcal{H}}' = \hbar \begin{bmatrix} 0 & \frac{\Omega_0}{2} \\ \frac{\Omega_0}{2} & -\frac{i\Gamma}{2} - \delta \end{bmatrix}, \quad (6)$$

For this modified Hamiltonian, the equation of evolution for the interaction picture density operator can be expressed as

$$\frac{\partial}{\partial t} \tilde{\rho} = \frac{\partial}{\partial t} \tilde{\rho}_{ham} + \frac{\partial}{\partial t} \tilde{\rho}_{source} + \frac{\partial}{\partial t} \tilde{\rho}_{trans-decay} \equiv \mathcal{Q}, \quad (7)$$

where the second term in the middle accounts for the influx of atoms into a state due to decay from another state, and the third term stands for any dephasing unaccompanied by population decay, often called transverse decay. In the case of a two-level system, we have:

$$\frac{\partial}{\partial t} \tilde{\rho}_{ham} = -\frac{i}{\hbar} [\tilde{\mathcal{H}}' \tilde{\rho} - \tilde{\rho} \tilde{\mathcal{H}}'^*], \quad (8a)$$

$$\frac{\partial}{\partial t} \tilde{\rho}_{source} = \begin{bmatrix} \Gamma \tilde{\rho}_{22} & 0 \\ 0 & 0 \end{bmatrix}, \quad (8b)$$

$$\frac{\partial}{\partial t} \tilde{\rho}_{trans-decay} = \begin{bmatrix} 0 & -\gamma_d \tilde{\rho}_{12} \\ -\gamma_d \tilde{\rho}_{21} & 0 \end{bmatrix}. \quad (8c)$$

For simplicity, we ignore the dephasing term in Equation (8c).

Substituting Equation (6) into Equation (8a), we get:

$$\frac{\partial}{\partial t} \tilde{\rho}_{\text{ham}} = \begin{pmatrix} \frac{1}{2}i\Omega_0(\tilde{\rho}_{12} - \tilde{\rho}_{21}) & \frac{1}{2}i((i\Gamma - 2\delta)\tilde{\rho}_{12} + \Omega_0(\tilde{\rho}_{11} - \tilde{\rho}_{22})) \\ -\frac{1}{2}i((-i\Gamma - 2\delta)\tilde{\rho}_{21} + \Omega_0(\tilde{\rho}_{11} - \tilde{\rho}_{22})) & \frac{1}{2}(-i\Omega_0(\tilde{\rho}_{12} - \tilde{\rho}_{21}) - 2\Gamma\tilde{\rho}_{22}) \end{pmatrix}. \quad (9)$$

Substituting Equations (8) and (9) into Equation (7), we get

$$\frac{\partial}{\partial t} \tilde{\rho} = \frac{\partial}{\partial t} \begin{pmatrix} \tilde{\rho}_{11} & \tilde{\rho}_{12} \\ \tilde{\rho}_{21} & \tilde{\rho}_{22} \end{pmatrix} = \begin{pmatrix} \frac{1}{2}i\Omega_0(\tilde{\rho}_{12} - \tilde{\rho}_{21}) + \Gamma\tilde{\rho}_{22} & \frac{1}{2}i(i(\Gamma + 2i\delta)\tilde{\rho}_{12} + \Omega_0(\tilde{\rho}_{11} - \tilde{\rho}_{22})) \\ -\frac{1}{2}i((-i\Gamma - 2\delta)\tilde{\rho}_{21} + \Omega_0(\tilde{\rho}_{11} - \tilde{\rho}_{22})) & \frac{1}{2}(-i\Omega_0(\tilde{\rho}_{12} - \tilde{\rho}_{21}) - 2\Gamma\tilde{\rho}_{22}) \end{pmatrix} = Q \equiv \begin{pmatrix} Q_{11} & Q_{12} \\ Q_{21} & Q_{22} \end{pmatrix} \quad (10)$$

In general, each of the matrix elements  $Q_{ij}$  can depend on all the  $\rho_{ij}$ . In order to find the steady-state solution, it is convenient to construct the following vector

$$A = \begin{bmatrix} \tilde{\rho}_{11} \\ \tilde{\rho}_{12} \\ \tilde{\rho}_{21} \\ \tilde{\rho}_{22} \end{bmatrix}. \quad (11)$$

Equation (10) can now be expressed as a matrix equation

$$\frac{\partial}{\partial t} A = MA, \quad (12)$$

where  $M$  is a  $(4 \times 4)$  matrix, represented formally as:

$$M = \begin{bmatrix} M_{11} & M_{12} & M_{13} & M_{14} \\ M_{21} & M_{22} & M_{23} & M_{24} \\ M_{31} & M_{32} & M_{33} & M_{34} \\ M_{41} & M_{42} & M_{43} & M_{44} \end{bmatrix}. \quad (13)$$

Of course, the elements of this matrix can be read-off from Equation (10). However, this task is quite cumbersome for an  $N$ -level system. Thus, it is useful to seek a general rule for finding this element without having to write down Equation (10) explicitly. Later on in this paper, we establish such a rule, and specify the algorithm for implementing it. Here, we can illustrate this rule with some explicit examples:

$$\begin{aligned} M_{11} &= Q_{11}, \text{ if we set } \tilde{\rho}_{11} = 1 \text{ and } \tilde{\rho}_{ij(i \neq 11)} = 0 \text{ in Equation (7);} \\ M_{12} &= Q_{11}, \text{ if we set } \tilde{\rho}_{12} = 1 \text{ and } \tilde{\rho}_{ij(i \neq 12)} = 0 \text{ in Equation (7);} \\ M_{13} &= Q_{11}, \text{ if we set } \tilde{\rho}_{21} = 1 \text{ and } \tilde{\rho}_{ij(i \neq 21)} = 0 \text{ in Equation (7);} \\ M_{14} &= Q_{11}, \text{ if we set } \tilde{\rho}_{22} = 1 \text{ and } \tilde{\rho}_{ij(i \neq 22)} = 0 \text{ in Equation (7);} \\ M_{21} &= Q_{12}, \text{ if we set } \tilde{\rho}_{11} = 1 \text{ and } \tilde{\rho}_{ij(i \neq 11)} = 0 \text{ in Equation (7);} \\ M_{22} &= Q_{12}, \text{ if we set } \tilde{\rho}_{12} = 1 \text{ and } \tilde{\rho}_{ij(i \neq 12)} = 0 \text{ in Equation (7);} \\ M_{23} &= Q_{12}, \text{ if we set } \tilde{\rho}_{21} = 1 \text{ and } \tilde{\rho}_{ij(i \neq 21)} = 0 \text{ in Equation (7);} \\ M_{24} &= Q_{12}, \text{ if we set } \tilde{\rho}_{22} = 1 \text{ and } \tilde{\rho}_{ij(i \neq 22)} = 0 \text{ in Equation (7);} \\ \text{and so on ...} & \end{aligned} \quad (14)$$

This is the key element of the algorithm presented in this paper. Explicitly, in a computer program, such as the one in Appendix 1, every time a parameter is changed, the elements of the  $M$  matrix are obtained by evaluating Equation (7), while setting all but one of the elements of the density matrix to zero. For numerical integration as a

function of time, one can then use a Taylor expansion to solve Equation (12).

To find the steady-state solution, we set  $\frac{\partial}{\partial t} A = 0$ , so that:

$$\begin{bmatrix} M_{11} & M_{12} & M_{13} & M_{14} \\ M_{21} & M_{22} & M_{23} & M_{24} \\ M_{31} & M_{32} & M_{33} & M_{34} \\ M_{41} & M_{42} & M_{43} & M_{44} \end{bmatrix} \begin{bmatrix} \tilde{\rho}_{11} \\ \tilde{\rho}_{12} \\ \tilde{\rho}_{21} \\ \tilde{\rho}_{22} \end{bmatrix} = 0. \quad (15)$$

Expanding this equation, we get:

$$\begin{cases} M_{11}\tilde{\rho}_{11} + M_{12}\tilde{\rho}_{12} + M_{13}\tilde{\rho}_{21} = -M_{14}\tilde{\rho}_{22} \\ M_{21}\tilde{\rho}_{11} + M_{22}\tilde{\rho}_{12} + M_{23}\tilde{\rho}_{21} = -M_{24}\tilde{\rho}_{22} \\ M_{31}\tilde{\rho}_{11} + M_{32}\tilde{\rho}_{12} + M_{33}\tilde{\rho}_{21} = -M_{34}\tilde{\rho}_{22} \\ M_{41}\tilde{\rho}_{11} + M_{42}\tilde{\rho}_{12} + M_{43}\tilde{\rho}_{21} = -M_{44}\tilde{\rho}_{22} \end{cases}. \quad (16)$$

For a closed system, there cannot be any net influx or outflux of atoms from the system. Thus, the rate of change of one of the diagonal (population) terms of the density matrix is the negative sum of the rates of change of the other diagonal (population) terms. Thus, one of the equations in the above system of equations is rendered redundant. We also know that for a closed system, sum of the diagonal elements of the density matrix equals unity. In the case of the two-level system, we thus have  $\tilde{\rho}_{11} + \tilde{\rho}_{22} = 1$ . We can thus choose to eliminate the last equation, for example, and replace  $\tilde{\rho}_{22}$  with  $(1 - \tilde{\rho}_{11})$  in the remaining three equations, to get

$$\begin{bmatrix} M_{11} & M_{12} & M_{13} \\ M_{21} & M_{22} & M_{23} \\ M_{31} & M_{32} & M_{33} \end{bmatrix} \begin{bmatrix} \tilde{\rho}_{11} \\ \tilde{\rho}_{12} \\ \tilde{\rho}_{21} \end{bmatrix} \equiv M' \begin{bmatrix} \tilde{\rho}_{11} \\ \tilde{\rho}_{12} \\ \tilde{\rho}_{21} \end{bmatrix} = \begin{bmatrix} M_{14} \\ M_{24} \\ M_{34} \end{bmatrix} \tilde{\rho}_{11} - \begin{bmatrix} M_{14} \\ M_{24} \\ M_{34} \end{bmatrix} \quad (17a)$$

so that

$$\begin{bmatrix} (M_{11} - M_{14}) & M_{12} & M_{13} \\ (M_{21} - M_{24}) & M_{22} & M_{23} \\ (M_{31} - M_{34}) & M_{32} & M_{33} \end{bmatrix} \begin{bmatrix} \tilde{\rho}_{11} \\ \tilde{\rho}_{12} \\ \tilde{\rho}_{21} \end{bmatrix} = - \begin{bmatrix} M_{14} \\ M_{24} \\ M_{34} \end{bmatrix}. \quad (17b)$$

Here, we have defined  $M'$  as the reduced matrix resulting from  $M$  after eliminating the last row and column, for convenience of discussion during the presentation of the general algorithm later on. To simplify the notation further, we define:

$$B \equiv \begin{bmatrix} \tilde{\rho}_{11} \\ \tilde{\rho}_{12} \\ \tilde{\rho}_{21} \end{bmatrix}, S \equiv \begin{bmatrix} M_{14} \\ M_{24} \\ M_{34} \end{bmatrix}, W \equiv \begin{bmatrix} (M_{11} - M_{14}) & M_{12} & M_{13} \\ (M_{21} - M_{24}) & M_{22} & M_{23} \\ (M_{31} - M_{34}) & M_{32} & M_{33} \end{bmatrix}. \quad (18)$$

Using these definitions in Equation (17), we get:

$$WB = -S.$$

Thus, the steady-state solution is simply given by:

$$B = -W^{-1}S. \quad (19)$$

In a computer code, such as the one in Appendix 1, the elements of  $W$  and  $S$  can be determined in an automated fashion by using a simple algorithm based on a generalization of this example. We get the values of  $\tilde{\rho}_{11}$ ,  $\tilde{\rho}_{12}$ , and  $\tilde{\rho}_{21}$  by using Equation (19). Using the condition  $\tilde{\rho}_{11} + \tilde{\rho}_{22} = 1$ , we can then find the value of  $\tilde{\rho}_{22}$ .

For the two-level system, the elements of  $M$ ,  $W$ , and  $S$  can be worked out by hand, without employing the general rules, with relative ease. However, for arbitrarily large systems, it can become exceedingly cumbersome. In what follows, we describe a compact algorithm for determining the elements of  $M$ ,  $W$ , and  $S$  for a system with  $N$  energy levels.

To start with, determine the elements of the complex effective Hamiltonian of Equation (6), as well as the elements of  $\tilde{\rho}_{\text{source}}$  for the  $N$ -level system. These matrices can be used to calculate the elements of  $Q$ , as defined in Equations (7) and (10). The elements of  $M$  can then be found by using the following algorithm. Let  $M_{np}$  denote the element corresponding to the  $n$ -th row and  $p$ -th column of the  $M$  matrix. Similarly, let  $Q_{\alpha\beta}$  denote the element corresponding to the  $\alpha$ -th row and  $\beta$ -th column of the  $Q$  matrix, and  $\tilde{\rho}_{\varepsilon\sigma}$  denote the elements corresponding to the  $\varepsilon$ -th row and  $\sigma$ -th column of the  $\tilde{\rho}$  matrix. Then one can use the following prescription to obtain  $M_{np}$ :

$$M_{np} = Q_{\alpha\beta} \text{ if we set } \tilde{\rho}_{\varepsilon\sigma} = 1 \text{ and } \tilde{\rho}_{ij(i \neq \varepsilon\sigma)} = 0 \text{ in Equation (7).}$$

Thus, the crux of the algorithm is to obtain a way of finding  $\alpha$ ,  $\beta$ ,  $\varepsilon$ , and  $\sigma$  efficiently, for a given set of values of  $\{n, p\}$ . These indices are obtained as follows:

$$\begin{aligned} \beta &= \text{nzrem}[n/N]; & \alpha &= 1 + (n - \beta)/N; \\ \alpha &= \text{nzrem}[p/N]; & \varepsilon &= 1 + (p - \alpha)/N, \end{aligned} \quad (20)$$

where *nzrem* is a user-defined function prescribed as follows: *nzrem*[A/B] = *remainder*[A/B] if the remainder is non-zero; otherwise *nzrem*[A/B] = B. As an example, consider the case of the last line in Equation (14). Here,  $n = 2$ ,  $p = 4$ , and  $N = 2$ . Thus, applying Equation (20), we get:  $\beta = 2$ ,  $\alpha = 1$ ,  $\varepsilon = 2$ , and  $\sigma = 2$ , in agreement with the last line of Equation (14). We should note that there are other ways to determine these coefficients as well, using the *greatest integer* function, for example.

Once  $(\alpha, \beta)$  and  $(\varepsilon, \sigma)$  have been obtained, set  $\tilde{\rho}_{\varepsilon\sigma}$  to be 1 while setting the other elements to 0, evaluate the  $Q$  matrix using Equation (7), and then pick out  $Q_{\alpha\beta}$  and

assign it to  $M_{np}$ . Then repeat this procedure of evaluating the  $Q$  matrix every time with different element of the  $\tilde{\rho}$  matrix set to 1 sequentially, until all elements of the  $M$  matrix have been calculated.

The steps for finding  $S$  and  $W$ , as defined in Equation (18) for the case of a two-level system, are rather simple. The last column of the  $M$  matrix barring the very last element is the  $S$  matrix. In order to determine the elements of  $W$ , find first the  $M'$  matrix, which is obtained from  $M$  by eliminating the last row and the last column, as illustrated in Equation (17a) for a two-level system. Define  $W_i$  and  $M'_i$  as the  $i$ -th column of the  $W$  and the  $M'$  matrix, respectively. Then, update a selected set of  $W_i$ , using an index  $k$  running from 1 to  $(N - 1)$ , as follows:

$$W_{(k-1)N+k} = M'_{(k-1)N+k} - S. \quad (21)$$

To illustrate this rule, consider, for example, the case where  $N = 3$ . In this case,  $W_1 = M_1 - S$  (for  $k = 1$ ) and  $W_5 = M_5 - S$  (for  $k = 2$ ), and the other six columns remain the same. With  $S$  and  $W$  thus determined, Equation (20) is used to find the steady-state solution vector: B. A particular element of the density matrix,  $\tilde{\rho}_{jk}$  (excluding  $\tilde{\rho}_{NN}$ ), corresponds to the  $((j - 1)N + k)$ -th element of the B vector. The population in the  $N$ -th level,  $\tilde{\rho}_{NN}$  is simply obtained from the knowledge of the steady-state populations in all other levels and the constraint  $\sum_{i=1}^N \tilde{\rho}_{ii} = 1$ . Explicitly, we can write:

$$\tilde{\rho}_{NN} = 1 - \sum_{j=1}^{(N-1)} B((j-1)N + j), \quad (22)$$

where we have used the notation that  $B(k)$  represents the  $k$ -th element of the B vector.

A Matlab code for an  $N$ -level system, applied to the case of two levels, is shown in Appendix 1. The code is

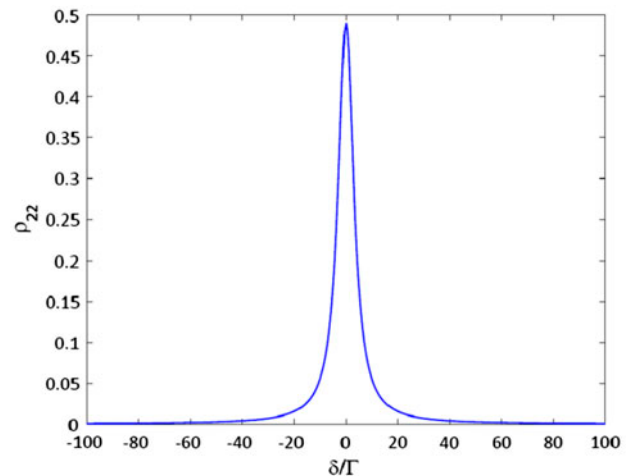


Figure 2. Population of excited state for a two-level system calculated using this algorithm. See text for details. (The colour version of this figure is included in the online version of the journal.)

valid for a general system; only  $N$  (number of levels in the system), and the effective, complex Hamiltonian (Equation (6)) and the source terms (Equation (8)) need to be changed. *The rest of the program does not have to be changed.* Of course, the plotting commands would have to be defined by the user based on the information being sought. As an example, the population of the excited state as a function of the detuning,  $\delta$ , produced by this code, is plotted in Figure 2.

### 3. A three-level system

The two-level problem discussed above is somewhat trivial, and may mask the generality of the algorithm. Therefore, we include here the specific steps for a three-level  $\Lambda$  system [6–11], shown in Figure 3, in order to elucidate how the algorithm is completely scalable to an arbitrary number of energy levels involved. In this case, the Hamiltonian under electric dipole and rotating wave approximations is given by

$$\mathcal{H} = \hbar \begin{pmatrix} \omega_1 & 0 & \frac{\Omega_a}{2} e^{i\omega_a t} \\ 0 & \omega_2 & \frac{\Omega_b}{2} e^{i\omega_b t} \\ \frac{\Omega_a}{2} e^{i\omega_a t} & \frac{\Omega_b}{2} e^{i\omega_b t} & \omega_3 \end{pmatrix}, \quad (23)$$

where  $\hbar\omega_1$ ,  $\hbar\omega_2$ , and  $\hbar\omega_3$  are the energies of the three levels, and  $\omega_a$  and  $\omega_b$  are the frequencies of the laser fields.

After applying the interaction picture transformation using the following matrix

$$R = \begin{bmatrix} e^{i\theta t} & 0 & 0 \\ 0 & e^{i\beta t} & 0 \\ 0 & 0 & e^{i\epsilon t} \end{bmatrix}, \quad (24)$$

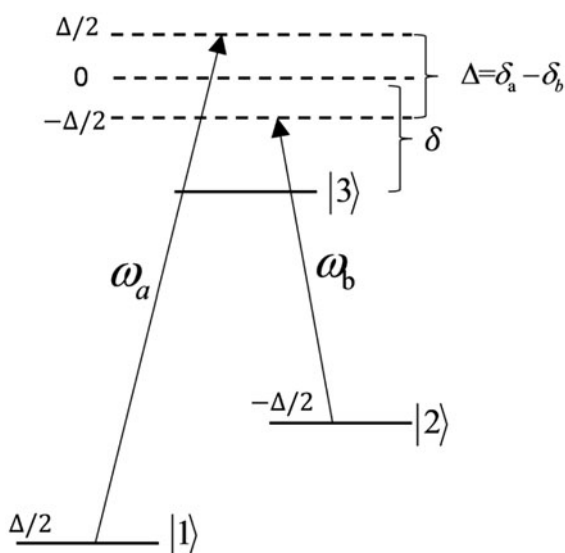


Figure 3. Schematic illustration of a three-level system. See text for details.

Where  $\theta = \omega_1 - \frac{\Delta}{2}$ ,  $\beta = \omega_2 + \frac{\Delta}{2}$ ,  $\Delta = \delta_a - \delta_b$ ,  $\delta = (\delta_a + \delta_b)/2$ ,  $\delta_a = \omega_a - (\omega_3 - \omega_1)$ ,  $\delta_b = \omega_b - (\omega_3 - \omega_2)$ , the Hamiltonian can be expressed as

$$\tilde{\mathcal{H}} = \frac{\hbar}{2} \begin{pmatrix} \Delta & 0 & \Omega_a \\ 0 & -\Delta & \Omega_b \\ \Omega_a & \Omega_b & -2\delta \end{pmatrix}. \quad (25)$$

The transformed state vector for each atom can be written as

$$|\tilde{\psi}\rangle = R|\psi\rangle = \begin{bmatrix} \tilde{C}_1(t) \\ \tilde{C}_2(t) \\ \tilde{C}_3(t) \end{bmatrix}. \quad (26)$$

The time-independent Hamiltonian  $\tilde{\mathcal{H}}$  of Equation (25) can be written down by inspection, following the discussion presented earlier for the two-level system. First, we observe that the energy difference between  $|1\rangle$  and  $|3\rangle$  ( $\tilde{\mathcal{H}}_{11} - \tilde{\mathcal{H}}_{33}$ ) is  $\hbar\delta_a$ , and the energy difference between  $|2\rangle$  and  $|3\rangle$  ( $\tilde{\mathcal{H}}_{22} - \tilde{\mathcal{H}}_{33}$ ) is  $\hbar\delta_b$ . Next, we make a judicious but arbitrary choice that  $\tilde{\mathcal{H}}_{11} = \frac{\hbar}{2}\Delta$ . We then get that  $\tilde{\mathcal{H}}_{33} = -\hbar\delta$  which in turn implies that  $\tilde{\mathcal{H}}_{22} = \frac{\hbar}{2}\Delta$ . The off-diagonal terms are, of course, obvious, with non-zero elements for transitions excited by fields. This approach is generic, and can be used to find the time independent Hamiltonian by inspection for an arbitrary number of levels. We should note that a complication exists when closed-loop excitations are present. In that case, it is wiser to work out the Hamiltonian explicitly using the transformation matrix approach outlined here. We now add the decay term to get the complex Hamiltonian

$$\tilde{\mathcal{H}}' = \frac{\hbar}{2} \begin{pmatrix} \Delta & 0 & \Omega_a \\ 0 & -\Delta & \Omega_b \\ \Omega_a & \Omega_b & -i\Gamma - 2\delta \end{pmatrix}. \quad (27)$$

We assume that the population of the excited state decays at the same rate ( $\Gamma/2$ ) from  $|3\rangle$  to  $|1\rangle$  and from  $|3\rangle$  to  $|2\rangle$ . Now we construct the  $M$  matrix for the three-level system which satisfies the following equation under the steady-state condition:

$$\begin{bmatrix} M_{11} & M_{12} & M_{13} & M_{14} & M_{15} & M_{16} & M_{17} & M_{18} & M_{19} \\ M_{21} & M_{22} & M_{23} & M_{24} & M_{25} & M_{26} & M_{27} & M_{28} & M_{29} \\ M_{31} & M_{32} & M_{33} & M_{34} & M_{35} & M_{36} & M_{37} & M_{38} & M_{39} \\ M_{41} & M_{42} & M_{43} & M_{44} & M_{45} & M_{46} & M_{47} & M_{48} & M_{49} \\ M_{51} & M_{52} & M_{53} & M_{54} & M_{55} & M_{56} & M_{57} & M_{58} & M_{59} \\ M_{61} & M_{62} & M_{63} & M_{64} & M_{65} & M_{66} & M_{67} & M_{68} & M_{69} \\ M_{71} & M_{72} & M_{73} & M_{74} & M_{75} & M_{76} & M_{77} & M_{78} & M_{79} \\ M_{81} & M_{82} & M_{83} & M_{84} & M_{85} & M_{86} & M_{87} & M_{88} & M_{89} \\ M_{91} & M_{92} & M_{93} & M_{94} & M_{95} & M_{96} & M_{97} & M_{98} & M_{99} \end{bmatrix} \begin{bmatrix} \tilde{\rho}_{11} \\ \tilde{\rho}_{12} \\ \tilde{\rho}_{13} \\ \tilde{\rho}_{21} \\ \tilde{\rho}_{22} \\ \tilde{\rho}_{23} \\ \tilde{\rho}_{31} \\ \tilde{\rho}_{32} \\ \tilde{\rho}_{33} \end{bmatrix} = 0. \quad (28)$$

The elements of the  $M$  matrix can be found explicitly by following the same steps as shown in Equations (7) through (13) for the two-level system. Alternatively, these can be found by using the algorithmic approach outlined in Equation (20), and implemented by a

computer code. The  $M$ -matrix can be obtained in  $O(N^2)$  steps as opposed  $O(N^4)$  steps that would be needed using the method prescribed thus far, but it is non-intuitive and masks the understanding of the algorithm. We have outlined the faster method in the appendix.

Substituting  $\tilde{\rho}_{11} + \tilde{\rho}_{22} + \tilde{\rho}_{33} = 1$  into Equation (28), we get

$$\begin{bmatrix} M_{11} & M_{12} & M_{13} & M_{14} & M_{15} & M_{16} & M_{17} & M_{18} \\ M_{21} & M_{22} & M_{23} & M_{24} & M_{25} & M_{26} & M_{27} & M_{28} \\ M_{31} & M_{32} & M_{33} & M_{34} & M_{35} & M_{36} & M_{37} & M_{38} \\ M_{41} & M_{42} & M_{43} & M_{44} & M_{45} & M_{46} & M_{47} & M_{48} \\ M_{51} & M_{52} & M_{53} & M_{54} & M_{55} & M_{56} & M_{57} & M_{58} \\ M_{61} & M_{62} & M_{63} & M_{64} & M_{65} & M_{66} & M_{67} & M_{68} \\ M_{71} & M_{72} & M_{73} & M_{74} & M_{75} & M_{76} & M_{77} & M_{78} \\ M_{81} & M_{82} & M_{83} & M_{84} & M_{85} & M_{86} & M_{87} & M_{88} \end{bmatrix} \begin{bmatrix} \tilde{\rho}_{11} \\ \tilde{\rho}_{12} \\ \tilde{\rho}_{13} \\ \tilde{\rho}_{21} \\ \tilde{\rho}_{22} \\ \tilde{\rho}_{23} \\ \tilde{\rho}_{31} \\ \tilde{\rho}_{32} \end{bmatrix} = \begin{bmatrix} M_{19} \\ M_{29} \\ M_{39} \\ M_{49} \\ M_{59} \\ M_{69} \\ M_{79} \\ M_{89} \end{bmatrix} \tilde{\rho}_{11} + \begin{bmatrix} M_{19} \\ M_{29} \\ M_{39} \\ M_{49} \\ M_{59} \\ M_{69} \\ M_{79} \\ M_{89} \end{bmatrix} \tilde{\rho}_{22} - \begin{bmatrix} M_{19} \\ M_{29} \\ M_{39} \\ M_{49} \\ M_{59} \\ M_{69} \\ M_{79} \\ M_{89} \end{bmatrix} \quad (29a)$$

or

$$\begin{bmatrix} (M_{11} - M_{19}) & M_{12} & M_{13} & M_{14} & (M_{15} - M_{19}) & M_{16} & M_{17} & M_{18} \\ (M_{21} - M_{29}) & M_{22} & M_{23} & M_{24} & (M_{25} - M_{29}) & M_{26} & M_{27} & M_{28} \\ (M_{31} - M_{39}) & M_{32} & M_{33} & M_{34} & (M_{35} - M_{39}) & M_{36} & M_{37} & M_{38} \\ (M_{41} - M_{49}) & M_{42} & M_{43} & M_{44} & (M_{45} - M_{49}) & M_{46} & M_{47} & M_{48} \\ (M_{51} - M_{59}) & M_{52} & M_{53} & M_{54} & (M_{55} - M_{59}) & M_{56} & M_{57} & M_{58} \\ (M_{61} - M_{69}) & M_{62} & M_{63} & M_{64} & (M_{65} - M_{69}) & M_{66} & M_{67} & M_{68} \\ (M_{71} - M_{79}) & M_{72} & M_{73} & M_{74} & (M_{75} - M_{79}) & M_{76} & M_{77} & M_{78} \\ (M_{81} - M_{89}) & M_{82} & M_{83} & M_{84} & (M_{85} - M_{89}) & M_{86} & M_{87} & M_{88} \end{bmatrix} \begin{bmatrix} \tilde{\rho}_{11} \\ \tilde{\rho}_{12} \\ \tilde{\rho}_{13} \\ \tilde{\rho}_{21} \\ \tilde{\rho}_{22} \\ \tilde{\rho}_{23} \\ \tilde{\rho}_{31} \\ \tilde{\rho}_{32} \end{bmatrix} = - \begin{bmatrix} M_{19} \\ M_{29} \\ M_{39} \\ M_{49} \\ M_{59} \\ M_{69} \\ M_{79} \\ M_{89} \end{bmatrix}. \quad (29b)$$

To simplify the above expression, we define the following objects as before

$$B = \begin{bmatrix} \tilde{\rho}_{11} \\ \tilde{\rho}_{12} \\ \tilde{\rho}_{13} \\ \tilde{\rho}_{21} \\ \tilde{\rho}_{22} \\ \tilde{\rho}_{23} \\ \tilde{\rho}_{31} \\ \tilde{\rho}_{32} \end{bmatrix} \quad S = \begin{bmatrix} M_{19} \\ M_{29} \\ M_{39} \\ M_{49} \\ M_{59} \\ M_{69} \\ M_{79} \\ M_{89} \end{bmatrix} \quad W = \begin{bmatrix} (M_{11} - M_{19}) & M_{12} & M_{13} & M_{14} & (M_{15} - M_{19}) & M_{16} & M_{17} & M_{18} \\ (M_{21} - M_{29}) & M_{22} & M_{23} & M_{24} & (M_{25} - M_{29}) & M_{26} & M_{27} & M_{28} \\ (M_{31} - M_{39}) & M_{32} & M_{33} & M_{34} & (M_{35} - M_{39}) & M_{36} & M_{37} & M_{38} \\ (M_{41} - M_{49}) & M_{42} & M_{43} & M_{44} & (M_{45} - M_{49}) & M_{46} & M_{47} & M_{48} \\ (M_{51} - M_{59}) & M_{52} & M_{53} & M_{54} & (M_{55} - M_{59}) & M_{56} & M_{57} & M_{58} \\ (M_{61} - M_{69}) & M_{62} & M_{63} & M_{64} & (M_{65} - M_{69}) & M_{66} & M_{67} & M_{68} \\ (M_{71} - M_{79}) & M_{72} & M_{73} & M_{74} & (M_{75} - M_{79}) & M_{76} & M_{77} & M_{78} \\ (M_{81} - M_{89}) & M_{82} & M_{83} & M_{84} & (M_{85} - M_{89}) & M_{86} & M_{87} & M_{88} \end{bmatrix}$$

Substituting them into Equation (29b), we get

$$WB = -S \text{ or } B = -W^{-1}S. \quad (30)$$

The Matlab program shown in Appendix 2 implements our algorithm for the three-level system. Note that *this program is essentially the same as the program for the two-level case* with the following modifications: we have (a) defined additional parameters relevant to this system, (b) entered proper elements in the Hamiltonian, and (c) added appropriate source terms for the populations. As an example, we have shown in Figure 4 a plot of the population of the excited state, produced using this code, displaying the well-known coherent population trapping dip.

#### 4. Applying the code to a system with an arbitrary number of energy levels

There are many examples in atomic and molecular physics where it is necessary to include a large number of energy levels. One example is an atomic clock employing coherent population trapping [12]. The basic process employs

only three Zeeman sublevels. However, the other Zeeman sublevels have to be taken into account in order to describe the behavior of the clock accurately. Using alkali atoms for other applications such as atomic interferometry, magnetometry, and Zeno-effect based switching also requires taking into account a large number of Zeeman sublevels [13–16]. Another example is the cooling of molecules using lasers. In this case, many rotational and vibrational levels have to be considered [17]. The code presented here can be applied readily to these problems, with the following modifications: (a) define additional parameters to characterize the problem; (b) develop the time independent Hamiltonian (possibly by inspection using the technique described earlier, if no closed-loop excitation is present); (c) add proper decay terms to the Hamiltonian; (d) add appropriate source terms for the

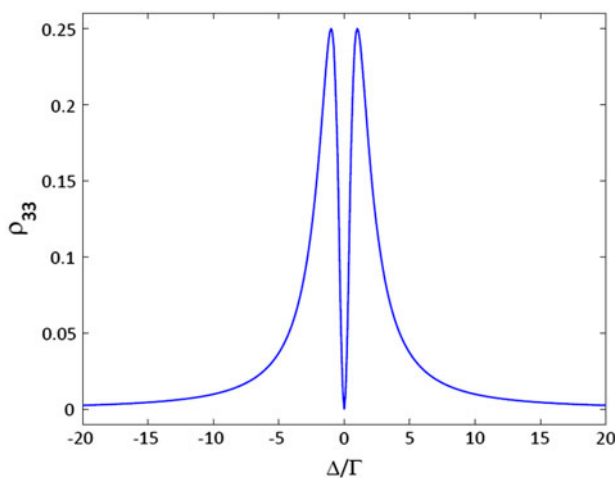


Figure 4. Population of the excited state for a three-level system calculated using this algorithm. See text for details. (The colour version of this figure is included in the online version of the journal.)

populations & transverse decay terms; and (e) add plotting instructions for components of interest from the solution vector. Of course, if numerical techniques are to be employed for finding time-dependent solutions, the code can be truncated after the  $M$  matrix is determined, followed by application of Equation (12) along with a proper choice of initial conditions.

### 5. Applying the code to a specific system with 15 energy levels: an optically controlled waveplate

As an explicit example of a system involving a non-trivial number of energy levels and optical transitions, we

consider here a process where a ladder transition in  $^{87}\text{Rb}$  is used to affect the polarization of a probe beam (upper leg) by varying parameters for the control beam (lower leg). The excitation process is illustrated schematically in Figure 5, for one particular configuration where the control beam is right circularly polarized, and the probe is linearly polarized. Because of the asymmetry introduced by the control, it is expected that the left circular component of the probe would experience a much larger phase shift, which in turn would induce an effective rotation of the probe polarization. Thus, the system can be viewed as an optically controlled waveplate for the probe. Here, we use the generalized algorithm to compute the response of this system. Of course, the response of the system under various experimental conditions would be quite different. The interactions of the pump ( $\sim 795$  nm) and the probe ( $\sim 1323$  nm) are modeled as follows. The pump is either left or right circularly polarized, and is tuned between the  $5\text{S}_{1/2}, F = 1$  to  $5\text{P}_{1/2}, F' = 1$  and the  $5\text{S}_{1/2}, F = 1$  to  $5\text{P}_{1/2}, F' = 2$  transitions, with a detuning of  $\delta_p$ , as illustrated in Figure 5. The probe, linearly polarized, is tuned to the  $5\text{P}_{1/2}, F' = 1$  to  $6\text{S}_{1/2}, F'' = 1$  transition, with a detuning of  $\delta_s$ . Due to Doppler broadening, it is important to consider the interaction of the  $5\text{P}_{1/2}, F' = 2$  level with both the pump and probe optical fields. For example,  $\delta_p = 814.5$  MHz corresponds to the situation where the pump is resonant with the  $5\text{S}_{1/2}, F = 1$  to  $5\text{P}_{1/2}, F' = 2$  transition and  $\delta_s = -814.5$  MHz corresponds to the situation where the probe is resonant with the  $5\text{P}_{1/2}, F' = 2$  to  $6\text{S}_{1/2}, F'' = 1$  transition. In our model, we ignore the coherent coupling between  $5\text{S}_{1/2}, F = 2$  and the  $5\text{P}_{1/2}$  manifold, because of the large frequency difference between  $5\text{S}_{1/2}, F = 1$  and  $5\text{S}_{1/2}, F = 2$ ,

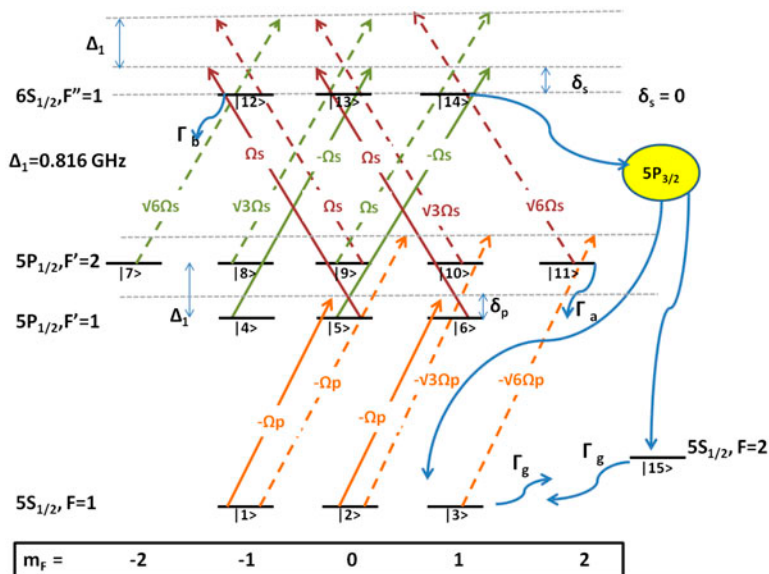


Figure 5. Fifteen-level system for polarization rotation in  $^{87}\text{Rb}$ .  $|n\rangle$ : Eigenstate of the system ( $n = 1, 2, \dots, 15$ );  $m$ : Zeeman sublevels ( $m = -2, -1, 0, 1, 2$ ). The decay rates of  $6\text{S}_{1/2}$  and  $5\text{P}_{1/2}$  levels are  $\Gamma_a$  and  $\Gamma_b$ , respectively.  $\Gamma_g$ : ground state dephasing rate. Rabi frequencies on the various legs are proportional to dipole strength matrix elements. (The colour version of this figure is included in the online version of the journal.)

$F = 2$  ( $\sim 6.8$  GHz for  $^{87}\text{Rb}$ ). However, we take into account the decay of atoms from the  $5\text{P}_{1/2}$  manifold to the  $5\text{S}_{1/2}$ ,  $F = 2$  state. Furthermore, we account for collisional relaxation (at a rate  $\Gamma_g$ ) between  $5\text{S}_{1/2}$ ,  $F = 1$  and  $5\text{S}_{1/2}$ ,  $F = 2$  manifolds, in order to model the behavior of atoms in a vapor cell. Finally, we also take into account the decay of atoms from  $6\text{S}_{1/2}$ ,  $F'' = 1$  to the  $5\text{S}_{1/2}$  manifold via the  $5\text{P}_{3/2}$  manifold in an approximate manner.

The Rabi frequency of each transition is proportional to the corresponding dipole moment matrix elements. In Figure 5, all the Rabi frequencies are expressed as a multiple of the Rabi frequency corresponding to the weakest transition [18]. For example, the dipole matrix elements of  $\sigma^+$  transitions for the  $5\text{S}_{1/2}$ – $5\text{P}_{1/2}$  excitation are tabulated in Table 1. Thus, if we set the coupling between  $|1\rangle$  and  $|5\rangle$  to be  $\tilde{H}_{1,5} = -\frac{\Omega_{p+}}{2}$ , then the other coupling terms for the lower leg are as follows:

$$\begin{aligned}\tilde{H}_{1,9} &= -\frac{\Omega_{p+}}{2}, \tilde{H}_{2,6} = -\frac{\Omega_{p+}}{2}, \tilde{H}_{2,10} = -\frac{\sqrt{3}\Omega_{p+}}{2}, \\ \tilde{H}_{3,11} &= -\frac{\sqrt{6}\Omega_{p+}}{2}.\end{aligned}$$

The decay rates between any two Zeeman sub-levels are assumed to be proportional to the squares of the dipole moment matrix elements such that the sum of all the decay rates equals the net decay rate from that level. We assume all the Zeeman sub-levels in the  $5\text{P}_{1/2}$  and  $6\text{S}_{1/2}$  manifold decay at the same rate,  $\Gamma_a$  and  $\Gamma_b$ , respectively. To illustrate how the decay terms are determined, consider, for example, state  $|5\rangle$ , which denotes the Zeeman sublevel  $5\text{P}_{1/2}$ ,  $F' = 1$ ,  $m_F = 0$ . The dipole matrix elements for all allowed transitions from this state to the various sublevels within the  $5\text{S}_{1/2}$  manifold are shown in Figure 6. With the decay rate from  $|5\rangle$  to the  $5\text{S}_{1/2}$  manifold being  $\Gamma_a$ , the decay rate from  $|5\rangle$  to  $|1\rangle$  (or  $|2\rangle$ ) is  $\Gamma_a/12$ . The decay from  $|5\rangle$  to  $|15\rangle$  ( $5\text{S}_{1/2}$ ,  $F = 2$ ) is calculated by adding the squares of the matrix elements for all transitions between  $|5\rangle$  and the Zeeman levels of  $|15\rangle$ , and this turns out to be  $5\Gamma_a/6$ .

We have also taken into account the sourcing of atoms into the ground states from the  $6\text{S}_{1/2}$  state via the  $5\text{P}_{3/2}$  state. These additional source terms are modeled using an ‘effective decay rate’ ( $\Gamma_{bi}$ ) directly from the Zeeman sub-levels in the  $6\text{S}_{1/2}$ ,  $F'' = 1$  level to the  $5\text{S}_{1/2}$  manifold. It is then assumed that all the Zeeman

Table 1.  $^{87}\text{Rb}$  D1 ( $5\text{S}_{1/2}$ – $5\text{P}_{1/2}$ ) dipole matrix elements for  $\sigma^+$  transition ( $F = 1$ ,  $m_F \rightarrow F'$ ,  $m'_F = m_F + 1$ ).

	$m_F = -1$	$m_F = 0$	$m_F = 1$
$F' = 2$	$-\sqrt{\frac{1}{12}}$	$-\sqrt{\frac{1}{4}}$	$-\sqrt{\frac{1}{2}}$
$F' = 1$	$-\sqrt{\frac{1}{12}}$	$-\sqrt{\frac{1}{12}}$	

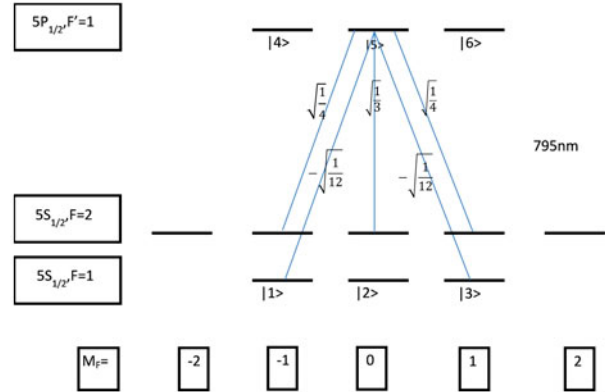


Figure 6. Dipole matrix elements for all allowed transitions from the  $5\text{P}_{1/2}$ ,  $F' = 1$ ,  $m_F = 0$  sublevel to the various sublevels in the  $5\text{S}_{1/2}$  manifold. (The colour version of this figure is included in the online version of the journal.)

sub-levels at the  $6\text{S}_{1/2}$ ,  $F'' = 1$  level decays equally to the Zeeman sub-levels of  $F = 1$  and  $F = 2$  levels at this rate. In Figure 7, the branching ratios between the various hyperfine levels and the effective decay rates from the  $6\text{S}_{1/2}$ ,  $F'' = 1$  level to the  $5\text{S}_{1/2}$  manifold are shown. For our initial computations, we used a rough estimate for  $\Gamma_{bi}$ . A more detailed calculation, taking into account the various branching ratios into and from all the hyperfine levels of the  $5\text{P}_{3/2}$  state can be used to determine  $\Gamma_{bi}$ . However, we found that the results did not change significantly when  $\Gamma_{bi}$  was changed slightly and hence using an approximate value is justified.

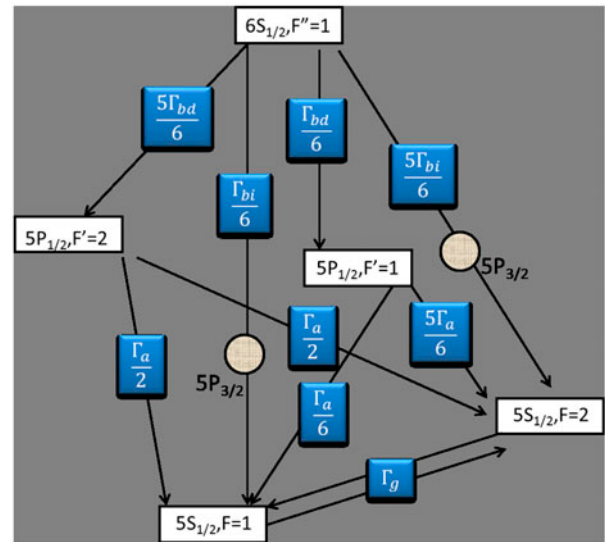


Figure 7. Branching ratios between the hyperfine levels and the effective decay rates from the  $F'' = 1$  level to the  $5\text{S}_{1/2}$  manifold. See text for details. (The colour version of this figure is included in the online version of the journal.)

The goal of simulating the process illustrated in Figure 5 is to determine how the state of a linearly polarized probe beam (at 1323 nm) is affected by its passage through a vapor cell of length  $L$  and density  $n$ , in the presence of a circularly polarized pump beam (at 795 nm). Thus, before presenting the details of the atom-laser interaction, we specify the terminology relevant for characterizing the probe beam, using the Jones vector formulation. We consider the direction of propagation as the  $z$ -axis, and the input probe to be linearly polarized in the  $x$  direction. Thus, the input probe can be described as:

$$\vec{J}_{\text{probe,input}} = \begin{bmatrix} 1 \\ 0 \end{bmatrix} = \frac{1}{2} \begin{bmatrix} 1 \\ i \end{bmatrix} + \frac{1}{2} \begin{bmatrix} 1 \\ -i \end{bmatrix}. \quad (31)$$

The second part of Equation (31) indicates that the linear polarization has been decomposed into a right circular polarization and a left circular polarization. The effect of propagation through the cell can now be modeled by expressing the output Jones vector as follows:

$$\vec{J}_{\text{probe,output}} = \frac{1}{2} \begin{bmatrix} 1 \\ i \end{bmatrix} e^{-\alpha_+ + j\Phi_+} + \frac{1}{2} \begin{bmatrix} 1 \\ -i \end{bmatrix} e^{-\alpha_- + j\Phi_-}, \quad (32)$$

where  $\alpha_+$  ( $\alpha_-$ ) and  $\Phi_+$  ( $\Phi_-$ ) are the attenuation and phase shift experienced by the right (left) circular component, respectively.

In order to make the system behave as an ideal half waveplate, for example, the phase difference between the right and left polarization components ( $|\emptyset_+ - \emptyset_-|$ ) should be equal to  $\pi$ , and the attenuation for each component should equal zero ( $\alpha_+ = \alpha_- = 0$ ). In that case, the output expression can be simplified as:

$$\begin{aligned} \vec{J}_{\text{probe,output}} &= \frac{1}{2} \begin{bmatrix} 1 \\ i \end{bmatrix} e^{j\emptyset_+} + \frac{1}{2} \begin{bmatrix} 1 \\ -i \end{bmatrix} e^{j\emptyset_-} = \frac{1}{2} e^{j\emptyset_-} \\ &\times \left( \begin{bmatrix} 1 \\ i \end{bmatrix} e^{j\pi} + \begin{bmatrix} 1 \\ -i \end{bmatrix} \right) = e^{j(\emptyset_- - \frac{\pi}{2})} \begin{bmatrix} 0 \\ 1 \end{bmatrix}, \end{aligned} \quad (33)$$

which is polarized linearly in the  $y$ -direction. In practice, the attenuation coefficients are non-vanishing. However, if they are equal to each other (i.e.  $\alpha_+ = \alpha_-$ ), then they simply reduce the amplitude of the signal, without affecting the sense of polarization. Of course, the phase difference ( $\Phi_+ = \Phi_-$ ) can have a wide range of values, corresponding to different output polarization states. In what follows, we solve the density matrix equation of motion for the 15-level system shown in Figure 5, in order to determine the four quantities of interest:  $\Phi_+$ ,  $\Phi_-$ ,  $\alpha_+$ ,  $\alpha_-$ .

The time-independent Hamiltonian after moving to a rotating basis and the RWA can be written down using the method we described in Sections 2 and 3. Given the large number of levels, we use below a

compact notation, rather than a matrix, to express the Hamiltonian. Specifically,  $\tilde{H}$  is given by (setting  $\hbar = 1$ ):

$$\begin{aligned} \tilde{H}_{1,1} &= -i \frac{\Gamma_g}{2}, \tilde{H}_{1,5} = -\frac{\Omega_P}{2}, \tilde{H}_{1,9} = -\frac{\Omega_P}{2}; \\ \tilde{H}_{2,2} &= -i \frac{\Gamma_g}{2}, \tilde{H}_{2,6} = -\frac{\Omega_P}{2}, \tilde{H}_{2,10} = -\frac{\sqrt{3}\Omega_P}{2}; \\ \tilde{H}_{3,3} &= -i \frac{\Gamma_g}{2}, \tilde{H}_{3,11} = -\frac{\sqrt{6}\Omega_P}{2}; \\ \tilde{H}_{4,4} &= -\delta_P - i \frac{\Gamma_a}{2}, \tilde{H}_{4,13} = -\frac{\Omega_s}{2}; \\ \tilde{H}_{5,1} &= \tilde{H}_{1,5}^*, \tilde{H}_{5,5} = -\delta_P - i \frac{\Gamma_a}{2}, \tilde{H}_{5,12} = \frac{\Omega_s}{2}, \tilde{H}_{5,14} = -\frac{\Omega_s}{2}; \\ \tilde{H}_{6,2} &= \tilde{H}_{2,6}^*, \tilde{H}_{6,6} = -\delta_P - i \frac{\Gamma_a}{2}, \tilde{H}_{6,13} = \frac{\Omega_s}{2}; \\ \tilde{H}_{7,7} &= \Delta - \delta_P - i \frac{\Gamma_a}{2}, \tilde{H}_{7,12} = \frac{\sqrt{6}\Omega_s}{2}; \\ \tilde{H}_{8,8} &= \Delta - \delta_P - i \frac{\Gamma_a}{2}, \tilde{H}_{8,13} = \frac{\sqrt{3}\Omega_s}{2}; \\ \tilde{H}_{9,1} &= \tilde{H}_{1,9}^*, \tilde{H}_{9,9} = \Delta - \delta_P - i \frac{\Gamma_a}{2}, \tilde{H}_{9,12} = \frac{\Omega_s}{2}, \tilde{H}_{9,14} = \frac{\Omega_s}{2}; \\ \tilde{H}_{10,2} &= \tilde{H}_{2,10}^*, \tilde{H}_{10,10} = \Delta - \delta_P - i \frac{\Gamma_a}{2}, \tilde{H}_{10,13} = \frac{\sqrt{3}\Omega_s}{2}; \\ \tilde{H}_{11,3} &= \tilde{H}_{3,11}^*, \tilde{H}_{11,11} = \Delta - \delta_P - i \frac{\Gamma_a}{2}, \tilde{H}_{11,14} = \frac{\sqrt{6}\Omega_s}{2}; \\ \tilde{H}_{12,5} &= \tilde{H}_{5,12}^*, \tilde{H}_{12,7} = \tilde{H}_{7,12}^*, \tilde{H}_{12,9} = \tilde{H}_{9,12}^*, \\ \tilde{H}_{12,12} &= -\delta_S - \delta_P - i \frac{\Gamma_b}{2}; \\ \tilde{H}_{13,4} &= \tilde{H}_{4,13}^*, \tilde{H}_{13,6} = \tilde{H}_{6,13}^*, \tilde{H}_{13,8} = \tilde{H}_{8,13}^*, \\ \tilde{H}_{13,10} &= \tilde{H}_{10,13}^*, \tilde{H}_{13,13} = -\delta_S - \delta_P - i \frac{\Gamma_b}{2}; \\ \tilde{H}_{14,5} &= \tilde{H}_{5,14}^*, \tilde{H}_{14,9} = \tilde{H}_{9,14}^*, \tilde{H}_{14,11} = \tilde{H}_{11,14}^*, \\ \tilde{H}_{14,14} &= -\delta_S - \delta_P - i \frac{\Gamma_b}{2}; \\ \tilde{H}_{15,15} &= -i \frac{\Gamma_g}{2}. \end{aligned}$$

All the other terms of  $\tilde{H}$  are equal to zero. We then add the population source terms to the Hamiltonian. We assume the decay rates from  $F'' = 1$  to  $5P_{1/2}$  ( $\Gamma_{bd}$ ) are equal to the effective decay rate from  $F'' = 1$  to  $5S_{1/2}$  ( $\Gamma_{bi}$ ). Thus,  $\Gamma_{bd} = \alpha\Gamma_b$ ,  $\Gamma_{bi} = (1 - \alpha)\Gamma_b$  where  $\alpha = 0.5$ ,

$$\begin{aligned}
\frac{d\rho_{11}}{dt} &= (\rho_{44} + \rho_{55} + \rho_{99}) \frac{\Gamma_a}{12} + \rho_{77} \frac{\Gamma_a}{2} + \rho_{88} \frac{\Gamma_a}{4} \\
&\quad + (\rho_{12,12} + \rho_{13,13} + \rho_{14,14}) \frac{\Gamma_{bi}}{18} + \rho_{15,15} \frac{\Gamma_g}{3}, \\
\frac{d\rho_{22}}{dt} &= (\rho_{44} + \rho_{66}) \frac{\Gamma_a}{12} + \rho_{88} \frac{\Gamma_a}{4} + \rho_{99} \frac{\Gamma_a}{3} + \rho_{10,10} \frac{\Gamma_a}{4} \\
&\quad + (\rho_{12,12} + \rho_{13,13} + \rho_{14,14}) \frac{\Gamma_{bi}}{18} + \rho_{15,15} \frac{\Gamma_g}{3}, \\
\frac{d\rho_{33}}{dt} &= (\rho_{55} + \rho_{66} + \rho_{99}) \frac{\Gamma_a}{12} + \rho_{10,10} \frac{\Gamma_a}{4} + \rho_{11,11} \frac{\Gamma_a}{2} \\
&\quad + (\rho_{12,12} + \rho_{13,13} + \rho_{14,14}) \frac{\Gamma_{bi}}{18} + \rho_{15,15} \frac{\Gamma_g}{3}, \\
\frac{d\rho_{44}}{dt} &= \rho_{12,12} \frac{\Gamma_{bd}}{12} + \rho_{13,13} \frac{\Gamma_{bd}}{12}, \\
\frac{d\rho_{55}}{dt} &= \rho_{12,12} \frac{\Gamma_{bd}}{12} + \rho_{14,14} \frac{\Gamma_{bd}}{12}, \\
\frac{d\rho_{66}}{dt} &= \rho_{13,13} \frac{\Gamma_{bd}}{12} + \rho_{14,14} \frac{\Gamma_{bd}}{12}, \\
\frac{d\rho_{77}}{dt} &= \rho_{12,12} \frac{\Gamma_{bd}}{2},
\end{aligned}$$

$$\begin{aligned}
\frac{d\rho_{88}}{dt} &= \rho_{12,12} \frac{\Gamma_{bd}}{4} + \rho_{13,13} \frac{\Gamma_{bd}}{4}, \\
\frac{d\rho_{99}}{dt} &= \rho_{12,12} \frac{\Gamma_{bd}}{12} + \rho_{13,13} \frac{\Gamma_{bd}}{3} + \rho_{14,14} \frac{\Gamma_{bd}}{12}, \\
\frac{d\rho_{10,10}}{dt} &= \rho_{13,13} \frac{\Gamma_{bd}}{4} + \rho_{14,14} \frac{\Gamma_{bd}}{4}, \\
\frac{d\rho_{11,11}}{dt} &= \rho_{14,14} \frac{\Gamma_{bd}}{2}, \\
\frac{d\rho_{15,15}}{dt} &= (\rho_{1,1} + \rho_{2,2} + \rho_{3,3})_{\Gamma_{gg}} + (\rho_{44} + \rho_{55} + \rho_{66}) \frac{5\Gamma_a}{6} \\
&\quad + (\rho_{77} + \rho_{88} + \rho_{99} + \rho_{10,10} + \rho_{11,11}) \frac{\Gamma_a}{2} \\
&\quad + (\rho_{12,12} + \rho_{13,13} + \rho_{14,14}) \frac{5\Gamma_{bi}}{6}.
\end{aligned}$$

The attenuation and the additional phase shift introduced by the Rb medium (as compared to free space propagation) of the signal beam can be expressed as:  
phase:

$$\begin{aligned}
\phi_+ &= kL \frac{\beta_+}{2} \operatorname{Re}(a_{13,4}\rho_{13,4} + a_{14,5}\rho_{14,5} + a_{12,7}\rho_{12,7} \\
&\quad + a_{13,8}\rho_{13,8} + a_{14,9}\rho_{14,9}),
\end{aligned}$$

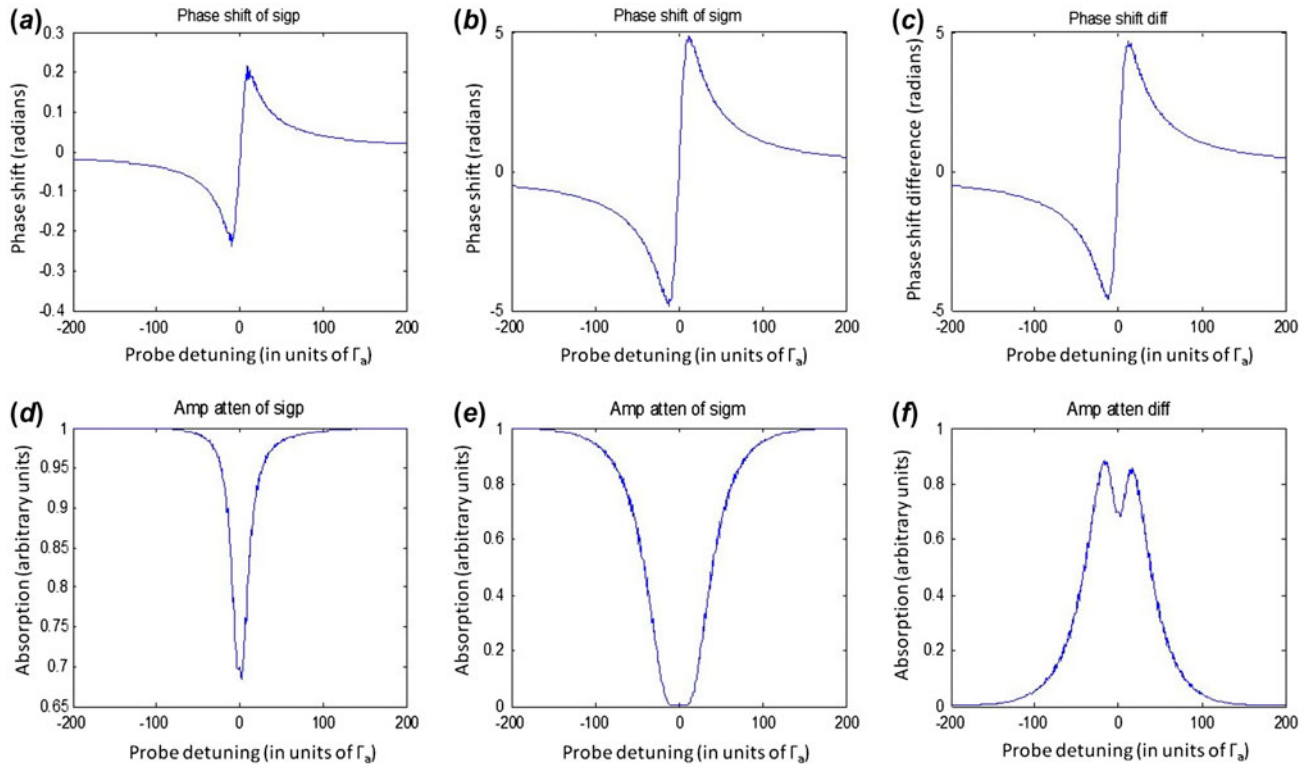


Figure 8. Simulation result of an optically controlled waveplate using 15 levels in  $^{87}\text{Rb}$ . See text for details. (The colour version of this figure is included in the online version of the journal.)

$$\phi_- = kL \frac{\beta_-}{2} \text{Re}(a_{12,5}\rho_{12,5} + a_{13,6}\rho_{13,6} + a_{12,9}\rho_{12,9} + a_{13,10}\rho_{13,10} + a_{14,11}\rho_{14,11}).$$

attenuation:

$$\alpha_+ = e^{-kL\beta_+ \text{Im}(a_{13,4}\rho_{13,4} + a_{14,5}\rho_{14,5} + a_{12,7}\rho_{12,7} + a_{13,8}\rho_{13,8} + a_{14,9}\rho_{14,9})/2},$$

$$\alpha_- = e^{-kL\beta_- \text{Im}(a_{12,5}\rho_{12,5} + a_{13,6}\rho_{13,6} + a_{12,9}\rho_{12,9} + a_{13,10}\rho_{13,10} + a_{14,11}\rho_{14,11})/2}.$$

and

$$\beta_{\pm} = b_{\min}^2 \frac{3n_{\text{atom}}\Gamma\lambda^3}{4\pi^2\Omega_{\min}},$$

where  $k$  is the wavevector of the signal beam, which is at 1323 nm,  $L$  is the length of the cell, which is set to be 15 cm,  $n_{\text{atom}}$  is the density of Rb atoms, which is set to be  $10^{16}/\text{m}^3$ ,  $\Omega_{\min}$  is the Rabi frequency for the weakest probe transition (for example, the  $|14\rangle - |9\rangle$  transition in our model) and the various  $a_{ij}$ 's are the ratios of the Rabi frequency ( $\Omega_{ij}$ ) of the  $|i\rangle - |j\rangle$  transition to  $\Omega_{\min}$ . For example,  $a_{12,7} = \Omega_{12,7}/\Omega_{14,9} = \sqrt{6}$ .  $b_{\min}^2$  is the fraction of the atoms (<1) that decay along the transition corresponding to  $\Omega_{\min}$ , among all allowed decay channels from the decaying level. In our model, the amplitudes for all possible transitions from  $|14\rangle$  are in the ratio 1:1:1: $\sqrt{3}$ : $\sqrt{6}$  and hence the fraction of atoms that decay along the different channels are in the ratio 1:1:1:3:6. Thus,  $b_{\min}^2 = 1/(1+1+1+3+6) = 1/12$ .

Setting the pump frequency at a certain value ( $\delta_p = \Delta$ , which corresponds to the situation when the pump is resonant with the  $F = 1$  to  $F' = 2$  transition) and scanning the probe detuning ( $\delta_s$ ), we can plot the various quantities of interest ( $\Phi_+$ ,  $\Phi_{-\alpha_+}$ ,  $\alpha_-$ ) as a function of  $\delta_s$ , as shown in Figure 8. The relevant parameters used for this particular simulation are as follows. The decay rates  $\Gamma_a$ ,  $\Gamma_b$  and  $\Gamma_g$  are  $2\pi \times 5.75 \text{ s}^{-1}$ ,  $2\pi \times 3.45 \text{ s}^{-1}$ , and  $2\pi \times 0.1 \text{ s}^{-1}$ , respectively. We perform our calculations by setting  $\Gamma_a$  to unity and rescaling all parameters in units of  $\Gamma_a$ . The separation  $\Delta$ , between  $F' = 1$  and  $F' = 2$  is  $2\pi \times 814.5 \text{ s}^{-1}$  ( $= 141.4\Gamma_a$ ) and the probe detuning ( $\delta_s$ ) ranges from  $-200\Gamma_a$  to  $200\Gamma_a$ . The Rabi frequencies have been chosen to be  $\Omega_p = 5\Gamma_a$ , and  $\Omega_s = 0.1\Gamma_a$ . Figures 8(a) and 8(b) show the additional phase shifts produced by the Rb medium for the right and left circular polarization parts of the signal beam and Figure 8(c) shows the difference between them. Figures 8(d)–8(f) show the corresponding figures for attenuation. For example, at  $\delta_s = 200$ , we have a differential attenuation of  $\sim 0$  and a differential phase shift of about  $30^\circ$ . Since the main purpose of this paper is to illustrate the application of the algorithm for obtaining the solution to the density matrix equations for a large quantum system, we refrain from exploring the parameter space in detail. Actual experimental results and conditions necessary to produce a differential phase shift of  $\pi$  with virtually no

differential attenuation (and thus allowing us to use the optically controlled waveplate for all-optical switching) are presented in a separate paper [19].

## 5. Conclusion

We have presented a novel algorithm for efficiently finding the solution to the density matrix equations for an atomic system with arbitrary number of energy levels. For this purpose, the Liouville equation that describes the time evolution of the density matrix is formulated as a matrix-vector equation. We presented an algorithm that allows us to find the elements of the evolution matrix with ease for systems with arbitrarily large value of  $N$ . As examples, we then used the algorithm to find steady-state solutions for atomic systems consisting of two- and three- levels. We also described a comprehensive model (consisting of 15 levels) for an optically controlled waveplate using the  $5S_{1/2}-5P_{1/2}-6S_{1/2}$  cascade system. Finally, we used the algorithm to obtain the steady state solution for the 15-level system. The algorithm and the Matlab codes presented here should prove very useful for the atomic and molecular physics community.

## Funding

This work was supported by AFOSR [grant number FA9550-10-01-0228], [grant number FA9550-09-01-0652]; NASA [grant number NNX09AU90A]; NSF [grant number 0630388]; the DARPA ZOE program [grant number W31P4Q-09-1-0014].

## References

- [1] Sargent, M.; Scully, M.O.; Lamb, W. E. *Laser Physics*; Addison-Wesley: 1977.
- [2] Scully, M.O.; Zubairy, M.S. *Quantum Optics*; Cambridge University Press: 1997.
- [3] Allen, L.; Eberly, J.H. *Optical Resonances and Two-Level Atoms*; Dover: New York, 1975.
- [4] Shore, B.W. *The Theory of Coherent Atomic Excitation*; Wiley, New York, 1990.
- [5] Metcalf, H.J.; van der Straten, P. 1999 *Laser Cooling and Trapping*; Springer: Berlin, 1999; pp 4–6.
- [6] Shahriar, M.S.; Hemmer, P.; Katz, P. D.; Lee, A.; Prentiss, M. *Phys. Rev. A: At., Mol., Opt. Phys.* **1997**, *55*, 2272–2282.
- [7] Radmore, P.M.; Knight, P.L. *J. Phys. B: At. Mol. Phys.* **1982**, *15*, 561–573.
- [8] Arimondo, E. *Prog. Opt.* **1996**, *35*, 257–354.
- [9] Whitley, R.M.; Stroud, C.R., Jr *Phys. Rev. A: At., Mol., Opt. Phys.* **1976**, *14*, 1498–1513.
- [10] Gray, H.R.; Whitley, R.M.; Stroud, C.R., Jr *Opt. Lett.* **1978**, *3*, 218–220.
- [11] Arimondo, E.; Oriols, G. *Lett. Nuovo Cimento Soc. Ital. Fis.* **1976**, *17*, 333–338.
- [12] Hemmer, P.; Shahriar, M.S.; Natoli, V.; Ezekiel, S. *J. Opt. Soc. Am. B* **1989**, *6*, 1519–1528.
- [13] White, G.R.; Lough, J.; Duncan, D.; Davis, J.P.; Narducci, F.A. *J. Mod. Opt.* **2009**, *56*, 2013–2021.

- [14] Shahriar, M.S.; Tan, Y.; Jheeta, M.; Morzinksy, J.; Hemmer, P.R.; Pradhan, P. *J. Opt. Soc. Am. B* **2005**, *22*, 1566–1570.
- [15] Kasevich, M.; Chu, S. *Phys. Rev. Lett.* **1991**, *67*, 181–184.
- [16] Itano, W.M.; Heinzen, D.J.; Bollinger, J.J.; Wineland, D.J. *Phys. Rev. A: At., Mol., Opt. Phys.* **1990**, *41*, 2295–2300.
- [17] Nguyen, J.H.V.; Odom, B. *Phys. Rev. A: At., Mol., Opt. Phys.* **2011**, *83*, 053404.
- [18] Steck, D.A. In *Alkali D Line Data*; <http://steck.us/alkalidata/rubidium87numbers.pdf> (accessed May 01, 2012).
- [19] Shahriar, M.S.; Wang, Y.; Krishnamurthy, S.; Tu, Y.; Pati, G.S.; Tseng, S. Algorithm for Solving Density Matrix Equations for an *N*-Level System Via Automated Vectorization of the Liouville Equations. <http://lapt.ece.northwestern.edu/preprints/Waveplate.pdf>.

**Appendix 1: Matlab program for solving the two-level problem**

```

omeg=5; % express rabi freq, normalized to gamma
N=2; % number of energy levels
R=401 % number of points to plot
% initialize and set dimensions for all matrices
delta=zeros(1,R); %detuning array
M=zeros(N^2,N^2); %M-matrix
rho=zeros(N,N); %dens mat
Ham=zeros(N,N); %Hamiltonian with decay
Q=zeros(N,N); %matrix corresponding to derivative of the density matrix

W=zeros((N^2-1), (N^2-1)); %W-matrix
S=zeros((N^2-1),1); %S-vector
B=zeros((N^2-1),1); %B-vector
A=zeros(N^2,R); %A-vectors, for all detunings

for m=1:R %start the overall-loop
    delta(1,m)=(m-(R+1)/2)/2; %define the detuning, normalized to gamma
    Ham=[0 omeg/2; omeg/2 (delta(1,m)+0.5i)*(-1)]; %elements of Hamiltonian

    for n=1:N^2 %start the outer-loop for finding elements of M;
        for p=1:N^2 %start inner-loop for finding elements of M;

            %M(n,p) equals Q(alpha,beta) with only rho(epsilon,
            %sigma)=1, and other elements of rho set to zero.

            %determining dummy coefficients alpha and beta
            remain=rem(n,N);
            if remain==0
                beta=N;
            else beta=remain;
            end
            alpha=(1+(n-beta)/N);

            %determining dummy coefficients epsilon and sigma
            remain=rem(p,N);
            if remain==0
                sigma=N;
            else sigma=remain;
            end
            epsilon=(1+(p-sigma)/N);

            rho=zeros(N,N); %reset rho to all zeros
            rho(epsilon,sigma)=1; %pick one element to be unity
            Q=(Ham*rho-rho*conj(Ham))*(0-li); %find first part of Q matrix
            Q(1,1)=Q(1,1)+rho(2,2); %add pop source term to Q
            %For an N-level system, add additional
            %source terms as needed
            M(n,p)=Q(alpha,beta);
        end %end the inner-loop for finding elements of M
    end %end of the outer-loop for finding elements of M

    S=M(1:(N^2-1),N^2:N^2); %find S-vector
    W=M(1:(N^2-1),1:(N^2-1)); %initialize W-matrix

    for d=1:(N-1)

```

```

W(:, ( (d-1)*N+d) )=W(:, ( (d-1)*N+d) )-S; %update W by subtracting
%from selected columns
end

B=(W\S) * (-1); %find B-vector: primary solution

rhonn=1; %initialize pop of N-th state
%determine pop of N-th state
for f=1:(N-1)
    rhonn=rhonn-B(((f-1)*N+f), 1);
end %determine the elements of the A vector
A(1:(N^2-1),m)=B;
A(N^2,m)=rhonn;

end %end of over-all loop
plot(delta,real(A((N^2-0),:)))

```

**Appendix 2: Matlab program for solving the three-level problem**

```

oma=1; omb=1;      % express omega rabi freqs, in units of gamma
dels=0;            % common detuning set to zero
N=3;               % number of energy levels
R=401;             % number of points to plot
                   % initialize and set dimensions for all matrices
del=zeros(1,R);   % diff detuning array
M=zeros(N^2,N^2); % M-matrix
rho=zeros(N,N);   % density matrix
Ham=zeros(N,N);   % Hamiltonian with decay
Q=zeros(N,N);     % matrix representing derivative of density matrix
W=zeros((N^2-1), (N^2-1)); % W-matrix
S=zeros((N^2-1), 1); % S-vector
B=zeros((N^2-1), 1); % B-vector
A=zeros(N^2,R);    % A-vectors, for all detunings

for m=1:R          % start the overall-loop
    del(1,m)=(m-(R+1)/2)/10; % define the detuning
    Ham=[del(1,m)/2 0 oma/2; 0 del(1,m)*(-1)/2 omb/2; ...
          oma/2 omb/2 (dels+0.5i)*(-1)];
    for n=1:N^2        % start the outer-loop for finding elements of M;
        for p=1:N^2      % start inner-loop for finding elements of M;
            %finding alpha and beta
            remain=rem(n,N);
            if remain==0
                beta=N;
            else beta=remain;
            end
            alpha=(1+(n-beta)/N);

            %finding epsilon and sigma
            remain=rem(p,N);
            if remain==0
                sigma=N;
            else sigma=remain;
            end
            epsilon=(1+(p-sigma)/N);

            rho=zeros(N,N);           %reset rho to all zeros
            rho(epsilon,sigma)=1;     %pick one element to unity
            Q=(Ham*rho-rho*conj(Ham))*(0-1i); %find first part of Q matrix

            Q(1,1)=Q(1,1)+rho(3,3)/2; %add pop source term to Q
            Q(2,2)=Q(2,2)+rho(3,3)/2; %add pop source term to Q
            %Modify as needed for general
            %systems
            M(n,p)=Q(alpha,beta);
        end      %end the inner-loop for finding elements of M
    end        %end of the outer-loop for finding elements of M

    S=M(1: (N^2-1), N^2:N^2); %find S-vector
    W=M(1: (N^2-1), 1: (N^2-1)); %initialize W-matrix

    for d=1:(N-1)
        W(:, ((d-1)*N+d))=W(:, ((d-1)*N+d))-S; %update W by subtracting
    end

```

```

        %from selected columns

end

B=(W\S)*(-1);           %find B-vector: primary solution

rhonn=1;                 %initialize pop of N-th state
                         %determine pop of N-th state

for f=1:(N-1)
    rhonn=rhonn-B(((f-1)*N+f), 1);
end
                         %determine elements of A vector

A(1:(N^2-1),m)=B;
A(N^2,m)=rhonn;

end                     %end of over-all loop
plot(del,real( A ( (N^2-0),: ) ) )

```

### Appendix 3: Algorithm optimization

The crux of the algorithm is to obtain the  $M$  matrix in an automated fashion. The most obvious, but rather elaborate ( $O(N^4)$  operations) way to perform this task has been illustrated previously. However, several simplifications can be made to the algorithm so that the entire process can be accomplished using  $O(N^2)$  operations and also avoid some other redundant operations, thereby increasing the speed by a factor of  $\sim N^2$ . To do this, we first observe that instead of evaluating the  $M$  matrix row-wise as was shown before, it is more beneficial to evaluate it column wise. Each column in the  $M$  matrix is simply obtained by successively setting each of the density matrix elements to 1, while setting all others to 0. Thus, the entire first column can be obtained by setting  $\rho_{11}=1$  and all other  $\rho_{ij}=0$ , second column with  $\rho_{12}=0$  and all other  $\rho_{ij}=0$  and so on. In general, by setting  $\rho_{e\sigma}=1$  and all other density matrix elements to 0, we obtain the  $((\varepsilon-1)N+\sigma)$ th column of the  $M$  matrix where each of  $\varepsilon$  and  $\sigma$  vary from 1 to  $N$ .

Furthermore, it is to be noted that the computation  $H_p - \rho H^+$  involve multiplication of extremely sparse matrices, since only one of the elements of the  $p$  matrix is 1 each time. It is evident that each column of the  $M$  matrix will simply be made up of certain columns of the Hamiltonian. Thus, the task is reduced to (a) figuring out the pattern of columns that are picked out from the Hamiltonian and (b) identify the locations in the  $M$ -matrix, where they would be filled. To illustrate this clearly, it is convenient to treat the calculation of the  $M$ -matrix as arising from two separate computations:  $H_p$  and  $\rho H^+$ . Let us consider a specific

case when  $\rho_{e\sigma}=1$ . The  $\rho H^+$  computations would pick the  $\sigma$ th column of the Hamiltonian (with its elements conjugated) to be placed between rows  $(\varepsilon-1)N+1$  and  $\varepsilon N$  of the  $((\varepsilon-1)N+\sigma)$ th column of the  $M$  matrix. The  $H_p$  computations, on other hand, would pick the elements of the  $\varepsilon$ th column of the Hamiltonian (with the elements picking up an extra negative sign) and populate the following rows of the  $((\varepsilon-1)N+\sigma)$ th column of the  $M$  matrix:  $\sigma$ th row,  $(\sigma+N)$ th row,  $(\sigma+2N)$ th row and so on until the  $(\sigma+N(N-1))$ th row. When, this process is repeated for each element of the density matrix, the  $M$ -matrix, barring the source terms would have been computed.

Finally, the addition of the source terms can also be simplified by choosing to modify the  $M$ -matrix only when one of the diagonal elements of the density matrix is set to 1, i.e.  $\rho_{ee}=1$ , where  $e=1$  to  $N$ . Furthermore, instead of adding the source terms in-line, as was done previously, we can simply pre-define a ‘source matrix’ and simply pick off the elements of this matrix that would then be added to the appropriate entries in the  $M$ -matrix. For example, one way of defining such a ‘source matrix’ would be to have the coefficients of the  $\rho_{ee}$  in all the source equations (from  $d\rho_{11}/dt$  to  $d\rho_{NN}/dt$ ) along the  $e$ th column of the source matrix. Now, all that needs to be done is to simply add the  $e$ th column of the source matrix to the  $((\varepsilon-1)N+\varepsilon)$ th column of the previously computed  $M$  matrix whenever  $\rho_{ee}=1$ . As an illustration of these optimization steps, we reproduce below a modified version of the code for a three-level system, which should be contrasted with the un-optimized code for the same system presented in Appendix 2.

```

oma=1; omb=1;      % express omega rabi freqs, in units of gamma
dels=0;            % common detuning set to zero
N=3;               % number of energy levels
R=401;              % number of points to plot
                    %initialize and set dimensions for all matrices
del=zeros(1,R);    %diff detuning array
M=zeros(N^2,N^2);    %M-matrix
rho=zeros(N,N);      %density matrix
Ham=zeros(N,N);      %Hamiltonian with decay
W=zeros((N^2-1), (N^2-1));    %W-matrix
S=zeros((N^2-1),1);      %S-vector
B=zeros((N^2-1),1);      %B-vector
A=zeros(N^2,R);          %A-vectors, for all detunings
Q_source=[0 0 1/2;
          0 0 1/2;
          0 0 0];

for m=1:R      %start the overall-loop
  del(1,m)=(m-(R+1)/2)/10; %define the detuning
  Ham=[del(1,m)/2 0 oma/2;
        0 del(1,m)*(-1)/2 omb/2; ...
        oma/2 omb/2 (dels+0.5i)*(-1)];

  col=0; % index for column of M-matrix that will filled.
  index1=1:N;
  index2=1:N:N*(N-1)+1;
  index3=1:N+1:N^2;
  for n=1:N      %n keeps track of where in the M matrix the elements of
                  %Ham have to be entered
    for p=1:N %p picks the pth column from the Ham
      col=col+1;
      M(index1+(n-1)*N,col)=li*conj(H(:,p));
      M(index2+p-1,col)=M(index2+p-1,col)-li*(H(:,n));
      if n==p
        M(index3,col)=M(index3,col)+Q_source(:,n);
      end
    end      %end the inner-loop for finding elements of M
  end
  S=M(1:(N^2-1),N^2:N^2);      %find S-vector
  W=M(1:(N^2-1),1:(N^2-1));    %initialize W-matrix

  for d=1:(N-1)
    W(:,((d-1)*N+d))=W(:,((d-1)*N+d))-S; %update W by subtracting
                                                %from selected columns
  end

  B=(W\S)*(-1);          %find B-vector: primary solution!

  rhonn=1;                %initialize pop of N-th state
  for f=1:(N-1)
    rhonn=rhonn-B(((f-1)*N+f), 1);
  end

  A(1:(N^2-1),m)=B;
  A(N^2,m)=rhonn;
  M=zeros(N^2,N^2);
end      %end of over-all loop
plot(del,real( A ( (N^2-0),: ) ) )

```